

CASI

NASA Grant Report

11-45-12

63418

218 p.

## **Study of Application of TRMM Data to the Study of African Climate**

**Sharon E. Nicholson**  
Department of Meteorology  
Florida State University  
Tallahassee, FL 32306-3034

NASA GRANT NAG 5-1587  
MAY 1991

FSU Budget No. 1338-634-26

## Table of Contents

### Final Report

#### Appendix

- A "Temporal and Spatial Variability of Surface Radiation Budget over the African Continent as derived from METEOSAT. Part I: Derivation of Global Solar Irradiance and Surface Albedo" by M.B. Ba, G. Dedieu, and S.E. Nicholson
- B "Temporal and Spatial Variability of Surface Radiation Budget over the African Continent as derived from METEOSAT. Part II: Climatologies and Interannual Variability of Surface Global Solar Irradiance, Albedo and Net Radiation" by M.B. Ba and S.E. Nicholson
- C "Contrasting Conditions of Surface Water Balance in Wet Years and Dry Years as a Possible Land Surface-Atmosphere Feedback Mechanism in the West African Sahel" by A.R. Lare and S.E. Nicholson.
- D "Satellite-Derived Interannual Variability of West African Rainfall during 1983-88" by M.B. Ba, R. Frouin, and S.E. Nicholson.
- E "Reduction of bidirectional effects in NOAA/AVHRR data acquired during the HAPEX-SAHEL Experiment" by M.B. Ba, G. Dedieu, Y.H. Kerr, S.E. Nicholson, and J. Lecocq.
- F "Rainfall in the Sahel during 1994" by S.E. Nicholson, M.B. Ba, and J. Kim.
- G "On the Use of NDVI for Estimating Rainfall Fields in the Kalahari of Botswana" by J. Grist, S.E. Nicholson, and A. Mpolokang.
- H "The mean surface water balance over Africa and its interannual variability" by S.E. Nicholson, J. Kim, and M.B. Ba.

## 1.0 Introduction

During the course of our TRMM investigation, we made considerable progress in six areas. These include the creation of a basic geographic information system (GIS) for Africa, satellite assessments of rainfall, surface radiation balance, water balance and its interannual variability, the potential dynamic effects of latent heating of the atmosphere, and improvements in our surface energy and water balance model.

Surface radiation balance parameters were assessed from satellite information, water balance from the afore-mentioned model. During the considerable time lapse between our current studies and the availability of TRMM data, we anticipate further model improvements. For this reason, we have produced preliminary estimates of surface water balance and have emphasized a) the production of a data base to be used in modelling efforts and b) the development of a model which readily lends itself to improvements in parameterization and in the incorporation of TRMM data, as they become available.

For the TRMM project as a whole, the data base may be the most important product of this investigation. The investigation has resulted in seven relevant articles submitted to or appearing in journals, six additional articles for which partial support was provided, and two currently in preparation and soon to be submitted. These are listed at the end of this report. Copies of the most relevant articles are included in the appendix.

## 2.0 GIS for Africa

Perhaps the most important product of our TRMM project is the data base we produced, consisting of geographic and climatic information for Africa. This will become available via an anonymous FTP server to all interested individuals. It should provide information that is useful for both input and verification of climate models. It will also provide rainfall data for verifying TRMM results.

Since our own work has focused on an approximately 1400 station network of rainfall data, we have attempted to organize the data base around these stations. Wherever possible, geographic and climatic parameters are given for each station. In view of the goal of the TRMM mission to produce areally averaged data, we have also produced a coarser resolution gridded data set consisting of areal averages, as derived from available station data or based on interpolation for the roughly 70 % of the grid-squares containing no stations. The areal averages are simple arithmetic averages of all stations in each 1 by 1 degree square. Interpolation is performed using NCAR's BIVAR package (Bivariate Interpolation and Smooth Surface Fitting).

An overview of the data base is presented in Fig. 1. The geographic information consists of soil type, soil texture and vegetation type. Information is stratified by station. Soil type is taken from the FAO soils map for Africa. Soil texture is taken from works of Zabler and Webb et al.. Vegetation type is taken from White's vegetation map of Africa. The climatic data include rainfall and PET (monthly and annual means) and both station and gridded data are included. Rainfall is from the P.I.s archive. PET is from FAO's two volumes of agriclimatological data for Africa and is calculated using the Penman formula, with interpolated values calculated for the stations not available through FAO.

Rainfall is the most extensive parameter in the data base. We have in our archive monthly data since the beginning of observations for nearly 1400 African stations. The records for over three quarters of the stations begin prior to 1925 and most extend to at least 1990, so that calculated parameters are generally based on at least 65 years. The individual monthly data are not included, but monthly and annual means, standard deviations and coefficients of variation are. Additionally, because the TRMM mission will collect data for 5 years, we have calculated for each station the maximum and minimum rainfall for any consecutive five-year period and the variance of these five-year means. These will help to assess the validity of rainfall data assessed during a relatively brief period by the TRMM satellite.

Satellite data were used to derive incident solar radiation, surface albedo, longwave fluxes, and surface net radiation. Due to the expense of obtaining appropriate data, these were derived for several months from daily limited samples. All months were available from July 1983 to July 1988 except July 1987 and December 1983. Included in the data base are gridded mean values (1 degree by 1 degree) of global radiation at the surface, surface albedo, and surface net radiation for January, April, July, October and the annual mean. Longwave data, provided by Darnell et al. and used to produce the net radiation data, are not included in the FTP data base.

Using a significantly revised version of Lettau's climatology model (see Nicholson et al., 1996), we have produced station-specific and gridded values of surface water balance parameters (Fig. 1). Only the gridded data are available via the FTP server. These include mean of evapotranspiration, runoff, and soil moisture for January, July and the whole year. The dryness ratio and evaporation and runoff ratios are calculated for annual data only.

### 3. Rainfall Assessment

We have applied satellite methodologies to the assessment of rainfall over various sectors of Africa (Fig. 2). In the first case, rainfall over the Sahel during the years 1983 to 1988 was estimated and analyzed using two cloud-based methods: cold-cloud frequency and mean infrared radiances. For annual rainfall, both methods were able to account for over 80% of the variance throughout the region (Ba et al., 1995). This study also demonstrated the accuracy of the methods in evaluating the interannual variability of rainfall and its usefulness in analyzing the interannual variability of the ITCZ (both position and intensity).

These methods were later applied to evaluating more recent rainfall conditions. They were particularly useful in assessment rainfall conditions during 1994, a year claimed by some to be the wettest in at least 30 years. The satellite methods were useful in evaluating conditions over the eastern Sahel, in an area nearly devoid of rainfall stations, and in documenting conditions during 1994 in detail (Ba, Nicholson and Kim, 1996).

We have also applied these methods to studying the interannual variability of the Sahel-Sahara boundary, in the context of assessing claims concerning long-term desertification. The study (Nicholson, Tucker and Ba, 1996) demonstrated that this boundary, as assessed from vegetation index data (NDVI), exhibits fluctuations closely paralleling rainfall changes. This clearly negates the concept of a long-term "advance" of the desert.

A different methodology was applied to assessing rainfall over Botswana, in southern Africa. Much of the country consists of the desolate Kalahari "desert", a



sparsely populated semi-desert region nearly devoid of rainfall stations. We produced a map of mean annual rainfall conditions in this area (Fig. 3), with rainfall "predicted" (Fig. 4) on the basis of regressions between rainfall and NDVI (Nicholson, Grist and Mpolokang, 1996). The result provided much more detail about the region's rainfall than was available from conventional station data.

#### 4. Surface Radiation Balance

We have produced monthly mean data of global solar irradiance and surface albedo over the African continent at  $\sim 0.25^\circ$  latitude  $\times$   $0.25^\circ$  longitude using a physically based method (Ba et al., 1996, Ba and Nicholson, 1996). Monthly mean surface net radiation data were also produced at  $2.5^\circ$  latitude  $\times$   $2.5^\circ$  longitude using a complementary data on surface net radiation estimates from Darnell et al. (1992). The monthly mean datasets were obtained using data collected during the period of July 1983 through July 1988; during the time of processing the data for December 1983 and July 1987 were missing. Our results were compared with other satellite based estimates namely those of Darnell *et al.* (1992), Pinker and Laszlo (1992) and Bishop and Rossow (1991). Agreement is good between our estimates of global solar irradiance and all other estimates. The agreement is particularly good between our estimates and those of Darnell *et al.* (1992) with biases less  $5 \text{ Wm}^{-2}$ . Good agreement was also obtained between our surface albedo estimates and those of Darnell et al. (1992) which represent clear-sky albedo obtained from broadband ERBE data. Figures 5 and 6 present the mean annual global solar irradiance and the mean annual surface albedo at  $1^\circ$  latitude  $\times$   $1^\circ$  longitude. Figure 7 presents the mean surface net radiation at  $2.5^\circ$  latitude  $\times$   $2.5^\circ$  longitude.

This study has produced some surprising results. One is the complex relationship between surface albedo, rainfall and vegetation. It is generally assumed that dry season albedo is higher than wet season albedo, but our results showed this to be the case only in semi-arid regions with relatively sparse vegetation cover. In more humid regions or semi-arid regions with dense vegetation, the wet season albedo is higher. Secondly, we have found unexpected large interannual variability in regions of relatively stable climate, such as the Saharan desert. In general, this result suggests the need for improved correction of the radiation data for water vapor and aerosols. Finally, our study showed that calibrations in current use appear to be in error. Thus, if satellite data are to be applied to studying the interannual variability of radiative parameters, improvements must be made in both calibration and atmospheric corrections.

#### 5. Water Balance

We have used the climatonomy model to produce mean estimates of surface water balance parameters over the African continent. Precipitation, total runoff, evapotranspiration and soil moisture are estimated on an annual basis and for the most extreme months, January and July. Annual maps for runoff, ET and soil moisture are presented in Figs. 8, 9 and 10.

The results (Nicholson, Kim, Ba and Lare, 1996) indicate that ET generally exceeds  $1500 \text{ mm/an}$  in the equatorial regions, with a few areas where ET is in excess of  $2000 \text{ mm/an}$ . It ranges from about  $500$  to  $750 \text{ mm/an}$  in the semi-arid regions of eastern Africa and about  $200$  to  $750 \text{ mm/mo}$  in the semi-arid regions of the

subtropics. On a monthly scale, maxima are on the order of 100 mm/mo or more. It is on the order of 5 to 50 mm/an in the semi-arid regions bordering the deserts. Runoff is about 200 to 500 mm/an in the equatorial latitudes, but generally less than 50 mm/an in semi-arid regions of Africa. It approaches zero for mean annual rainfall below 500 mm.

Interannual variability is particularly large for ET. In some areas, the difference between wet and dry years exceeds 500 mm/an; it can exceed 250 mm/an over much of the continent. Runoff can vary by over 100/an from year to year in wetter regions of West Africa. In the equatorial latitudes, even zonal means can vary by over 200 mm/an, compared to a long-term mean on the order of 350 mm/an. In the semi-arid sub-equatorial latitudes, the zonal means can vary by 100 to 150 mm/an.

Overall, there is good agreement between our calculations of ET and those of several other studies. Nevertheless, a considerable range of values for the African continent appears in the literature. Some earlier studies appear to have dramatically underestimated both soil moisture and ET. This is partly a consequence of the relatively low values of net radiation obtained from traditional formula, as compared to modern satellite estimates.

## 6. Relation between Water Balance and Latent Heating: a Sahel Case Study

Lare and Nicholson (1994) calculated the surface water balance for large areas of West and Southern Africa, in order to evaluate the importance of latent heating as a possible land-atmosphere feedback mechanism. The surface latent heat flux was determined for wet and dry years. For the Sahel, calculations were done for surface fields and also for a transect running from the desert to the humid regions to the south. One important result is the demonstration of a large change in the north-south gradient of latent heat flux between wet years and dry years, because higher rainfall in the wetter regions to the south is translated into increased runoff, with little change of evapotranspiration. Based on a crude atmospheric heating model and considerations of thermal wind, the work showed that the change of wind speed in the area of the African Easterly Jet, as a result of the change in this gradient, is roughly comparable to that between wet years and drought years. This implies that surface effects are significant enough to affect the large-scale atmospheric forcing in the region.

We hope that this problem can be continued when TRMM data become available. The latent heating profile can allow us to produce a much more realistic calculation of the effect of surface latent heat flux on atmospheric processes.

## 7. Model Improvements

During the course of the TRMM project, the climatology model of surface water balance was improved in several ways. The empirical relationships were converted to physical ones and the surface hydrology was made more realistic. An improved runoff formulation was developed. Some of these improvements are described in Lare and Nicholson (1994) and in Nicholson, Lare, Marengo and Santos (1996). More recent ones will be described in the paper dealing with surface water balance over Africa (Nicholson, Kim, Ba and Lare, 1996).

We are at present still working on an improved parameterization of runoff. It utilizes rainfall intensity information deduced from monthly data. A regression is developed based on the frequency distribution of rainfall events of various intensities as a function of monthly total. Thus, for such a runoff formulation the TRMM data on rainfall intensity can play a major role. It has the potential to dramatically improve GCM calculations of surface runoff, one of the weakest aspects of current models.

## 8. Other Efforts Receiving Some TRMM Support

During the course of the TRMM investigation, Dr. Mamoudou Ba received most of his support from TRMM. In addition the working on projects directly related to TRMM, as indicated above, Dr. Ba also did some work on correction of vegetation index data (Ba et al., 1996). This will ultimately be relevant our future work which grows out of the TRMM project. We will use TRMM rainfall estimates in our work balance work and in examining vegetation-water relationships. The corrected data set will give us better results.

There was much synergism between our TRMM project and our HAPEX-Sahel work. The common denominator is the surface energy and water balance model which we developed and utilized to study conditions over Africa. The model was improved and validated, using joint support from the two projects. HAPEX-Sahel experimental data was used for the validation.

## 9. Dissemination of Results

### 9.1 Published Works

- 1994 Contrasting conditions of surface water balance in wet years and dry years as a possible land surface-atmosphere feedback mechanism in the West African Sahel. *Journal of Climate*, 7, 653-668 (A.R. Lare and S.E. Nicholson).
- 1995 Satellite-derived interannual variability of West African rainfall 1983-88. *Journal of Applied Meteorology* (M. B. Ba, R. Frouin, S. E. Nicholson), 34, 411-431.
- 1996 Reduction of bidirectional effects on NOAA/AVHRR data acquired during HAPEX-SAHEL Experiment (M. Ba, G. Dedieu, Y. H. Kerr and S. E. Nicholson). *Journal of Hydrology*, in press.
- 1996 Application of evapoclimatology to surface energy and water balance at the HAPEX-Sahel supersites. Daily resolution of water balance parameters (J. A. Marengo, S. E. Nicholson, and A.R. Lare). *Proceedings of the Conference on Hydrology*, American Meteorological Society, 137-140.
- 1996 Application of Evapoclimatology to monthly surface water balance at the HAPEX-Sahel supersites. In press, *Journal of Applied Meteorology* (J.A. Marengo, S.E. Nicholson, A. R. Lare, B. A. Monteny, S. Galle).

- 1995 A simple model of vegetation-atmosphere interactions (S.E. Nicholson and P. Santos). *Proceedings of the Conference on Hydrology*, American Meteorological Society, 129-132.
- 1996 A revised version of Lettau's Evapoclimatology model (S.E. Nicholson, A.R. Lare, J.A. Marengo, P. Santos). In press, *Journal of Applied Meteorology*.
- 1996 A daily resolution Evapoclimatology model applied to surface energy and water balance calculations at the HAPEX-Sahel supersites (S.E. Nicholson, J. A. Marengo, J. Kim, A.R. Lare, S. Galle, and Y. Kerr). In press, *Journal of Hydrology*.
- 1996 Rainfall in the Sahel during 1994 (S. E. Nicholson, M. B. Ba, J.Kim). In press, *J. Climate*.
- 1996 On the use of NDVI for estimating rainfall fields over the Kalahari of Botswana (S. E. Nicholson, J. Grist, A. Mpolokang). In press, *Journal of Arid Environments*.
- 1996 Temporal and spatial variability of surface radiation budget over the African continent as derived from Meteosat. Part I: Derivation of global solar irradiance and surface albedo (M. B. Ba, G. Dedieu, S. E. Nicholson). Submitted to *J. Climate*.
- 1996 Temporal and spatial variability of surface radiation budget over the African continent as derived from Meteosat. Part II: Climatology and interannual variability of surface global solar irradiance, albedo and net radiation (M. B. Ba and S. E. Nicholson). Submitted to *J. Climate*.
- 1996 The mean surface water balance over Africa and its interannual variability (S. E. Nicholson, J. Kim, M. B. Ba and A. R. Lare), Submitted to *J. Climate*.

## 9.2 Work in Progress

- 1996 Use of the Normalized Difference Vegetation Index (NDVI) to examine the question of desert advance over West Africa (S. E. Nicholson, M. B. Ba, C. J. Tucker).
- 1996 A re-examination of Budyko's dryness ratio concept and other water and energy balance parameters, as related to global vegetation formations.

## CAPTIONS

Figure 1: Chart flow of the Geographic Information System for the African continent.

Figure 2: Spatial distribution of 6-yr (1983-88) mean seasonal rainfall derived from cold cloud frequency in  $1^{\circ} \times 1^{\circ}$  grid boxes.

Figure 3: Spatial distribution of 11-yr mean annual rainfall derived from NDVI over BOTSWANA. The delineated areas represent different soil types. For each soil type, specific predictive regression was used.

Figure 4: Time series of estimated monthly rainfall and observed monthly rainfall 1982-1993 using predictive regression equations specific to each soil type.

Figure 5: Spatial distribution of 6-yr (1983-88) mean global solar irradiance ( $\text{Wm}^{-2}$ ) over the African continent in  $1^{\circ} \times 1^{\circ}$  grid boxes.

Figure 6: Spatial distribution of 6-yr (1983-88) surface albedo (%) over the African continent in  $1^{\circ} \times 1^{\circ}$  grid boxes.

Figure 7: Spatial distribution of 6-yr (1983-88) mean surface net radiation ( $\text{Wm}^{-2}$ ) over the African continent in  $2.5^{\circ} \times 2.5^{\circ}$  grid boxes.

Figure 8: Spatial distribution of mean annual evapotranspiration computed at the surface network stations.

Figure 9: Spatial distribution of mean annual runoff computed at the surface network stations.

Figure 10: Spatial distribution of mean annual soil moisture computed at the surface network stations.

## OVERVIEW OF THE GIS SYSTEM

### GEOGRAPHIC DATA

#### STATION DATA, 1338 AFRICAN STATIONS

- SOIL TYPE
- SOIL TEXTURE
- VEGETATION TYPE

### CLIMATE DATA

#### STATION AND GRIDDED DATA (1 ° x 1 °)

##### RAINFALL

- Monthly and annual means
- Minimum and maximum means of five consecutive years
- Variance of five-year annual and monthly means

##### POTENTIAL EVAPOTRANSPIRATION

### MODELLED/REMOTELY SENSED DATA

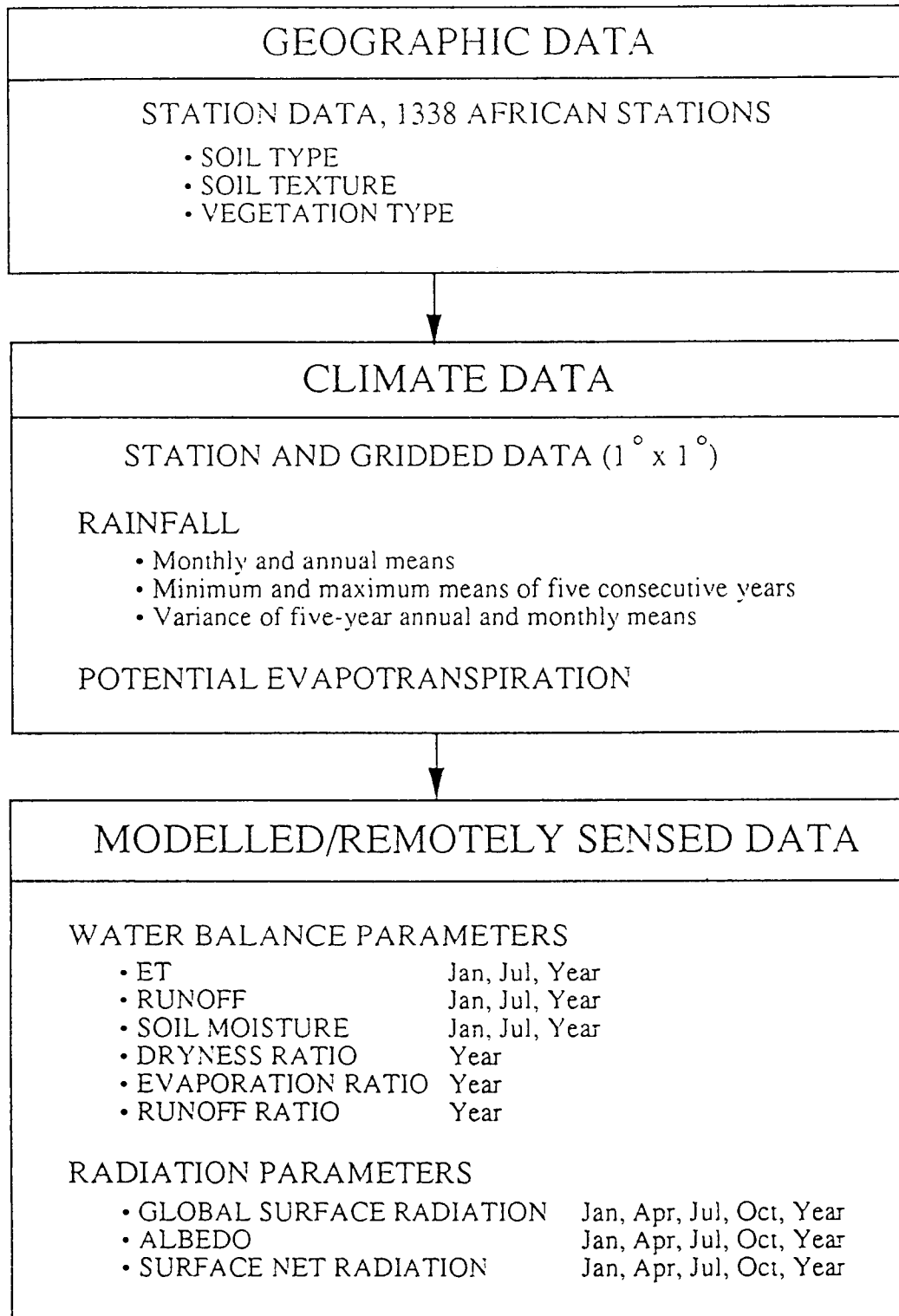
#### WATER BALANCE PARAMETERS

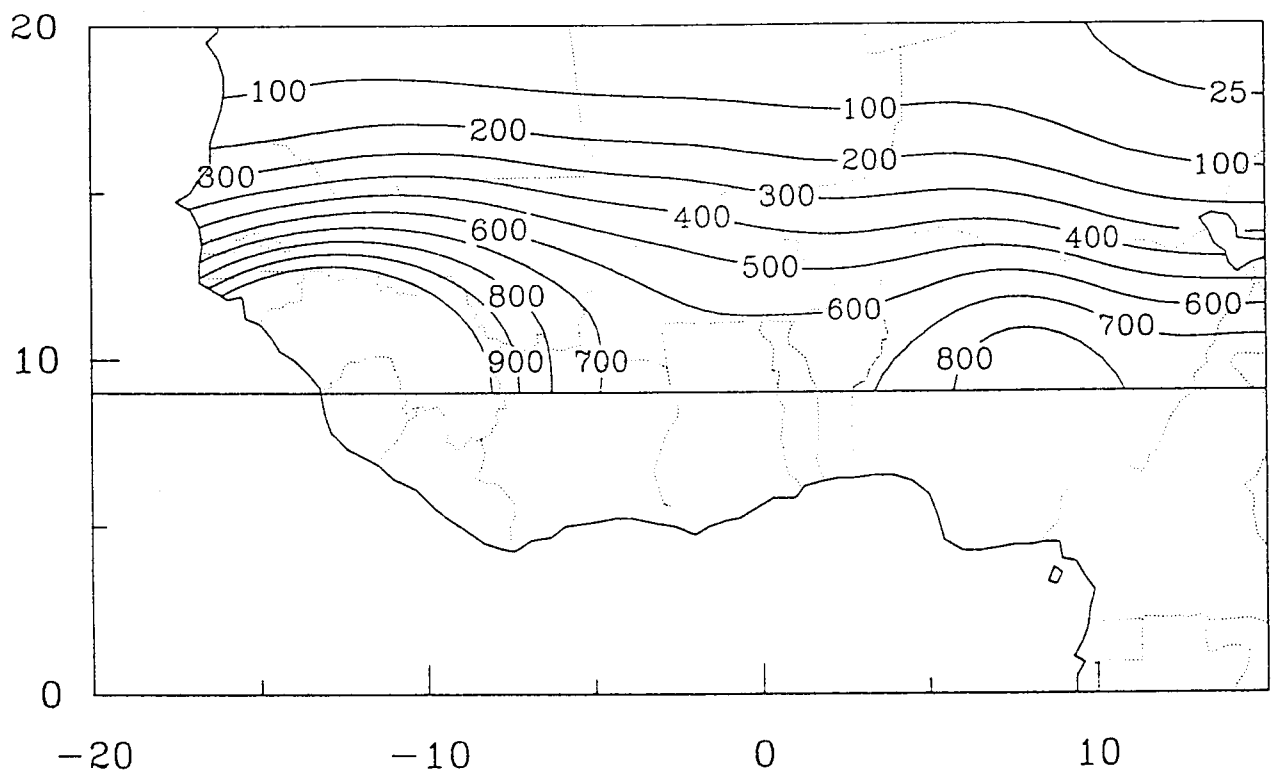
- ET Jan, Jul, Year
- RUNOFF Jan, Jul, Year
- SOIL MOISTURE Jan, Jul, Year
- DRYNESS RATIO Year
- EVAPORATION RATIO Year
- RUNOFF RATIO Year

#### RADIATION PARAMETERS

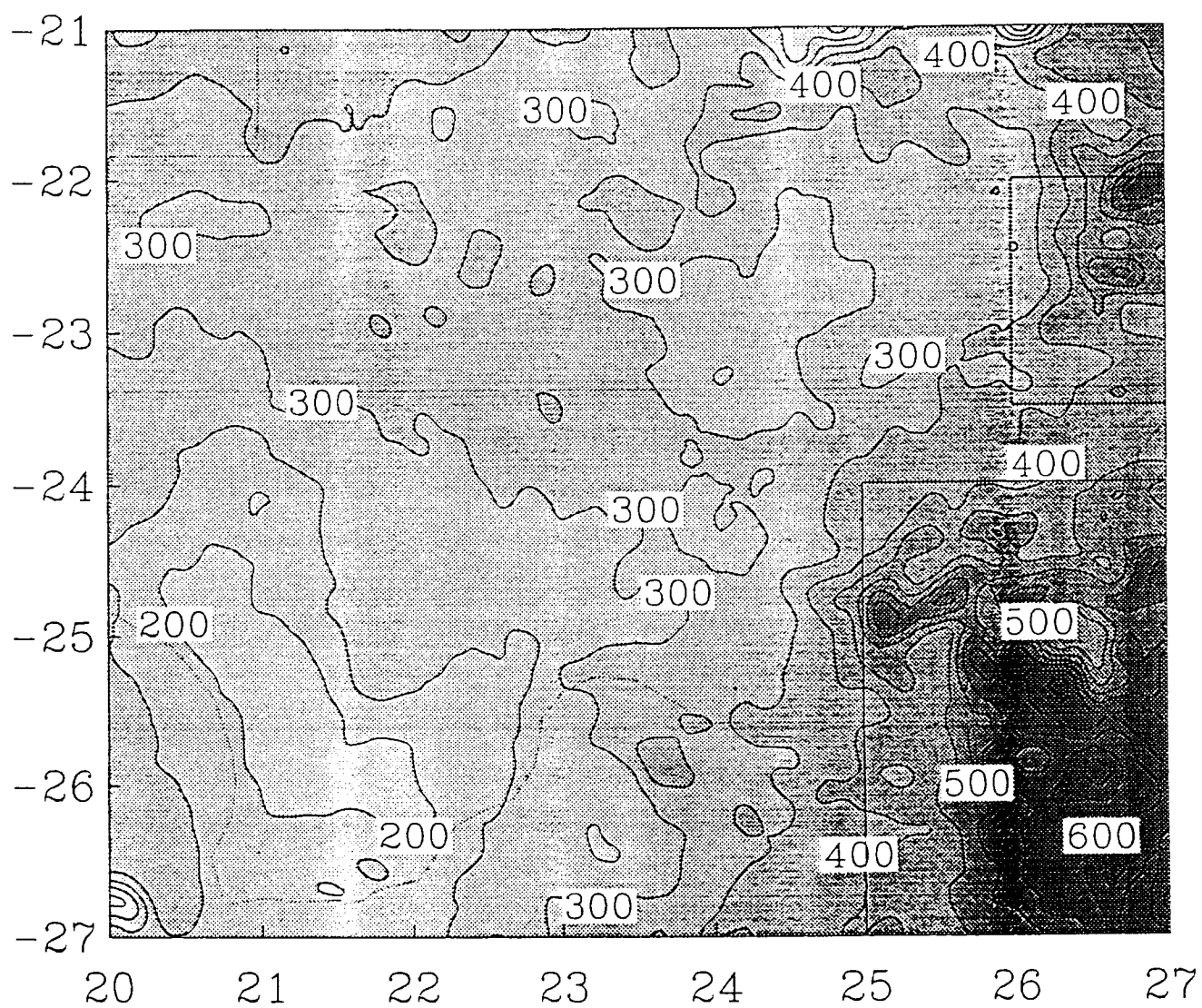
- GLOBAL SURFACE RADIATION Jan, Apr, Jul, Oct, Year
- ALBEDO Jan, Apr, Jul, Oct, Year
- SURFACE NET RADIATION Jan, Apr, Jul, Oct, Year

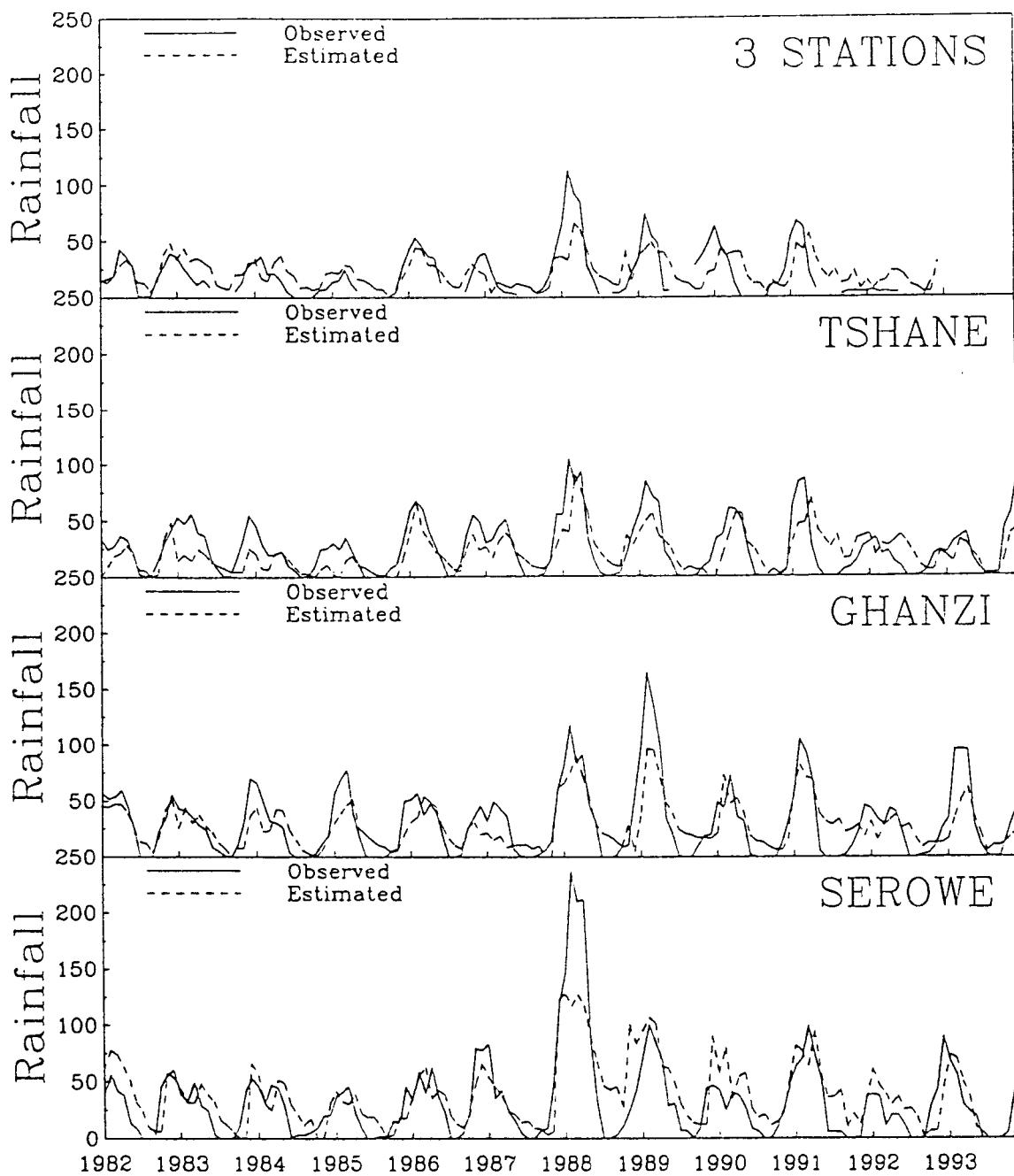
# OVERVIEW OF THE GIS SYSTEM

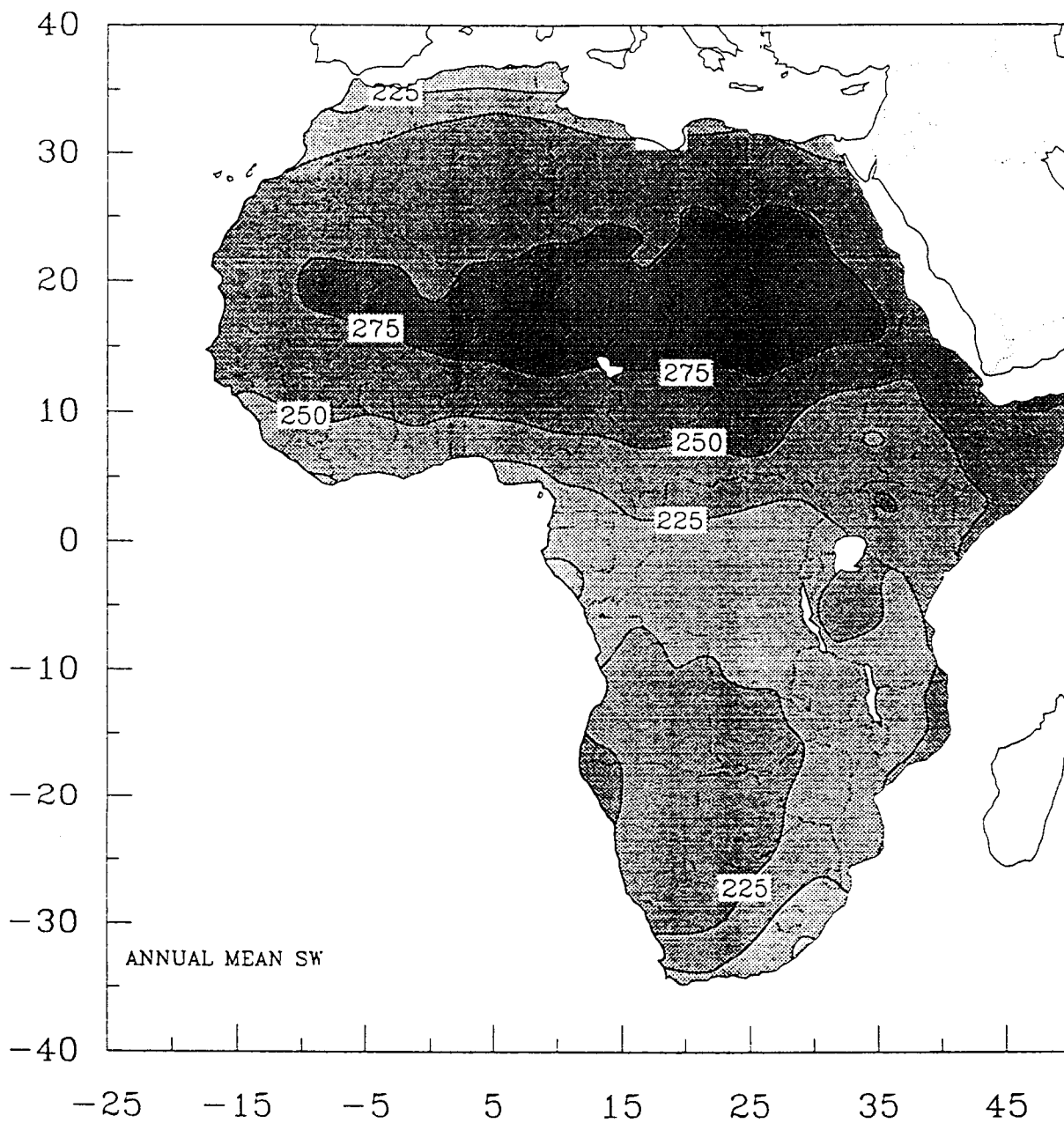


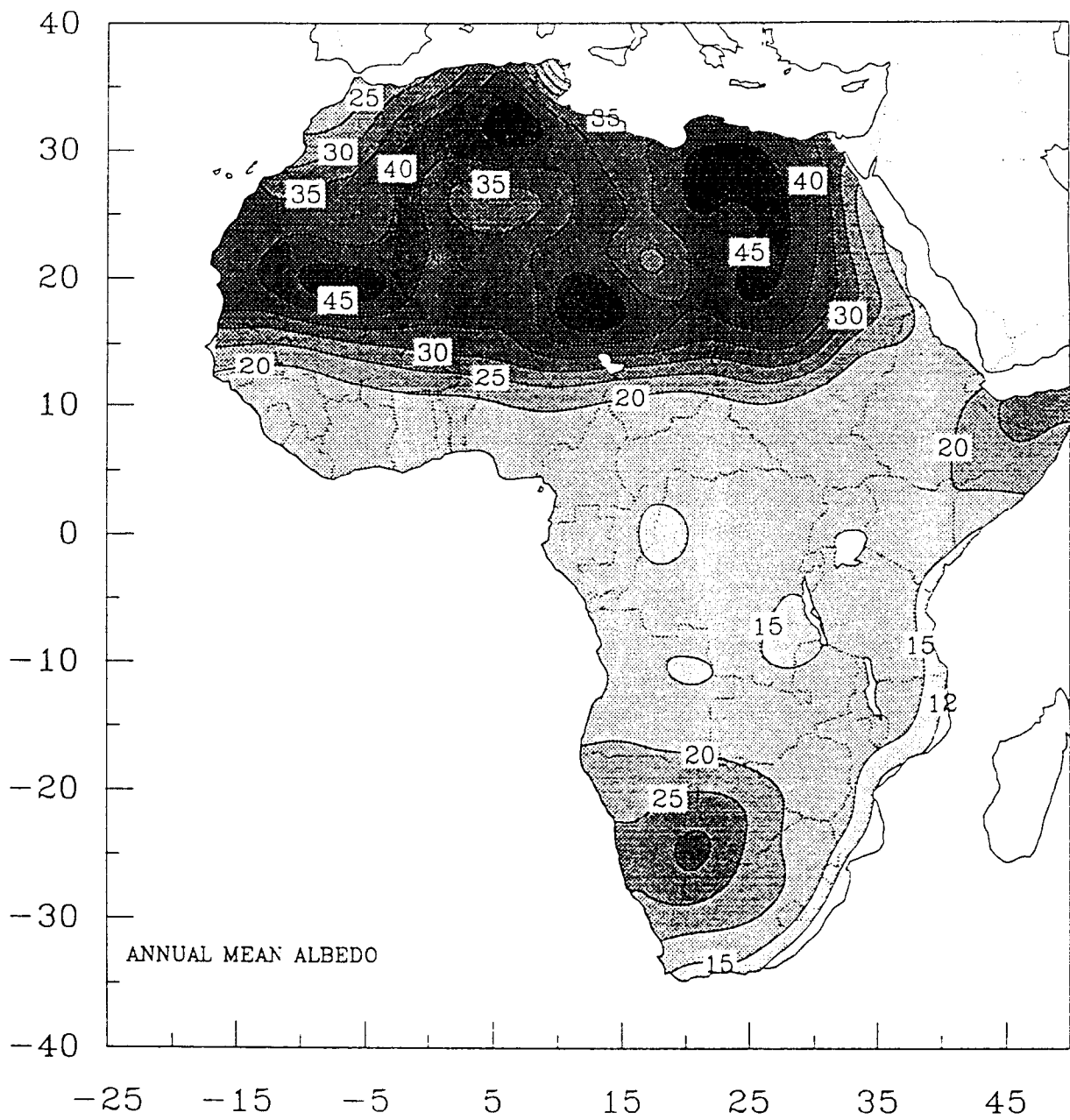


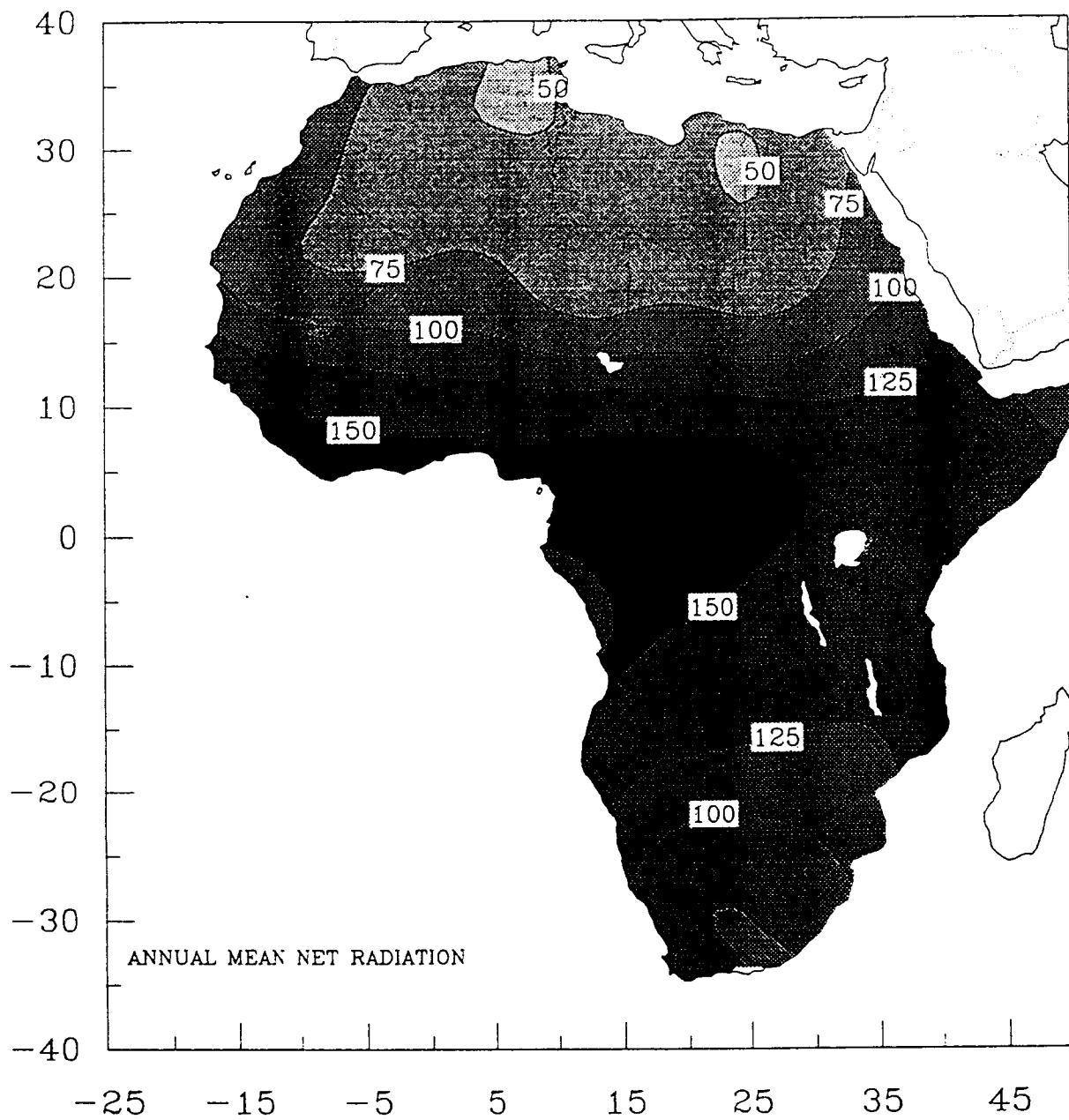


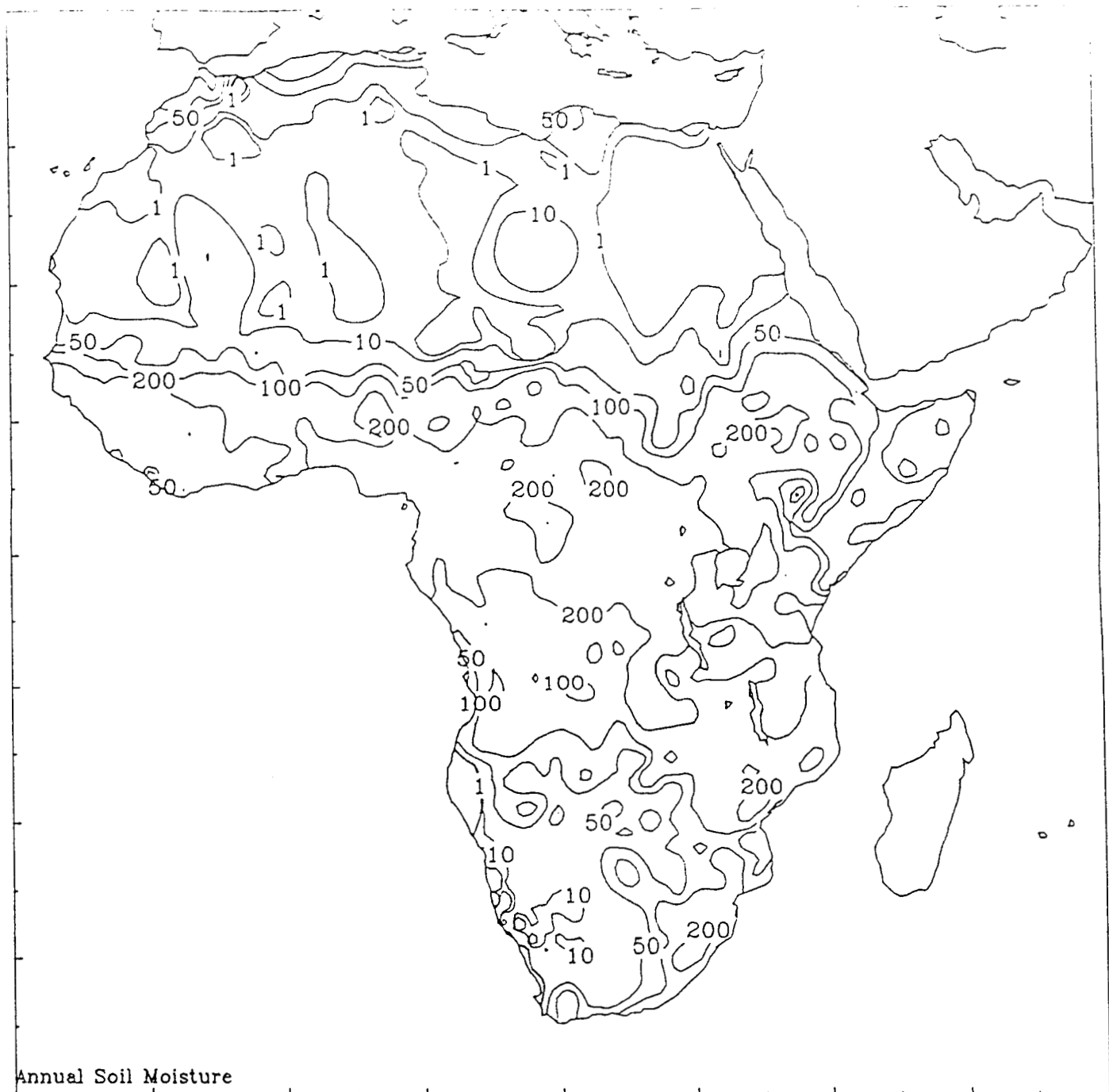




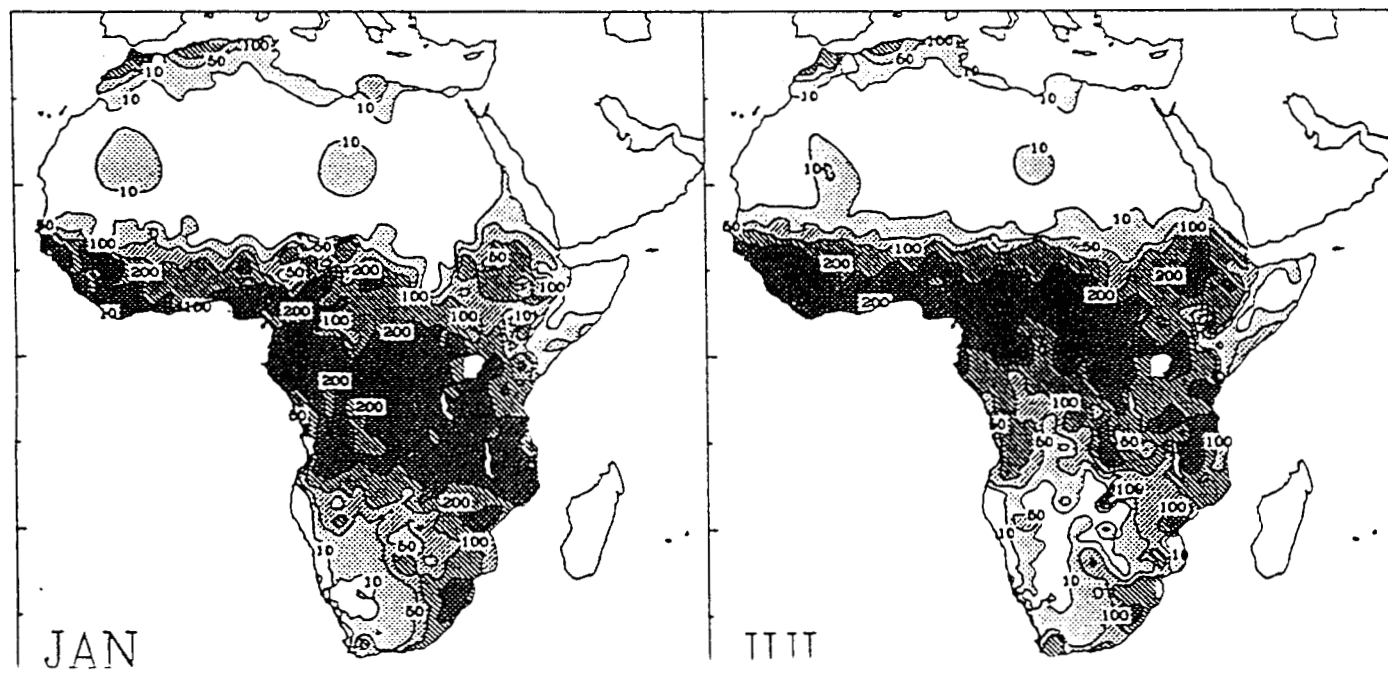


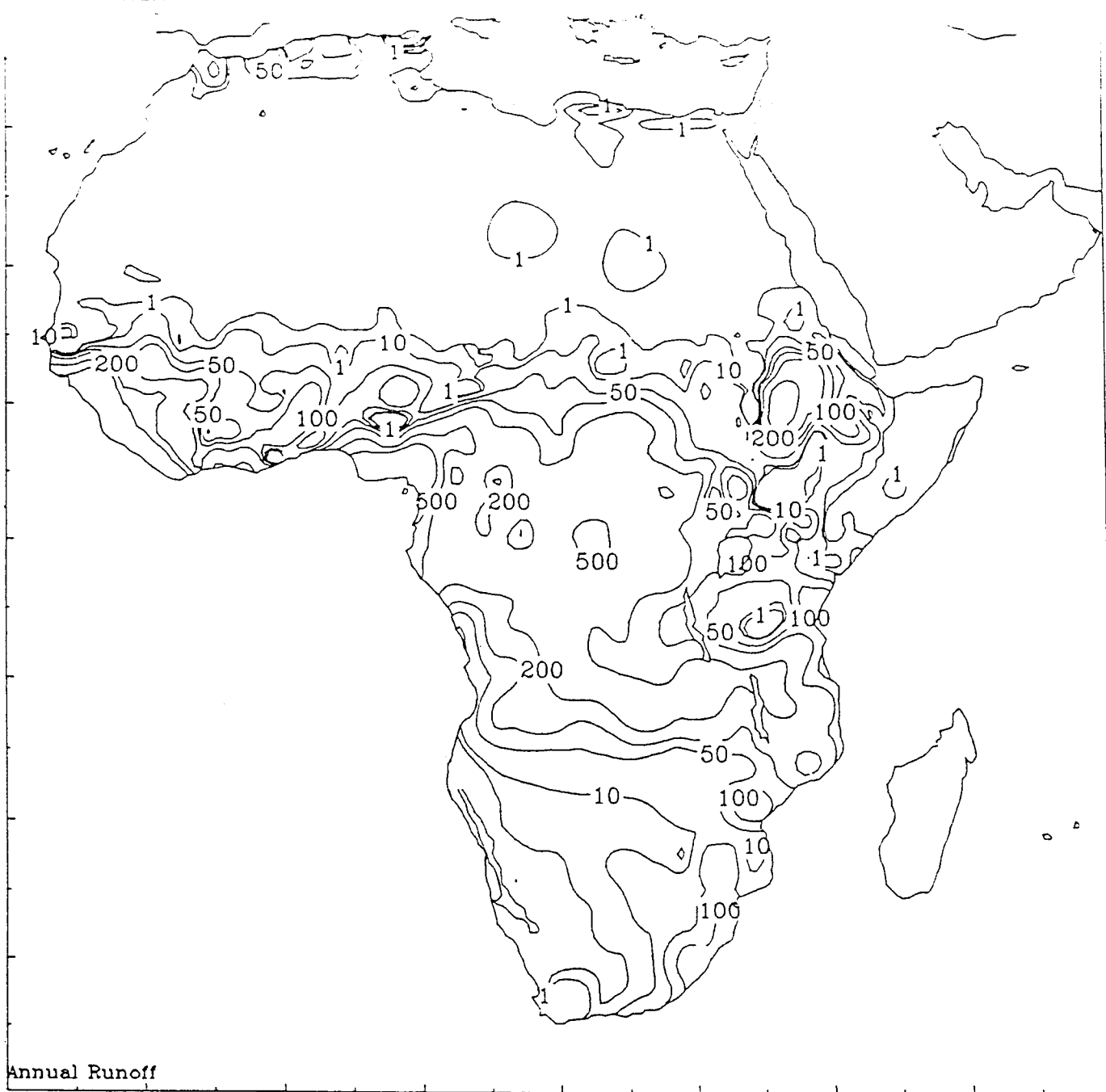




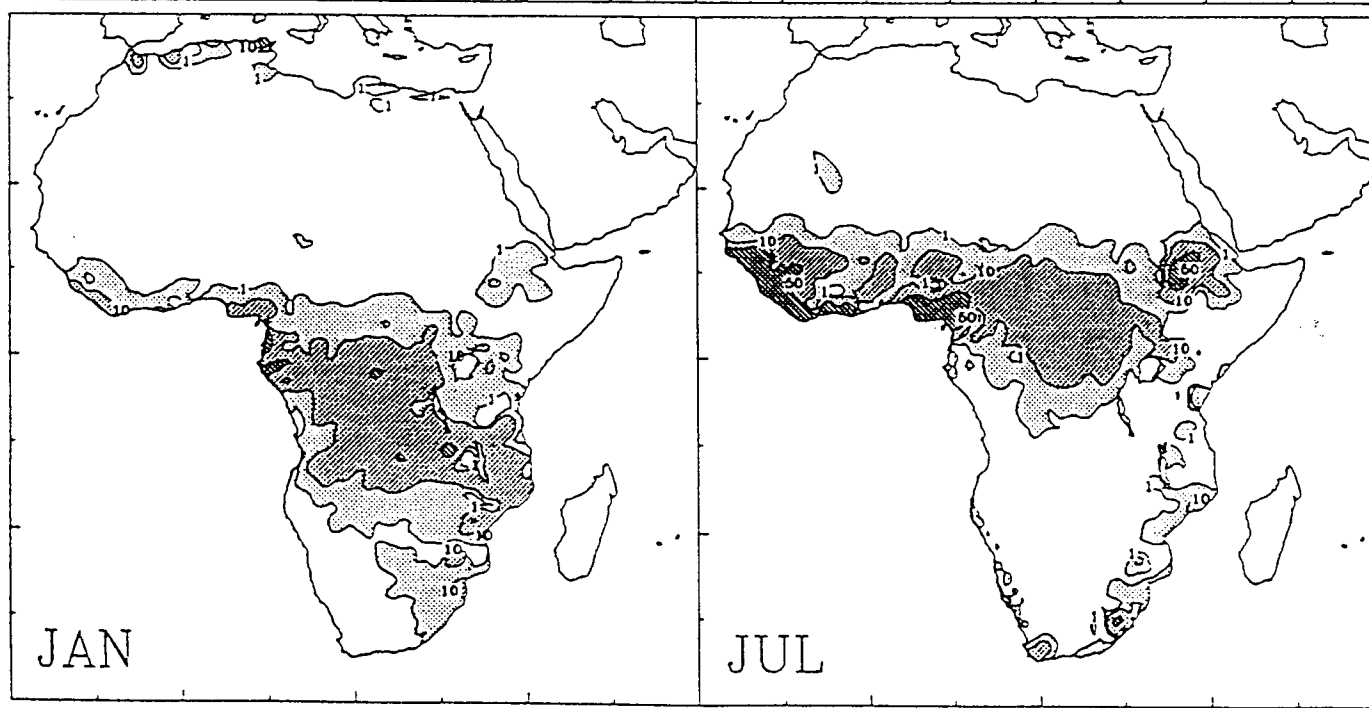


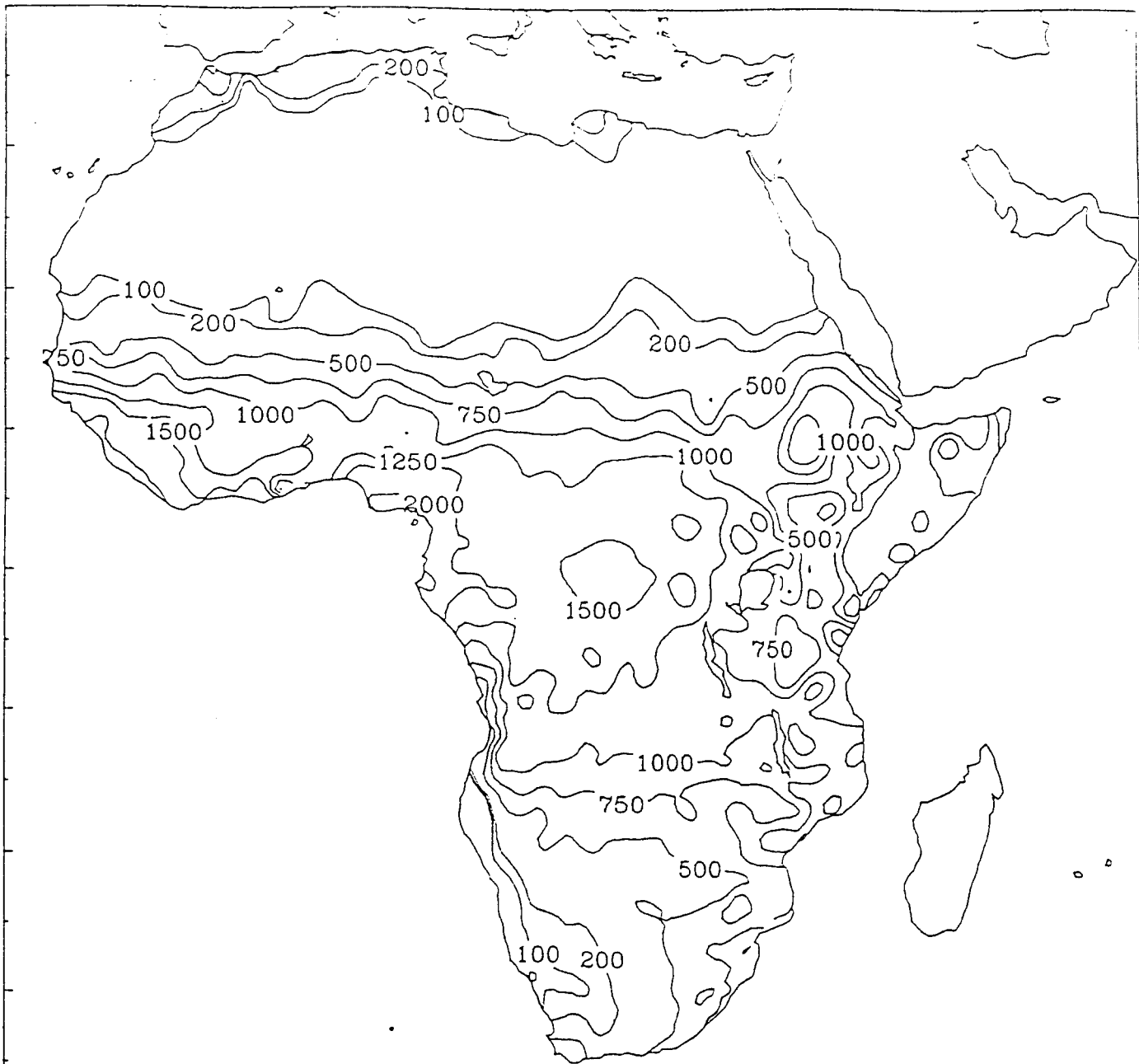
Annual Soil Moisture



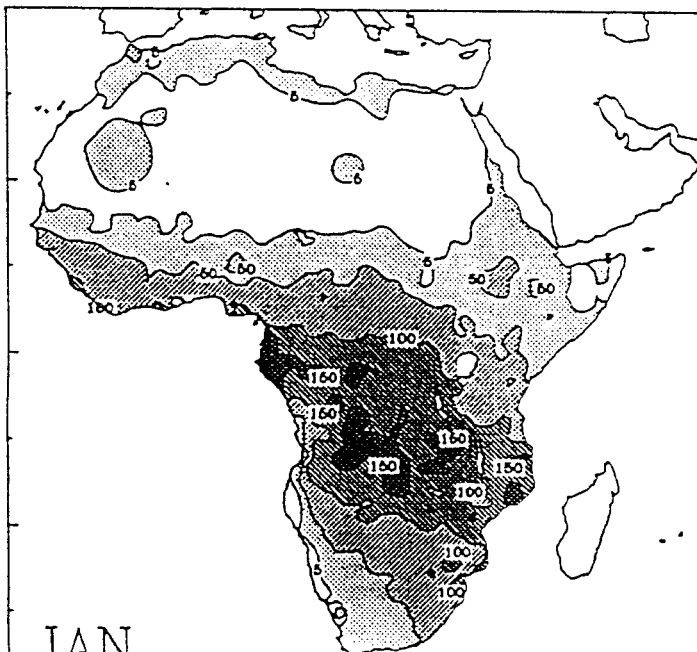


Annual Runoff

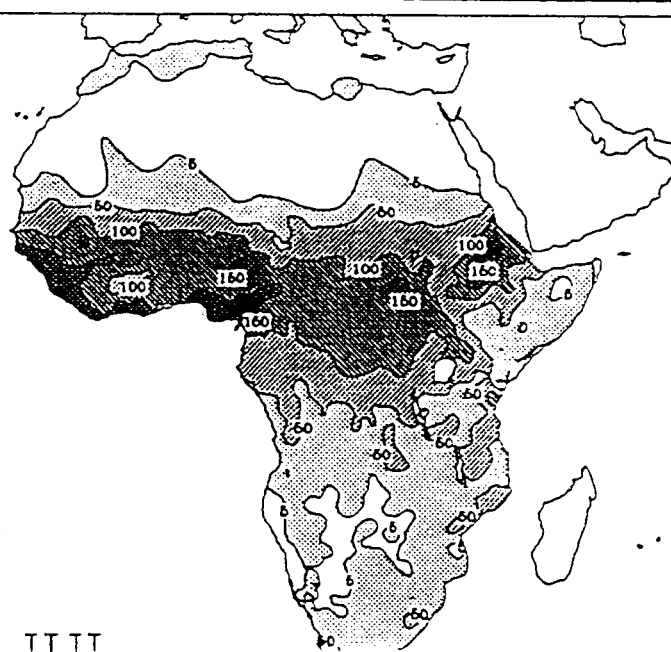




Annual Evapotranspiration



JAN



TTTT



## **Appendix A**

### **Temporal and Spatial Variability of Surface Radiation Budget over the African Continent as derived from METEOSAT. Part I: Derivation of Global Solar Irradiance and Surface Albedo**

Temporal and Spatial Variability of Surface Radiation Budget over the African  
Continent as derived from METEOSAT.

Part I: Derivation of Global Solar Irradiance and Surface Albedo.

Mamoudou B. Ba<sup>1</sup>, Gérard Dedieu<sup>2</sup>, and Sharon E. Nicholson<sup>1</sup>

March, 1996

---

<sup>1</sup> Department of Meteorology, Florida State University, Tallahassee, FL 32306-3034

<sup>2</sup> CESBIO, 18 av. E. Belin, 31055 Toulouse Cedex, France

## ABSTRACT

In this paper, a physically based model is used to derive global solar irradiance and surface albedo. METEOSAT B2 data for the period 1983-88 were used. A simple linear function involving the cosine of the Solar Zenith Angle (SZA) is shown to adequately correct the directional effects on surface albedo due to seasonal variations of the SZA. The results show that for a known constant-radiance target in the Libyan desert, the clear-sky TOA (Top Of Atmosphere) reflectance computed using the ISCCP (Satellite Cloud Climatology Project) calibration varies significantly over time. This suggests an error in the ISCCP calibration. Here an adjustment is performed to minimize these errors due to calibration uncertainties using this site as a constant-radiance target. This allows the removal of the interannual variability in surface albedo due to that of the calibration. The results of global solar irradiance and surface albedo are compared with those obtained by other algorithms. These comparisons show that our results agree well with two of these algorithms, namely those using the ERBE broadband albedo in the short-wave radiation retrieval scheme. Some differences were found with two other algorithms that use vegetation type dependency to convert from narrowband to broadband albedo.

## 1. Introduction

Better scientific understanding and predictive capabilities for climate fluctuations depend, in part, upon improvements in the modeling of land surface processes. This requires a good knowledge and extensive description of surface properties at reasonable time and space scales. Among others, the Surface Radiation Budget (SRB) components are essential parameters for such a description. For instance, large scale modification of surface albedo can alter the surface energy balance sufficiently to influence surface temperature. This, in turn, might modify the general atmospheric circulation patterns. In particular, surface albedo has been of interest in the African drought problem because of the hypothesis of Charney (1975) and others that increased surface albedo accompanying drought or human-induced desertification, might exacerbate or even trigger drought.

Satellite data offer a unique opportunity to build the necessary observational base of SRB components. Numerous attempts at estimating surface radiative fluxes from satellite data have been made (e.g., Tarpley 1979, Gauthier *et al.* 1980, Pinker and Ewing 1985, Raschke *et al.* 1987, Dedieu *et al.* 1987a, Darnell *et al.* 1988, Darnell *et al.* 1992, Gupta 1989, Pinker and Laszlo 1992, Bishop and Rossow 1991, Rossow and Zhang 1995, Zhang *et al.* 1995). Recently, global sets of satellite observations from the ISCCP (International Satellite Cloud Climatology Project) became available,

allowing implementation of satellite algorithms for the SRB on a global scale in the framework of the World Climate Research Program (WCRP)/SRB project (Whitlock *et al.* 1995).

While these methods give good estimates of global solar irradiance with the necessary accuracy needed for climatic purposes, important efforts still need to be made in order to have representative estimates of surface albedos. This is not a trivial task because the spectral signature of land surface reflectivity is governed by soil characteristics, vegetation types and morphology (see Dickinson, 1983). Numerous satellite estimates of surface albedo over West Africa have been made using quite different methodologies to treat the problems of atmospheric and bi-directional effects. Most ignore the latter problem, producing essentially surface reflectances (e.g., Courel *et al.* 1984, Pinty *et al.* 1985, Pinty and Szejwach 1985, Dedieu *et al.* 1987b, Pinty and Tanré, 1987, Pinty and Ramond 1987).

The determination of daily mean surface albedo by expanding the Dedieu *et al.* (1987a) method is the primary objective of the present paper. Through a significantly large seasonal variability of surface albedos over the Sahara, we will point out the dependence on seasonal variations of the Solar Zenithal Angle (SZA) and the need to correct these directional effects for a proper seasonal variability analysis. Finally, we will compare our surface global solar irradiance and albedo estimates to four major current

satellite-based methods in order to validate our results. In a companion paper (Ba and Nicholson 1996a), we will use the present results to study the temporal and spatial variability of global solar irradiance and surface albedo over the African continent.

## Data and Method

### 2.1 Data

The data of the International Satellite Cloud Climatology Project (ISCCP), named METEOSAT B2, are used. These data have been obtained from the European Satellite Operation Center (ESOC). They contain 3-h, 8-bit digitized images in three spectral bands: 0.4-1.0  $\mu\text{m}$  (visible channel), 10.5-12.5  $\mu\text{m}$  (thermal infrared channel), and 5.7-7.7  $\mu\text{m}$  (water vapor channel). During the period of study, July 1983 to July 1988, METEOSAT data are available for all months except December 1983 and July 1987.

A METEOSAT B2 image has 30 km spatial resolution and is obtained by sampling the original full resolution image (about 5 km at the Nadir) every six rows and six columns. All images are geometrically corrected and navigated to a fixed reference. In the validation analysis, surface albedo and global solar irradiance products of Pinker and Staylor (see Whitlock *et al.* 1995), Darnell *et al.* (1992), and Bishop and Rossow (1991) are used. These datasets are mapped to the ISCCP equal-area grid with

approximate dimensions of 278 km x 278 km (2.5 latitude x 2.5° longitude). For comparison, the products obtained from METEOSAT were degraded from 0.25 x 0.25° to match the 2.5 x 2.5° ISCCP grid boxes.

## 2.2 Method

### 2.2.1 Global solar irradiance

We used a physically based model (Dedieu *et al.*, 1987a) to derive global solar irradiance ( $G_s$ ) at the surface from METEOSAT satellite measurements in the wavelength between 0.4 and 1.1  $\mu\text{m}$ , using the formula:

$$G_s(t) = E_0 \frac{1 - \rho(t)}{1 - \rho_s} \quad (1)$$

in which  $E_0$  (given in Eq. 2) is the clear-sky radiation at time  $t$ ,  $\rho_s$  is the surface bi-directional reflectance, and  $\rho(t)$  is the bi-directional reflectance of the cloud-surface system at time  $t$ . The time  $t$  corresponds to a viewing geometry of the scene defined by the solar zenith angle ( $\theta_s$ ), the solar azimuth angle ( $\phi_s$ ), and the satellite viewing and azimuth angles ( $\theta_v$  and  $\phi_v$ , respectively). To evaluate  $\rho_s$ , it is necessary to determine a clear-sky condition by applying a cloud screen to the observations. To do this, we used a composite technique based on both visible and infrared

measurements to cloud screen the observations, as described in the section 2.2.3.

The clear-sky radiation  $E_0$  is given by:

$$E_0 = E d^2 \cos(\theta_s) T(\theta_s) \quad (2)$$

where  $E$  is the solar constant,  $d$  the radius vector (the ratio of actual to mean sun-earth distance), and  $T(\theta_s)$  a clear-sky transmission factor, accounting for gaseous absorption, and Raleigh and Mie scattering. Recent satellite measurements show that  $E$  is about 1363-1372  $\text{Wm}^{-2}$  (Ramanathan *et al.* 1989). A value of 1372  $\text{Wm}^{-2}$  is used for the present study.

The absorption due to atmospheric water vapor and ozone has been computed using the Lacis and Hansen (1974) formulae. These require an estimation of the total water vapor and ozone atmospheric contents. Climatologies of vertically integrated water vapor content (Tuller, 1968) and vertically integrated ozone content (London *et al.*, 1976) for ten degree latitudinal zones for each month of the year were used in the present study. The absorption due to oxygen and carbon dioxide has been calculated using the Yamamoto (1962) formulae. These were expressed as functions of the nominal surface air pressure (in atmospheres). We considered here a constant pressure of 1013 mb (1 atm). The term of the transmission representing atmospheric backscattering has been



approximated using the Darnell *et al.* (1988) equation. The attenuation factor for aerosols has been approximated using the formula of Darnell *et al.* (1992). This attenuation, determined by a residual technique (Darnell *et al.* 1988), is expressed as a linear function of the water vapor content.

In the parameterization of  $G_s$ , for a cloudy atmosphere, we consider cloud and molecular scattering and gaseous absorption as in the clear sky case, but no absorption by clouds. We also assume that the cloud layer and the surface behave as perfect lambertian reflectors. Molecular transmission under cloudy conditions is assumed to be about the same as under clear sky conditions. This is justified because most of the ozone is above the cloud top and the saturation of water vapor bands makes its absorption weakly sensitive to the increasing optical path due to the presence of clouds (Davies *et al.*, 1984).

By integrating Eq. 1 between sunrise and sunset, we obtain the daily global solar irradiance. Eq. 1 becomes:

$$G_s = \sum_{i=1}^N E_0 \frac{1-p(t)}{1-p_s} \quad (3)$$

where  $N$  is the number of total observations.  $G_s$  is estimated only when there are at least two observations available in the day.  $E_0$  is evaluated over a time interval surrounding each observation and multiplied by the term  $\frac{1-p(t)}{1-p_s}$  to account for cloud attenuation. The daily global solar

irradiance is then obtained by summing the values for each observation time during the day. To obtain  $G_s$ , we first evaluate the bi-directional reflectances  $\rho_s$  and  $\rho(t)$ .

### 2.2.2 Surface albedo

The bi-directional reflectance is defined as the ratio of surface reflected solar energy in a given direction to the incoming solar irradiance. This quantity is dependent upon the Bi-directional Reflectance Distribution Function (BRDF) of the surface and is defined as:

$$f_r(\theta_s, \phi_s; \theta_v, \phi_v) = \frac{L_r(\theta_s, \phi_s; \theta_v, \phi_v)}{L_i(\theta_s, \phi_s) \cos \theta_s d\omega_s} \quad (4)$$

where  $L_r(\theta_s, \phi_s; \theta_v, \phi_v)$  represents the luminance reflected in the direction  $(\theta_v, \phi_v)$  and  $L_i(\theta_s, \phi_s)$  represents the incident luminance within the solid angle  $d\omega_s$ . It is very difficult to evaluate the BRDF. In practice, the Bi-directional Reflectance Factor (BRF) is used instead. The BRF is defined as the ratio of the actual flux reflected by the surface in the direction  $(\theta_v, \phi_v)$ ,  $dF_r$ , to the flux that would be reflected by an ideal lambertian surface,  $dF_{r,ideal}$ :

$$\rho(\theta_s, \phi_s; \theta_v, \phi_v) = \frac{dF_r}{dF_{r,ideal}} \quad (5)$$

Assuming that  $\omega_s$  is an infinitesimal quantity, one can establish the following equation:

$$\rho(\theta_s, \phi_s; \theta_v, \phi_v) = \pi f r(\theta_s, \phi_s; \theta_v, \phi_v) \quad (6)$$

For a radiometer onboard the satellite sensing the energy reflected by the surface in the direction  $(\theta_v, \phi_v)$ , the Top Of Atmosphere (TOA) BRF is given by:

$$\rho(\theta_s, \phi_s; \theta_v, \phi_v) = \frac{\pi d^2 L_r(\theta_s, \phi_s; \theta_v, \phi_v)}{E_0 \cos \theta_s} \quad (7)$$

where  $E_0$  and  $d$  were given in the previous section. The surface BRF ( $\rho_s(\theta_s, \phi_s; \theta_v, \phi_v)$ ) is then computed by applying atmospheric corrections to the TOA BRF ( $\rho(\theta_s, \phi_s; \theta_v, \phi_v)$ ). The following equation is inverted for  $\rho_s(\theta_s, \phi_s; \theta_v, \phi_v)$ :

$$\rho(\theta_s, \phi_s; \theta_v, \phi_v) = t_g \left[ \rho_a(\theta_s, \phi_s; \theta_v, \phi_v) + \frac{T \rho_s(\theta_s, \phi_s; \theta_v, \phi_v)}{(1 - \rho_s(\theta_s, \phi_s; \theta_v, \phi_v) S)} \right] \quad (8)$$

where  $t_g$  is the total gaseous absorption,  $\rho_a(\theta_s, \phi_s; \theta_v, \phi_v)$  is the atmosphere BRF,  $T$  is the total-scattering transmission on double path, and  $S$  is the single-scattering albedo of the atmosphere. All terms of Eq. 8 are integrated over METEOSAT sensor spectral bands and normalized by the integration of the sensor spectral response over the range of the detector (0.4-1.1  $\mu\text{m}$ ). The corrections of gaseous absorption, and those accounting for aerosol effects, are based on analytical functions (the Simplified

Method for Atmospheric Corrections (SMAC), Rahman and Dedieu (1994) and are derived from 5S code (Tanré *et al.*, 1990). Aerosol optical depth has been set to a constant of 0.23 at 550 nm (23 km of horizontal visibility).

The surface albedo ( $A_s$ ) can be obtained by integrating Eq. 8:

$$A_s = \frac{1}{\pi} \int_0^{2\pi} \int_0^{\frac{\pi}{2}} \rho_s(\theta_s, \phi_s; \theta_v, \phi_v) \cos \theta_v \sin \theta_v d\theta_v d\phi_v \quad (9)$$

This quantity, used in the surface energy budget, is the ratio in percent of the total solar energy reflected by the surface to the total incoming solar irradiance. It is not an easy task to evaluate this quantity using the present satellite sensors which generally view the Earth in only one direction at time. Since our interest in the present study is limited to the daily value of the surface albedo ( $A_s$ ), we can rearrange Eq. 3 to get an estimate of  $A_s$  :

$$A_s = 1 - \frac{\sum_{i=1}^N E_0 (1 - \rho(t))}{G_s} \quad (10)$$

where  $G_s$  is the daily estimate of the global solar irradiance as given in Eq.

3.

### 2.2.3 Cloud and large optical depth screening procedures

In Eq. 1, surface bi-directional reflectance must be known. This is not trivial because it is not always easy to distinguish between clear and cloudy conditions. Moreover, large optical depth must be eliminated when computing the surface bi-directional reflectance. Therefore, a good cloud screening technique would be one that not only eliminates the cloudy conditions but also the hazy ones and cloud shadows. In this study, we used a composite method (Arino *et al.*, 1991) which combines both the visible and IR measurements.

Using a minimum visible measurement over a period of time one can eliminate the cloudy conditions because the clouds are generally more reflective than the underlying surface. However, this approach tends to favor some particular atmospheric conditions. This can result in an underestimation of the surface reflectance over bright regions due to the presence of absorbing aerosols (Legrand *et al.*, 1985, 1988). Large atmospheric aerosol loading strongly reduces the signal received by the satellite. On the other hand, the use of maximum IR measurements efficiently eliminates high optical depth observations, but may fail to discriminate the presence of low clouds with high temperature, as these are usually present over tropical forests and highlands.

In this study, a combination of both IR and visible methods over a monthly period has been used to optimize the cloud-screening procedures

in order to address the main problems encountered: large optical depth in the case of the visible method and low clouds in the case of the IR method. We used a maximum IR measurement over a ten-day period within the month to select three days during the month. Then we used the visible criteria to select the minimum value out of the three days selected to choose the day when the measurement would be taken as the least affected by atmospheric conditions.

While visually examining some of the composite images obtained by the above procedure, we noticed that the technique sometimes failed to eliminate all low clouds. Therefore, we used a threshold of 0.15, defined as the high limit of spatial variability of surface reflectance for a given month. This threshold is defined as the ratio ( $r_0$ ) of the standard deviation to the mean computed from nine pixels encompassing a given pixel. This threshold is empirically set after examining most of the possible values of the ratio,  $r_0$ , corresponding to clear sky conditions over the entire image. Whenever this ratio is greater than the threshold, the day corresponding to the minimum visible value selected over the entire month is then chosen as the month's surface measurement.

#### 2.2.4 Calibration

Satellite measurements are generally digitized in 6-bit or 8-bit counts. The luminance ( $L_r$ ) detected by the satellite is generally a linear function of the numerical count and is calculated by:

$$L_r = \alpha(CN - CN_0) \quad (11)$$

where  $CN$  represents the satellite numerical count,  $CN_0$  the space count, and  $\alpha$  a calibration factor of the sensor ( $\alpha = 0.58 \text{ W m}^{-2} \text{ sr}^{-1} \text{ count}^{-1}$  for 8-bit counts for METEOSAT 2). However, this calibration factor changes over time due to the aging process of the electronic device. Consequently, the monitoring of the time stability of the detected signal as obtained in Eq. 11 is necessary.

For this study, we used calibration coefficients obtained for the ISCCP data set (Brest and Rossow, 1992, Desormeaux *et al.* 1993) to adjust the luminance obtained in Eq. 11. These coefficients were obtained by the comparison of the geostationary satellite measurements to those of the NOAA/AVHRR.

The calibration procedure is done by two steps (see Desormeaux *et al.*, 1993). The first step is to normalize the geostationary radiances (i.e. METEOSAT) by those sensed by the current NOAA/AVHRR at the same time and location with the same viewing geometry. The second step of the procedure is to examine the time history of the distribution of radiances in

each image of the series to detect sudden, systematic changes that exceed some minimum magnitude. Small adjustments are performed if necessary to remove these changes. These calibration factors are used to alter the luminance ( $L_r$ ) values by:

$$L^*_{rn} = A (L^*_r) + B \quad (12)$$

where  $L^*_{rn}$  is the normalized METEOSAT values of scaled radiance with respect to the current AVHRR measurement (see Rossow *et al.* 1992).  $L^*_r$  is scaled radiance and is defined as:

$$L^*_r = \frac{\pi L_r}{E_0} \quad (13)$$

where  $E_0/\pi$  is the effective "solar constant" of the instrument in  $\text{Wm}^{-2}\text{sr}^{-1}$ .

We examined the performance of these calibrations for the same month from one year to another over a test site in the Libyan desert ( $24^\circ$ - $25^\circ\text{N}$ ,  $12^\circ$ - $13^\circ\text{E}$ ), the Ténéré desert ( $17.5$ - $18.5^\circ\text{N}$ ,  $10.5$ - $11.5^\circ\text{E}$ ), and in eastern Mauritania ( $19.5$ - $20.5^\circ\text{N}$ ,  $9.5$ - $10.5^\circ\text{W}$ ). The site in Libya was chosen because it presents a good spatial uniformity, a high reflectance  $> 0.40$  which allows the minimization of the atmospheric contribution to the signal, a temporal stability, and a low cloud coverage frequency (see Arino *et al.* 1991). The two other desert sites were chosen to validate the calibration adjustment made using the Libyan site.



If the calibrations were correct, we would expect that there would be little interannual variability in the TOA reflectances for a region of constant surface characteristics such as the test site in the Libyan desert. An analysis of reflectances shows otherwise and a comparison with digital counts and calibration coefficients suggests a problem with calibrations.

Time series of clear-sky digital visible counts corresponding to 11H30 TU observations is shown in Fig. 1a.. Most evident is the month-to-month variability, a manifestation of the changing conditions of radiation during the course of the year. However, there is also a significant increase in the visible signal after May 1987. In general, the signal presents small variations for the other years. These small variations may be caused mostly by atmospheric constituents. The big increase in the signal from June 1987 to July 1988 is a consequence of a gain change in the visible channel of METEOSAT 2 (see Rossow *et al.* 1992)

Time series of slope values of the ISCCP calibration are generally consistent with those of clear-sky data (Fig. 1b). One should expect that the decrease in the satellite signal will correspond to an increase in the slope, indicating that the instrument is degrading. This is the case for January 1985. However, the big increase in the slope for February 1985 was not followed by a decrease in the satellite signal, indicating that the calibration may be incorrect.

The changing response of the satellite sensor to a constant-radiance target due to the aging process is generally negative. A signal increasing in time does not usually occur unless there are onboard temperature variations or gain changes from ground controllers. There is a gain change in the visible channel in May 1987 that explains the big increases in all counts from June 1987 to July 1988. This is also consistent with the decrease in slope values of the ISCCP calibration and in those obtained by Moulin *et al.* 1994. The ISCCP slopes decrease from a value of 1.194 in April 1987 to 1.002 in May 1987.

Figure 1c indicates TOA reflectances computed without ISCCP calibration. The fluctuations in time series of TOA reflectances are quite similar to those corresponding to clear-sky digital counts (Fig. 1a). This tends to confirm the temporal stability of the site.

When we applied the monthly calibration obtained from ISCCP, significant fluctuations in TOA reflectances appear, particularly for February 1985 and May 1987. These fluctuations are similar to those of the time series of ISCCP monthly calibration factors. For instance, the TOA reflectances for 1988 are generally much lower than for other years. We also notice the drop in TOA reflectance for May 1987. These large variations of TOA albedo for a certain number of months are not due to underlying surface property changes but to uncertainties of the calibration. The ISCCP calibration procedure assumed all thick clouds with optical

depths  $\geq 0.80$  as a constant-radiance target. This is not always true because the viewing geometry and cloud spectral proprieties may be different from one year to another. This may be the cause of the year to year fluctuations in calibrated TOA reflectances.

To make observations comparable from one year to another, the calibration factor must adequately compensate for all changes in the detected signal due to the degradation of the sensor. We computed an adjustment factor ( $\varepsilon$ ) to correct TOA reflectances ( $\rho_a$ ) corresponding to months having  $\rho_a$  values that depart significantly from its monthly mean. The adjustment factor is defined as the normalized departure from the monthly mean:

$$\varepsilon = \frac{\rho_a - \bar{\rho}_a}{\bar{\rho}_a} \quad (13)$$

where  $\rho_a$  is the TOA reflectance computed using ISCCP calibration and  $\bar{\rho}_a$  is the monthly mean reflectance computed the same way. The adjustment factors (see Table 1) are determined over the Libyan site.

The TOA reflectance ( $\rho_a$ ) computed using ISCCP calibration is modified as:

$$\rho_{acorr} = \rho_a + \varepsilon \rho_a \quad (14)$$

Figure 2 shows time series of TOA reflectance corresponding to two other desert sites before and after applying Eq. 14. On the left-hand side are

shown time series of reflectance using the unadjusted ISCCP calibration. On the right-hand side are shown time series of reflectance after adjustments were made using Eq. 14. As can be seen, the large fluctuations due to calibration errors are significantly reduced. In the present study, all TOA reflectances computed using ISCCP calibration are modified according to Eq. 14. The accuracy of these adjustments for precise intercomparisons may be questioned, but the computed surface albedo values over the Sahara show very little interannual variability (see the companion paper by Ba and Nicholson 1996a).

### 3. Correction of the SZA effects on estimated surface albedo

As indicated in section 2.2, the retrieval of surface reflectance was obtained by removing atmospheric effects from the TOA reflectances using the SMAC code (Rahman and Dedieu, 1994). However, this code assumes a lambertian surface, while a number of studies (Kriebel 1978, Kimes 1983, Deering 1989, Gutman 1992, Ba *et al.* 1995) have demonstrated angular variation effects on surface reflectance. Computations with radiative transfer codes that account for these effects exist but are complicated because the BDRF of the surface is unknown in most cases. Recently Ba *et al.* (1996b) have shown that a simple bi-directional function can be used to correct NOAA/AVHRR surface reflectance computed from 5S code.

Since METEOSAT viewing geometry is fixed for a given location and the solar azimuth is highly correlated with SZA, the directional function in such geometry can be expressed only in SZA terms. Fig. 3a illustrates the SZA dependence of surface albedos. More than 50% of the variance in surface albedo is explained by a simple linear function of  $\sec(\theta_s)$  in regions located north of 15°N in central Africa and the Congo basin. This shows that directional effects due to changing solar geometry are not negligible and must be removed to study the seasonal variability of surface albedo properly.

We used a similar equation in Ba et al. (1996b) in which the surface albedo is expressed as a product of an isotropic component of the albedo and a temporal and directional function. For this study, we did not include the temporal component of the reflectance because this would require a large number of observations to retrieve constants involved in the temporal function. The following equation is used to derive the constant of the directional function  $G_i(\theta_{si})$ :

$$A_{si} = A_{s0i} + b \sec(\theta_{si}) = A_{s0i} G_i(\theta_{si}) \quad (15)$$

where  $G_i(\theta_{si}) = (1 + b/A_{s0i} \sec(\theta_{si}))$  represents the surface directional function,  $A_{s0i}$  is the isotropic component of the surface albedo, and  $i$  is the pixel number in the METEOSAT image. A daily mean of  $\cos(\theta_{si})$  was computed for the 15th of each month to represent the monthly mean. For

each pixel in the METEOSAT image, the monthly mean of the surface albedo obtained for the period 1983-88 was used to compute values of the constants  $A_{S0i}$  and  $b_i$ .

Shaded areas in Fig. 3b represent regions where the determination of the parameters  $A_{S0}$  and  $b$ , using Eq. 15, are statistically significant at the 99% confidence level. The correction of the surface albedos for directional effects is only performed in these areas. Elsewhere, the level of statistical significance is not satisfactory for a determination of the parameters  $A_{S0}$  and  $b$ . However, the variance in surface albedo explained by the SZA in these areas is not significant, indicating that other factors contribute more to seasonal variations of surface albedo.

#### 4. Sensitivity tests and Validation

##### 4.1 Sensitivity tests

Arino et al. (1992) conducted an extensive study on the accuracy of surface reflectance determinations made from METEOSAT. Their error analysis has identified three main problems: calibration uncertainty, atmospheric corrections and spectral and directional effects of the surface. Their study concluded that calibration accuracy is within 10%, which can cause a relative uncertainty in the surface reflectance of 10%. Spectral effects can account for a maximum bias of 0.01 for a vegetated surface,

and directional effects can lead to a bias of 0.035 between two determinations of surface reflectance made from two different observations taken at different times. These occur at the same view angle over savannas. The maximum error due to the atmosphere is estimated to be on the order of 0.03 in reflectance on the order of 0.40 and 0.01 for a surface reflectance of 0.10.

The sensitivity of the model to input data was tested, specifically water vapor and the aerosol optical path. This determines how much uncertainty may be caused in the calculated parameters by uncertainties in these input parameters. Three different sites were selected to conduct these tests: the first site is located in the Libyan Desert ( $24.5^{\circ}\text{N}$  and  $12.5^{\circ}\text{E}$ ) with a high surface albedo ( $A_s = 0.50$ ), the second site is located in northern Burkina Faso (Dori:  $14.05^{\circ}\text{N}$  and  $0^{\circ}$ ) with a surface albedo around 0.3, and the third site is located in southern Burkina Faso (Fada Ngourma  $12.06^{\circ}\text{N}$  and  $0.4^{\circ}\text{E}$ ) with 0.20 as the surface albedo. Monthly surface global solar irradiance and surface albedo values were computed for each of these three sites for January and July 1986. The climatological value of water vapor and a standard value of 0.23 (at 550 nm) of aerosol optical thickness were varied by  $\pm 25\%$ . A large optical thickness observed at Niamey during January 1986 and 1987 (Mohamed *et al.*, 1992) is also used. We recall here that the aerosol optical thickness of 0.23 is used only to correct the TOA reflectance measured by METEOSAT (see section 2).

Table 2 summarizes all sensitivity test results. The numbers in the table represent the difference in the results obtained by increasing and by decreasing input data by 25%.

When water vapor is varied over this range, the global solar irradiance changes by 15-27  $\text{Wm}^{-2}$ . This corresponds to less than 10% of the value computed with a climatological value. The largest differences between January and July 1986 are observed over the Libyan site (12  $\text{Wm}^{-2}$ ) while the differences between these two months over the Burkina Faso sites are only 5  $\text{Wm}^{-2}$ . The differences in surface albedo are 0.01 (Fada Ngourma) and 0.02 for the Dori and Libyan sites. These changes represent 5, 7 and 4%, respectively, of the value computed with a climatological value of water vapor.

When the optical thickness ( $\tau_a = 0.23$ ) is varied by  $\pm 25\%$ , the surface global solar irradiance remains nearly constant. However, when a much greater value of  $\tau_a = 0.8$  is used, the differences become significant during July over Burkina Faso. We expected that increasing  $\tau_a$  would affect January values more than July values because of the larger optical path. This is the case over the Libyan site but the opposite is obtained over Burkina Faso. This apparent contradiction is due to the fact that the algorithm performs the same correction for aerosols whether in clear or cloudy conditions. However, above high reflective clouds (i.e., convective



clouds), there is a lower concentration of aerosols. Consequently, when a high value of  $\tau_a$  is used in the presence of such clouds, the algorithm will underestimate the global solar irradiance because of a significant increase in the cloud albedo. This is the case for July over Burkina Faso, a region affected by the increasing convective clouds associated with the Inter-Tropical Convergence Zone (ITCZ).

In the case of surface albedo, the results of varying  $\tau_a$  by  $\pm 25\%$  are about the same as with water vapor. When using a much higher value of  $\tau_a$ , the differences are very large when surface albedos are high (i.e., in a desert). This indicates that the analytical functions used to perform these corrections are not valid for such high values of aerosol optical thickness over high reflective surfaces. The value of  $\tau_a = 0.8$  (5 km of horizontal visibility) corresponds to the limit of the validity of the aerosol model (Tanré *et al.* 1990). However, the cloud filtering procedure we applied also tends to select days with the lowest aerosol burden (Arino *et al.* 1991). The uncertainties presented in table 1 for surface albedo retrieval are probably maximum values.

## 4.2 Validation

In the validation procedure, we did not use surface measurements. Surface data can be found, but a World Climate Research Program (WCRP)

committee considered that most surface radiation measurements over Africa are not reliable (Charlock 1995, personal communication). For this reason, validation will be based on a comparison with other satellite estimates.

Four satellite algorithms were compared to the results obtained in the present study: Pinker and Staylor (see Whitlock *et al.* 1995), Darnell *et al.*, 1992 (hereafter Darnell), and Bishop and Rossow, 1991 (hereafter Bishop). All these methods are based on radiative transfer models and use ISCCP satellite data as input. These are mapped to the ISCCP equal-area grid with approximate dimensions of  $278 \times 278 \text{ km}^2$  ( $2.5^\circ$  latitude  $\times$   $2.5^\circ$  longitude) (Whitlock *et al.*, 1995). All four algorithms were validated against measurements of global solar irradiance. For the purpose of the comparison, the products obtained in this paper were degraded from  $0.25^\circ \times 0.25^\circ$  to the  $2.5^\circ \times 2.5^\circ$  ISCCP grid boxes. A comparison between our estimates and the four other techniques are made using data estimated at every grid box over the African continent. Coastal area pixels were not considered in the comparison because our estimates were made only over land. In the comparison, we used data for January 1986-88 and July 1985-86 because data from Staylor and Pinker were only available for these years.

Table 3 shows comparison statistics between surface global solar irradiance and albedo estimates of these different satellite algorithms for

January 1986-88 and July 1985-86, respectively. Both the Darnell and Staylor models are a modified version of an earlier algorithm by Darnell *et al.* 1988. This explains why there is a very good agreement between the two model results.

There is a rather good agreement between our estimates and those of both Darnell and Staylor for both January and July (see Fig. 4a,b, Fig. 5a,b, and also Table 3a,b). The biases are less than  $5 \text{ Wm}^{-2}$  and a RMSE less  $18 \text{ Wm}^{-2}$  for global solar irradiance. For surface albedo, the biases are between -0.01 and 0.01 and a RMSE less 0.05.

Biases are significant with Bishop's global solar irradiance estimates (Table 3a). Bishop's estimates are systematically biased high by 17-19  $\text{Wm}^{-2}$  for both January and July with a RMSE less than  $18 \text{ Wm}^{-2}$ . The same is also observed (Table 3a) in the comparison of both of the Staylor and Darnell estimates with those of Bishop.

In January, our estimates of global solar irradiance are low for vegetated regions and high for arid and semi-arid regions in comparison with Pinker's values. The differences between vegetated regions and arid regions (not shown here) are also apparent between both the Darnell and Staylor estimates and those of Pinker.

Figure 5 represents a comparison between our surface albedo and those of Staylor (a,b), Darnell (c,d), Bishop (e,f), and Pinker (g,h) for

January (left-hand side) and July (right-hand side). There is very good agreement between our estimates and those of both Staylor and Darnell for both January and July. For these comparisons, the scatterplot is nearly centered around the  $45^\circ$  line. By contrast, there is little correlation between the Pinker estimates and ours for surface albedo higher than 0.20 for January (Fig. 5g). The same is observed between Pinker's estimates and those of both Darnell and Staylor (Table 3b). The scatterplot corresponding to July gives much better correlation but still Pinker's values are much lower for values over 0.20 (Fig. 5h).

Bishop's values represent spectral surface albedos ( $0.6 \mu\text{m}$ ). These are linearly well correlated (the coefficient of correlation is 0.97 for both January and July) with METEOSAT spectral surface albedos ( $0.4\text{-}1.1 \mu\text{m}$ ) and the broadband albedos of both Staylor and Darnell (Table 3b). These results are in good agreement with those obtained by Arino *et al.* (1992) between METEOSAT broadband reflectances and narrowband visible reflectances of NOAA/AVHRR.

The reasons for differences between the Pinker and Bishop global solar irradiance estimates on the one hand, and ours and those of both Darnell and Staylor on the other hand, are not established. However, we believe that some differences may be due to the differences in surface albedo used as input for the global solar irradiance calculation. Both

Darnell and Staylor's albedos are based on angularly corrected, broadband ERBE clear-sky satellite data. These are more comparable with those we obtained from the visible channel of METEOSAT.

By contrast, Pinker's radiative transfer model uses the spectral dependence of surface reflectance in the target grid using the vegetation map of Matthews (1983). A transformation of the narrowband to broadband and anisotropic correction were then applied accordingly. Similarly, Bishop's transfer model used the area-weighted average of spectral ratios for eight vegetation types (with seasonal adjustments), land ice, sea ice and fresh snow. Over the African continent, they used a surface reflectance corresponding to the ISCCP surface visible ( $0.6 \mu\text{m}$ ) reflectance, which is an area-averaged value. They then derived the near-infrared reflectance from the visible reflectance.

## 5. Summary

To understand and forecast the interannual climate variability in key climatic parameters (e.g. SRB components), it is necessary to have some understanding of the global distributions of these parameters. Physical models, coupled with satellite observations, are now well developed in most cases to retrieve such climatic parameters with an accuracy suitable for General Circulation Models (GCM).

The objective of this paper was twofold: 1) to expand the theoretical-broadband model of Dedieu *et al.* (1987a) in order to derive estimates of surface albedo on the continental scale and 2) to perform an intercomparison with four major current satellite radiation codes.

The results have demonstrated that using thick clouds as a constant-radiation target failed sometimes to adequately compensate all changes due to the sensor degradation. Calibration errors introduce large interannual variability of TOA reflectance over a known stable surface such as the Libyan desert. For the months that this happened, a correction factor, computed from a normalized departure from the monthly mean over the Libyan site, was used to adjust the value of TOA reflectance. This allowed for the removal of the interannual variability in surface albedo over desert regions due to that of the calibration. Although directional effects due to the SZA were minimized, our values of albedo may still not be true surface albedos because they are based on only one viewing angle.

The parameterization used to correct aerosol effects is not valid for a very turbid atmosphere (horizontal visibility little than five km). This poses problems because such high concentrations of aerosols are often observed in the Sahelian region of West Africa. However, on the monthly scale, the cloud filtering procedure used to obtain clear-sky observations tends to also select days with the lowest aerosol burden.

In our scheme, we also considered all clouds as a non-absorbent medium. This may be true to a first approximation and may explain why our results compared well with those obtained from models accounting for cloud absorption. This indicates that uncertainties due to this assumption are less important to those due to aerosol and bi-directional effects.

The sensitivity tests of the model have shown that a variation of 50% in the water vapor amount induced a change of up to  $27 \text{ Wm}^{-2}$  of the global solar radiation. An error of this magnitude could be of concern for climate studies and other studies requiring accurate characterization of surface radiation balance.

All the problems mentioned above will be, to some extent, addressed when the Earth Observing System (EOS) era satellite observations (see Wielicki et al. 1995) operate. EOS will make a great advance in our ability to more precisely observe key variables for estimating surface and TOA radiative fluxes. The Multiangle Imaging Spectroradiometer (MISR) and the Polarization and Directionality of the Earth Reflectance (POLDER) onboard ADEOS will also view the same surface target under several angles, allowing for better determination of the bi-directional functions.

## Acknowledgments

We wish to thank Dr. R. Frouin of California Space Institute, Scripps

Institution of Oceanography, San Diego, California, for providing METEOSAT data, and Mr. J. Kim of the Florida State University for programming support. Satellite products used for the comparison were provided by Ms. Nancy Ritchey of Lockheed Engineering and Sciences Company, Hampton, Virginia, Dr. Thomas Charlock of NASA Langley Research Center, Hampton, Virginia, and by Dr. J. Bishop of Lamont-Doherty Geological Observatory, Columbia University, Palisades, New York. This work was sponsored by the TRMM project via NASA Grant NAG5-1587.

#### References:

- Arino, O., G. Dedieu, and P. Y. Deschamps, 1991: Accuracy of satellite land surface reflectance determination. *J. Appl. Meteor.*, **30**, 960-972.
- Arino, O., G. Dedieu, and P. Y. Deschamps, 1992: Determination of land surface spectral reflectances using METEOSAT and NOAA/AVHRR shortwave channel data. *Int. J. Remote Sens.*, **13**, 2263-2287.
- Ba, M. B., P. Y. Deschamps, and R. Frouin, 1995: Error reduction in NOAA satellite monitoring of the land surface vegetation during FIFE. *J. Geophys. Res.*, **100**, 25,537-25,548.
- Ba, M. B., and S. E. Nicholson, 1996a: Temporal and spatial variability of surface radiation budget over the African continent as derived from METEOSAT. Part II: Climatologies and interannual variability of surface global solar irradiance, albedo and net radiation. This issue.



- Ba, M. B., G. Dedieu, Y. H. Kerr, and S. E. Nicholson, 1996b: Reduction of bi-directional effects in NOAA/AVHRR data acquired during the HAPEX-SAHEL Experiment. *J. Hydrol.*, in press.
- Bishop, J. K. B., and W. B. Rossow, 1991: Spatial and temporal variability of global surface solar irradiance. *J. Geophys. Res.*, 96, 16,839-16,858.
- Brest, C. L., and W. B. Rossow, 1992: Radiometric calibration and monitoring of NOAA/AVHRR data for ISCCP. *Int. J. Remote Sens.*, 13, 235-273.
- Charney, J. G., 1975: Dynamics of deserts and droughts in the Sahel. *Quart. J. Roy. Meteor. Soc.*, 101, 193-202.
- Courel, M. F., R. S. Kandel, S. I. Rasool, 1984: Surface albedo and the Sahel drought. *Nature*, 307, 528-531.
- Darnell, W., F. Staylor, S. K. Gupta, and F. M. Denn, 1988: Estimation of surface global solar irradiance using sun-synchronous satellite data. *J. Climate*, 1, 820-835.
- Darnell, W., F. Staylor, S. K. Gupta, N. A. Ritchey, and A. C. Wilber, 1992: seasonal variation of surface radiation budget derived from International Satellite Cloud Climatology Project C1 data. *J. Geophys. Res.*, 97, 15,741-15,760.
- Davies, R., W. L. Ridgway, and K-E. Kim, 1984: Spectral absorption of solar radiation in cloudy atmospheres: A  $20\text{ cm}^{-1}$  model. *J. Atmos. sci.*, 41, 2126-2137.

- Dedieu, G., P. Y. Deschamps, and Y. H. Kerr, 1987a: Satellite estimation of solar irradiance at the surface of the earth and of surface albedo using a physical model applied to METEOSAT data. *J. Climate Appl. Meteor.*, 26, 79-87.
- Dedieu G., P.Y. Deschamps, Y.H. Kerr, and P. Raberanto, 1987b : A global survey of surface climate parameters from satellite observations: Preliminary results over Africa. *Adv. Space Res.*, 11, 129-137.
- Desormeaux, Y., W. B. Rossow, C. L. Brest, G. G. Campbell, 1993: Normalization and calibration of geostationary satellite radiances for the International Satellite Cloud Climatology Project. *J. Atmos. Oceanic Technol.*, 10, 304-325.
- Deering, D.W., 1989: Field measurements of bidirectional reflectance. *Theory and Applications of Optical Remote Sensing*, John Wiley, Ed., New York, 14-65.
- Dickinson, R. E., 1983: Land surface processes and climate-surface albedos and energy balance. *Adv. Geophys.*, 25, 305-353.
- Gauthier, C., G. Diak, and S. Masse, 1980: A simple physical model to estimate incident solar radiation at the surface from GOES satellite data. *J. Appl. Meteor.*, 19, 1005-1012.
- Gupta, S. K., 1989: A parameterization for longwave surface radiation from sun-synchronous satellite data. *J. Climate*, 2, 305-320.

- Gutman, G. G., 1992: Anisotropy of visible and near-IR reflectances over land as observed from NOAA AVHRR. *IRS '92: Current problems in Atmospheric Radiation*, A. Deepak Publishing, 436-439.
- Kimes, D.S., 1983: Dynamics of directional reflectance factor distribution for vegetation canopies. *Applied Optics*, 22, 1364-1372.
- Kriebel, K.T., 1978: Measured spectral bidirectional reflection properties of four vegetated surfaces. *Applied Optics*, 17, 253-259.
- Lacis, A. A., and J. E. Hansen, 1974: A parameterization for absorption of solar radiation in the earth's atmosphere. *J. Atmos. Sci.*, 31, 118-133.
- Legrand, M., J. J. Bertrand, and M. Desbois, 1985: Dust clouds over West Africa: A characterization by satellite data. *Ann. Geophys.*, 3, 777-784.
- Legrand, M., M. Desbois, and K. Vovor, 1988: Satellite detection of Saharan dust: Optimized imaging during nighttime. *J. Climate*, 1, 256-265.
- London, J., R. D. Bojkov, S. Oltmans, and J. I. Kelley, 1976: Atlas of the global distribution of total ozone July 1957 - June 1967. NCAR/TN-113 + STR.
- Matthews, E., 1983: Global vegetation and land-use: New high-resolution data bases for climate studies. *J. Climate Appl. Meteor.*, 22, 474-487.

- Mohamed, A. B., J. P. Frangi, J. Fontan, and A. Druilhet, 1992: Spatial and temporal variation of atmospheric turbidity and related parameters in Niger. *J. Appl. Meteor.*, **31**, 1286-1294.
- Moulin, C, C. E. Lambert, F. Guillard, J. Poitou, F. Cabot, G. Dedieu, and F. Dulac, 1994: Calibration of long time series of METEOSAT visible images. Proceedings of the tenth of METEOSAT Scientific Users' Conference, Cascais, Portugal, pp. 351-358, EUMETSAT.
- Pinker, R. T., and J. A. Ewing, 1985: Modeling surface solar radiation: Model formulation and validation. *J. Climate Appl. Meteor.*, **24**, 389-401.
- Pinker, R. T., and I. Laszlo, 1992: Modeling surface solar irradiance for satellite applications on a global scale. *J. Appl. Meteor.*, **31**, 194-211.
- Pinty, B., and G. Szejwach, 1985: A new technique for inferring surface albedo from satellite observations. *J. Climate Appl. Meteor.*, **24**, 741-750.
- Pinty, B., G. Szejwach, and J. Stum, 1985: Surface albedo over the Sahel from METEOSAT radiances. *J. Climate Appl. Meteor.*, **24**, 108-113.
- Pinty, B., and D. Tanré, 1987: The relationship between incident and double-way transmittances: An application for the estimate of surface albedo from satellites over the African Sahel. *J. Climate Appl. Meteor.*, **26**, 892-896.

- Pinty, B., and D. Ramond, 1987: A Method for estimate of broadband directional surface albedo from a geostationary satellite. *J. Climate Appl. Meteor.*, 26, 1709-1722.
- Rahman, H., and G. Dedieu, 1994: SMAC : A simplified method for the atmospheric correction of satellite measurements in the solar spectrum. *Int. J. Rem. Sens.*, 15, 123-143.
- Ramanathan, V., B. R. Barkstrom, and E. F. Harrison, 1989: Climate and the earth radiation budget. *Physics Today*, 42, 22-32.
- Raschke, E., A. Gratzki, and M. Rieland, 1987: Estimates of global radiation at the ground from the reduced data sets of the International Satellite Cloud Climatology Project. *J. Climatol.*, 7, 205-213.
- Rossow, W. B., Y. Desormeaux, C. L. Brest, and A. Walker, 1992: International Satellite Cloud Climatology Project (ISCCP) radiance calibration report. WMO/TD-No. 520, WCRP-77, World Meteorological Organization, Geneva, 104 pp.
- Rossow, W. B., and Y. -C. Zhang, 1995: Calculation of surface and top-of-atmosphere radiation fluxes from physical quantities based on ISCCP Datasets, Part II: Validation and first results. *J. Geophys. Res.*, 100, 1167-1197.
- Tanré , D., C. Deroo, P. Duhaut, M. Herman, J. J. Morcrette, J. Perbos, and P. Y. Deschamps, 1990: Description of computer code to simulate the

- satellite signal in the solar spectrum: the SS code. *Int. J. Rem. Sens.*, 11, 659-668.
- Tarpley, J. D., 1979: Estimating incident solar radiation at the surface from geostationary satellite data. *J. Appl. Meteor.*, 18, 1172-1181.
- Tuller, S. E., 1968: World distribution of mean monthly and annual precipitable water. *Mon. Wea. Rev.*, 96, 785-797.
- Wielicki, B. A., R. D. Cess, M. D. King, D. A. Randall, and E. F. Harrison, 1995: Mission to Planet Earth: role of clouds and radiation in climate. *Bull. Amer. Meteor. Soc.*, 76, 2125-2153.
- Whitlock, C. H., T. P. Charlock, W. F. Staylor, R. T. Pinker, I. Laszlo, A. Ohmura, H. Gilgen, T. Konzelman, R. C. DiPasquale, C. D. Moats, S. R. LeCroy, and N. A. Ritchey, 1995: First global WCRP shortwave surface radiation budget dataset. *Bull. Amer. Meteor. Soc.*, 76, 905-922.
- Yamamoto, G., 1962: Direct absorption of solar radiation by atmospheric water vapor, carbon dioxide and molecular oxygen. *J. Atmos. Sci.*, 19, 182-188.
- Zhang, Y. -C., W. B. Rossow, and A. A. Lacis, 1995: Calculation of surface and top-of-atmosphere radiation fluxes from physical quantities based on ISCCP datasets, Part I: Method and sensitivity to input data uncertainties. *J. Geophys. Res.*, 100, 1149-1165.

Table 1: Adjustment factors ( $\epsilon$ ) defined as a normalized departure from TOA monthly mean reflectance computed using the Libyan desert as a constant-radiance target.  $\epsilon = 0$  means no adjustment was made for that month. Stars indicate no METEOSAT data were available for that month.

	1983	1984	1985	1986	1987	1988
JAN	*	0	0	0	0	0
FEB	*	0	-0.106	0	0	0.062
MAR	*	0	0	0	0	0.044
APR	*	0	0	0	0	0.076
MAY	*	0	0	0	0.145	0.075
JUN	*	0	0	0	0	0.122
JUL	-0.087	-0.063	0	0	*	0.085
AUG	-0.064	-0.056	0	0	0	*
SEP	-0.100	-0.052	0	0	0	*
OCT	-0.119	0	0	0	0	*
NOV	-0.094	0	0	0	0	*
	*	0	0	0	0	*

Table 2: Monthly mean absolute changes at three different locations in short-wave fluxes ( $\text{Wm}^{-2}$ ) and surface albedos produced by altering the climatological values of the water vapor amount (WV) and the standard aerosol optical path ( $\tau_a = 0.23$ ) by indicated amounts. All tests were performed for January and July 1986.

	January		July	
Libyan Desert (25.5°N-12.5°E)				
	$\Delta SW$ (Wm <sup>-2</sup> )	$\Delta A_s$	$\Delta SW$ (Wm <sup>-2</sup> )	$\Delta A_s$
(WV+25%)-(WV -25%)	-15	0.02	-27	0.02
( $\tau_a$ +25%)-( $\tau_a$ - 25%)	-3	0.02	-1	0.02
( $\tau_a$ = 0.8 )-( $\tau_a$ = 0.23)	-10	0.14	-4	0.09
Dori: Burkina Faso (14.05°N-0)				
	$\Delta SW$ (Wm <sup>-2</sup> )	$\Delta A_s$	$\Delta SW$ (Wm <sup>-2</sup> )	$\Delta A_s$
(WV+25%)-(WV -25%)	-20	0.02	-25	0.02
( $\tau_a$ +25%)-( $\tau_a$ - 25%)	0	0.01	-3	0
( $\tau_a$ = 0.8 )-( $\tau_a$ = 0.23)	0	0.06	-17	0.03
Fada Ngourma: Burkina Faso(12.06°N-0.4°E)				
	$\Delta SW$ (Wm <sup>-2</sup> )	$\Delta A_s$	$\Delta SW$ (Wm <sup>-2</sup> )	$\Delta A_s$
(WV+25%)-(WV -25%)	-20	0.01	-24	0.01
( $\tau_a$ + 25%)-( $\tau_a$ +-25%)	-1	0.01	-3	0
( $\tau_a$ = 0.8 )-( $\tau_a$ = 0.23)	-2	0.02	-21	0.02



Table 3a: Comparison statistics between five (5) different satellite based algorithms: Surface downward fluxes.

	January 86-88			July 85-86		
	NBP = 819			NBP = 546		
	Coef. of Corr. (R)	RMSE (Wm <sup>-2</sup> )	BIAS (Wm <sup>-2</sup> )	Coef. of Corr. (R)	RMSE (Wm <sup>-2</sup> )	BIAS (Wm <sup>-2</sup> )
This study vs.						
Darnell	0.94	14	4	0.96	17	4
Staylor	0.93	15	2	0.97	16	3
Pinker	0.88	20	4	0.90	26	6
Bishop	0.92	17	-17	0.97	14	-19
Darnell vs.						
Staylor	0.99	4	2	0.99	3	1
Pinker	0.95	16	-1	0.96	12	-2
Bishop	0.97	10	-22	0.98	8	-23
Staylor vs.						
Pinker	0.96	11	2	0.94	15	3
Bishop	0.98	8	-20	0.98	8	-22
Pinker vs.						
Bishop	0.95	16	-22	0.95	14	-25

Table 3b: Comparison statistics between five (5) different satellite based algorithms: Surface albedos.

	January 86-88 NBP = 819			July 85-86 NBP = 546		
	Coef. of Corr. (R)	RMSE	BIAS	Coef. of Corr. (R)	RMSE	BIAS
This study vs.						
Darnell	0.94	0.04	0.01	0.95	0.03	0
Staylor	0.94	0.04	0.01	0.95	0.04	-0.01
Pinker	0.73	0.08	0.05	0.89	0.05	0.01
Bishop	0.97	0.03	0.13	0.97	0.03	0.11
Darnell vs.						
Staylor	1	0	0	0.99	0.02	0
Pinker	0.79	0.07	0.05	0.90	0.05	0.02
Bishop	0.94	0.04	0.12	0.95	0.04	0.11
Staylor vs.						
Pinker	0.78	0.07	0.05	0.91	0.04	0.02
Bishop	0.94	0.03	0.13	0.95	0.04	0.12
Pinker vs.						
Bishop	0.75	0.07	0.08	0.91	0.05	0.09

## CAPTIONS

Figure 1: Time monitoring of the METEOSAT 2 visible channel and ISCCP calibration coefficients (A): (a) time series of clear-sky digital counts over the Libyan desert, (b) the ISCCP calibration coefficient (A), (c) TOA reflectances computed without ISCCP calibration, and (d) TOA reflectances computed with ISCCP calibration applied.

Figure 2: Time series of TOA reflectances over the Ténéré desert (Top), and over northeast of Mauritania (Bottom). On the left-hand side are TOA reflectances computed using ISCCP calibration coefficients; on the right-hand side are adjusted TOA reflectances using a normalized departure from monthly mean computed over the Libyan desert.

Figure 3: Spatial distribution of statistics between computed surface albedos and  $\sec(\theta_s)$ : (a) explained variances (%), (b) statistic significance at the 99% confidence level (shaded areas).

Figure 4: Comparison of the present study surface downward estimates and those of (a,b) Darnell, (c,d) Staylor, (e,f) Bishop, and (g,h) Pinker during January 1986-88 (left) and July 1985-88 (right).

Figure 5: Comparison of the present study surface albedo estimates and those of (a,b) Darnell, (c,d) Staylor, (e,f) Bishop, and (g,h) Pinker during January 1986-88 (left) and July 1985-88 (right).

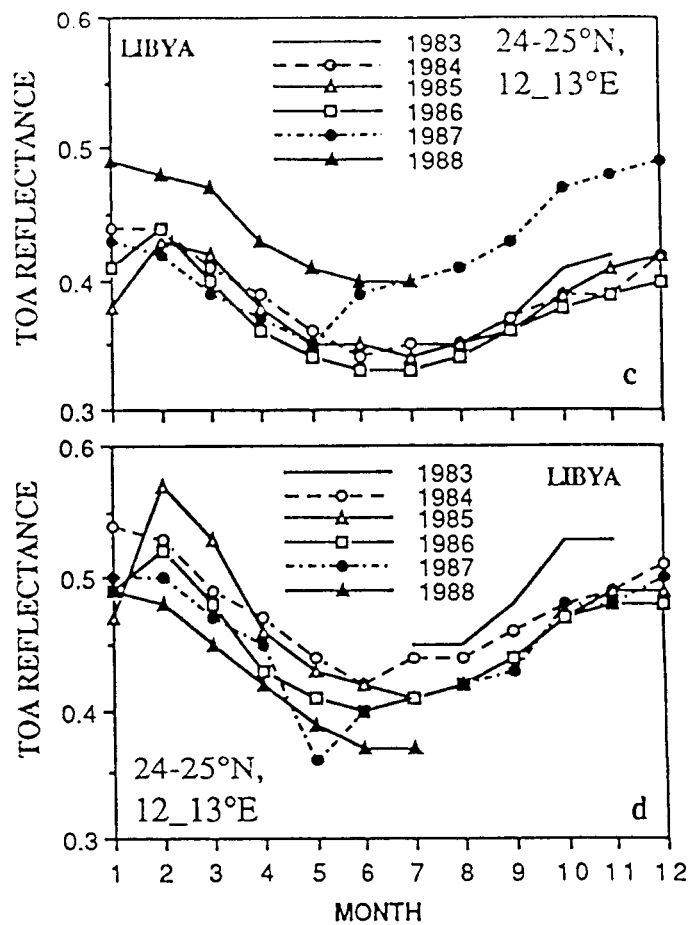
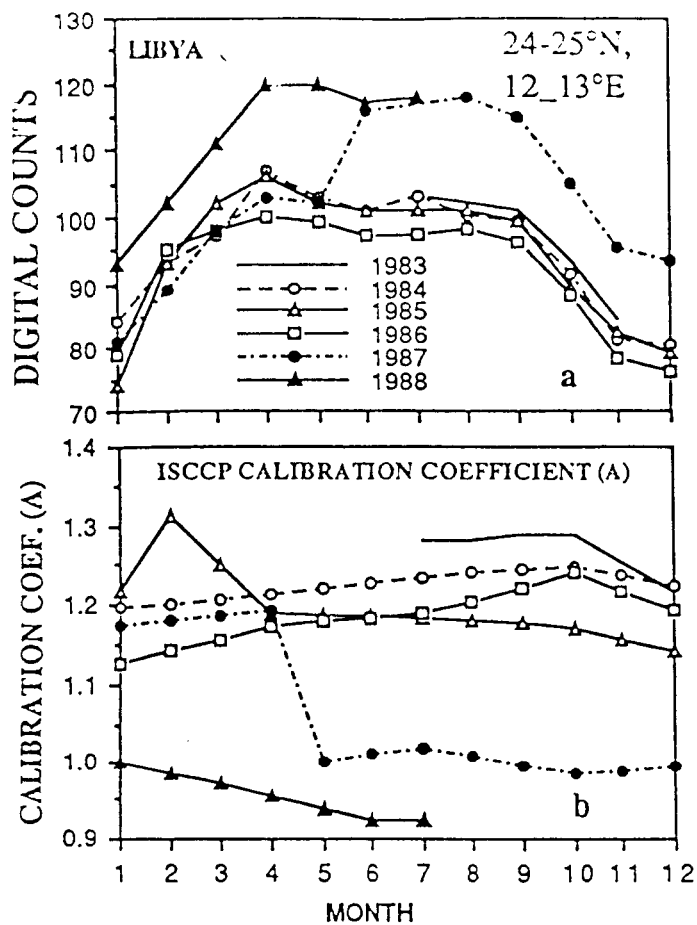


Figure 1

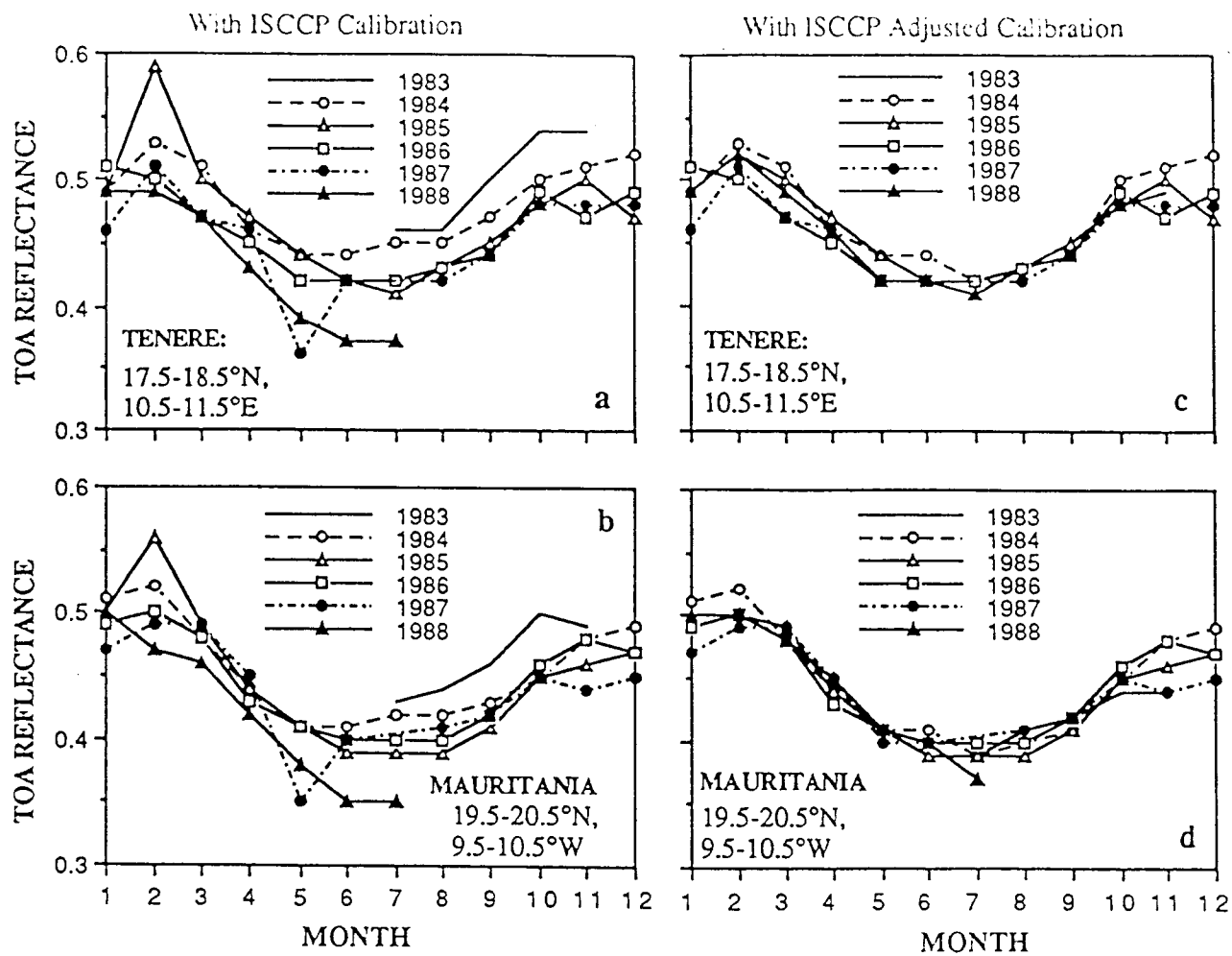


Figure 2

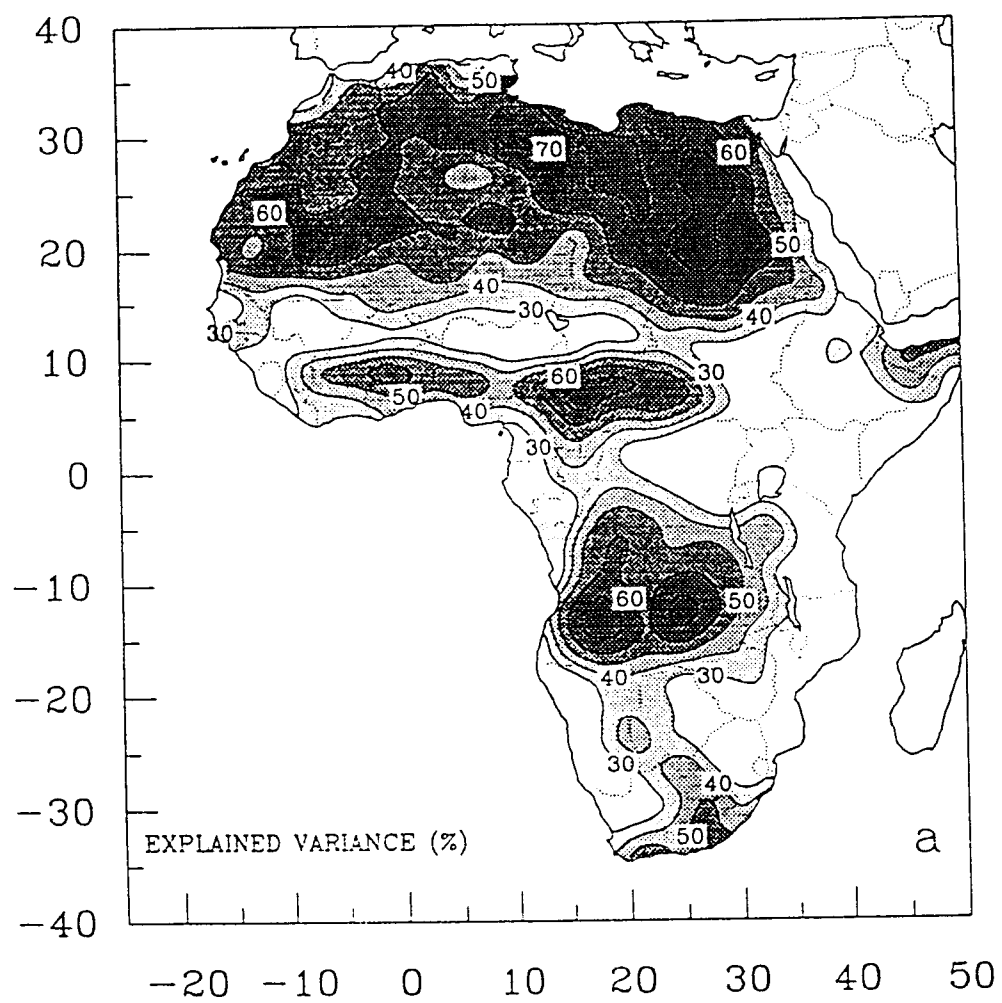


Figure 3 a

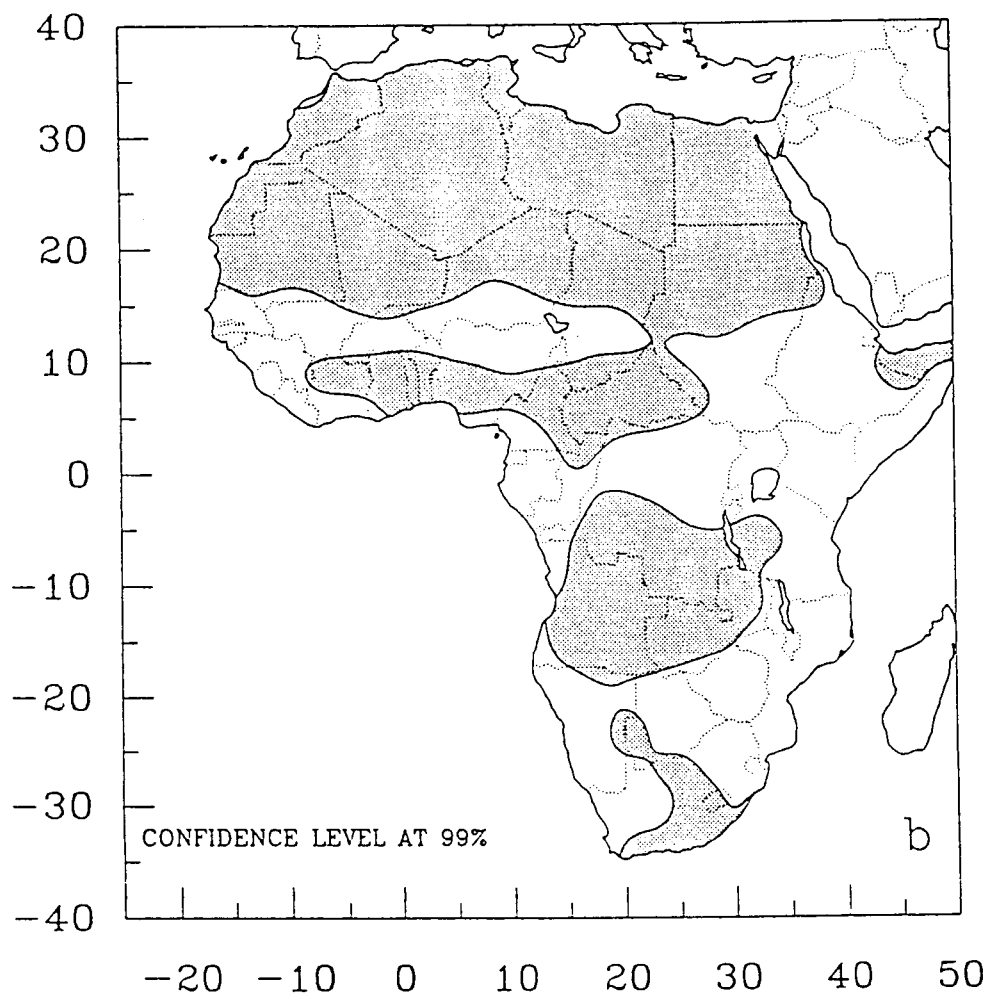


Figure 3b



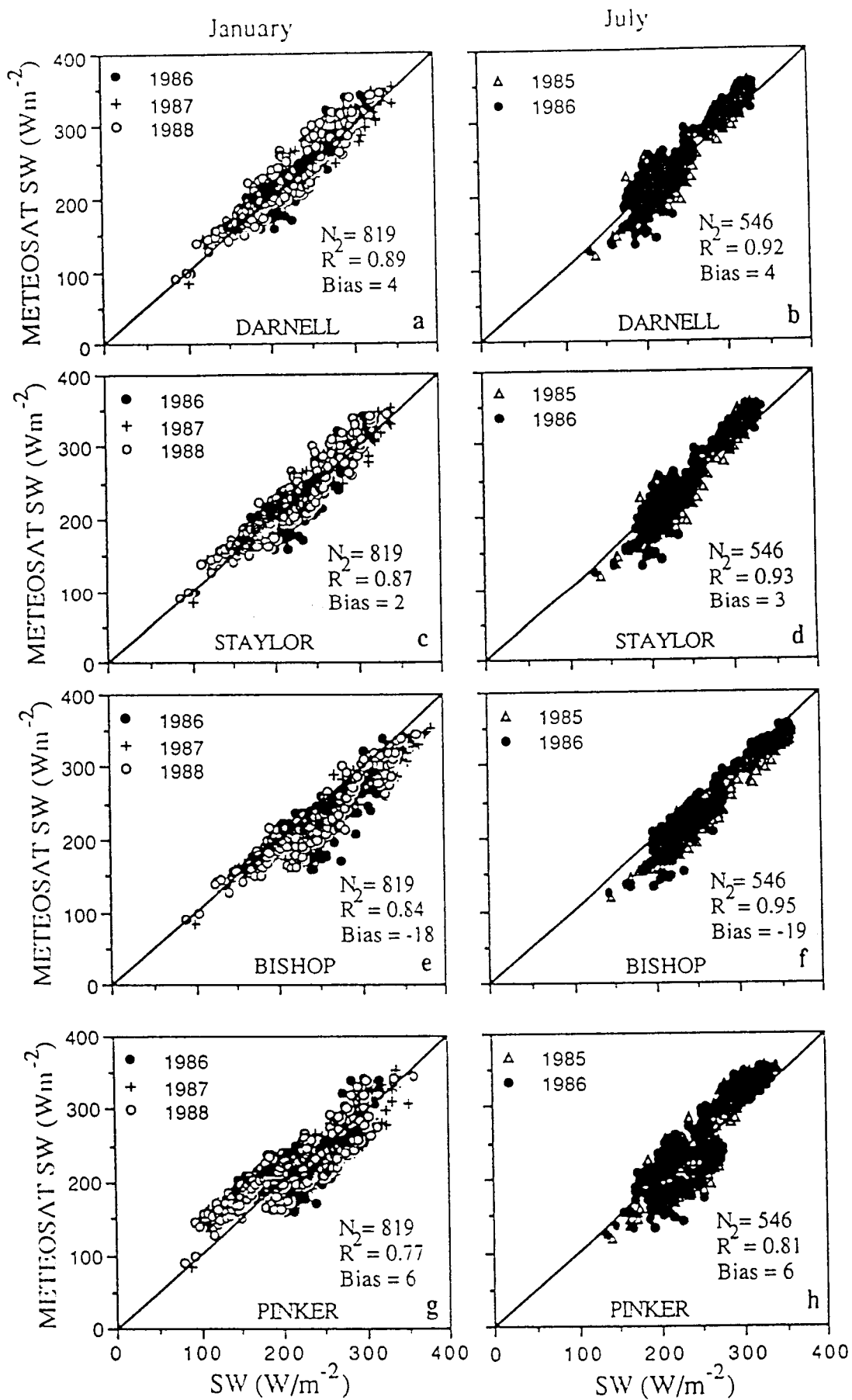


Figure 4

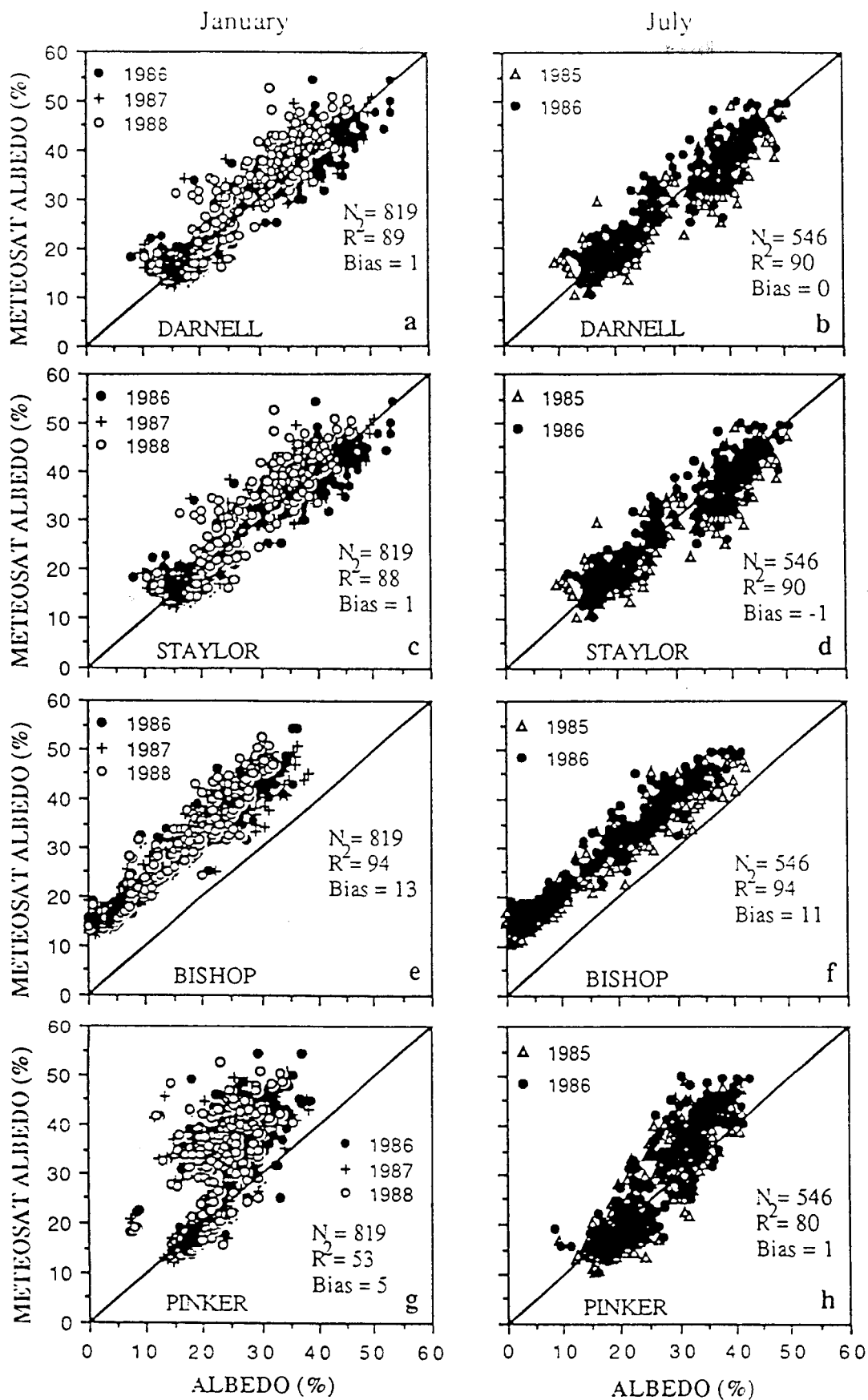


Figure 5

## **Appendix B**

**Temporal and Spatial Variability of Surface  
Radiation Budget over the African Continent as  
derived from METEOSAT. Part II: Climatologies  
and Interannual Variability of Surface Global  
Solar Irradiance, Albedo and Net Radiation**

Temporal and Spatial Variability of Surface Radiation Budget over the African  
Continent as derived from METEOSAT.

Part II: Climatologies and Interannual Variability of Surface Global Solar Irradiance,  
Albedo and Net Radiation.

Mamoudou B. Ba, Sharon E. Nicholson

Department of Meteorology  
Florida State University  
Tallahassee, FL 32306\_3034

March, 1996

## Abstract

The temporal and spatial variability of the Surface Radiation Budget (SRB) over the African continent has been studied using METEOSAT data for the period 1983-88. Continental maps of land-surface albedo, global solar irradiance and surface net radiation for the midseasonal months of January, April, July and October are presented.

The results show that, except for the Sahel, the continental pattern of surface albedo does not exhibit a zonal character. The patterns of surface albedo over the Sahara match the distribution of soils reasonably well, indicating a strong dependence of surface reflectivity on soil characteristics. Substantial seasonal variations characterize the tropical regions located south of  $10^{\circ}\text{N}$ .

## 1. Introduction

In part one of this article (Ba *et al.*, 1996), we described a methodology for deriving estimates of solar irradiance and surface albedo using METEOSAT data and compared our results with those of other investigators. Here in part II, the methodology is applied to studying the radiation balance of the African continent.

The results have several potential applications because of the importance of solar irradiance at the surface in driving the global climate system. It is the primary energy source for the system and controls the surface energy balance. It is also the key factor controlling primary productivity of vegetation. For this reason, accurate estimates of surface radiation balance are necessary for climate modelling. Likewise accurate estimates of surface albedo are needed, particularly in General Circulation Models (GCMs). Although GCMs require surface albedo estimates with an accuracy of 0.01 to 0.05 on the monthly time scale, most GCMs currently use inaccurate maps of surface albedo and/or adopt a typical albedo value for a given vegetation class. It would be preferable to map surface albedo over long time periods, possibly over several spectral bands, and to develop models of surface albedo variation as a function of vegetation type and seasonal evolution. This can be done only via satellites.

For the African continent, albedo is of special interest because of the hypothesis of Charney (1975) and others that increased surface albedo,

accompanying drought of human-induced desertification, might exacerbate or even trigger drought. Numerous satellite estimates of surface albedo have been made over West Africa (e.g., Norton *et al.* 1979; Courel *et al.* 1984; Pinty *et al.* 1985; Pinty and Szejwach, 1985; Dedieu *et al.*, 1987; Pinty and Tanré, 1987; Pinty and Ramond 1987). Fewer estimates of continental scale albedo have been made, notably those of Li and Garand (1994), Pinker and Laszlo (1992), and Darnell *et al.* (1992). While most have emphasized methodologies, Norton *et al.* (1979) and Courel *et al.* (1984) have examined the seasonal and interannual variations in an attempt to evaluate Charney's hypothesis.

The aim of this paper is to present temporal and spatial variations of global solar irradiance and surface albedo over Africa as deduced from satellite estimates for the period of 1983-88. A study of surface net radiation is also presented using complementary data on surface net longwave radiation estimates of Darnell *et al.* 1992. We first focus on the regional and seasonal distribution of these three parameters. Then we examine their interannual variability during the period of study using longitudinal transects at 10°W and 19°E.

## 2. Data

Multi-year METEOSAT visible data and climatologies of vertically integrated water vapor content (Tuller, 1968) and vertically integrated ozone content (London *et al.* 1976) were used for the present study.

Surface net longwave radiation estimates of Darnell *et al.* (1992) were also used to compute surface net radiation. The datasets of Darnell *et al.* (1992) were mapped to the ISCCP equal-area grid with approximate dimensions of 278 km x 278 km (2.5° latitude x 2.5° longitude). The global solar irradiance and surface albedo obtained from METEOSAT were computed at 0.25° x 0.25°, but we preferred to illustrate the maps at a 1° x 1° spatial resolution to have a smoother field for easier analysis. To compute the surface net radiation, METEOSAT products were degraded from 0.25 x 0.25° to match the 2.5 x 2.5° ISCCP grid boxes.

### 3. Temporal and spatial variability of surface radiation budget

Continental maps of land-surface albedo, global solar irradiance and surface net radiation for the midseasonal months of January, April, July and October are produced. Longitudinal transects at 10°W and 19°E are also produced to study the interannual variability of the Surface Radiation Budget (SRB) components during the period of 1983-88.

#### 3.1. Seasonal variation of surface global solar irradiance

Figure 1 presents the continental distribution of the monthly mean global solar irradiance at a spatial resolution of 1° latitude x 1° longitude for the months of January, April, July, and October.



The January surface global solar irradiance (Fig. 1a) is characterized by nearly a zonal distribution over northern Africa above  $10^{\circ}\text{N}$  with values not exceeding  $225 \text{ Wm}^{-2}$ . Between  $0^{\circ}$  and  $10^{\circ}\text{N}$ , values exceeding  $250 \text{ Wm}^{-2}$  dominate this region. The equatorial regions of southern Africa are characterized by values ranging from 225 to below  $200 \text{ Wm}^{-2}$ . Over southwestern Africa (Namibia), the surface global solar irradiance exceeds  $300 \text{ Wm}^{-2}$ .

During April (Fig. 1b), peak values exceeding  $300 \text{ Wm}^{-2}$  occurred over the Sahara. At the northern and southern Saharan boundaries, values ranging from 275 to  $300 \text{ Wm}^{-2}$  characterized the global solar irradiance field. The equatorial regions of southern Africa, with global solar irradiance not exceeding  $225 \text{ Wm}^{-2}$ , are marked by very little spatial variation.

During July, the Saharan regions continue to represent high surface global solar irradiance, which now exceeds  $325 \text{ Wm}^{-2}$  over the northern Saharan regions (see Fig. 1c). Meanwhile, the surface global solar irradiance significantly decreases in Sahelo-Soudanian regions, a consequence of the increasing cloudiness associated with the migration of the Inter-Tropical Convergence Zone (ITCZ) to the north. The pattern of the surface global solar irradiance distribution is nearly zonal over these regions with a relatively high north-south gradient. Values of surface

global solar irradiance lower than  $200 \text{ Wm}^{-2}$  are now present over the Guinea coast and over Cameroon. Meanwhile, in southern Africa, the surface global solar irradiance reaches its low values of the year.

The global solar irradiance during October does not reach  $300 \text{ Wm}^{-2}$  (Fig. 1d). The maxima lie over Sahelian regions and in the southwest of southern Africa. The lowest values are found over the equatorial regions and the northernmost and the southernmost parts of the continent.

### 3.2 Interannual variability of global solar irradiance

The interannual variability of global solar irradiance is due to variations in atmospheric conditions (cloudiness, water vapor and aerosol content). Clouds are an especially important determinant of the downward short-wave flux as they attenuate the incoming radiation.

Latitudinal transects of zonal variations of global solar irradiance for January and July were used to analyze the variability during the period of 1983-88. Fig. 2 represents latitudinal cross sections of monthly global solar irradiance at  $10^{\circ}\text{W}$  (top) and at  $19^{\circ}\text{E}$  (bottom). On the left-hand side is the January transect; on the right-hand side is the July transect.

A look at various latitudes shows that there is little interannual variability of short-wave radiation during the dry season. Examples are the area of approximately  $5^{\circ}\text{N}$  to  $12^{\circ}\text{N}$  in January and  $10^{\circ}\text{S}$  to  $30^{\circ}\text{S}$  in July.

Short-wave radiation is also relatively constant from year-to-year over the Saharan region from about 18°N to 25°N, particularly during July. As to be expected, there is considerable interannual variability during the wet season in the respective hemispheres and conditions are more variable in the southern hemisphere than in the northern. The most variable conditions are in the areas of the ITCZ (e.g., south of 15°N at 10°W and around 5°N to 10°N at 19°E). Variability is also fairly high north of the Sahara during the wet season in January.

Two features in these transects are particularly striking: anomalously low values in January 1985 and 1988 over North Africa and in January 1984 in southern equatorial latitudes. The January 1985 anomaly runs from about 12°N to 18°N; the difference between this and other Januaries reaches a maximum of about 50 Wm<sup>-2</sup> near 15°N. The analysis of the monthly mean infrared image for January 1985 shows that the reduced global solar irradiance is due to a persistent cloud band stretching from the Atlantic coast of Senegal to the Mediterranean coast of Libya. This is consistent with a transect drawn from Darnell *et al.* (1992) estimates and is probably likewise linked to winter cloudiness over the central Sahara in association with such cloud bands or similar systems. The 1988 anomaly is likewise apparent in the Darnell *et al.* data set and probably also represents persistent cloudiness.

The January 1984 anomaly near  $2^{\circ}\text{S}$  to  $12^{\circ}\text{S}$  is more difficult to explain, as is the generally high variability in these latitudes of year-round rainfall, where the interannual variability of rainfall is generally small. This does suggest rather marked interannual variability of cloudiness in the southern equatorial latitudes during January, which is well within the wet season in these latitudes.

### 3.3. Spatial heterogeneity of the surface albedo field

Figure 3 represents the continental distribution of the monthly mean surface albedo (1983-88) at a spatial resolution of  $1^{\circ}$  latitude  $\times$   $1^{\circ}$  longitude for four individual months, each representing a season. Similar maps were also derived for each month of the year, but are not presented here. These show a large range of albedo, from low values in equatorial Africa that never exceed 0.20 to values exceeding 0.50 in some desert regions of the subtropics. Values in the Sahel of West Africa exhibit a strong zonal character, but this is generally not the case elsewhere over the continent.

The most prominent features of the geographical pattern of surface albedo are the maxima over the Sahara desert and the Kalahari desert. These features are relatively invariant throughout the year. In four desert regions, surface albedo reaches 0.50 during all or most of the year. These are located in the eastern part of Mauritania at its border with Mali, the

central Algerian Sahara, the Ténéré desert located north-north west of Lake Chad, and the Libyan desert. In general, the pattern of surface albedo over the Sahara matches that of soil distribution, as shown by the FAO (1977) Soil Map of the World. This indicates a strong dependence of surface reflectivity on soil characteristics.

Over West Africa, from the southern Sahel near  $12^{\circ}\text{N}$  to the central desert regions of Mali and Mauritania, our estimates range between about 0.20 and 0.50, being somewhat lower in July than in January. Within this same area, the estimates of Pinty and Ramond (1987) range from about 0.20 to 0.50; those of Li and Garand (1994) from 0.15 to 0.45. In the northern Sahelian zone from  $18^{\circ}\text{N}$  to  $20^{\circ}\text{N}$  and  $2^{\circ}\text{W}$  to  $10^{\circ}\text{W}$ , our albedo averages are 0.45 for January and 0.44 for July, compared to 0.44 and 0.46 estimates for February and July, 1979, by Pinty and Ramond (1987). These are also in relatively good agreement with early assessments by Courel *et al.* (1984) (ranging from 0.40 to .50) and Rockwood and Cox (1978) (0.42 or greater), based on METEOSAT and SMS data, respectively. Of note is the strong gradient in surface albedo, with values increasing from 0.20 to 0.40 within 5 degrees of latitude over the western Sahel.

For the Sahelian region, our results can be directly compared with previous estimates using specific point comparisons for three intensively studied locations in Burkina Faso (Table 1). The studies used for comparison are those of Pinty and Tanré (1987), Deschamps and Dedieu

(1986), and Pinty and Ramond (1987). Pinty and Tanré (1987) used measurements of surface global solar radiation together with METEOSAT radiances to derive mean albedo on 18 February and 2 July 1979. Pinty and Ramond's (1987) values correspond to surface albedo estimates corrected for atmospheric and angular effects using METEOSAT data obtained near the local noon on 18 February and 2 July 1979. Deschamps and Dedieu's values correspond to reflectances computed at 11.30 TU.

Generally, our values agree well with those obtained by all three investigators mentioned above (Table 1). Our February values are somewhat higher than those obtained by Pinty and Ramond at Dori and Ouagadougou. During July, our estimates are generally lower than those obtained by the others for Ouagadougou and Fada Ngourma. Although our estimates and those of Pinty and Ramond are made for different years, they are the most comparable because both represent the daily mean surface albedo. Those obtained by Deschamps and Dedieu and those of Pinty and Tanré correspond to surface albedo obtained at one point in time near the local noon.

In equatorial regions, from  $10^{\circ}\text{N}$  to  $10^{\circ}\text{S}$ , our values are generally on the order of 0.14 to 0.20 in both January and July, and are in good agreement with those of Li and Garand (1994). Over southern Africa, our estimates range from 0.15 to 0.30 over most of the region, likewise in agreement with the results of Li and Garand (1994). Thus, the surface

albedo over the semi-arid portions of southern Africa is significantly lower than over the equivalent regions of northern Africa. The spatial gradients of albedo are also comparatively weak, the maximum being a change from 0.15 to 0.25 within 10 degrees of latitude in the far southwest.

### 3.4 Seasonal variability of surface albedo

During January (Fig. 3a), the northern equatorial regions located between  $0^{\circ}$  and  $12^{\circ}\text{N}$  are marked by surface albedo below 0.20 with a minima lower than 0.15 centered over the Central African Republic. Values exceeding 0.15 dominate the southern equatorial regions. In April (Fig. 3b), the pattern of surface albedo in West Africa does not change significantly, while in the southern equatorial region values below 0.15 appear over the Congo basin. During July (Fig. 3c) values below 0.20 characterize part of West Africa located south of  $10^{\circ}\text{N}$ , except two sectors of values above 0.20 over the southeastern Ivory Coast and another located over southeastern Guinea. Values below 0.15 now dominate in the Congo basin and over coastal regions of southeastern Africa. During October (Fig. 3d), values below 0.20 still dominate western Africa except a sector located over southeastern Ivory Coast.

Bi-directional effects due to changing solar geometry are minimized by the normalization of data by the directional function (see the companion paper of Ba *et al.* 1996). Therefore most of the seasonal

changes in surface albedo in vegetated regions are due to changing plant phenology. However, over West Africa, bush fires also contribute to lowering values of surface albedo during the dry season (see Leroux *et al.* 1994).

Both these seasonal changes and the latitudinal variations in albedo are underscored in the transects in Figs. 4 and 5. The former shows longitudinal transects of surface albedo for four months at 10°W and 19°E, respectively. The latter provides a map of seasonality index ( $S$ ) of surface albedo, defined as:

$$S = 100(As_{jul} - As_{feb})/As_{feb} \quad (1)$$

where  $As_{jul}$  and  $As_{feb}$  refer to July and February surface albedo, respectively.

For the transect at 10°W seasonal variations are readily evident for the region located below 12°N. During January and April, the surface albedo slightly exceeds 0.15, while it reaches 0.20 during July and October. The seasonal cycle approaches 0° near 12°N, then reverses further north. Surface albedo abruptly increases from 0.25 to 0.50 from 15°N to 18°N, showing a broad maximum centered around 20°N. From there northward to 28°N, it shows a relatively steady decrease to about 0.30. A secondary maximum appears, however, near 25°N. Overall, the amplitude of the seasonal cycle of albedo is large from about 18°N to 22°N, although there is



little change in vegetation cover in this sector during the course of the year.

The transect at 19°E is interesting because it allows one to compare the gradients of surface albedo between the arid and semi-arid regions of northern and southern hemisphere regions. In the southern hemisphere, surface albedo decreases steadily from arid to tropical regions, ranging from ~ 33% at about 25°S to ~15% throughout the equatorial latitudes from c. 15°S to 0°. In the northern hemisphere, surface albedo is likewise about 10% in the equatorial latitudes, but it increases sharply from 10°N to a maximum of nearly 50% around 15°N to 17°N. It decreases to about 35% from about 20°N to 24°N, then increases to over 50% further north. The sharper gradient in the northern hemisphere corresponds to a steeper rainfall gradient; the lower albedo over the southern hemisphere corresponds to a denser vegetation cover and wetter climate, with no desert region equivalent to the Sahara.

More difficult to explain are the desert areas with relatively high seasonal variability and the minimum in surface albedo at c. 20°N - 24°N at 19°E. In the former case, we suspect that the apparent variability is produced by the seasonal fluctuations of atmospheric aerosols. Near 10°W, aerosol content is greatest in July (N'Tchayi Mbourou *et al.* 1996) and is consistent with the relatively low albedo in July. It is also greatest in the central and southern Sahel, accounting for the greater seasonal contrasts

at about 18°N to 22°N than in areas further north. At 19°E aerosol content is lower than further west but likewise has a maximum in July, accounting for the lower seasonal variation over the desert in this transect.

The secondary minimum in this transect at c. 20°N - 24°N is probably related to the Tibesti massif. Vegetation is somewhat higher here, as rainfall is significantly higher than in the surrounding lower plain. The topography itself might also influence the apparent surface albedo and the aerosol effect here is lower than elsewhere in the Sahara and Sahel.

Overall, a somewhat surprising picture of surface albedo emerges from these transects. At both 10°W and 19°E, the seasonal variation of surface albedo reverses north and south of about 13°N and 10°N, respectively. To the north, minimum surface albedo corresponds to the wet season, maximum albedo to the dry season, as would probably be anticipated. However, the opposite is true to the south, with higher surface albedo during the wet season. In the southern hemisphere, maximum albedo also coincides with the wet season with the minimum occurring at the end of the wet season and during the dry season.

The seasonal cycle is summarized in Fig. 5, showing the seasonality index  $S$ . Several general patterns are apparent. First of all, the amplitude of the cycle is largest in the subtropical latitudes, which experience well-defined dry and wet seasons. It is lowest in the equatorial latitudes, with nearly year-round rainfall, and in the desert regions of southwestern

Africa. Further evident is a reversal in sign at  $10^{\circ}\text{N}$  to  $13^{\circ}\text{N}$  and  $0^{\circ}$  to  $4^{\circ}\text{N}$ . This is consistent with the results described above in the transects and shows that in the Sahel, dry season albedo is higher than wet season albedo, while in equatorial regions and the southern hemisphere the opposite is true.

The explanation for the above pattern is not readily apparent, but it may relate to the peculiar spectral signature of vegetation, with vigorous green vegetation having a very high albedo in the infrared wavelengths (Dickinson 1983). This would mean that in the case of a reasonably sparse cover with considerable bare ground exposed, albedo is high during the dry season with maximum exposed soil and minimum soil moisture. Such a situation occurs in the Sahel, where dry-season brushfires may further enhance this effect. For a region with relatively dense cover, the vigor of the vegetation would govern the albedo, with the infrared effect being dominant and producing high albedos during the growth season. This is clearly the case in wet equatorial latitudes with forests and relatively dense woodlands. It is probably true of the southern subtropics as well, since vegetation density there is considerably higher than in the Sahel, despite similar conditions of rainfall (Nicholson and Farrar 1994).

### 3.5 Interannual variability of surface albedo

The interannual variability of surface albedo reflects changes in surface properties, particularly in vegetation cover. Therefore, one may expect larger variability in regions, such as the Sahel, where the interannual variability of rainfall is much higher than elsewhere on the continent. In contrast, one should expect a lesser interannual variability over the Sahara.

Figure 6 illustrates interannual variability of surface albedo for January 1984-88 (left-hand side) and July 1983-88 (right-hand side) for latitudinal transects at  $10^{\circ}\text{W}$  (top) and at  $19^{\circ}\text{E}$  (bottom).

These transects do not show the anticipated patterns of surface albedo. The Sahelian region (c.  $12^{\circ}\text{N}$  -  $17^{\circ}\text{N}$  in the west,  $11^{\circ}\text{N}$  to  $15^{\circ}\text{N}$  in the east) there is a relatively high degree of interannual variability, but it is no larger than in the lower latitudes or in the equivalent latitudes of the southern hemisphere. Also, the interannual variability is relatively large throughout the southern hemisphere during both July and January. This is a puzzling result because July rainfall is virtually zero in all years south of  $10^{\circ}\text{S}$  or  $15^{\circ}\text{S}$  and the vegetation index also shows only weak interannual variability in these latitudes. The high degree of interannual variability over the latitudes of the Sahara is likewise surprising but might be attributed to year-to-year changes in aerosol content.

The variability in the desert is generally less than 5 % of the monthly mean. In contrast, in tropical regions located between 15°N and 15°S, the relative variations are large in comparison to monthly mean (Fig. 6). The differences between the maximum and minimum observed values reached c. 0.035 for a mean surface albedo of about 0.20, which represents 15% of the regions located between 5°N and 10°N during July. In equatorial regions, this difference reaches 20% of the mean value of the surface albedo, which is approximately 0.15 for July.

### 3.6 Seasonal variation of surface net radiation

To study the seasonal and interannual variations of net radiation, we completed our surface radiation estimates with longwave radiation estimates of Darnell *et al.* (1992).

Figure 7 shows the continental distribution of the monthly mean surface net radiation at spatial resolutions of 2.5° x 2.5° for the individual months of January, April, July, and October. As expected, the pattern of net radiation shows that over northernmost and southernmost Africa the minimum (less than 25 Wm<sup>-2</sup>) occurs in January and July, respectively. This results from reduced incoming solar radiation during January over northern Africa, and during July over southern Africa.

The pattern of net radiation shows that the maximum (more than  $150 \text{ Wm}^{-2}$ ) occurs over the equatorial regions located between  $10^{\circ}\text{N}$  and  $10^{\circ}\text{S}$ . Values higher than  $150 \text{ Wm}^{-2}$  dominate the April field over these regions (Fig. 7b) with a peak maximum of  $175 \text{ Wm}^{-2}$  over the Guinea coast and Cameroon. During July, the peak maximum, exceeding  $150 \text{ Wm}^{-2}$ , moves toward the north and is centered around  $10^{\circ}\text{N}$ . During October, peak of maximum values exceeding  $150 \text{ Wm}^{-2}$  are located in the equatorial regions (Fig. 7d).

### 3.7 Interannual variation of surface net radiation

The interannual variability of the net surface radiation reflects that of both the net global solar irradiance and the net longwave radiation.

Figure 8 illustrates the interannual variability of surface net radiation during January 1984-88 (left-hand side) and July 1983-88 (right-hand side), corresponding to latitudinal transects at  $10^{\circ}\text{W}$  (top) and at  $19^{\circ}\text{E}$  (bottom).

For January, the latitudinal variation of the surface net radiation is very similar to that of the surface global solar irradiance at  $10^{\circ}\text{W}$ . The values during 1985 are as low as  $25 \text{ Wm}^{-2}$ , lower than other Januaries for regions located between  $12^{\circ}\text{N}$  and  $20^{\circ}\text{N}$ . This was the case for the surface global solar irradiance. Important fluctuations are present on the  $19^{\circ}\text{E}$

transect for January over southern Africa, especially around  $10^{\circ}\text{S}$ . In contrast, north of  $5^{\circ}\text{N}$ , the net radiation shows little interannual variability.

During July, variations of the surface net radiation from one year to another are generally small for the  $10^{\circ}\text{W}$  transect, except for 1988. Values of the surface net radiation are generally much higher during July 1988 than any other year, especially between  $15^{\circ}$  and  $25^{\circ}\text{N}$  at  $10^{\circ}\text{W}$ . These high values are due to much higher values of net longwave radiation estimates of Darnell *et al.* (1992) (not shown here). These systematic high estimates of net longwave radiation during July 1988 are questionable.

#### 4. Conclusion

Overall, neither the seasonal cycle nor the interannual variability of surface albedo or surface irradiance conform to those anticipated from regional climate dynamics. In some cases, the explanation appears to lie in the complex spectral signature of green vegetation. In general, however, it appears that both variability of atmospheric constituents, particularly aerosols, and calibration problems introduce errors in the seasonal cycle and in year-to-year fluctuations. These problems must be overcome if satellite methods are to be used to study interannual variability of surface radiation balance on a continental scale.

Two patterns are relatively clear, however. One is that the seasonal changes within a climatic region are relatively small compared to the

contrast between regions of diverse climate. Secondly, both the seasonal and interannual changes are small compared to those required for surface albedo changes to influence rainfall variability or the occurrence of drought.

### Acknowledgments

We would like to thank Dr. R. Frouin of California Space Institute, Scripps Institution of Oceanography in San Diego for providing METEOSAT data, and Mr. J. Kim of the Florida State University for programming support. Longwave radiation data used in the study were provided by Ms. Nancy Ritchey of Lockheed Engineering and Sciences Company, Hampton, Virginia. This work was sponsored by the TRMM project via NASA Grant NAG5-1587.

### References:

- Ba, M. B., G. Dedieu, and S. E. Nicholson, 1996: Temporal and spatial variability of surface radiation budget over the African continent as derived from METEOSAT. Part I: Derivation of global solar irradiance and surface albedo. This issue.
- Charney, J. G., 1975: Dynamics of deserts and droughts in the Sahel. *Quart. J. Roy. Meteor. Soc.*, 101, 193-202.



- Courel, M. F., R. S. Kandel, and S. I. Rasool, 1984, Surface albedo and the Sahel drought, *Nature*, 307, 528-531.
- Darnell, W., F. Staylor, S. K. Gupta, N. A. Ritchey, and A. C. Wilber, 1992: Seasonal variation of surface radiation budget derived from International Satellite Cloud Climatology Project C1 data. *J. Geophys. Res.*, 97, 15,741-15,760.
- Dedieu G., P.Y. Deschamps, Y.H. Kerr, and P. Raberanto, 1987: A global survey of surface climate parameters from satellite observations : Preliminary results over Africa. *Adv. Space Res.*, 11, 129-137.
- Deschamps, P. Y., and G. Dedieu, 1986: Comments on "surface albedo over the Sahel from METEOSAT radiances". *J. Climate Appl. Meteor.*, 25, 575-576.
- Dickinson, R. E., 1983: Land surface processes and climate-surface albedos and energy balance. *Adv. Geophys.*, 25, 305-353.
- FAO, 1977: *Soil Map of the World, vol. VI, Africa*, UNESCO, Paris.
- Leroux, X., J. Polcher, G. Dedieu, J. C. Menaut, and B. Monteny, 1994: Radiation exchanges above west African moist savannas: Seasonal patterns, and comparison with a GCM simulation. *J. Geophys. Res.*, 99, 25857-25868.
- Li, Z., and L. Garand, 1994: Estimation of surface albedo from space: A parameterization for global application. *J. Geophys. Res.*, 99, 8335-8350.

- London, J., R. D. Bojkov, S. Oltmans, and J. I. Kelley, 1976: Atlas of the global distribution of total ozone July 1957-June 1967. NCAR/TN-113 + STR.
- Nicholson, S. E., and T. J. Farrar, 1994: The influence of soil type on the relationships between NDVI, rainfall, and soil moisture in semiarid Botswana. I. NDVI response to rainfall. *Rem. Sens. Environ.*, **50**, 107-120.
- Norton, C. C., F. R. Mosher, and B. Hinton, 1979: An investigation of surface albedo variations during the recent Sahel drought. *J. Appl. Meteor.*, **18**, 1252-1262.
- N'Tchayi, G. M., J. J. Bertrand, and S. E. Nicholson, 1996: The diurnal and seasonal cycles of desert dust over Africa north of the equator Submitted to *J. Appl. Meteor.*.
- Pinker, R. T., and I. Laszlo, 1992: Modeling surface solar irradiance for satellite applications on a global scale. *J. Appl. Meteor.*, **31**, 194-211.
- Pinty, B., and G. Szejwach, 1985: A new technique for inferring surface albedo from satellite observations. *J. Climate Appl. Meteor.*, **24**, 741-750.
- Pinty, B., G. Szejwach, and J. Stum, 1985: Surface albedo over the Sahel from METEOSAT radiances. *J. Climate Appl. Meteor.*, **24**, 108-113.
- Pinty, B., and D. Tanré, 1987: The relationship between incident and double-way transmittances: An Application for the estimate of

surface albedo from satellites over the African Sahel. *J. Climate Appl. Meteorol.*, 26, 892-896.

Pinty, B., and D. Ramond, 1987: A method for estimate of broadband directional surface albedo from a geostationary satellite. *J. Climate Appl. Meteor.*, 26, 1709-1722.

Rockwood, A. A., and S. K. Cox, 1978: Satellite inferred surface albedo over northwestern Africa. *J. Atmos. Sci.*, 35, 513-522.

Tuller, S. E., 1968: World distribution of mean monthly and annual precipitable water. *Mon. Wea. Rev.*, 96, 785-797.

Table 1: Mean Surface albedo over three different sites in Burkina Faso

Sites	Pinty and Ramond (1987)		Deschamps and Dedieu(1986)		Pinty and Tanré (1987)	This Study		
	Feb. 79	Jul. 79	Jul. 83	Jul. 84	Jul. 79	Jul. 83	Feb. 84	Jul. 84
Dori (14.05N,0)	0.34	0.29	0.26	0.26	0.29	0.29	0.37	0.28
Ouagadougou (12.42N,0)	0.25	0.22	0.21	0.21	0.23	0.19	0.29	0.19
Fada Ngourma (12.06N,0.4E)	0.24	0.23	0.20	0.20	0.22	0.18	0.25	0.19

## CAPTIONS

Figure 1: Distribution of global solar irradiance ( $\text{Wm}^{-2}$ ) for (a) January, (b) April, (c) July, and (d) October .

Figure 2: Interannual variation of global solar irradiance ( $\text{Wm}^{-2}$ ) for north-south transects at  $10^{\circ}\text{W}$  (top) and at  $19^{\circ}\text{E}$  (bottom) for January (left) and July (right).

Figure 3: Distribution of surface albedo (%) for (a) January, (b) April, (c) July , and (d) October.

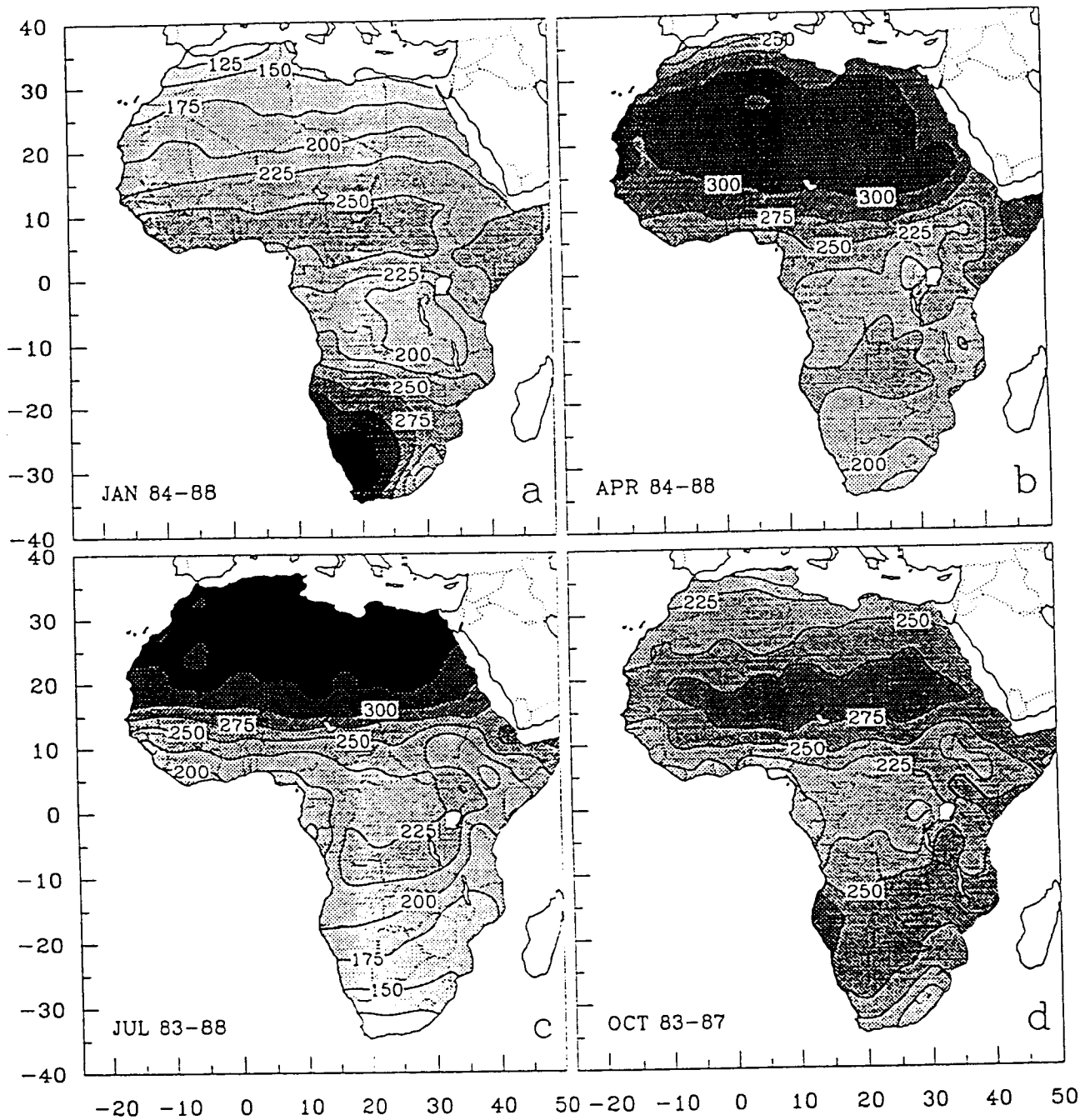
Figure 4: Seasonal variation of surface albedo (%) for north-south transects at  $10^{\circ}\text{W}$  (top) and at  $19^{\circ}\text{E}$  (bottom) for the midseasonal months of January (solid line), April (dotted line), July (dashed line), and October (dashed-dotted line).

Figure 5: Seasonality index (S) of surface albedo. S expressed in percent, represents the difference between values of July and February normalized by that of February.

Figure 6: Interannual variation of surface albedo (%) for north-south transects at 10°W (top) and at 19°E (bottom) for January (left) and July (right).

Figure 7: Distribution of surface net radiation ( $\text{Wm}^{-2}$ ) for (a) January, (b) April, (c) July , and (d) October.

Figure 8: Interannual variation of surface net radiation ( $\text{Wm}^{-2}$ ) for north-south transects at 10°W (top) and at 19°E (bottom) for January (left) and July (right).



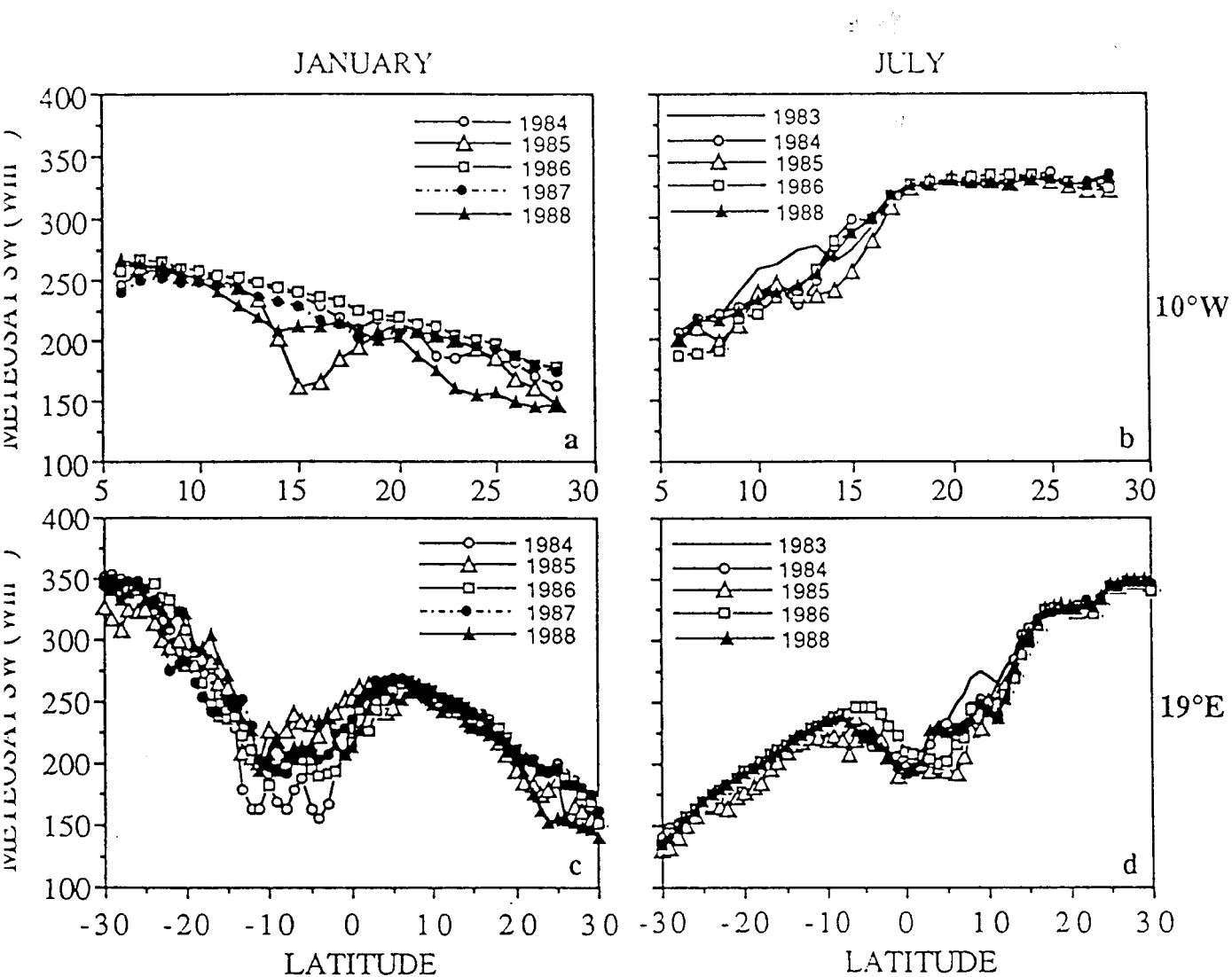


Figure 2



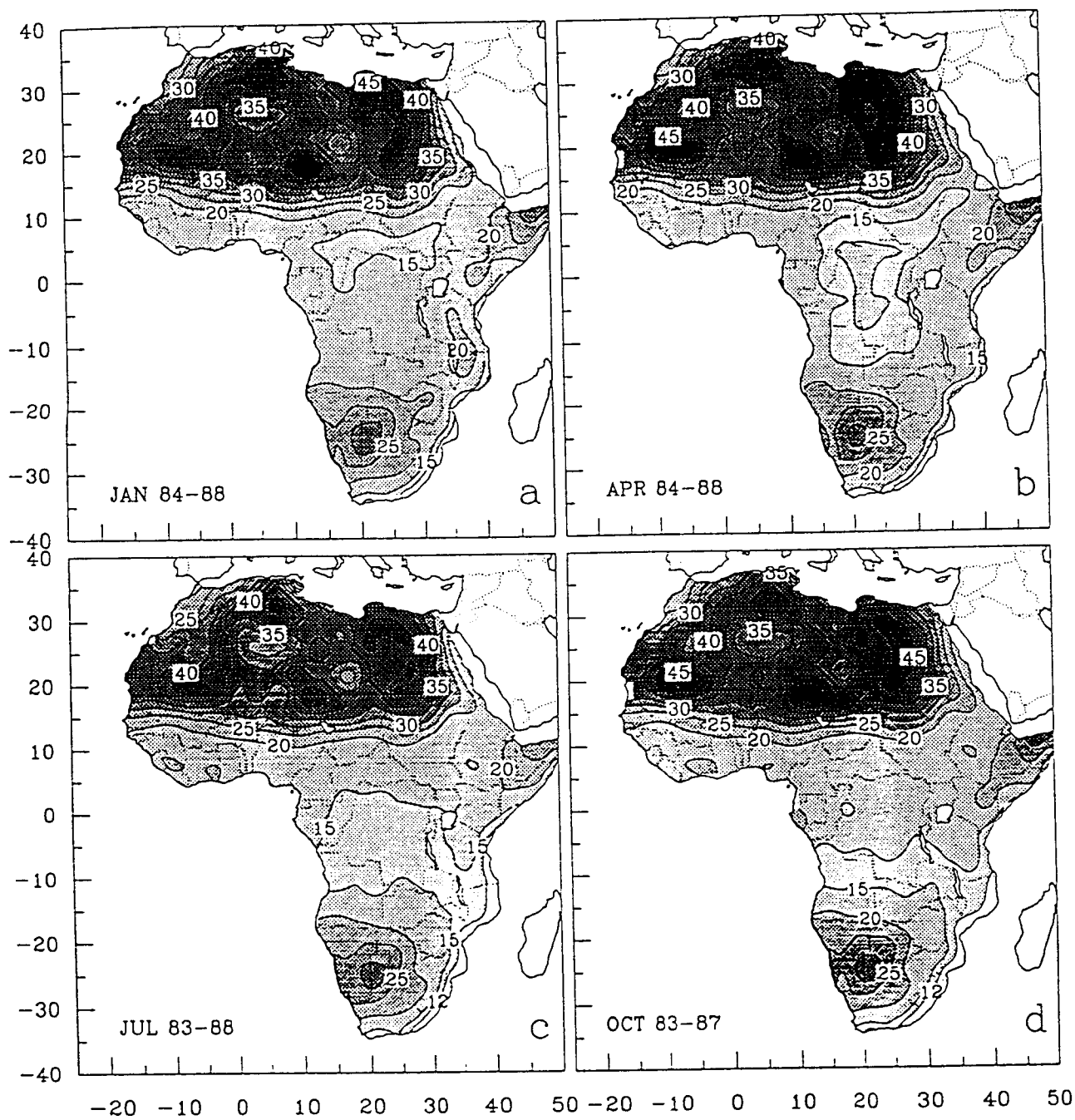


Figure 3

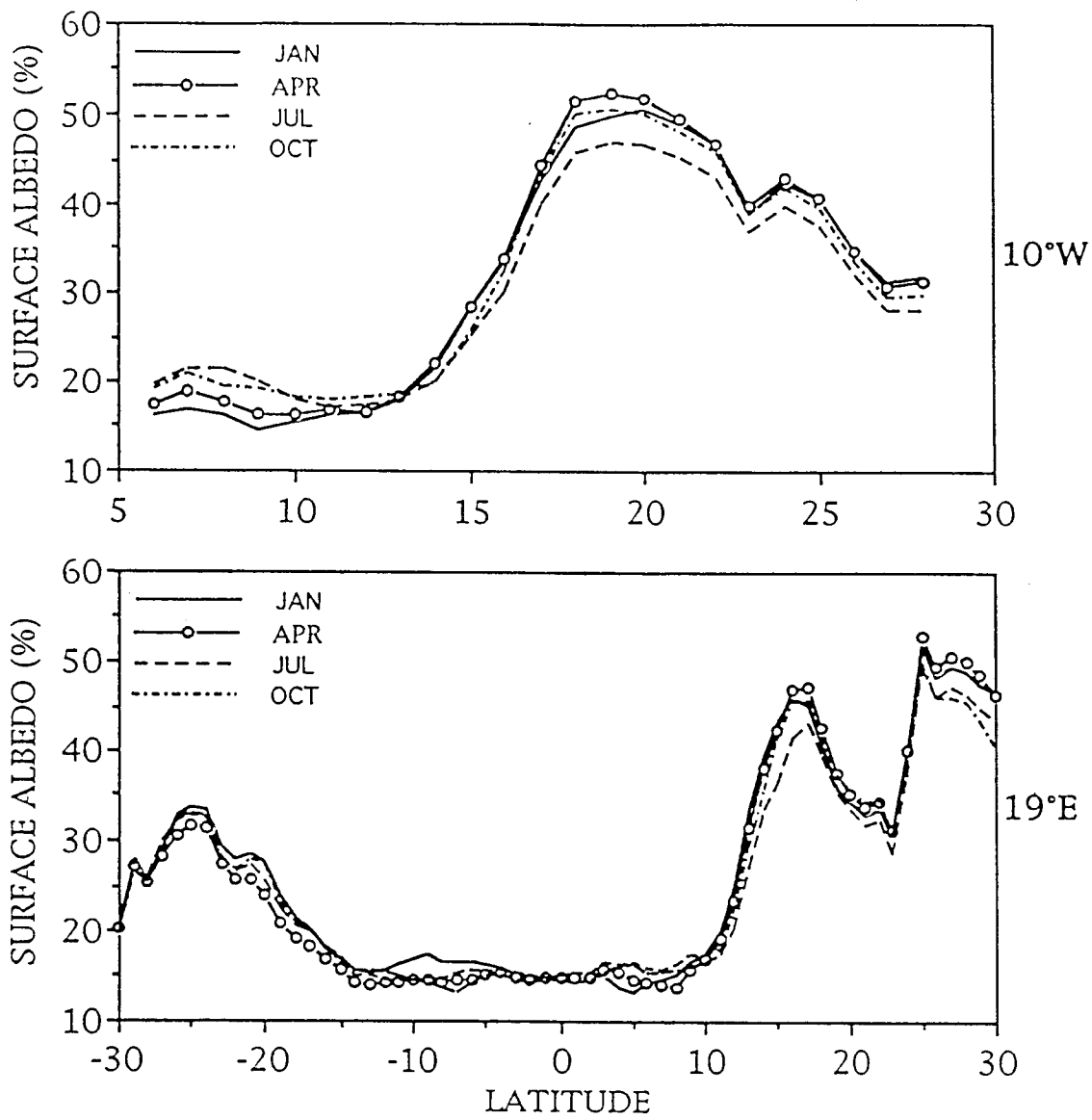


Figure 4

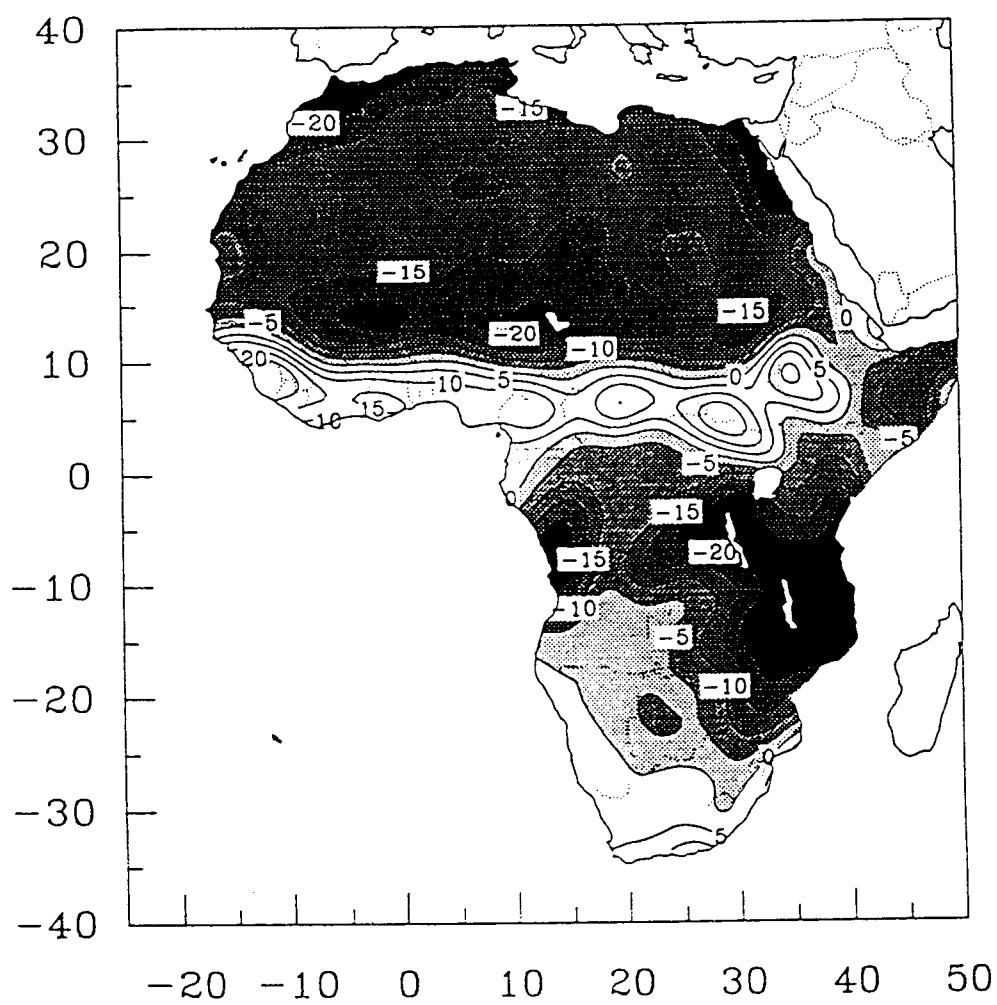
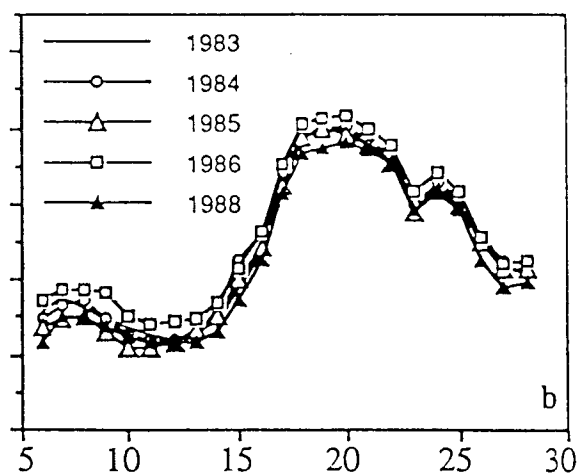
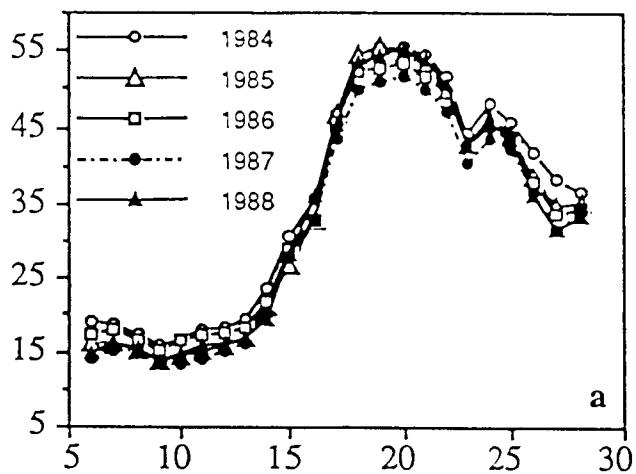


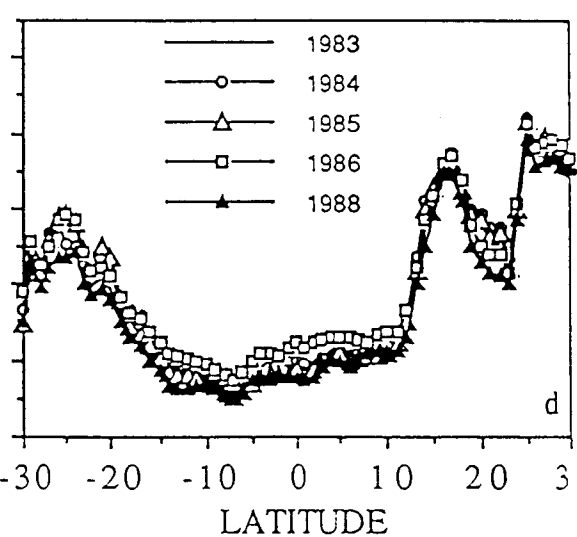
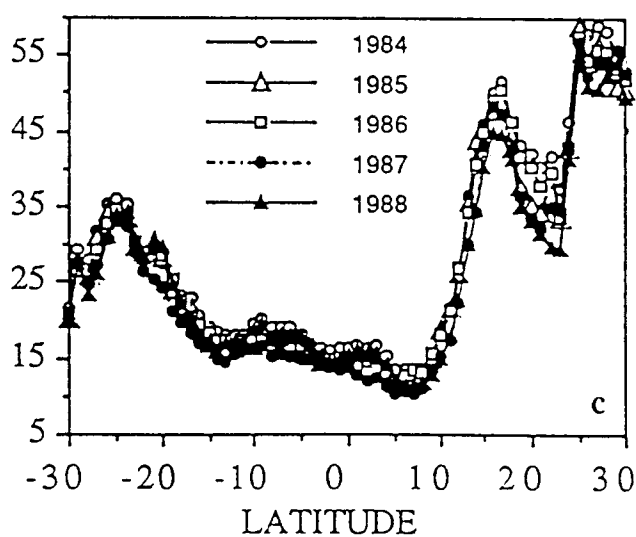
Figure 5

JANUARY

JULY



10°W



19°E

Figure 6

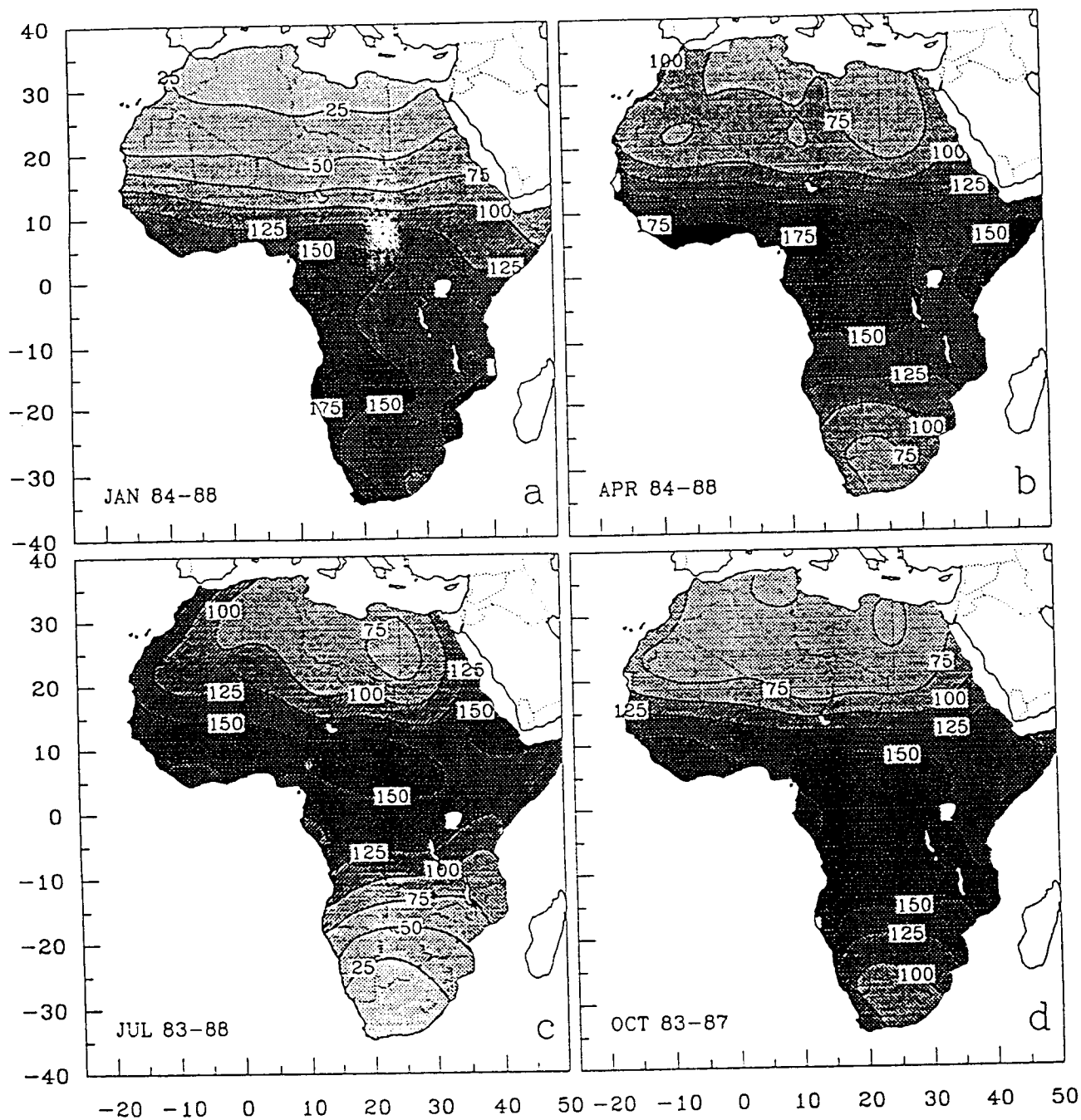


Figure 7

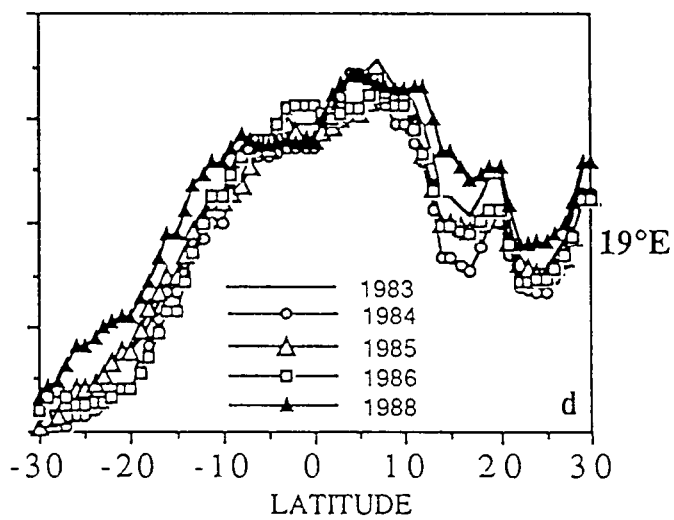
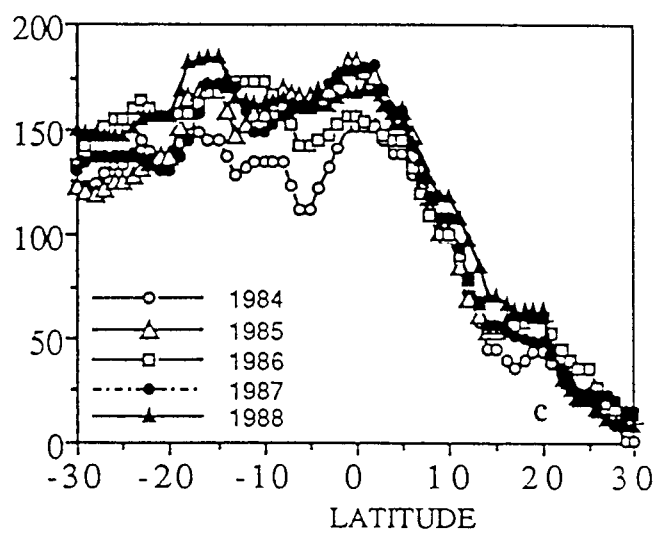
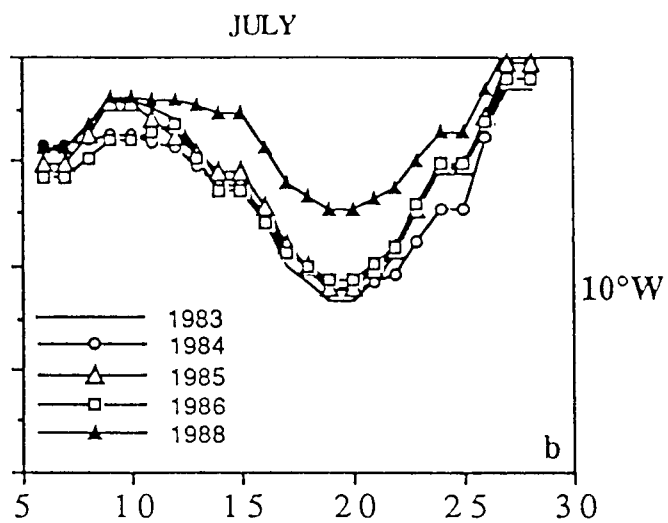
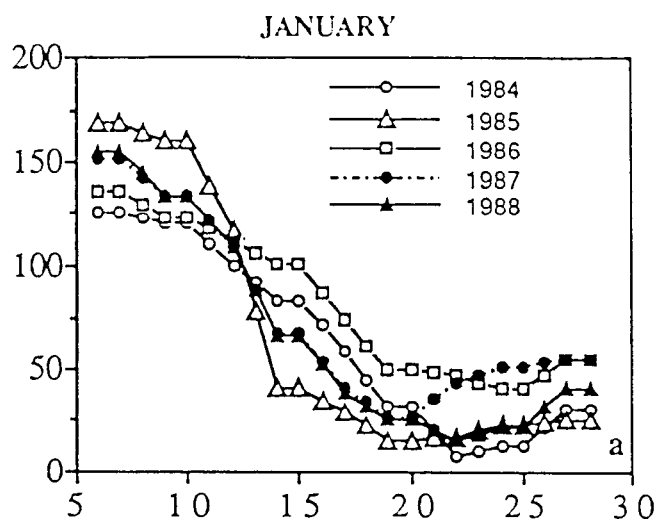


Figure 8

## **Appendix C**

### **Contrasting Conditions of Surface Water Balance in Wet Years and Dry Years as a Possible Land Surface-Atmosphere Feedback Mechanism in the West African Sahel**

## Contrasting Conditions of Surface Water Balance in Wet Years and Dry Years as a Possible Land Surface–Atmosphere Feedback Mechanism in the West African Sahel

A. R. LARE AND S. E. NICHOLSON

*Department of Meteorology, The Florida State University, Tallahassee, Florida*

(Manuscript received 18 February 1992, in final form 10 August 1992)

### ABSTRACT

The climate of West Africa, in particular the Sahel, is characterized by multiyear persistence of anomalously wet or dry conditions. Its Southern Hemisphere counterpart, the Kalahari, lacks the persistence that is evident in the Sahel even though both regions are subject to similar large-scale forcing. It has been suggested that land surface–atmosphere feedback contributes to this persistence and to the severity of drought. In this study, surface energy and water balance are quantified for nine stations along a latitudinal transect that extends from the Sahara to the Guinea coast. In the wetter regions of West Africa, the difference between wet and dry years is primarily reflected in the magnitude of runoff. For the Sahel and drier locations, evapotranspiration and soil moisture are more sensitive to rainfall anomalies. The increase in evapotranspiration, and hence latent heating, over the Sahel in wet years alters the thermal structure and gradients of the overlying atmosphere and thus the strength of the African easterly jet (AEJ) at 700 mb. The difference between dry and wet Augusts corresponds to a decrease in magnitude of the AEJ at 15°N on the order of  $2.6 \text{ m s}^{-1}$ , which is consistent with previous studies of observed winds.

Spatial patterns were also developed for surface water balance parameters for both West Africa and southern Africa. Over southern Africa, the patterns are not as spatially homogeneous as those over West Africa and are lower in magnitude, thus supporting the suggestion that the persistence of rainfall anomalies in the Sahel might be due, at least in part, to land–atmosphere feedback, and that the absence of such persistence in the Kalahari is a consequence of less significant changes in surface water and energy balance.

### 1. Introduction

During the past decade, the African continent has been anomalously dry (Fig. 1). Two of the most severely affected regions are the semiarid Sahel of West Africa and its Southern Hemisphere counterpart, the Kalahari. The rainfall fluctuations in both regions are correlated on the scale of decades and, somewhat less so, for individual years. One notable difference is apparent, however, in the year-to-year persistence of the anomalous rainfall. In the Sahel, the duration of dry or wet episodes is on the order of one or two decades. Rainfall has not exceeded the mean since 1969 (Fig. 2). In contrast, rainfall exceeded the mean in every year from 1950 to 1959. Although on the average rainfall has been abnormally low in the Kalahari during most of the same period and anomalously high in the 1950s, the remarkable persistence so readily apparent in the Sahel series is lacking in the Kalahari. In the latter region, no sequence of “wet” or “dry” years is longer than 4 or 5 years.

We are hypothesizing that the persistence in the Sahel is a manifestation of land–atmosphere feedback, invoked by the changes of surface energy balance in-

duced by anomalously high or low rainfall. A corollary to this hypothesis is that drought or wet years are triggered by large-scale factors in the general atmospheric circulation and/or over the global oceans, acting synchronously in the Sahel and the Kalahari. According to this scenario, the land surface changes induced by the anomalous rainfall (e.g., vegetation, albedo, temperature, soil moisture) would reinforce the atmospheric conditions that produced the anomaly in the Sahel. This would prolong and intensify drought or wet conditions. The absence of such interannual persistence in the Kalahari would then suggest that either the land surface changes are too small in magnitude or spatial extent to have significant feedback on the overlying atmosphere or that the systems that produce rainfall in southern Africa are relatively insensitive to land surface characteristics and processes.

In this study, we examine this hypothesis by assessing the surface water balance for wet years and dry years for representative stations in both regions. The climatology model developed by Lettau (e.g., Lettau 1969; Lettau and Baradas 1973) is used to calculate soil moisture, evapotranspiration, and runoff for the mean conditions of the 10 wettest and 10 driest years at each station. The model is forced by precipitation and incoming solar radiation at the top of the atmosphere. The model is then adapted to produce mean

---

Corresponding author address: Dr. Andrew R. Lare, Applied Research Corporation, NASA GSFC (Code 913), Greenbelt, MD 20771.



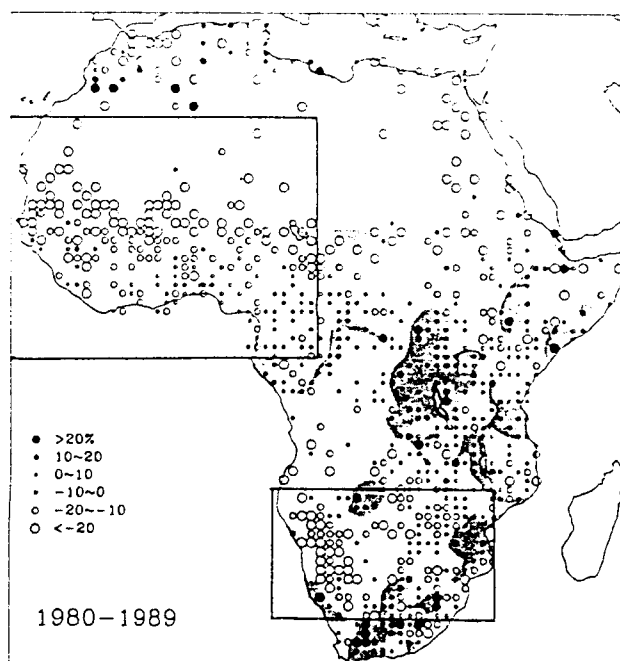


FIG. 1. Mean rainfall for the decade 1980-89 expressed as a percent departure from the long-term mean (i.e., the mean for the entire length of record, commencing in 1901 or as soon thereafter as rainfall observations begin). Station data are averaged over  $1^\circ$  squares to facilitate presentation. Boxed areas indicate regions of interest in this study.

spatial fields of the relevant variables for the 10 wettest and 10 driest years in both regions. The modifications, described in section 2d, facilitate data input for a large number of stations.

The stations and analysis regions are shown in Fig. 3, together with isohyets of mean annual rainfall. The nine Sahelian stations (Fig. 3a) were chosen to represent the north-south rainfall gradient from the Sahara to the Guinea Coast. They run roughly along a north-east-southwest transect, which shifts abruptly to the west at about  $8^\circ\text{N}$ , in order to bypass the anomalous dry zone (Trewartha 1961) of southern Ghana. Six Kalahari stations (Fig. 3b) were chosen to typify a range of conditions. The range is smaller than in the Sahel, however, because in selecting appropriate stations, we limited choices to regions that exhibit significant contrast in rainfall between the 10 wettest and 10 driest years for the Kalahari as a whole.

## 2. The climatology model

### a. Overview

The model used in this study is an adaptation of the Lettau three-part "climatology" model that was developed in the late 1960s (Lettau 1969; Lettau and Lettau 1969, 1975). Climatology was conceived as a regional-scale model of surface energy and water bal-

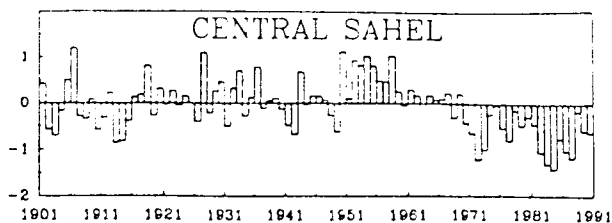


FIG. 2. Rainfall fluctuations in the West African Sahel (1901 to 1990) expressed as a regionally averaged standardized departure (departure from the mean divided by the standard departure).

ance, and it has been applied to a number of geographic locations. Recently, the climatology model has been used to study surface water balance in the Great Plains (Pinker and Corio 1987; Corio and Pinker 1987), the West African Sahel (Nicholson and Lare 1990), and areas of the United States (Lettau and Hopkins 1991).

The accuracy of climatology model output has been verified in a number of experiments. Lettau (1969) applied the model to several areas in North America using observed data encompassing several

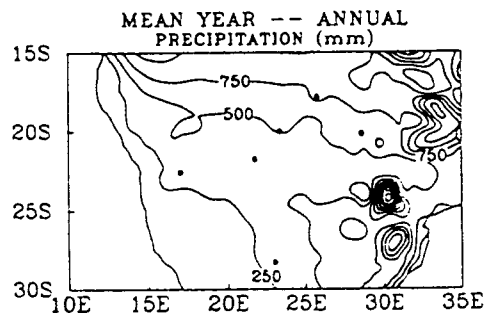
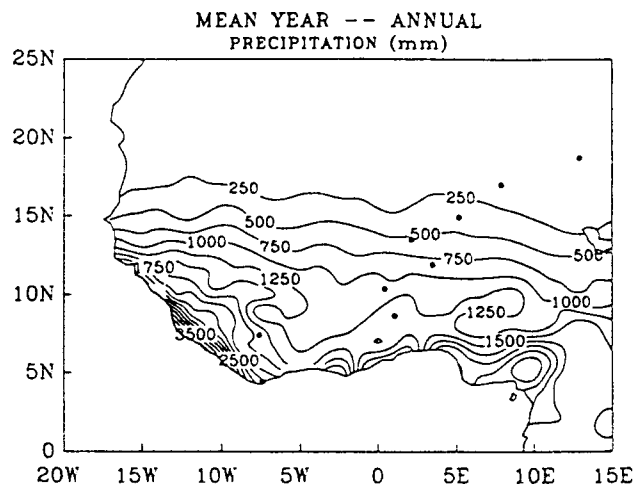


FIG. 3. Map of stations used in the study and isohyets of mean annual rainfall, in mm: (a) West Africa, (b) the Kalahari and surrounding regions.

years and found general agreement between monthly observed and calculated runoff, evapotranspiration, and soil moisture values. Lettau and Baradas (1973) applied the model to the Mabacan River watershed in the Philippines for a 12-yr period. Annual averages of observed runoff were found to be correlated at the 0.89 level with calculations, and monthly evapotranspiration calculations also compared well with empirical data for the region. Corio and Pinker (1987) tested the validity of the model on shorter temporal and smaller spatial scales than the climatic scales associated with previous studies, conducting an experiment for the state of Kansas as well as for several smaller individual watersheds. Calculated runoff compared well with observed values when the entire state was considered, resulting in phase differences of less than 1 month and similar amplitudes. Nicholson and Lare (1990) found good agreement with observed soil moisture and other parameters in the Sahel.

The model consists of three subunits: shortwave radiation climatology, evapoclimatology, and thermoclimatology (Lettau 1969; Lettau and Lettau 1969, 1975). The shortwave radiation submodel is used to calculate ground-absorbed solar radiation from incoming solar radiation (Lettau and Lettau 1969; Lare and Nicholson 1990). Absorbed solar radiation in combination with rainfall forces the evapoclimatology submodel, which in turn predicts monthly mean evapotranspiration ( $E$ ), runoff ( $N$ ), and soil moisture ( $m$ ). Precipitation, evapotranspiration and ground-absorbed radiation provide input to the third submodel.

In this study, only the evapoclimatology submodel is used. However, its input includes ground-absorbed solar radiation, which was calculated with the shortwave submodel. The evapoclimatology submodel is described in section 2c, while details of the shortwave model are summarized in section 2b and presented in Lare and Nicholson (1990). The shortwave model results for the locations described in this article will appear in a sequel concerned with surface energy balance.

### b. Shortwave radiation climatology

In the shortwave radiation submodel, extratmospheric irradiance is used as the forcing function. Five governing equations partition the incoming solar radiation into basic energy balance components and provide a description of the physical relationships between them. The five equations for clear skies relate to absorption by the atmosphere  $H^*$ , planetary albedo  $A^*$ , diffuse radiation  $d^*$ , and ground absorption  $(1 - a_s)G^*$  where  $a_s$  is surface albedo and  $G^*$  is global radiation:

$$1 - A^* = H^* + (1 - a_s)G^* \quad (1)$$

$$1 - G + d^* = \alpha + \sigma \quad (2)$$

$$A^* = \mu\sigma + (1 - \alpha)a_sG^*(1 - \kappa\sigma) \quad (3)$$

$$d^* = (1 - \alpha)\sigma + (1 - \alpha)a_sG^*\sigma \quad (4)$$

$$H^* = \alpha(1 - a_sG^*). \quad (5)$$

The parameters  $\alpha$  and  $\sigma$  denote that part of the solar beam which is absorbed and scattered, respectively, while  $\mu$  and  $\kappa$  represent the fraction of radiation that is effectively scattered back to space and the backscattering of ground-reflected radiation. Contributions by clouds are assumed to be additive for absorption processes and distributive for scattering processes. A more complete discussion of the governing equations and necessary parameterizations may be found in Lettau and Lettau (1969) and Lare and Nicholson (1990).

### c. Evapoclimatology

The evapoclimatology submodel is in essence a numerical solution to the integration of the basic hydrologic balance equation

$$P = E + N + dm/dt, \quad (6)$$

where  $P$  is rainfall,  $E$  is evapotranspiration,  $N$  is runoff, and  $dm/dt$  is the change in soil moisture storage. Three basic assumptions, which are paramount to the model's simplicity, are described below. The original model appeared in Lettau (1969).

The basic premise of the model is as follows:

1) For a stationary climate the long-term mean of  $dm/dt$  is zero, that is, there is no net change in soil moisture storage. Thus

$$\bar{P} = \bar{E} + \bar{N}, \quad (7)$$

In general, this assumption is most valid for the larger regions and the longer time periods.

2) Evapotranspiration and runoff can both be partitioned into immediate and delayed processes:

$$E = E' + E'' \quad (8)$$

$$N = N' + N'', \quad (9)$$

where the single primes denote "immediate" processes occurring in the same month as the rainfall and the double primes denote runoff and evaporation of rain that fell in previous months. The physical rationale for assumption 2 is the need to distinguish between the time variations of  $E$  and  $N$  coupled with concurrent precipitation and those supplied by subsurface moisture, which is dependent on rainfall from previous months.

3) The delayed processes of runoff  $N''$  and evapotranspiration  $E''$  vary directly with soil moisture  $m$  such that

$$N''(t) = \bar{N}''m(t)/\bar{m} \quad (10)$$

$$E''(t) = \bar{E}''m(t)/\bar{m}. \quad (11)$$

Equations (8) and (9) allow for the definition of a quantity called "reduced precipitation" ( $P'$ ), which

represents the amount of the mass input that is not lost by surficial processes of immediate runoff and evapotranspiration and thus is available for soil moisture storage. Therefore,

$$P' = P - N' - E'. \quad (12)$$

In view of the preceding discussion, the soil moisture storage term is reduced to

$$dm/dt = P' - (N'' + E''). \quad (13)$$

The above equation (13) is solved using two empirical concepts, "evaporivity"  $e^*$  and "residence time"  $t^*$ , which are subsequently defined and used to partition the immediate and delayed processes.

The sum of equations (10) and (11) yields an equation that defines a new characteristic dimensional parameter:

$$N'' + E'' = (\overline{N''} + \overline{E''})m/\bar{m} = m/t^*, \quad (14)$$

where  $t^* = \bar{m}/(N'' + E'')$  denotes a time interval most conveniently expressed in months. Physically,  $t^*$  can be interpreted as a "residence time" or "turnover period" that is characteristic of a basin and signifies the time required for a volume of water equal to the annual mean of exchangeable soil moisture to be depleted by the "delayed" processes of runoff and evapotranspiration. The actual value of  $t^*$  is a function of soil type and the potential evapotranspiration rate (PET), with higher PET values resulting in lower residence times. Residence time (Table 1) is calculated after Serafini and Sud (1987) as a function of PET, the wilting point ( $m_{wp}$ ; the point at which the vegetation cannot absorb enough moisture to sustain itself and begins to wilt), and field capacity ( $m_{fc}$ ), so that

$$t^* = \frac{\gamma}{\lambda \text{PET}} \ln \frac{e^{\lambda m_{fc}}}{e^{\lambda m_{wp}}}, \quad (15)$$

where

$$\lambda = \frac{\alpha_r}{m_{fc} - m_{wp}} \quad (16)$$

and

$$\gamma = 1 - e^{-\alpha_r}. \quad (17)$$

In the above equation,  $\alpha_r$  accounts for variations in vegetation type. According to Serafini and Sud (1987),  $\alpha_r$  may have a value from 16 to 20 for forest vegetation types, while a value of 2 may be more appropriate for desert vegetation. Mintz and Serafini (1984) suggested using  $\alpha_r = 6.81$  to cover most vegetation types. Wilting point and field capacity are determined after Saxton et al. (1986) as a function of soil type (i.e., percent sand and clay content). Finally, PET is taken from FAO (1984) and determined using a modified version of the Penman formula.

The parameterization of immediate processes is likewise achieved using proportionalities based on the

TABLE 1. Mean annual precipitation ( $P$ ), range of soil moisture residence times, and immediate runoff for West African and southern African base stations used in this study.

Station	$P$ (mm)	$t^*$ (months)	$N'$ (mm)
<i>West Africa</i>			
Bilma	17	0.9–1.5	0
Agadez	145	0.8–1.4	46
Tahoua	384	0.4–0.7	6
Niamey	559	0.5–0.9	19
Gaya	834	1.2–2.0	127
Mango	1084	1.5–2.1	312
Sokode	1375	1.8–2.7	486
Mar	1702	1.6–2.2	769
Tabou	2318	1.7–2.4	1234
<i>Southern Africa</i>			
Windhoek	327	1.4–4.2	56
Postmasburg	333	0.6–2.9	1
Ghanzi	429	0.7–2.8	3
Maun	473	1.1–3.2	0
Bulawayo	597	0.7–1.7	8
Livingstone	739	1.7–4.2	10

annual balance equations. For immediate evapotranspiration ( $E'$ ), Lettau (1969) defined an additional characteristic parameter ( $e^*$ ), termed the "evaporivity," which is applied in the following equations:

$$E'(t) = e^* \cdot P(1 - a_s)G^*/(1 - a_s)G^* \quad (18)$$

$$\overline{E'} = e^* \cdot \overline{P}. \quad (19)$$

In the above,  $(1 - a_s)G^*$  and  $(1 - a_s)\overline{G^*}$  are the monthly and annual "forcing functions," that is, energy input via absorbed solar radiation. Thus,  $e^*$  is a non-dimensional measure of the capacity of the land surface to use a portion of the monthly solar radiation to evaporate precipitation received during the same month. Tentative evaluations by Lettau (1971) and others have suggested that  $e^*$  will normally be between 0.2 and 0.8. Lettau chose a value of 0.7 for New Delhi, a semi-arid subtropical climate with summer rainfall, comparable to most of our study sites.

In the study of the central Sahel by Nicholson and Lare (1990), calculations were simplified by assuming  $N' = 0$ , which is generally the case in semiarid regions (Eagleson and Segarra 1985). In order to more accurately treat immediate runoff, an approach originally proposed by Milly and Eagleson (1982) and adapted by Warrilow (1986) has been used in the current study. In essence, immediate runoff (Table 1) is a function of mean monthly rainfall rate, mean monthly infiltration rate, and a proportionality constant based on the average fractional area of a grid or region in which precipitation occurs, such that

$$N' = P e^{-\alpha F/P}. \quad (20)$$

Furthermore, immediate runoff calculations are treated like observations, and therefore, represent a loss of effective rainfall input into the model. Rainfall rate is

determined using hourly synoptic observations and daily precipitation records. Infiltration rate, assumed invariant (Warrilow 1986), is represented as a function of the hydraulic conductivity. Hydraulic conductivity is determined by soil moisture content (immediate top soil surface is assumed to be saturated while infiltration occurs), and by soil type (i.e., sand and clay content) following Saxton et al. (1986). This rate, which is for bare ground, is modified by vegetation density and structure and ground cover as in Rawls et al. (1989), Rawls and Brakensiek (1989), and Wilcox et al. (1990). In general, infiltration rates are higher for soils with high sand content and lower for clay soils. They are also higher for soils where vegetation canopy, ground cover, surface rocks, or leaf litter are present (Gifford 1984). Finally, the proportionality constant  $\alpha$  is assumed to be 0.66 for convective rainfall after Eagleson et al. (1987).

Runoff is calculated as a function of the gravitational drainage of existing soil water and the surface runoff due to precipitation exceeding infiltration rate (Warrilow 1986). The annual mean delayed runoff  $N''$  is determined using Saxton et al. (1986). In doing so, it is assumed that there is a single layer of soil with spatially homogeneous soil moisture; that is, horizontal movements of water are neglected. Gravitational drainage varies with soil type, with larger values for coarser soils and smaller ones for fine-grained soils. It also increases with increasing soil moisture. Surface runoff is calculated as a function of the surface infiltration rate and is affected by the spatial variability of rainfall. The use of a proportionality constant accounts for the fact that although the entire region may experience total rainfall that is below the threshold for runoff, a certain percentage of the area may receive amounts great enough to produce runoff in individual locations.

The concepts described above transform the basic budget equation (6) into

$$P - E' - N'' = E'' + N''' + dm/dt \quad (21)$$

$$= m/t^* + dm/dt. \quad (22)$$

Subtracting the annual average of all terms from the above equation (22) yields

$$p'(t) = (m - \bar{m})/t^* + d(m - \bar{m})/dt, \quad (23)$$

where  $p'$  stands for the time series  $P - E' - N'' - (P - E' - N'')$ . The ordinary differential equation is solved by

$$m - \bar{m} = e^{-t/t^*} \left[ \text{const} + \int e^{t/t^*} p' dt \right], \quad (24)$$

where "const" denotes an integration constant that is determined by the requirement that the bracketed value (i.e., the annual mean) of the right side must vanish for a stable climate. This equation is solved using stepwise integration, starting with an assumed initial value

( $m_1$ ) of soil moisture. In a stable climate, the value for the 13th month ( $m_{13}$ ) must equal  $m_1$ . The procedure is iterated until reasonable agreement occurs, that is, until  $(m_{13} - m_1) < 0.005$  mm. Usually only two or three iterations are necessary.

#### d. Adaptations for deriving spatial fields

Derivation of spatial patterns of the surface water balance parameters requires more detail than that provided by the nine West African and the six southern African base stations in the analyses thus far described. To produce the spatial fields, additional stations were selected from the rainfall archive. Each was grouped with the base station most climatically similar to it. Ancillary data for the appropriate base station were then used for each station in the group. However, local information on rainfall, vegetation, and soil type was utilized for each station in the network; thus permitting reasonable approximation of spatial fields for wet and dry years, while keeping the required additional data input to a minimum. Thus, the model was run for each station using input for the appropriate base station together with the precipitation, soil type, and vegetation type at the station itself.

### 3. Data and climatic background

#### a. General climatology

This study focuses on the semiarid Sahel and Kalahari regions of Africa, and regions in geographical proximity. The Sahel has been defined in numerous ways in the literature. In the strictest sense, it is the latitudinal belt south of the Sahara, composed of savanna vegetation and with rainfall ranging from about 100 mm yr<sup>-1</sup> in the north to about 400 mm yr<sup>-1</sup> in the south. Here, the term "Sahel" is loosely used to denote the whole semiarid zone south of the Sahara to a latitude of roughly 12°–13°N. Mean annual rainfall ranges from about 500 mm yr<sup>-1</sup> in the north to 1200 mm yr<sup>-1</sup> in the south (Fig. 3a). In this region, the rainy season, which is limited to the summer or "high-sun" season, becomes increasingly shorter with increasing latitude, ranging from about 1 to 5 months. In the Kalahari, the rains likewise occur in the high-sun season and last about 5 to 6 months. In most areas, mean annual rainfall (Fig. 3b) is on the order of 250 to 600 mm yr<sup>-1</sup>. Rainfall is well distributed over the season, but strongly concentrated in the two or three wettest months in the Sahel. Hence, peak monthly intensity is greater over the Sahel, 200 to 300 mm mo<sup>-1</sup>, compared to 100 to 200 mm mo<sup>-1</sup> at most Kalahari stations.

There are two other major climatic differences between the Sahel and Kalahari. First, as a consequence of the Kalahari's higher latitude, its radiation regime is more typical of the midlatitudes than the tropics, with a more pronounced annual march. This has im-

plications for the water balance. Also in contrast to the Sahel, the rain-bearing disturbances of the Kalahari are to some extent tropical/extratropical hybrids. As a result, some rains are nearly frontal in nature, thus being longer in duration and lower in intensity than those generally associated with tropical systems. This likewise affects the runoff and evaporation, and, hence, surface water balance.

#### *b. Forcing functions of the model*

The patterns of climate described above are illustrated in Fig. 4, which shows the major forcing functions of the model: solar irradiance (the shortwave model), ground-absorbed solar radiation, and precipitation (evapoclimatology). Extra-atmospheric solar radiation is calculated from standard formulas (Sellers 1965) using Fourier series-type expressions for eccentricity and the solar declination after Spencer (1971). Ground-absorbed solar radiation is calculated using the shortwave submodel, as described fully in Lare and Nicholson (1990). The rainfall data derive from a continental archive described in Nicholson (1986).

Significant contrast is apparent between the Sahel and the Kalahari. The increasing intensity and duration of the Sahel rainy season from north to south (Fig. 4a) is clearly evident, as is the change to a bimodal seasonal distribution south of the Sahel (i.e., at Tabor, circa  $10^{\circ}\text{N}$ ). The peak intensity reaches at least  $200\text{ mm month}^{-1}$  in all but the driest stations. In the Kalahari, high rainfall is maintained for a longer period, but it barely exceeds  $100\text{ mm month}^{-1}$  at any but the wettest station. In the Sahel, the portion of the extraatmospheric solar insolation which is ultimately absorbed by the ground is somewhat smaller than in the Kalahari (Fig. 4b). In many Sahelian stations, ground-absorbed radiation actually reaches a minimum during the rainy season, as a result of cloud cover, and is somewhat lower than the amount received in the Kalahari during the rainy season. In the Kalahari, ground-absorbed radiation reaches a maximum during the rainy season.

#### *c. Ancillary data*

The input data required for model parameterizations in the shortwave model include atmospheric constituents, aerosols, cloud cover, and surface albedo (Table 2). Water vapor was obtained from FAO (1984); ozone, carbon dioxide, and oxygen were derived from standard sources (Sasamori et al. 1972; Lacis and Hansen 1974; London et al. 1976). Rayleigh scattering (Bird and Hulstrom 1981) was calculated from relative optical air mass, after Rodgers (1967). Monthly mean cloud cover was obtained from Warren et al. (1986). Although significant errors in ground-absorbed solar radiation, on the order of 3% to 9% in the dry season and 10% to 19% during the wet season (Lare and Nicholson 1990), occur as a result of a  $\pm 20\%$  error in cloud

amount, the effect of these errors on the evapoclimatology submodel is primarily manifested as a modulation in the amplitude of the annual cycle (Nicholson and Lare 1990). Surface albedo was taken from global monthly fields derived by Dorman and Sellers (1989) on the basis of vegetation type. Although the grid for these is coarse,  $4^{\circ} \times 5^{\circ}$ , sensitivity studies run in the model indicate that albedo errors as large as 50% resulted in soil moisture differences of less than 9% (Nicholson and Lare 1990). Aerosols were very roughly estimated based on regressions relating rainfall, visibility, and turbidity.

Input data required for the evapoclimatology submodel include vegetation cover, soil texture, potential evapotranspiration (PET), and evaporivity  $e^*$ . Vegetation cover was derived from Dorman and Sellers (1989), soil texture from FAO/UNESCO (1977), and PET from FAO (1984). Evaporivity was the most difficult parameter to quantify. Tentative evaluations by Lettau (1971) and others have suggested it will normally lie between 0.2 and 0.8, with 0.7 being typical of a semiarid subtropical climate with summer rainfall. The values used here were determined empirically, using results of previous studies (Lettau 1971; Pinker and Corio 1987; Nicholson and Lare 1990).

#### 4. Model results

The model is initially run for each of the stations shown in Fig. 2. The input variables are assumed to be representative of long-term (i.e., multiyear) means. The only highly variable input parameter is rainfall, and the mean values used in the model are averaged over the entire length of record at each station. In nearly all cases, the period of record is from 1921 to 1984 or longer. Thus, the model results represent averages for an approximately 60-yr period. On this time scale, the assumption of a stable climate ( $dm/dt = 0$ ) is quite reasonable.

Once the mean model output is derived, the model is rerun for each station, using as input for the "wet" case the monthly mean rainfall averaged for the 10 wettest years at each station and for the dry case, the mean for the 10 driest years. Other input parameters, such as cloud cover and aerosols, remain unchanged. Next, the model is adapted to derive spatial fields of the major output variables: ET, soil moisture, and runoff. Simplifications incorporated in the model to facilitate this are described in section 2d.

The assumption of no systematic changes of cloud cover from dry to wet years was found to be true for Niamey, a typical Sahelian station. This is due to the fact that not all disturbance lines that traverse the region are rain bearing; some are accompanied by nothing more than an increase in cloudiness. Furthermore, the difference between a wet year and a dry year is primarily due to the occurrence, or lack thereof, of as few as one or two intense rainfall events. The assumption of in-

variant aerosols is unrealistic, but inconsequential because aerosols have very little effect on the results of the evapotranspiration submodel in rainfall-limited, semiarid environments (Nicholson and Lare 1990).

*a. Water balance for typical wet and dry years at individual stations*

Figure 5 shows the results of the wet and dry cases for Sahelian stations. Mean rainfall for each period is given for each station, together with model-calculated soil moisture, evapotranspiration, and runoff. Except for the two southernmost stations, the reduction in rainfall in the dry years is essentially limited to the two or three wettest months (July to September). This is true even for stations with a considerably longer rainy season. At the coast (Tabou), where two rainy seasons are apparent, the later rainy season is most affected during the dry years. This includes the months of August and September, which is also when rainfall is reduced at Sahelian stations during the dry years. At the three stations most comparable to the Kalahari (Tahoua, Niamey, and Gaya), maximum monthly rainfall drops from about 200 to 300 mm in the wet years to about 100 to 150 mm during the dry years. From Agadez to Mango, maximum rainfall occurs in August in both dry and wet years.

At the northernmost stations, these changes are reflected primarily in evapotranspiration (ET) and soil moisture. Evapotranspiration reaches about 100 to 150 mm  $\text{mo}^{-1}$  in the rainy season during wet years (except at Bilma) and soil moisture at the same time is on the order of 75 to 200 mm. Both are reduced in the wet season by about 50% in the dry years. The changes, as with rainfall, are most apparent from July to September. Soil moisture tends to peak about 1 month after rainfall in both dry and wet years, while ET peaks in the same month as rainfall. It must be noted that the soil moistures depicted in Fig. 5 represent the sum of soil moisture available for evaporative processes and that unavailable due to strong adhesive forces (i.e., residual water content). For example, even though soil moistures at Bilma are higher than those at some wetter climates farther south, almost all of the soil moisture is residual and thus unavailable for evaporative processes. Residual water content is determined after Rawls and Brakensiek (1989) as a function of percent organic matter content, percent clay content, and cation exchange capacity; all of which are taken from FAO/UNESCO (1977).

An interesting change occurs at Gaya, where mean annual rainfall is 829 mm. There, the change in ET and soil moisture from wet to dry years is considerably smaller than farther north; south of Gaya they are virtually invariant. Instead, rainfall changes are manifested primarily in runoff. Also, from Gaya southward both ET and soil moisture tend to peak 1 month after rainfall. Another interesting change is apparent in going

southward in wet years (rainy season). ET begins to decrease because of increasing runoff. Maximum monthly values occur between about 12°N and 15°N (Gaya to Tahoua). During dry years, the maximum lies near Mango and Sokode, about 9°N to 10°N.

The contrast between wet and dry years at the Kalahari stations is considerably different. First of all, rainfall is significantly reduced in dry years in 5 to 6 months (compared to 2 or 3 in the Sahel). Also, the month of maximum rainfall tends to shift from January in wet years to December or February in dry years. As in West Africa, monthly rainfall is about 50% lower during dry years.

Changes of ET and soil moisture are likewise apparent in all months of the rainy season. At all six stations, ET reaches about 75 to 100 mm  $\text{mo}^{-1}$  during wet years; soil moisture, about 50 to 150 mm, except at Livingstone, where it reaches about 400 mm in the wettest months. Both are reduced by roughly 50% during dry years. In general, ET and soil moisture are higher in the Sahel than in the Kalahari. The annual march of ET parallels that of rainfall, but soil moisture tends to peak 2 to 3 months after rainfall at drier stations, 1 to 2 months later at wetter stations. The timing of maximum soil moisture shifts only slightly during the drier years. In general, runoff is low at the Kalahari stations and is close to zero at all of them during dry years. Large changes of runoff occur primarily at the two wettest stations, Bulawayo and Livingstone. Presumably, this would be different if wetter stations farther north were examined.

*b. Spatial patterns of hydrologic variables in dry and wet years*

Figure 6a shows the difference between the ten wettest and ten driest years in the Sahel. Values are given for August, the wettest month, for rainfall, soil moisture, evapotranspiration, and runoff. In interpreting the results, it must be kept in mind that the difference fields are related not only to the precipitation differences in August, but also to those of previous months. In much of the Sahel the contrast in rainfall exceeds 100 mm  $\text{mo}^{-1}$ , but to the south rainfall differences are small or negative. The corresponding changes of soil moisture are in excess of 20 mm for a large zone extending from about 12°N to 18°N. A large difference in evapotranspiration is evident over a greater area: in excess of 20 mm  $\text{mo}^{-1}$  in a zone roughly extending from about 13°N to 20°N, in excess of 50 mm  $\text{mo}^{-1}$  throughout most of the area between 14°N and 18°N. Since differences of the opposite sign prevail north and south of about 10°N, there is a strong change of the meridional gradient of soil moisture and ET between wet and dry years. The contrast in runoff between wet years and dry years is on the order of 50 to 100 mm  $\text{mo}^{-1}$  throughout much of the Sahel from about 10°N to 15°N. Further south, runoff is reduced, by over 50 mm  $\text{mo}^{-1}$  in some areas.

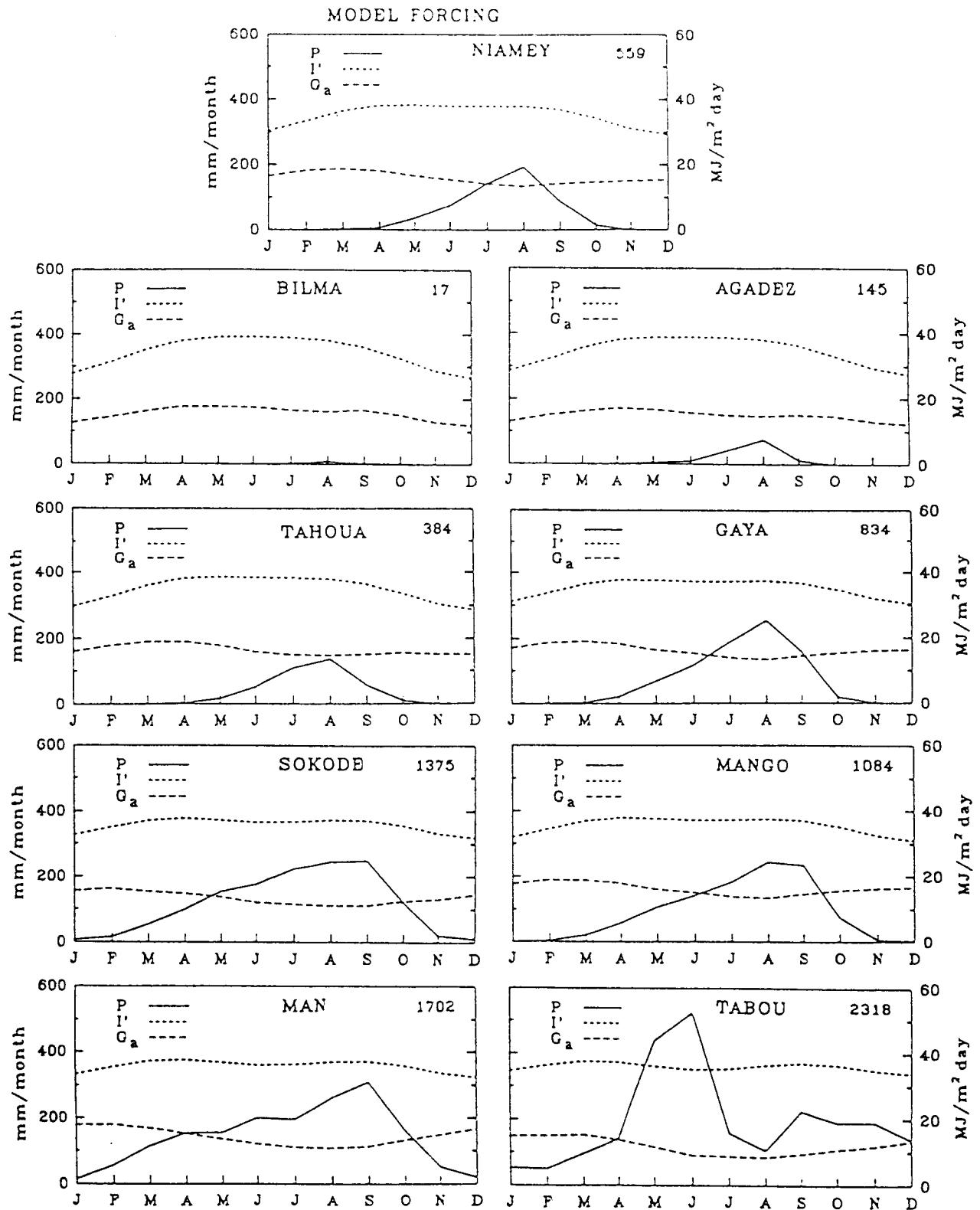


FIG. 4. Seasonal march of model forcing functions: solar irradiance  $I'$ , ground-absorbed radiation  $G_a$ , and monthly precipitation  $P$ ; mean annual rainfall is in upper right. (a) A typical central Sahel station (Niamey) and other West African stations along the north-south transect in Fig. 3a. (b) Stations in the Kalahari and surrounding regions.

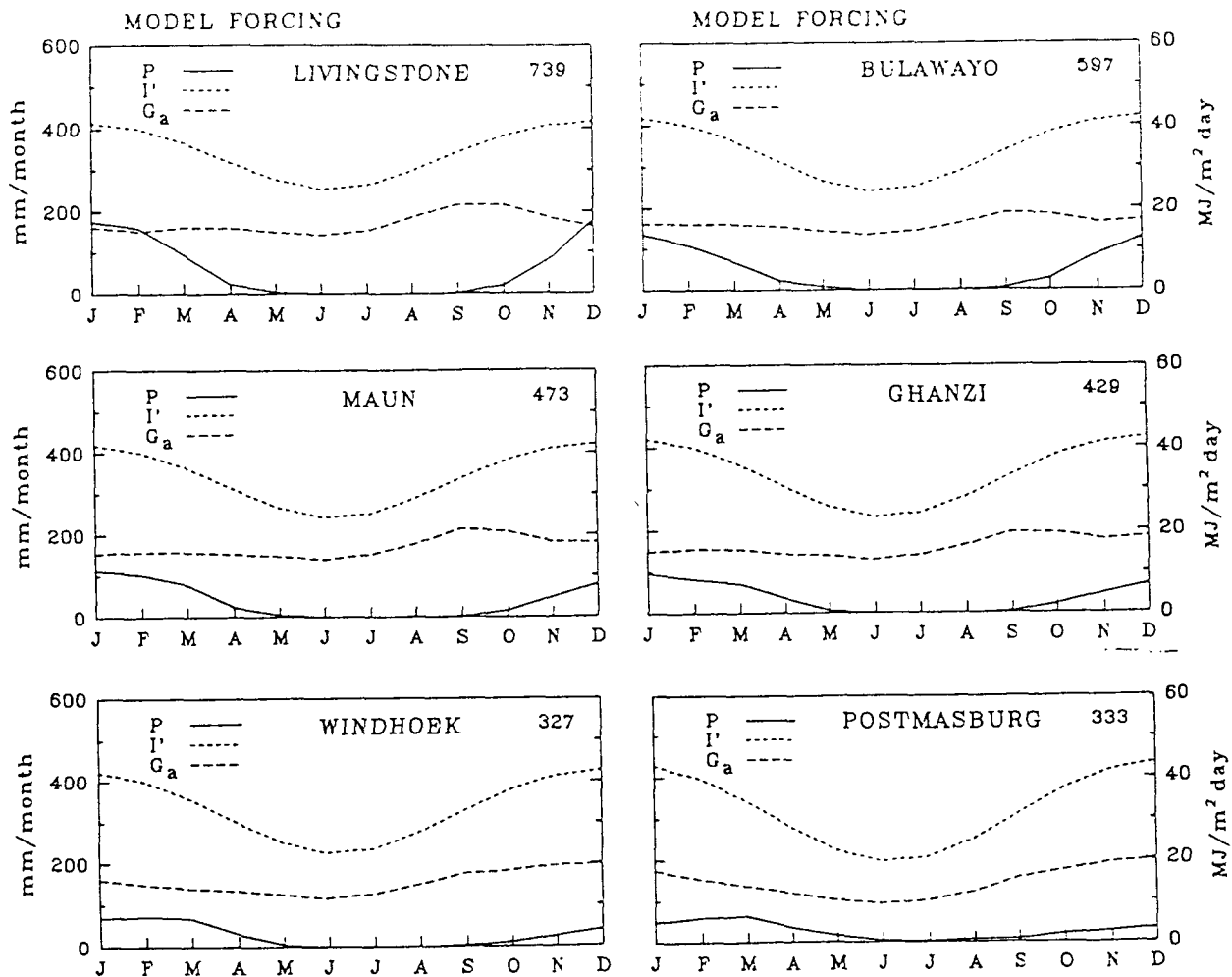


FIG. 4. (Continued)

TABLE 2. Parameters necessary for model input, as well as source used in study.

Parameter	Source
<i>Shortwave radiation submodel</i>	
Surface albedo	Dorman and Sellers (1989)
Cloud cover	Warren et al. (1986)
Rayleigh scattering	Bird and Hulstrom (1981)
Optical air mass	Rodgers (1967)
H <sub>2</sub> O <sub>v</sub>	Lacis and Hansen (1974); FAO (1984)
CO <sub>2</sub>	Sasamori et al. (1972)
O <sub>2</sub>	Sasamori et al. (1972)
O <sub>3</sub>	Lacis and Hansen (1974); London et al. (1976)
<i>Evapoclimatology submodel</i>	
Vegetation cover	Dorman and Sellers (1989)
Soil texture	FAO/UNESCO (1977)
PET	FAO (1984)
Evaporivity (e*)	Lettau (1971); Pinker and Corio (1987); Nicholson and Lare (1990)

The precipitation difference between wet and dry years in the Kalahari (Fig. 6b) is roughly comparable to that of the Sahel both in magnitude and in size of the affected area. Important contrasts are evident in the difference fields for other hydrologic variables, however. In most of the area, the difference in soil moisture between wet and dry years is less than 10 mm, and the difference in ET seldom exceeds 30 mm mo<sup>-1</sup>. Furthermore, the change of latitudinal gradients that are apparent over the Sahel are not apparent over the Kalahari. Also, the wet-dry contrast in runoff exceeds 50 mm mo<sup>-1</sup> in only a few locations.

An interesting feature occurs, in particular, over the northern Kalahari region, with respect to the water balance. Although the region has significantly higher rainfall in wet years compared to dry years (on the order of 50 to 100 mm mo<sup>-1</sup>), evapotranspiration rates are lower in wet years than in dry years. This is primarily due to a larger percentage of rainfall in wet years



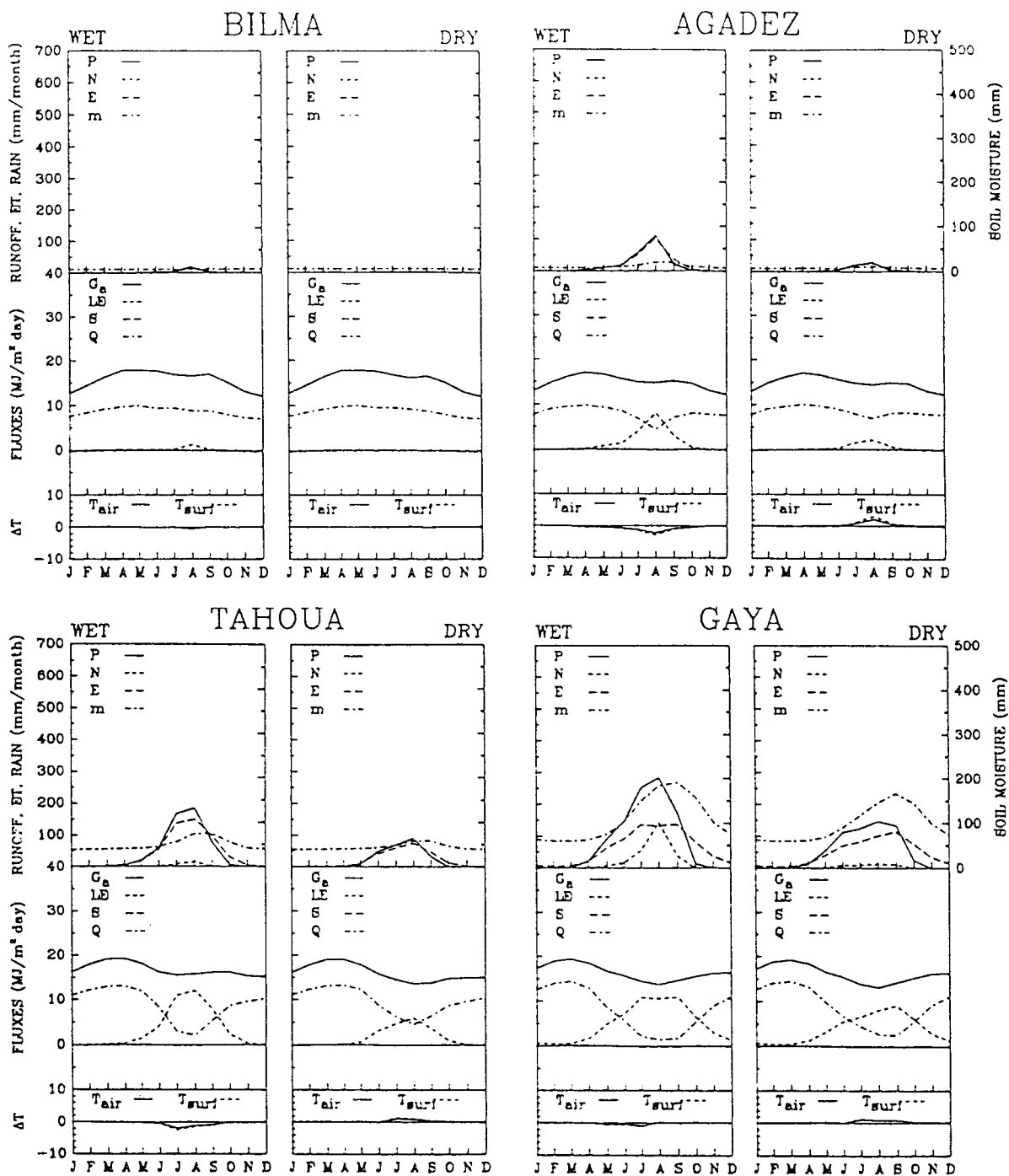


FIG. 5. Model results for the ten wettest years and ten driest years:  $P$  = precipitation,  $N$  = runoff,  $E$  = evapotranspiration,  $m$  = soil moisture. (a) Nine West African stations. (b) Six stations in or near the Kalahari.

being lost as immediate runoff, a direct manifestation of equation (20) if monthly mean infiltration rates are fairly low.

Overall, the contrast between the Kalahari and Sahel is probably primarily a result of timing, duration, and intensity of the rainy season. The season

is longer, and of lower peak intensity in the Kalahari, and it occurs, unlike in the Sahel, when absorbed solar radiation is at a maximum. The magnitude and spatial coherence of the rainfall anomalies also differ to some extent in the two regions, however.

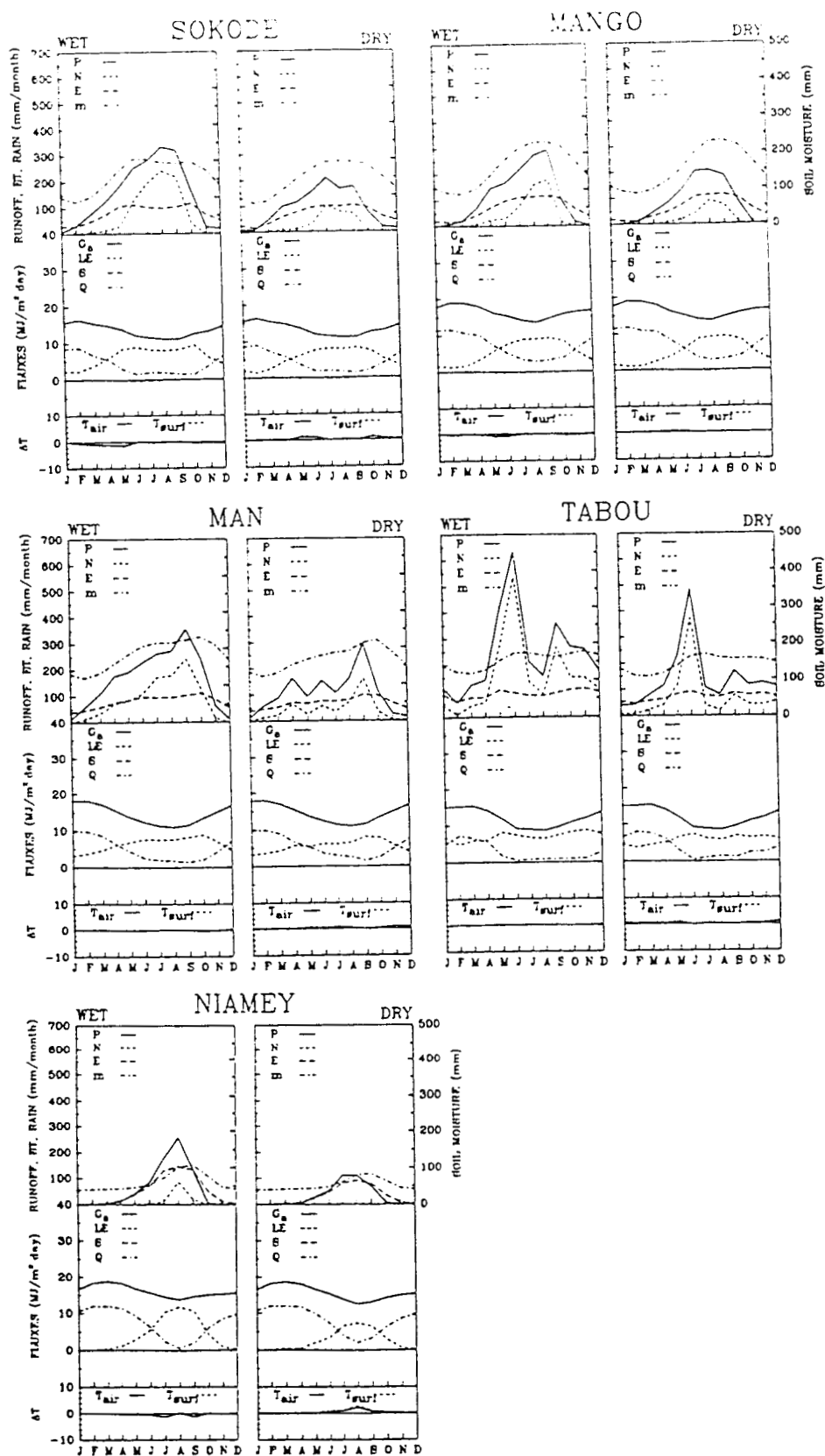


FIG. 5. (Continued)

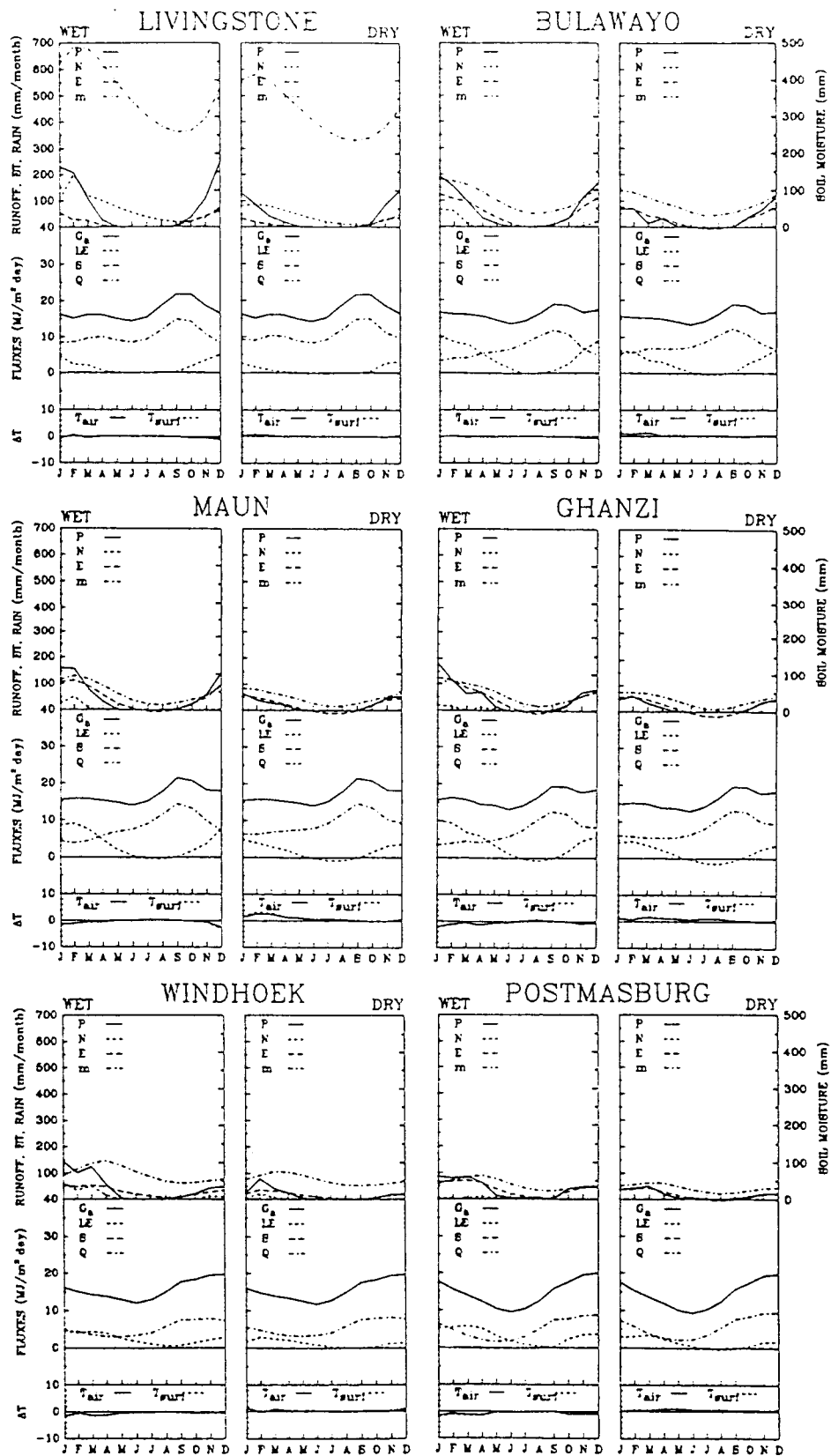


FIG. 5. (Continued)

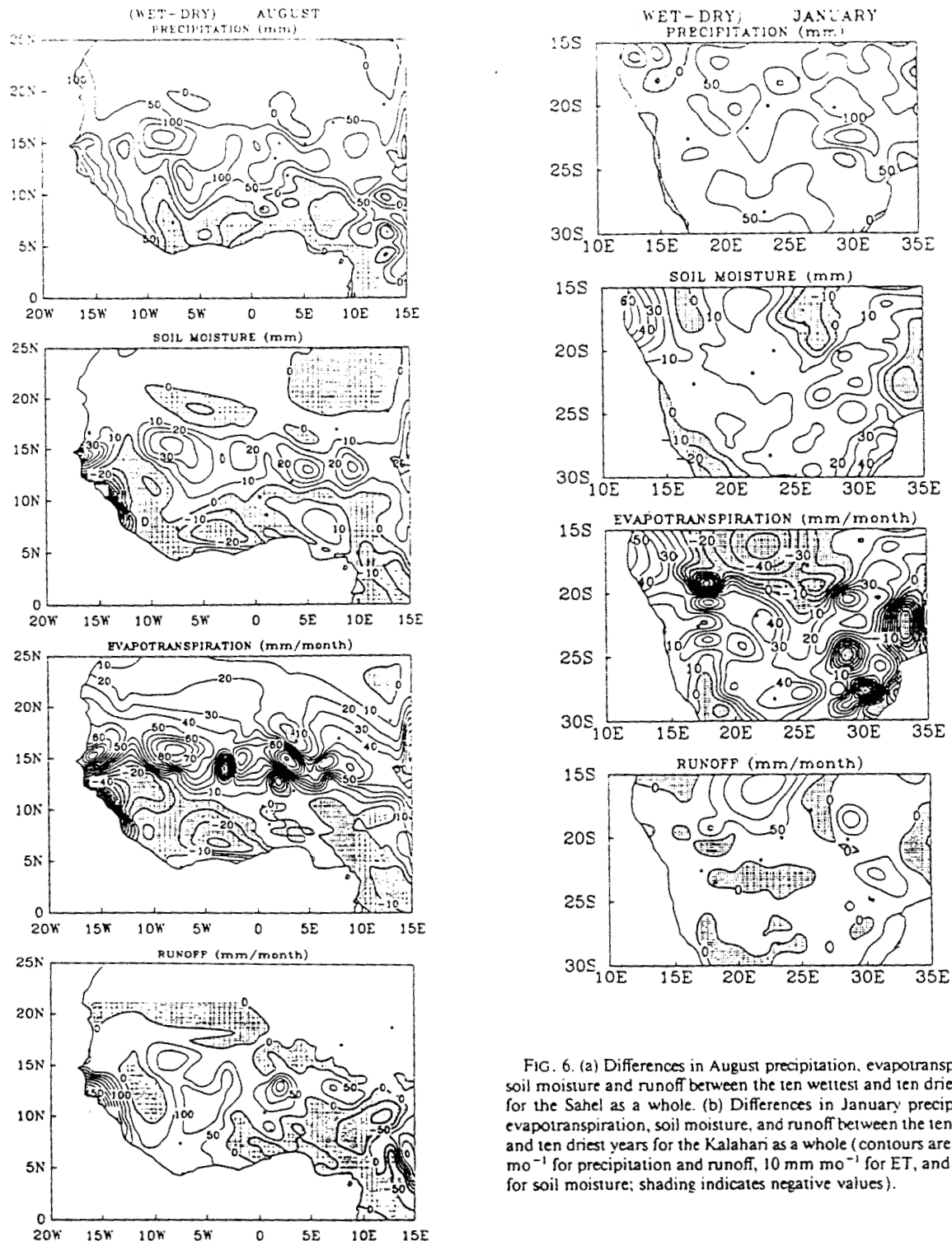


FIG. 6. (a) Differences in August precipitation, evapotranspiration, soil moisture and runoff between the ten wettest and ten driest years for the Sahel as a whole. (b) Differences in January precipitation, evapotranspiration, soil moisture, and runoff between the ten wettest and ten driest years for the Kalahari as a whole (contours are  $50 \text{ mm mo}^{-1}$  for precipitation and runoff,  $10 \text{ mm mo}^{-1}$  for ET, and  $10 \text{ mm}$  for soil moisture; shading indicates negative values).

c. *Meridional gradients of latent heat in West Africa between wet and dry years and their consequences*  
West Africa is somewhat unique in that the dynamical system most closely linked to rain-bearing distur-

bances, the African easterly jet (AEJ), is a direct manifestation of land surface processes. This jet, essentially an easterly wind maximum of about  $10 \text{ m s}^{-1}$ , with its core in the midtroposphere at about 650 to 700 mb,

is a consequence of the temperature gradient between the Sahara desert and the cooler Guinea Coast and Atlantic Ocean to the south. The AEJ is strongest at about 15°N.

The jet provides the energy and instability for the development, maintenance, and propagation of the rain-producing disturbances in the region. Cloud clusters produce about 90% of the rainfall in the Sahel; their frequency and the amount of rainfall they produce is modulated by transient easterly waves (Houze and Betts 1981). The westward-propagating waves originate as a consequence of the joint baroclinic-barotropic instability associated with the horizontal and vertical shear of the AEJ (Burpee 1972; Albignat and Reed 1980), and they are therefore confined to a relatively narrow latitudinal zone near and south of the jet core. There are consistent changes in intensity and shear of the jet between wet and dry years, with the jet (and shear) being stronger during dry years (Newell and Kidson 1984). Since the difference between an abnormally wet or dry rainy season month can be accounted for by as few as one or two intense disturbances, and the most intense systems are associated with easterly waves produced from the AEJ, the character of the rainy system is very sensitive to fluctuations in the jet. As the relevant jet shears and intensity are a function of the north-south temperature gradient in the region, the jet should be modulated by land surface fluxes such as latent heat. Thus, any land surface changes that are induced by anomalous wet or dry conditions should affect the surface radiation balance, and thereby, the AEJ. This in turn may result in the hypothesized positive feedback effect, and thus, enhance or prolong existing wet or dry conditions.

We have examined the latitudinal gradient of latent heating in wet and dry years along the transect shown in Fig. 3, using the nine Sahelian stations. The contrast between wet years and dry years is strong enough to affect the speed of the jet (Fig. 7). In the wet years, the latent heat flux to the atmosphere has a maximum at about 12°N to 13°N in July and September, and at about 15°N in August. The largest contrast between wet and dry years is apparent in August. In dry years, the maximum latent heating is at 10°N to 11°N in all months and there is little difference between wet and dry years from there southward. Latitudinally, the wet/dry contrast is largest at about 15°N in August and at about 12° or 13°N to 16°N in July and September. The flux of heat in these latitudes is about 4 to 6 MJ m<sup>-2</sup> day<sup>-1</sup> larger in wet years than in dry years.

It is difficult to assess the effect on the jet without a detailed model of atmospheric heating. Moreover, the differences in latent heat flux can act as a feedback mechanism producing interannual persistence only if it can be demonstrated that the heating anomaly persists until the following rainy season. Nevertheless, a rough estimate can be made of the effect on the jet's core speed and shear by considering the thermal wind

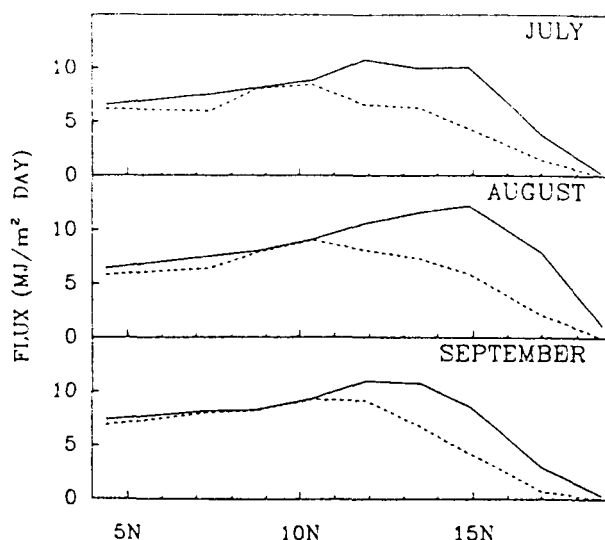


FIG. 7. Surface flux of latent heat as a function of latitude in July, August, and September in the ten wettest (solid) and ten driest (dashed) years in the West African Sahel.

equation and making certain assumptions about atmospheric heating.

The jet is a consequence of the temperature gradient, the relevant thermal wind speed  $U$  being computed according to

$$U = \frac{-R}{f} \left( \frac{\partial \bar{T}}{\partial y} \right)_p \ln \left( \frac{P_0}{P_1} \right), \quad (25)$$

where  $(\partial \bar{T} / \partial y)_p$  is the mean latitudinal temperature gradient in the layer between pressure levels  $P_0$  and  $P_1$ .  $R$  is the gas constant for dry air, and  $f$  is the Coriolis force. As the midtropospheric temperatures are higher to the north (i.e., over the Sahara) than to the south, the thermal wind (and the jet) is easterly.

Using the climatology output of surface temperature, two-meter air temperature, latent heat flux, and sensible heat flux, mean temperature profiles are derived for nine latitudinal bands, each corresponding to one of the base stations along the transect in Fig. 3. Appropriate means are derived for the bands using additional stations as described in section 2d. Calculations are made only for August. From the surface to the top of the surface layer (assumed to be 1/10 the height from the surface to the lifting condensation level), sensible heat flux is used to determine atmospheric temperature, as in Lettau and Lettau (1975). From the top of the surface layer to the lifting condensation level, that is, the mixed layer, a dry-adiabatic lapse rate is assumed. Once the lifting condensation level is reached, the temperature profile is assumed to follow a pseudoadiabatic, which is determined using moist static energy, an approximately conserved quantity during a convective process. For simplicity, no entrainment zone or upper-level inversions are incorporated. Inherent in the sur-

face temperatures for wet and dry years are implicit differences in saturation specific humidity and in the level at which condensation begins to occur. In other words, the moist static energy differs between wet and dry years.

Since the gradient of latent heating from south to north (about  $12^{\circ}$  or  $13^{\circ}\text{N}$  to  $18^{\circ}\text{N}$ ) is the inverse of the temperature gradient, the sharper gradient during wet years acts to reduce the temperature gradient, thereby weakening the jet and jet shear in wet years. This is consistent with the weaker jet and jet shear observed by Newell and Kidson (1984) in wet years.

Taking a linear least-squares fit of the temperatures at the 700-mb level for the nine latitudinal bands centered at  $15^{\circ}\text{N}$ , as calculated above, corresponding geostrophic winds are calculated with the aid of Eq. (25). The calculations indicate a weakening of the African easterly jet on the order of  $2.6\text{ m s}^{-1}$  between dry and wet years. That shown by Newell and Kidson (1984) is about  $2\text{ m s}^{-1}$ . At  $10^{\circ}\text{N}$ , Newell and Kidson show a decrease of over  $4\text{ m s}^{-1}$ . Our results show a decrease approximately twice that amount. At this latitude, however, the Coriolis force is very small and the thermal wind calculations are therefore highly sensitive to the north-south temperature gradient. Any slight discrepancy in the temperature gradient between that calculated and that observed will have a dramatic effect on the magnitude of the thermal wind speeds. A more detailed discussion of the effects of differences between wet and dry years on latent heating and on the African easterly jet will appear in a later article.

## 5. Summary and conclusions

The Lettau climatology model was used to examine the temporal and spatial effects of the Sahelian drought on land surface feedback. This was compared with the Sahelian Southern Hemisphere counterpart, the Kalahari, a region subject to similar large-scale atmospheric forcing, but lacking the Sahel's decadal persistence in rainfall anomalies. The effect of surface energy flux modification upon the midtropospheric winds, in particular the African easterly jet (AEJ), over West Africa was also explored. It is known that the AEJ is responsible for the development and maintenance of the West African disturbance lines, which bring most of the precipitation to West Africa.

These model results indicate that there are significant differences in the surface water balance between dry and wet years. The changes in the Sahel are more intensive, larger in spatial scale, and more spatially coherent than those in the Kalahari. Thus, the possibility of land surface-atmosphere feedback is higher in the Sahel than in the Kalahari. In drier regions, increased rainfall is manifested as higher soil moisture and ET. In wetter regions, it is manifested primarily as increased runoff.

South of the Sahara, this tends to decrease the surface gradient of latent heat exchange with the atmosphere

during wet years. Consequently, the temperature gradient in the midtroposphere, where the latent heat is released, is also reduced. This in turn reduces the thermal wind and the intensity of wind and wind shear in the African easterly jet. The calculated magnitudes of these changes are consistent with those observed by Newell and Kidson (1984) in a study contrasting wet and dry years in the Sahel.

The calculations were performed for the peak rainy season months. They suggest that the magnitude of the change in surface energy balance between a wet and dry year is large enough to significantly affect the general atmospheric circulation, and thereby, the rain-bearing systems. However, for this to provide a feedback mechanism that can produce the characteristic interannual persistence of Sahelian rainfall anomalies, there must be a "memory" extending to the following rainy season. A more detailed atmospheric model is required to test this hypothesis.

**Acknowledgments.** We would like to thank Heinz Lettau for many valuable discussions of the climatology model. We would also like to acknowledge support from NASA Grants NAG 5-764 and NGT 50475 and from NSF Grant ATM 9024340.

## REFERENCES

- Albignat, J. P., and R. J. Reed, 1980: The origin of African wave disturbances during Phase III of GATE. *Mon. Wea. Rev.*, **108**, 1827–1839.
- Bird, R., and R. L. Hulstrom, 1981: Review, evaluation, and improvement of direct irradiance models. *Trans. ASME J. Sol. Energy Eng.*, **103**, 182–192.
- Burpee, R. W., 1972: The origin and structure of easterly waves in the lower troposphere of North Africa. *J. Atmos. Sci.*, **29**, 77–90.
- Corio, L. A., and R. T. Pinker, 1987: Estimating monthly mean water and energy budgets over the central U.S. Great Plains. Part II. Evapoclimatology experiments. *Mon. Wea. Rev.*, **115**, 1153–1160.
- Dorman, J. L., and P. J. Sellers, 1989: A global climatology of albedo, roughness length, and stomatal resistance for atmospheric general circulation models as represented by the simple biosphere model (SiB). *J. Appl. Meteor.*, **28**, 833–855.
- Eagleson, P. S., and R. I. Segarra, 1985: Water-limited equilibrium of savanna vegetation systems. *Water Resour. Res.*, **21**, 1483–1493.
- , N. M. Fennessey, Q. Wang, and J. Rodriguez-Iturbe, 1987: Application of spatial Poisson models to air mass thunderstorm rainfall. *J. Geophys. Res.*, **92**, 9661–9678.
- FAO, 1984: *Agroclimatological Data, Vol. I and II*, Food and Agricultural Organization.
- FAO/UNESCO, 1977: *Soil Map of the World, Vol. VI, Africa*. UNESCO, 218 pp.
- Gifford, G. F., 1984: Vegetation allocation for meeting site requirement. *Development Strategies for Rangeland Management*. Westview Press, 35–116.
- Houze, R. A., Jr., and A. K. Betts, 1981: Convection in GATE. *Rev. Geophys. Space Phys.*, **19**, 541–576.
- Lacis, A. A., and J. E. Hansen, 1974: A parameterization for the absorption of solar radiation in the earth's atmosphere. *J. Atmos. Sci.*, **31**, 118–133.
- Lare, A. R., and S. E. Nicholson, 1990: A climatology description of the surface energy balance in the Central Sahel. Part I: Shortwave radiation. *J. Appl. Meteor.*, **29**, 123–137.

- Lettau, H. H., 1969: Evapotranspiration climatology. I: A new approach to numerical prediction of monthly evapotranspiration, runoff, and soil moisture storage. *Mon. Wea. Rev.*, **97**, 691–699.
- , and K. Lettau, 1969: Shortwave radiation climatology. *Tellus*, **21**, 208–222.
- , and M. W. Baradas, 1973: Evapotranspiration climatology. II: Refinement of parameterization, exemplified by application to the Macabán River watershed. *Mon. Wea. Rev.*, **101**, 636–649.
- , and —, 1975: Regional climatology of tundra and boreal forests in Canada. Climate of the Arctic. *Proc. 24th Alaskan Science Conference*, Fairbanks, AAAS and Amer. Meteor. Soc., 209–221.
- , and E. J. Hopkins, 1991: Evapoclimatology III: The reconciliation of monthly runoff and evaporation in the climatic balance of evaporable water on land areas. *J. Appl. Meteor.*, **30**, 776–792.
- Lettau, K., 1971: Radiation climate of New Delhi. Part II: Longwave radiation and energy budget. *Indian J. Meteor. Geophys.*, **22**, 529–540.
- London, J., R. D. Bojkov, S. Oltmans, and J. E. Kelley, 1976: Atlas of the Global Distribution of Total Ozone, July 1957–June 1967. Report No. NCAR/TN-113+STR, National Science Foundation, 276 pp. [NTIS PB258882.]
- Milly, P. C. D., and P. S. Eagleson, 1982: Parameterization of moisture and heat fluxes across the land surface for use in atmospheric general circulation models. Report No. 279, M.I.T., 226 pp. [Available from Ralph M. Parsons Laboratory, Cambridge, MA 02139.]
- Mintz, Y., and Y. Serafini, 1984: Global fields of monthly normal soil moisture, as derived from observed precipitation and an estimated potential evapotranspiration. Final scientific report under NASA Grant No. NAS 5-26, part V, Department of Meteorology, University of Maryland. [Available from Department of Meteorology, University of Maryland, College Park, MD 20742.]
- Newell, R. E., and J. W. Kidson, 1984: African mean wind changes between Sahelian wet and dry periods. *J. Climatol.*, **4**, 27–33.
- Nicholson, S. E., 1986: The spatial coherence of African rainfall anomalies: Interhemispheric teleconnections. *J. Climate Appl. Meteor.*, **25**, 1365–1381.
- , and A. R. Lare, 1990: A climatologic description of the surface energy balance in the central Sahel. Part II: The evapoclimatology submodel. *J. Appl. Meteor.*, **29**, 138–146.
- Pinker, R. L., and L. A. Cornio, 1987: Estimating monthly mean water and energy budgets over the central U.S. Great Plains. Part I: Evapoclimatology model formulation. *Mon. Wea. Rev.*, **115**, 1140–1152.
- Rawls, W. J., and D. L. Brakensiek, 1989: Estimation of soil water retention and hydraulic properties. *Unsaturated Flow in Hydrologic Modeling: Theory and Practice*, H. J. Morel-Seytoux, Ed. Kluwer Academic Publishers, 275–300.
- , —, and M. R. Savabi, 1989: Infiltration parameters for rangeland soils. *J. Range Manag.*, **42**, 139–142.
- Rodgers, C. D., 1967: The radiative heat budget of the troposphere and lower stratosphere. Rep. No. A2, Planetary Circulation Project, Department of Meteorology, M.I.T., 99 pp. [NTIS PB176-527.]
- Sasamori, T., J. London, and D. V. Hoyt, 1972: Radiation budget of the Southern Hemisphere. *Meteorology of the Southern Hemisphere, Meteor. Monogr.*, No. 13, Amer. Meteor. Soc., 9–23.
- Saxton, K. E., W. J. Rawls, J. S. Romberger, and R. J. Papendick, 1986: Estimating generalized soil-water characteristics from texture. *Soil Sci. Soc. Amer. J.*, **50**, 1031–1036.
- Sellers, W. D., 1965: *Physical Climatology*. The University of Chicago Press, 272 pp.
- Serafini, Y. V., and Y. C. Sud, 1987: The time scale of the soil hydrology using a simple water budget model. *J. Climatol.*, **7**, 585–591.
- Spencer, J. W., 1971: Fourier series representation of the position of the sun. *Search*, **2**, 172.
- Trewartha, G. T., 1961: *The Earth's Problem Climates*. The University of Wisconsin Press, 334 pp.
- Warren, S. G., C. J. Hahn, J. London, R. M. Chervin, and R. L. Jenne, 1986: Global distribution of total cloud cover and cloud type amounts over land. NCAR/TN-273+STR, 230 pp. [NTIS PR-360.]
- Warrilow, D. A., 1986: The sensitivity of the U.K. Meteorological Office atmospheric general circulation model to recent changes to the parameterization of hydrology. *Proc. International Satellite Land-Surface Climatology Project Conference, Rome, Italy*, ESA SP-248, 143–149.
- Wilcox, B. P., W. J. Rawls, D. L. Brakensiek, and J. R. Wight, 1990: Predicting runoff from rangeland catchments: A comparison of two models. *Water Resour. Res.*, **26**, 2401–2410.

## **Appendix D**

### **Satellite-Derived Interannual Variability of West African Rainfall during 1983-88**



## Satellite-Derived Interannual Variability of West African Rainfall during 1983–88

MAMOUDOU B. BA AND ROBERT FROUIN

*California Space Institute, Scripps Institution of Oceanography, La Jolla, California*

SHARON E. NICHOLSON

*Department of Meteorology, The Florida State University, Tallahassee, Florida*

(Manuscript received 19 January 1994, in final form 19 June 1994)

### ABSTRACT

Two satellite algorithms for rain estimation are used to study the interannual variability of West African rainfall during contrasting years of the period 1983–88. The first algorithm uses a frequency of occurrence index quantifying the number of times Meteosat thermal infrared radiance below  $2.107 \text{ W m}^{-2} \text{ sr}^{-1} \mu\text{m}^{-1}$  ( $-40^\circ\text{C}$ ) occurs during the rainy season. The second algorithm uses the average Meteosat thermal infrared radiance over the period of interest. Appropriate calibrations are performed using these satellite parameters and ground-based rainfall observations. Separate calibration and equations are considered for each of three suggested subrainfall zones in West Africa: two Sahelian zones located just north of  $9^\circ\text{N}$  (one east and one west of  $5^\circ\text{W}$ ) and the region extending south from  $9^\circ\text{N}$  to the coast. Over 80% of the variance in the ground-based rainfall data is explained by both algorithms in regions located north of  $9^\circ\text{N}$ , but poor correlations between observed and estimated rainfall exist south of  $9^\circ\text{N}$ . The interannual variability of rainfall in the Sahel is well described by that of cold clouds and average radiances. The satellite estimates also reveal substantial longitudinal variability in the anomaly fields, indicating that some Sahelo–Soudanian areas may receive above average rainfall during a year cataloged as dry. The latitudinal displacement and the extent of the cloud band associated with the intertropical convergence zone (ITCZ), as derived from cold cloud indices, indicate a northward displacement of the ITCZ in some, but not all, wet years in the Sahel. No systematic anomalous southward displacement of the ITCZ is evident in dry years. Drought in the Sahel appears to be more closely linked to the latitudinal extent and the intensity of the convection within the ITCZ.

### 1. Introduction

The Sahelo–Soudanian region of West Africa often experiences catastrophic droughts, as evidenced by large negative anomalies in long-term records of annual rainfall (e.g., Tanaka et al. 1975; Bunting et al. 1976; Nicholson 1989; Ward 1992). Since 1968 a prolonged drought has plagued the region, with maximum rainfall deficits occurring in 1972–73 and 1982–84 (Nicholson 1993). Following the first drought maximum, rainfall increased until the mid-1970s and it was commonly believed that the drought had ended. However, later observations (Nicholson 1983; Lamb 1982, 1983) indicated otherwise, revealing our lack of knowledge of the mechanisms at work.

Drought in the Sahelo–Soudanian region is a complex and multifaceted problem. Consequences are dramatic for human populations because the droughts are so intense and persistent, and because in that region vegetation growth, which includes primary production and agriculture, is governed by water availability. Ef-

fects on climate resulting from changes in vegetation cover are also potentially significant. Large-scale rainfall deficits destroy plant cover, reduce evapotranspiration, increase surface albedo, and alter other aspects of the water and energy balance (Lare and Nicholson 1994). This could modify the region's weather systems and precipitation patterns through feedback that might reduce rainfall even further (Charney 1975). The possibility of such feedback is real, as various numerical studies have indicated (e.g., Charney et al. 1977; Shukla and Mintz 1982; Nicholson 1988, 1989).

Studies have shown that numerous processes and factors, acting on various space scales and timescales, influence rainfall variability in West Africa (e.g., Kidson 1977; Kraus 1977; Kanamitsu and Krishnamurti 1978; Lamb 1978a,b, 1983; Nicholson 1980; Newell and Kidson 1984; Folland et al. 1986; Lough 1986; Palmer 1986; Shinoda 1990a,b; Janicot 1992a,b; Lamb and Peppler 1992; Ward 1992). The predominance of one process over another is not clear; linkages between local, synoptic, and regional or global-scale influences have not been well established, and some factors are clearly controversial. For example, some studies have concluded that rainfall deficits in West Africa appear to be associated with a southerly displacement of the

Corresponding author address: Dr. Mamoudou B. Ba, Department of Meteorology—3034, The Florida State University, Tallahassee, FL 32306-3034.

intertropical convergence zone (ITCZ) (e.g., Lamb 1978b), reduced interhemispheric contrast in SSTs (e.g., Folland et al. 1986), or El Niño–Southern Oscillation (ENSO) events (e.g., Semazzi et al. 1988; Wolter 1989), but evidence contradicting the role of these factors has also been presented (e.g., Tanaka et al. 1975; Nicholson 1980, 1989; Ropelewski and Halpert 1987). Researchers have also demonstrated the importance of such factors as the strengthening of the African easterly jet (AEJ) and the weakening of the Tropical easterly jet (TEJ) (e.g., Kidson 1977; Kanamitsu and Krishnamurti 1978), a decrease of the monsoonal flow (e.g., Lamb 1983), or the intensity of the convection in the ITCZ (e.g., Nicholson 1981; Janicot 1992b).

It has been difficult to definitively identify the causes of dry or wet conditions in West Africa. Variability in West Africa's atmospheric circulation, characterized by monsoon flow in the lower layers, easterly jets in the upper layers, and convective activity in the ITCZ (Hastenrath 1984; Fontaine and Janicot 1992), has neither been completely described nor completely understood. Modeling studies have been hindered by the coarse spatial resolution and crude convection schemes of general circulation models (the small-scale structure of the ITCZ cannot be reproduced). Perhaps more importantly, studies of rainfall variability are based on data from a network of stations that are unevenly distributed in space, sparse in critical regions, and/or reported irregularly.

Identifying the mechanisms that play a role in the long-term evolution of the West African climate, assessing the role of land–atmosphere feedback, modeling the effect of vegetation, and, consequently, improving both our understanding of and ability to predict Sahel droughts all require a better database for the analysis of rainfall variability. A long time series of measurements with good spatial resolution and temporally consistent coverage is necessary. Because of the large variability of rainfall on short space scales and time-scales (e.g., Thauvin and Lebel 1991), it is often impossible to obtain a sufficient rainfall dataset over wide areas from a conventional rain gauge network. Dense networks exist, such as the Estimation of Precipitation by Satellite–Niger (EPSAT–Niger) network (Cadet and Guillot 1991), but they are scarce and, by definition, limited spatially.

In contrast, satellite observations provide spatial coverage on a regular basis, allowing one to follow the convective activity responsible for most of the rain in West Africa, which is often organized in the form of propagating squall lines (e.g., Otomoshio 1985). To be useful though, satellite observations must be interpreted in terms of rainfall, a task that requires careful calibrations against ground-based measurements. The task is not easy because the algorithms, which are generally crude statistical relationships (Barrett and Martin 1981; Ba 1990), strongly depend on the rain gauge dataset

of reference and, therefore, are region and/or year specific.

In this paper, we evaluate and accurately calibrate two satellite algorithms suitable for the study of the interannual variability of seasonal rainfall in West Africa using Meteosat data for the period 1983–88. One algorithm is based on cold cloud-top frequency; the other is based on average thermal infrared radiance. We compare the satellite estimates with rainfall measurements from a surface rain gauge network. Through this comparison, we point out the limitations of the satellite techniques, particularly their general applicability. Most previous studies have dealt with individual years. We will also examine whether the methods can adequately assess interannual variability and whether this assessment is improved by using those techniques instead of ground-based rain gauge networks.

Since the study is limited to six years, all of which are relatively dry (Nicholson 1993), and since the period includes only one El Niño, this dataset cannot be used to quantitatively investigate relationships with large-scale phenomena. Instead, we assess the feasibility of utilizing satellite data in such studies by focusing on three specific problem areas, one of which relates to a suggested cause of West African rainfall variability. These include the mean rainfall field over West Africa, the year-to-year fluctuations of rainfall, and the location, extent, and intensity of the ITCZ. We also examine spatial variability in seasonal rainfall, including effects on zonal averages.

## 2. Area of study

The region of interest (Fig. 1) is limited to continental areas between 30°N and 0° and 18°W and 30°E. It is characterized by a wide range of vegetation zones, occurring in narrow latitudinal belts with various types

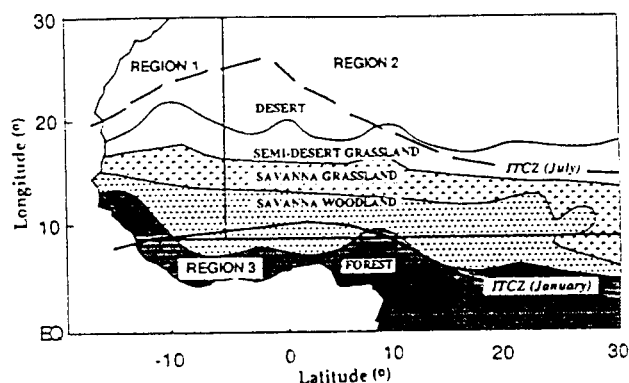


FIG. 1. Climatic zones and vegetation distribution in West Africa. Typical January and July ITCZ locations are plotted as solid and dashed lines, respectively. Orientation map indicates three suggested rainfall zones in West Africa: two Sahelian zones located just north of 9°N, one west of 5°W (region 1), the other east of 5°W (region 2), and a region extending southward from 9°N to the equator (region 3).

of savannas (savanna woodland, savanna grassland, and semidesert grassland) and bounded by forest to the south and desert to the north. The distribution of these vegetation zones is controlled by the amount and length of the summer rains, which are closely linked to the annual migration of the ITCZ (see Fig. 1 for the typical January and July ITCZ locations).

The source of moisture in the region is somewhat controversial, with various studies suggesting the Gulf of Guinea, the Indian Ocean, and even the Mediterranean (Newell and Kidson 1979) as critical source regions. A large part of the water vapor in the lower layers originates from the Gulf of Guinea (through evaporation) and is advected into the ITCZ by the low-level (below 700 hPa), southwest flow of the African monsoon (Lamb 1983). Some of this water vapor is lifted up while moving northward, feeding the AEJ at 700–600 hPa, which also acquires its moisture from eastern and central Africa (Cadet and Nnoli 1987). Several studies have shown that, at upper levels, the TEJ also feeds the region with moisture from the Indian Ocean (Flohn 1964; Newell and Kidson 1979; de Felice et al. 1982). However, the diagnostic study of Pierce and Mohanty (1984) and the numerical simulations of Joussaume et al. (1986) suggest that advection of

TABLE 1. Number of rainfall reporting stations during 1983–88.

Year	1983	1984	1985	1986	1987	1988
Number of stations	271	247	223	177	166	147

moist air from the Indian Ocean does not greatly affect West Africa (see also Cadet and Nnoli 1987).

The location of various rainfall regimes relative to the average position of the ITCZ is described by Germain (1968). Far to the south of the ITCZ is an area of stable and generally dry weather; to the north is the region of maximum convection. In the southern part of this region, much of the rainfall is characterized by isolated thunderstorms imbedded in the humid, southwesterly monsoon flow, but in the northern part, rainfall tends to be associated with organized synoptic and mesoscale systems. Rain diminishes progressively northward with the northernmost area reached by the ITCZ receiving rainfall only rarely.

The convective activity in the vicinity of the ITCZ is dominated by westward-propagating mesoscale disturbances. Squall and nonsquall disturbances are distinguished, but the former produce most of the rainfall

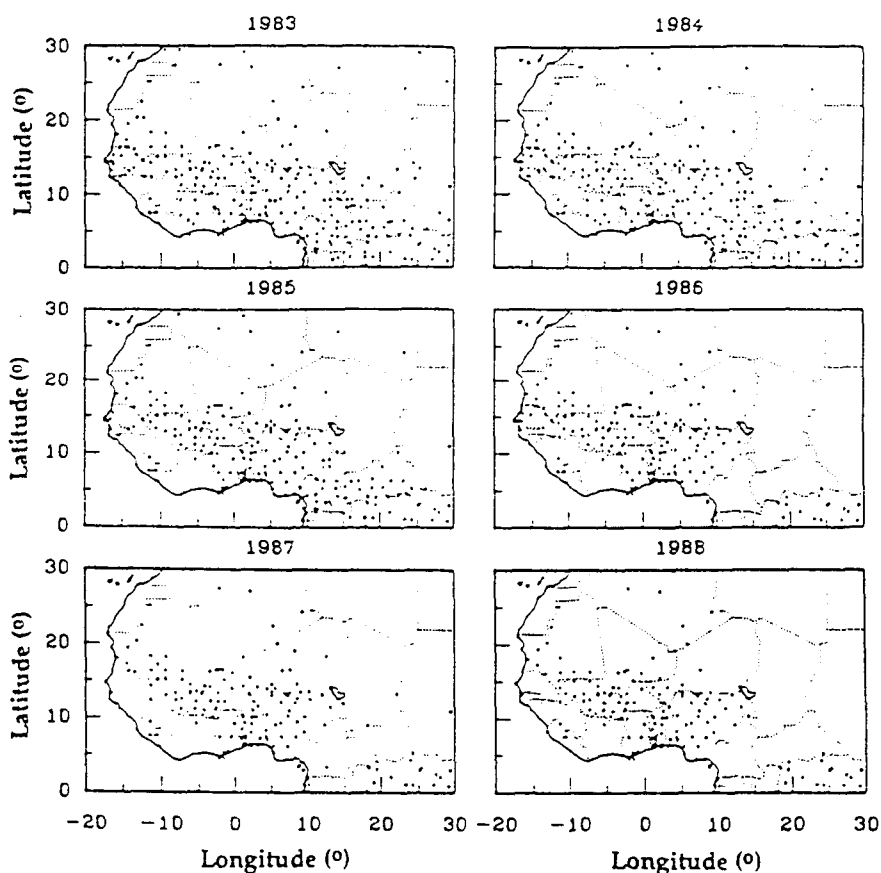


FIG. 2. Distribution of rainfall reporting stations available during 1983–88.

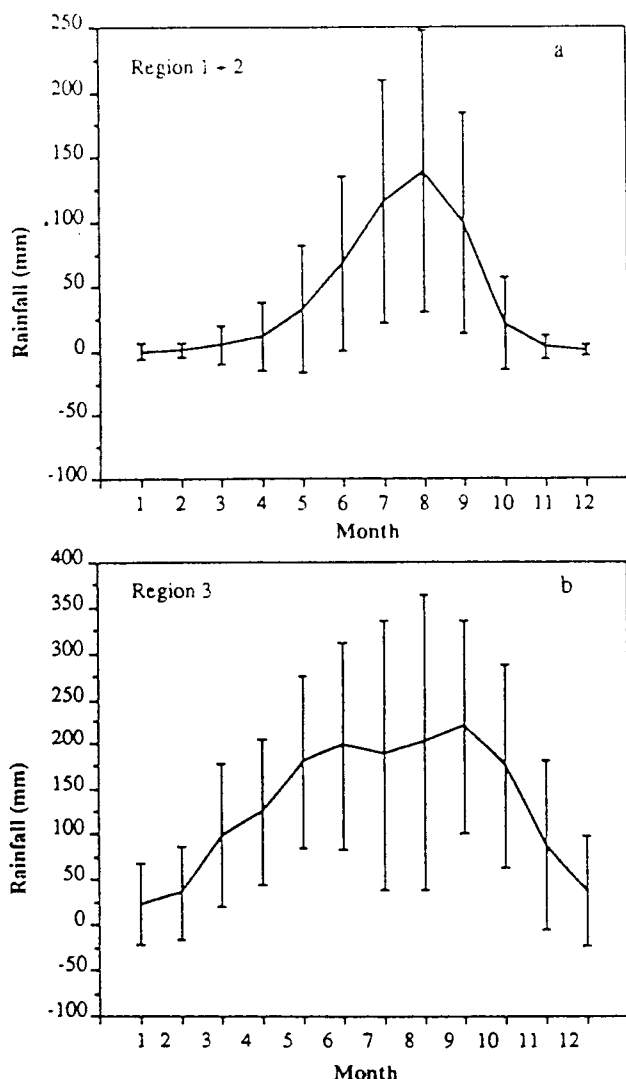


FIG. 3. Areal monthly mean rainfall for (a) region 1 + 2 and (b) region 3. Vertical lines indicate one standard deviation on either side of the mean.

in the region (Otomosho 1985). Few systems maintain themselves over more than a day (e.g., Aspliden et al. 1976; Martin and Schreiner 1981) while propagating westward. The developing clouds tend to aggregate into large areas of convective activity (sometimes called cloud clusters), which extend meridionally over a distance of about 10 to about 1000 km with no preferred size (Toledo et al. 1992). Imbedded in the clusters are huge, deep cumulonimbus clouds, recognizable by their anvils, which form a canopy displaced down from the relative wind at anvil level. The heaviest rainfall is associated with the cumulonimbus areas. Both the frequency of cloud clusters and the amount of rainfall associated with them appear to be modulated by transient synoptic-scale African waves (Thompson et al. 1979; Houze and Betts 1981), which propagate west-

ward. Thus, the rainfall is influenced by factors affecting the waves, such as the horizontal and vertical wind shear and latent heat release (Burpee 1972; Norquist et al. 1977; Albignat and Reed 1980).

Other factors, either of orographic nature or due to thermal contrasts, may affect the rainfall patterns significantly. In the Fouta Djallon region of Guinea, for instance, the effect of high mountains is to increase rainfall compared to that of surrounding regions. In coastal regions of Mauritania and Ivory Coast, on the contrary, the stabilizing effect of upwelling of cold water and cold ocean currents reduce rainfall locally.

Annual rainfall amounts vary from above 1500 mm in the forest zone to below 50 mm in the desert (e.g., Nicholson 1980). Interannual variability, expressed in

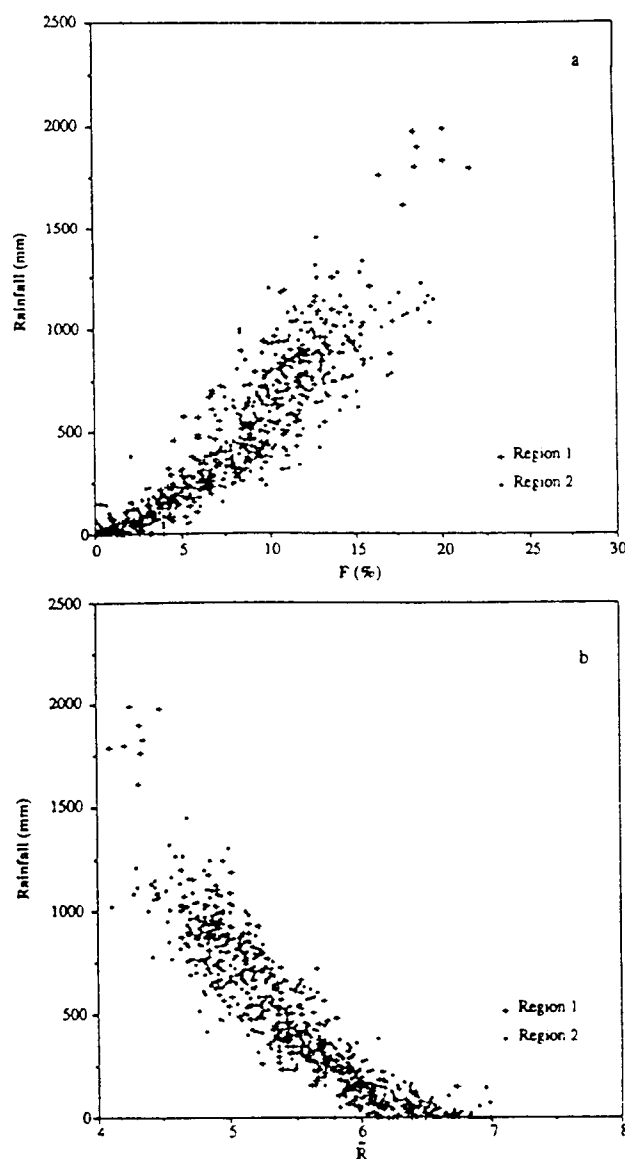


FIG. 4. Scatterplot of seasonal observed rainfall vs (a)  $F$  and (b)  $\bar{R}$  for region 1 + 2.

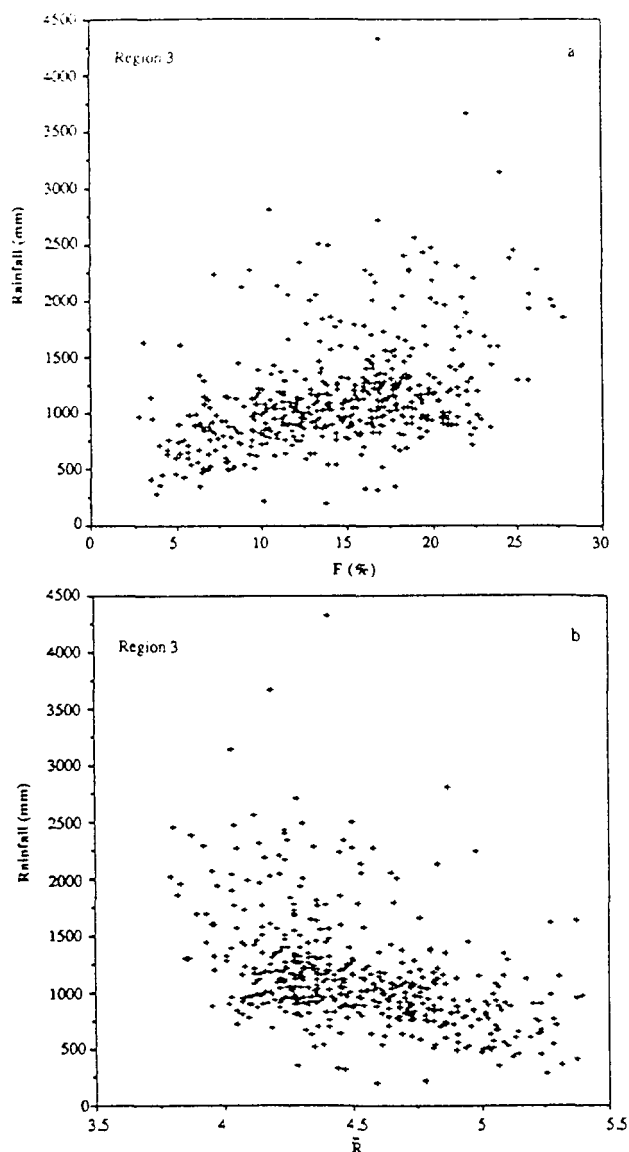


FIG. 5. Scatterplot of seasonal observed rainfall vs (a)  $F$  and (b)  $\bar{R}$  for region 3.

percentage of average values (or coefficient of variation), exceeds 50% in desert areas but is as low as 15%–20% in forest areas (Nicholson 1980) and is far from homogeneous. Nicholson (1980) and Bhatt (1989) have shown, for example, that the variability in the eastern Sahel is quite different from that in western Sahel. Janicot (1992a) and Nicholson and Palao (1993) have further demonstrated this difference and have identified three homogeneous sectors within West Africa that differ with respect to prevailing rainfall regime, intensity of coastal effects, and teleconnections to tropical circulations. Their divisions, although quite independently derived, are markedly similar.

In the present study, we investigate the accuracy of satellite estimates of rainfall in three regions that

roughly correspond to those divisions (Fig. 1) (section 5a). The first and second regions (hereafter referred to as regions 1 and 2), located between 9° and 30°N, are roughly the Sahelo–Soudanian sectors where rainfall is governed by squall lines and thunderstorms. Regions 1 and 2 are distinguished because of the oceanic influence in the former; the boundary between the two regions is fixed at 5°W. The third subregion (hereafter referred to as region 3) is located between the equator and 9°N. It is affected mainly by the localized convection of the monsoon with minimal influence of the synoptic and mesoscale systems of the Sahel.

### 3. Data

#### a. Surface data

The rainfall dataset used in this study is that of Nicholson (1993). This archive includes data published in *World Weather Records* and *Monthly Climatic Data of the World*, complemented by data gathered over the years from the French Office de la Recherche Scientifique et Technique (ORSTOM), the German Deutscher Wetterdienst, the U.K. Meteorological Office, and African Weather Services (Nicholson 1981). The dataset, provided in the form of monthly averages, includes the period 1983–88 during which Meteosat data are also available (see section 3b). The rain gauge stations are unevenly distributed, and the network is sparse above about 16°N (Fig. 2). The number of stations where data are available varies from one year to another (Table 1).

#### b. Satellite data

We use Meteosat data originating from the European Space Operation Centre (ESOC) in Darmstadt, Germany. At the time of the study, only data from 1983 through 1988 had been acquired. The dataset, in the International Satellite Cloud Climatology Project (ISCCP) B2 format, contains 3-h, 8-bit digitized images in three spectral bands: 0.4–1.1  $\mu\text{m}$  (shortwave band), 10.5–12.5  $\mu\text{m}$  (thermal infrared band), and 5.7–7.7  $\mu\text{m}$  (water vapor band). A B2 image is obtained by sampling the original full-resolution (about 5 km at the equator) image every six rows and six lines. All images are geometrically corrected and navigated to a fixed reference. For more details, see ESOC (1986).

TABLE 2. Performance of linear regression equations to estimated seasonal rainfall.

Variable	Region 1 + 2		Region 3	
	$F$	$\bar{R}$	$F$	$\bar{R}$
No. of points	744		487	
Mean rainfall (mm)	480		1152	
Coefficient of determination $r^2$	0.81	0.81	0.18	0.18
rms error (mm)	162	162	443	441

TABLE 3. Performance of nonlinear regression equations (second-order polynomials) to estimated seasonal rainfall.

Variable	Region 1		Region 2		Region 1 + 2	
	$F$	$\bar{R}$	$F$	$\bar{R}$	$F$	$\bar{R}$
No. of points	267		477		744	
Coefficient of determination $r^2$	86	89	80	86	81	85
Mean rainfall (mm)	470		488		480	
rms error (mm)	155	136	153	129	159	141
Terms of second-order polynomial at the 99% confidence level						
$a_0$	$-19 \pm 70$	$13756 \pm 1883$	$-69 \pm 52$	$7291 \pm 1039$	$-48 \pm 43$	$9258 \pm 963$
$a_1$	$37 \pm 17$	$-4173 \pm 684$	$63 \pm 13$	$-1967 \pm 370$	$51 \pm 11$	$-2632 \pm 345$
$a_2$	$2.6 \pm 0.9$	$317 \pm 62$	$0.4 \pm 0.7$	$131 \pm 33$	$1.3 \pm 0.6$	$187 \pm 31$

These data have been available since July 1983 (Ros-sow et al. 1985).

#### 4. Methods

In general, the satellite methods of rainfall estimation using observations in the visible and/or thermal infrared are based on the assumptions that 1) the higher the cloud albedo and the colder their tops, the more rain they produce, and 2) rainfall areas are located

directly beneath the clouds. The approach is either based on tracking cloud entities throughout their life-times (first approach) or on brightness temperature thresholding (second approach). Because of the difficulty in processing the huge amount of data constituting the full-resolution satellite images, the methods based on the first approach have been used only over limited areas and periods of time (Stout et al. 1979; Woodley et al. 1980; Griffith et al. 1978, 1981; Thiao et al. 1990). The methods based on the second ap-

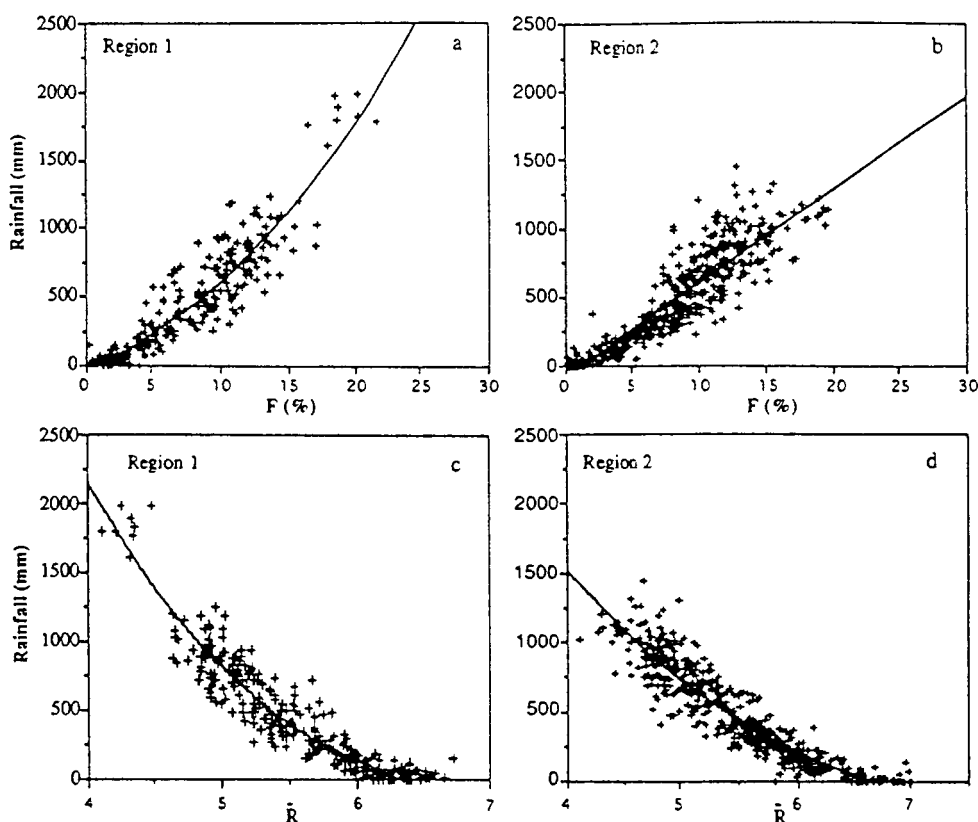


FIG. 6. Scatterplot of seasonal observed rainfall vs (a)  $F$  for region 1, (b)  $F$  for region 2, (c)  $\bar{R}$  for region 1, and (d)  $\bar{R}$  for region 2.

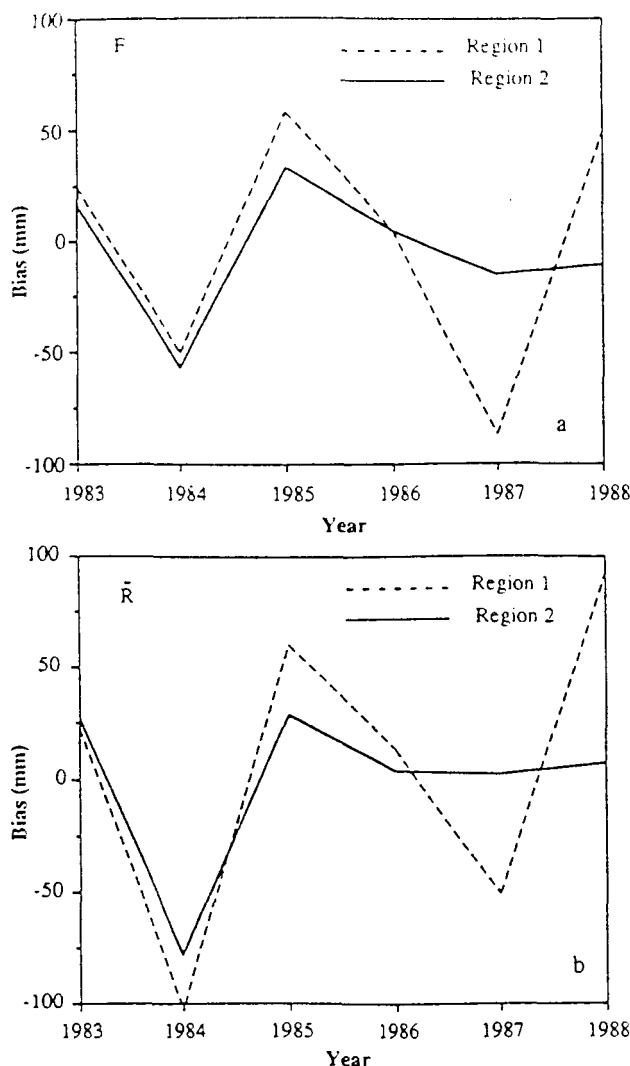


FIG. 7. Annual biases (surface observed minus satellite derived) associated with rainfall predicted by (a)  $F$  and (b)  $\bar{R}$ . Solid line is region 2; dashed line is region 1.

proach are intended to estimate rainfall for a period larger than 24 h. Arkin (1979), for instance, has shown that the fractional cloud cover of clouds colder than a certain temperature threshold is proportional to the accumulated precipitation. This technique seems to be reliable when it is applied over a large area (more than  $150 \text{ km} \times 150 \text{ km}$ ) and for time averages exceeding one day (Richards and Arkin 1981; Arkin and Meisner 1987). The algorithm has been used with both geostationary and polar-orbiting satellite data to create a rainfall climatology for the Tropics for the Global Precipitation Climatology Project (GPCP) (Arkin and Ardanuy 1989; Janowiak and Arkin 1990). In West Africa, similar techniques have been adapted in operational routines such as the method of the Tropical Agricultural Meteorology Satellite (TAMSAT) Group of the University of Reading (Dugdale et al. 1990) or

that of the EPSAT of the ORSTOM at Lannion, France (Carn et al. 1989). The methods based on time-averaged brightness temperature also have been used successfully to derive precipitation over the Tropics (Motell and Weare 1987; Ba and Deschamps 1990). Most of the methods use thermal infrared data only, although visible data alone (Kilonsky and Ramage 1976) or visible data combined with thermal infrared data (Barrett 1970; Barrett et al. 1986; Motell and Weare 1987) yield good predictive skills. In West Africa where rainfall often occurs at night, using visible data alone may bias the estimates.

Because of costly computing resources degradation of the temporal and spatial resolutions of satellite imagery is necessary when making rain estimates over very large areas such as West Africa. The ISCCP is designed to reduce these data for climatic use (Schiffer and Rossow 1983). Thus, the methods of the second category are more suitable for estimating rainfall for climatic purposes. However, degradation of temporal resolution of satellite data will decrease the skill of those methods by omitting the contributions of short-lived clouds. Consequently, for the Sahelo-Soudanian regions, they may not give good estimates of precipitation on timescales less than one month. This limitation is due to the nature of the phenomena affecting rainfall in these regions. Monthly precipitation is due to a few squalls and cloud clusters affecting an area with large variations in rainfall amounts between events. Therefore, a suitable relationship between rain gauge measurements and a satellite-based index could emerge only if the number of events is sufficient. For our study, whose objective is to analyze the interannual variability of rainfall, we have selected climatological methods utilizing radiance threshold (method 1) and time-averaged radiance (method 2).

In method 1, the predictor variable is a frequency of occurrence index quantifying the number of times thermal infrared radiance below a threshold value occurs during a given time period, typically a month or a season. This frequency of occurrence index, or  $F$ , is defined as

$$F = \left( \sum_i t_i \right) N^{-1}, \quad (1)$$

where the subscript  $i$  denotes the observation,  $N$  is the number of observations, and  $t_i$  is a discrete indicator variable taking the value 1 or 0 depending on the threshold,  $R_T$ :

$$t_i = \begin{cases} 1, & R \leq R_T \\ 0, & R > R_T. \end{cases} \quad (2a)$$

$$(2b)$$

In Eqs. (2a) and (2b),  $R$  is the radiance of a pixel. Correlation coefficients between satellite estimates of precipitation and surface measurements are rather insensitive to the "warm" threshold (Arkin 1979; Motell and Weare 1987; Ba and Deschamps 1990), which can

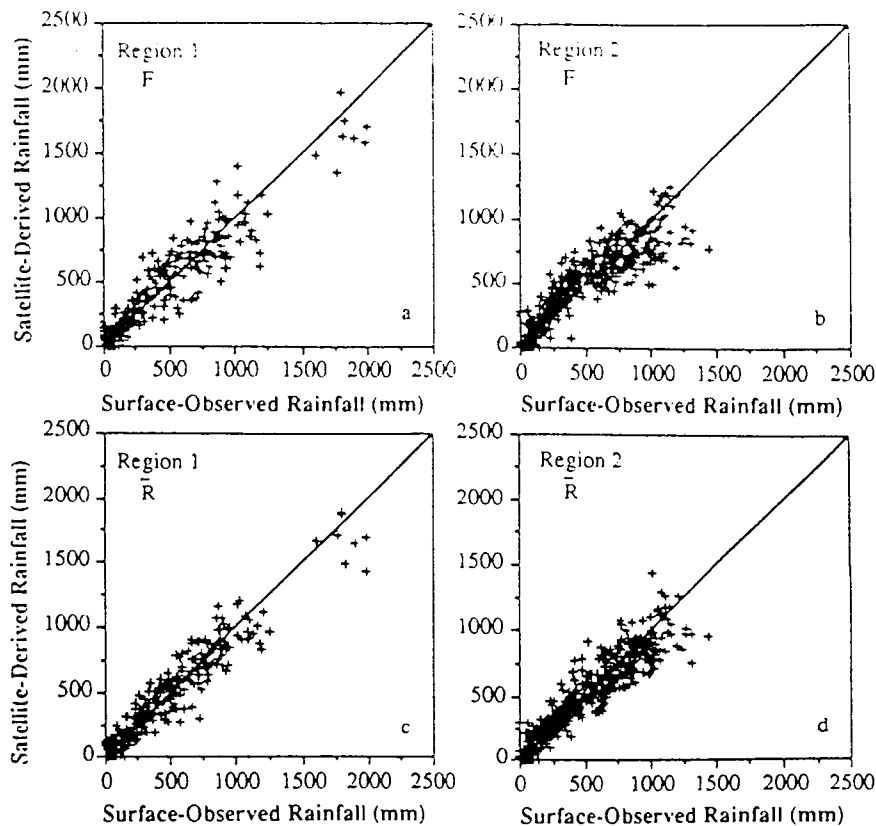


FIG. 8. Scatterplot of satellite-derived rainfall vs observed rainfall after correction of annual biases. Nonlinear regression equations are used with (a)  $F$  for region 1, (c)  $\bar{R}$  for region 1, and (d)  $\bar{R}$  for region 2. Linear regression equation is used with (b)  $F$  for region 2.

be as high as  $10^{\circ}\text{C}$  on monthly and seasonal timescales (Ba and Deschamps 1990). We chose a threshold of  $2.107 \text{ W m}^{-2} \text{ sr}^{-1} \mu\text{m}^{-1}$ , which corresponds to a brightness temperature of  $-40^{\circ}\text{C}$ . Atmospheric corrections are not used in this method since the cloud tops selected are located high in the atmosphere.

In method 2, the predictor variable is the average thermal infrared radiance over the period of interest,  $\bar{R}$ , defined as

$$\bar{R} = (\sum_i R_i) N^{-1}. \quad (3)$$

Since  $\bar{R}$  is a time average over all days, both clear and cloudy, it includes radiative effects from the surface, the atmosphere, and varied cloud types. The influence of water vapor absorption is significant. This is not a drawback because the absorption is related to water vapor content in the atmosphere, and water vapor content in the atmosphere modulates the evaporation rate of falling rain. In fact,  $\bar{R}$  implicitly takes into account two major parameters that are indirectly related to rainfall: the cloud-top temperature of precipitating systems and the surface temperature. The latter is modified by rainfall through evapotranspiration (Assad et al. 1987).

## 5. Results

### a. Comparison of rainfall statistics from satellite and conventional data

The skill of the two predictor variables defined above, namely  $F$  and  $\bar{R}$ , can be assessed by comparing observed and predicted rainfall at the surface stations. We compared six years (1983–88) of seasonal rainfall (May–October). Most of the rainfall occurs during those months (Nicholson 1980), especially in regions 1 and 2 (Fig. 3). Univariate, linear, and nonlinear regression analysis was used to compute performance statistics. For each station, we applied the satellite algorithms to the pixel that encompassed the verifying station. According to Ba (1990), more complex schemes involving weighted averages of surrounding pixels would not change the regression statistics significantly.

Figures 4 and 5 show, for regions 1 and 2 combined (hereafter referred to as region 1 + 2) and region 3, respectively, the relationship between seasonal rainfall and  $F$  or  $\bar{R}$ , and Table 2 lists the values of the coefficient of determination  $r^2$  (assuming a linear relationship). In region 1 + 2,  $r^2$  is high for both  $F$  and  $\bar{R}$  (0.81 significant at the 99% confidence level). For region 3,



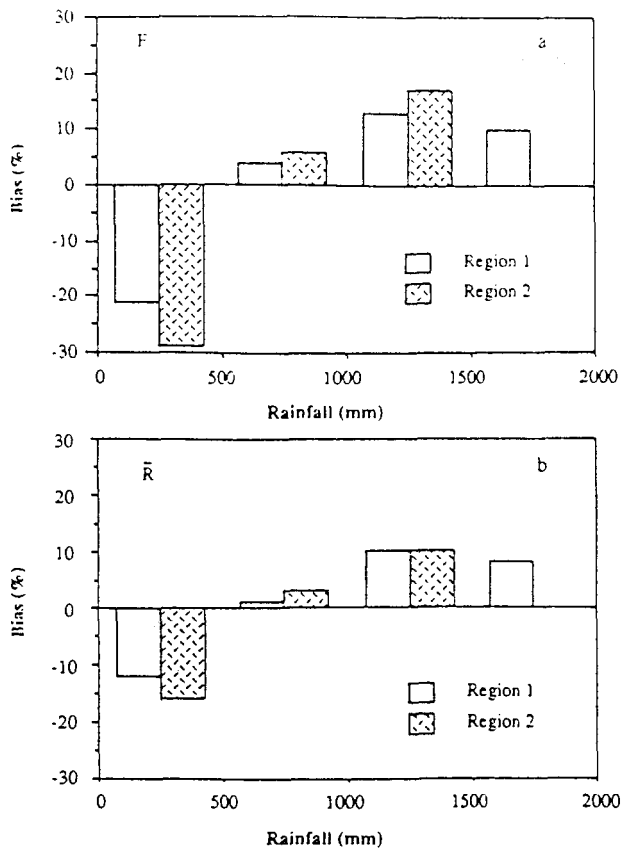


FIG. 9. Biases (surface observed minus satellite derived) associated with rainfall predicted by (a)  $F$  and (b)  $\bar{R}$ . The biases are expressed in percent of mean rainfall in 400-mm intervals.

$r^2$  is much lower, 0.18 for both  $F$  and  $\bar{R}$  (see also Fig. 5), indicating that neither  $F$  nor  $\bar{R}$  is a good predictor variable in that region. The low  $r^2$  values for region 3 may be explained by the rainfall regime, which is characterized during the boreal summer, by monsoon rain with a significant stratiform component. Consequently, the  $-40^\circ\text{C}$  threshold does not take all the precipitating clouds into account, decreasing the predictive skill of  $F$ . Due to orographic effects, rain in the highlands of Guinea and Cameroon also occurs without deep convection and, hence, cold cloud tops, further contributing to a degraded performance. In the case of  $\bar{R}$ , two factors contribute to a low coefficient of correlation, namely frequent cirrus cloud cover and large soil moisture content. The frequent cirrus cloud cover and the large soil moisture content (the result of continuous rain) inhibit the use of the intended technique  $\bar{R}$  to determine surface temperature effects (evaporation associated with rain generally results in a decrease in surface temperature).

Because of the poor predictive skill of  $F$  and  $\bar{R}$  in region 3, we focus on region 1 + 2. A simple linear regression between seasonal rainfall and predictor variables yields an rms error of about 160 mm (33%

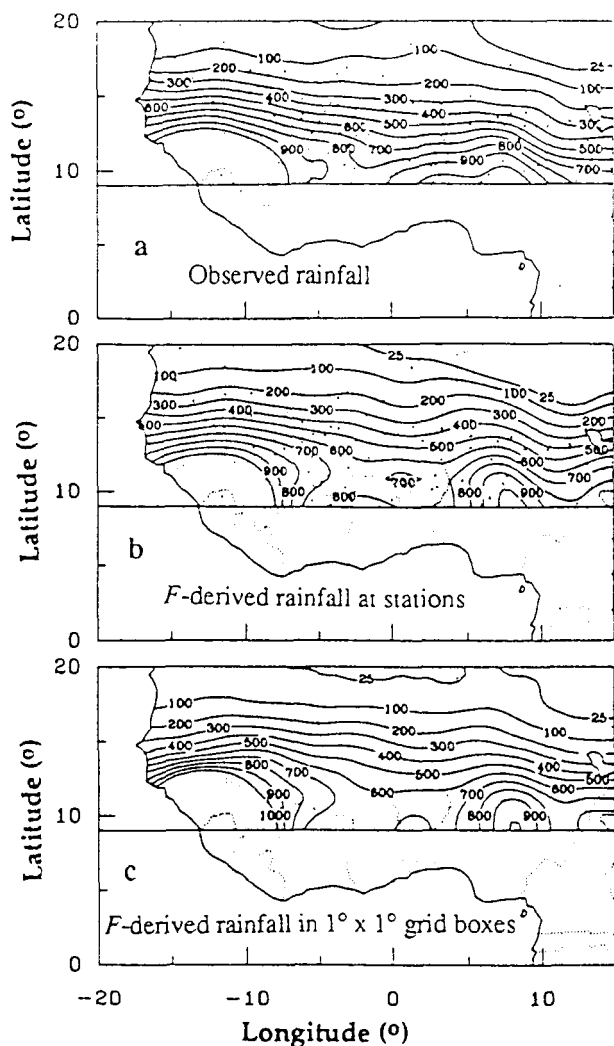


FIG. 10. Spatial distribution of 6-yr mean seasonal rainfall computed from observations (a) at the surface network stations, (b)  $F$  at the same stations, and (c)  $F$ -based estimates in  $1^\circ \times 1^\circ$  grid boxes.

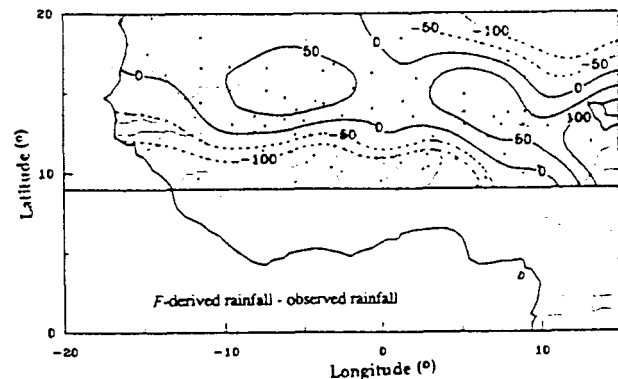


FIG. 11. Differences between  $F$ -derived rainfall computed at surface network stations and observed rainfall at the same stations.

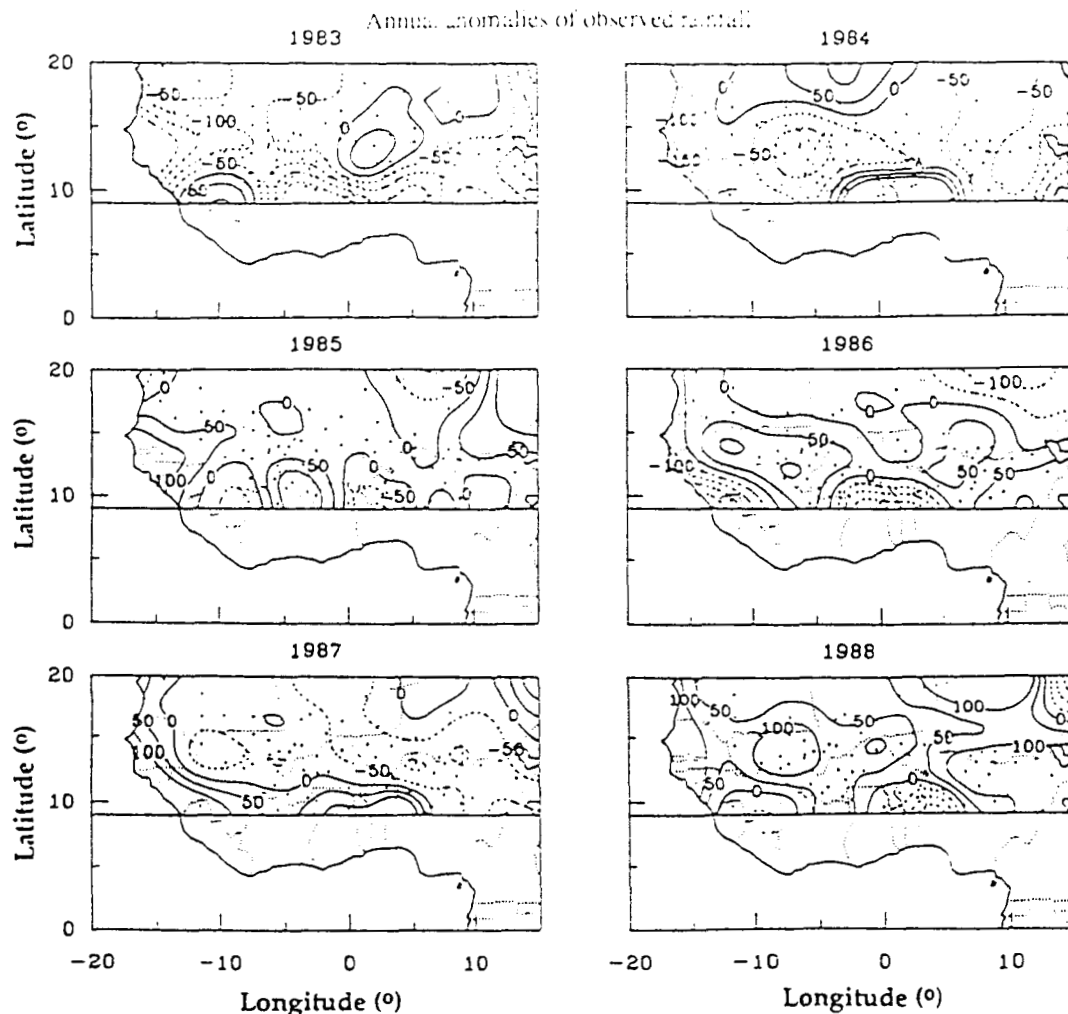


FIG. 12. Annual anomalies (1983–88) of observed rainfall with respect to the 6-yr mean. The contour plots are generated with observations at the surface network stations.

of the mean measured value) for both  $F$  and  $\bar{R}$  (Table 2). Examining Figs. 4a and 4b, we notice that the relationship between seasonal rainfall and predictor variables is not linear, suggesting that a nonlinear regression may improve the performance statistics. Using a second-order polynomial,  $r^2$  is slightly higher for  $\bar{R}$  (0.85 instead of 0.81), but remains the same for  $F$  (0.81) (Table 3). The terms of the second-order polynomial are statistically significant at the 99% confidence level (see Table 3). The rms error is practically unchanged for  $F$  (159 mm instead of 162 mm) but is significantly reduced (141 mm instead of 162 mm) for  $\bar{R}$ . In the case of  $F$ , the lack of improvement in the performance statistics may be due to the type of nonlinearities, which are not described properly by a second-order polynomial. In fact, Fig. 4a suggests that two distinct nonlinear regimes may exist, one below 500 mm and the other above. Applying separate second-order polynomials below and above 500 mm gives,

in fact, much better statistics ( $r^2 = 0.88$ , rms error of 120 mm), but continuity at 500 mm is not respected, and we prefer to use a single second-order polynomial.

Applying separate simple linear regression equations to regions 1 and 2 yields in region 1  $r^2$  values of 0.83 and 0.81 for  $F$  and  $\bar{R}$ , respectively. In region 2, the  $r^2$  values are 0.80 and 0.83 for  $F$  and  $\bar{R}$ , respectively. Using a second-order polynomial,  $r^2$  is much higher in region 1, particularly for  $\bar{R}$  (0.89 instead of 0.81) (see Table 3 and Fig. 6), but remains the same for  $F$  in region 2. The terms of the second-order polynomial are statistically significant at the 99% confidence level in both regions for  $\bar{R}$  and only in region 1 for  $F$  (Table 3). The second-order term ( $a_2$ ) is statistically uncertain for  $F$  in region 2 (Table 3) and, therefore, does not contribute useful information for the prediction of rainfall. Thus a first-order polynomial in  $F$  is used to estimate rainfall in region 2 and a second-order polynomial in region 1, but a second-order polynomial in

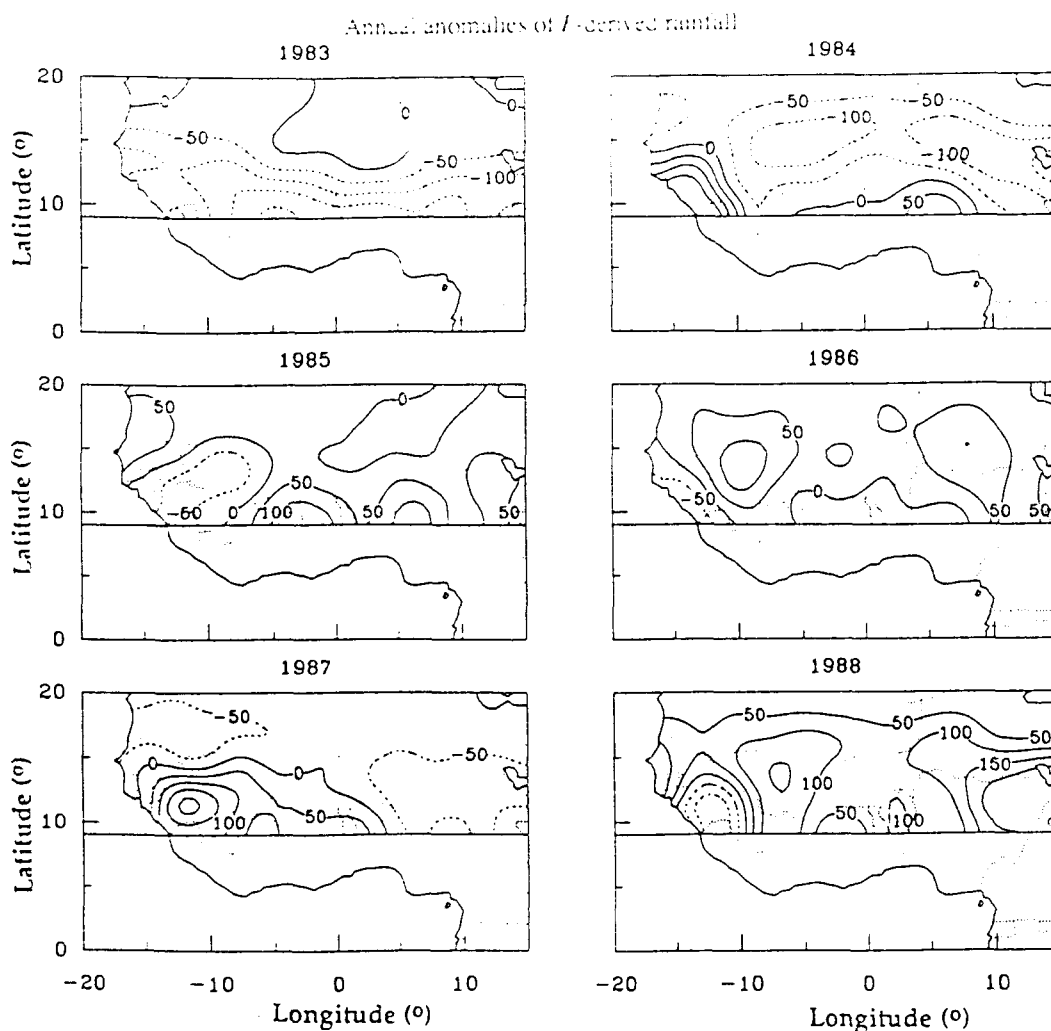


FIG. 13. Annual anomalies (1983–88) of  $F$ -derived rainfall with respect to the 6-yr mean. The contour plots are generated with estimates in  $1^\circ \times 1^\circ$  grid boxes.

$\bar{R}$  is used for both regions 1 and 2. Using distinct relationships between rainfall and either  $F$  or  $\bar{R}$  in regions 1 and 2 is also justified by different yearly biases computed for each region (see below).

Applying the regression equations (separate equations to regions 1 and 2) to data from individual years reveals positive and negative biases (defined as the mean difference between measured and predicted values), reaching magnitudes of 80 mm in 1987 ( $F$ ) and 100 mm in 1984 ( $\bar{R}$ ) (Figs. 7a,b). These biases are not negligible and must be removed to study the interannual variability of rainfall properly. For  $F$ , removing the biases yields  $r^2$  values of 0.87 and 0.81 in regions 1 and 2, respectively, and rms errors are 146 and 148 mm. For  $\bar{R}$ ,  $r^2$  values are 0.92 and 0.87 in regions 1 and 2, respectively, and rms errors are 119 and 122 mm. Thus, by removing the biases, the error statistics are not significantly improved overall, but estimates from different years become comparable. Since  $r^2$  rep-

resents the interannual rainfall variance explained by the algorithms, 13% and 8% (region 1) and 20% and 13% (region 2) of the variance still remains unexplained by  $F$  and  $\bar{R}$ , respectively.

If  $B_i$  and  $B'_i$  denote the biases for year  $i$  when using  $F$  and  $\bar{R}$ , respectively, the predictive seasonal rainfall equations in regions 1 and 2 are

$$P_{i1}(F) = (-19 + 37F + 3F^2) + B_{i1} \quad (4a)$$

$$P_{i2}(F) = (-85 + 68F) + B_{i2} \quad (4b)$$

$$P_{i1}(\bar{R}) = (13756 - 4173\bar{R} + 317\bar{R}^2) + B'_{i1} \quad (5a)$$

$$P_{i2}(\bar{R}) = (7291 - 1967\bar{R} + 131\bar{R}^2) + B'_{i2}, \quad (5b)$$

where  $P$  is seasonal rainfall (mm) and the subscripts 1 and 2 denote regions 1 and 2, respectively.

Figure 8 compares observed and predicted rainfall amounts when using Eqs. (4) ( $F$ ) and (5) ( $\bar{R}$ ). The scatterplot of  $F$ -derived rainfall versus observed rainfall

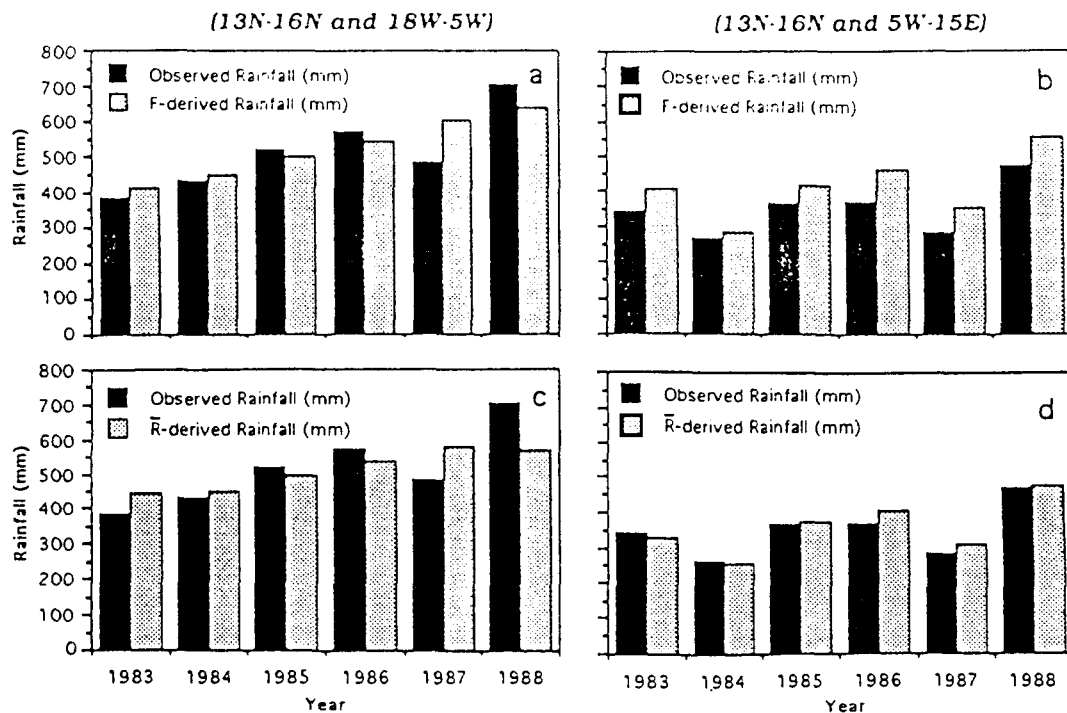


FIG. 14. Surface-observed and satellite-derived rainfall for strips located between 13°–16°N and 18°–5°W (left) and between 13°–16°N and 5°W–15°E (right). (top)  $F$ -based values; (bottom)  $\bar{R}$ -based values.

for region 1 increases gradually from low to high rainfall amounts and is nearly centered around the 45° line (Fig. 8a). By contrast, for region 2,  $F$  generally overestimates rainfall below 500 mm and the scatter, centered around the 45° line, is much higher, above 500 mm (Fig. 8b). In the case of  $\bar{R}$ , the scatter is well centered around the 45° line and slightly higher, above 500 mm for region 2 (Figs. 8c,d). A few points are characterized by rainfall amounts above 1500 mm. These correspond to two stations in Guinea-Bissau and one station in Sierra Leone located near 9°N, the southern boundary of regions 1 and 2. For those stations, both algorithms underestimate actual rainfall in most cases. Figure 9 shows the histograms of biases when using  $F$  and  $\bar{R}$ , respectively. Time average  $\bar{R}$  gives better results overall than  $F$  in both regions. The overall satellite-derived rainfall is overestimated below 500 mm, particularly in region 2, and underestimated in wetter regions.

Various sources of errors may affect algorithms to estimate surface rainfall from space. These pertain to the nature of rainfall, which is highly variable in space and time, and to the type of satellite observations available, which are not direct indicators of rainfall, but instead only assess parameters affecting rainfall. Augustine et al. (1981), for instance, have shown that three possible error sources may affect satellite-derived rain patterns: 1) the method of apportionment of satellite-derived rain at the surface, 2) resolution degra-

dation of the digital satellite imagery, and 3) anomalies of convective clouds in tropical regions. For the algorithms used in the present study, the spatiotemporal variability of atmospheric constituents (mainly water vapor) and surface temperature may cause other errors. The amount of water vapor available in lower levels affects the maintenance of the convection and, consequently, the rainfall. Therefore, when using a single relationship for a large area with nonhomogeneous low-level water vapor distribution (i.e., West Africa), the satellite algorithms will overestimate rainfall in drier regions and underestimate it in humid regions (Fig. 9). Water vapor also affects the thermal infrared radiances and, therefore,  $\bar{R}$  and, to a lesser extent,  $F$  (water vapor is not abundant above cold cloud tops). Surface temperature may be also governed by processes other than evapotranspiration, especially in the coastal zones (i.e., western Sahara) and southern regions of the area of study, thus biasing the estimates made by  $\bar{R}$  in those regions.

Our results show that generalizing the satellite algorithms is not straightforward. Both  $F$  and  $\bar{R}$  yield poor results south of 9°N where a large amount of the rainfall is produced by stratiform clouds. This suggests that applying the predictor variables everywhere within the tropical zone may lead to large errors. The algorithms may only work adequately in regions such as the Sahelian zone, which are homogeneous meteorologically (same type of rainfall) and where most of the

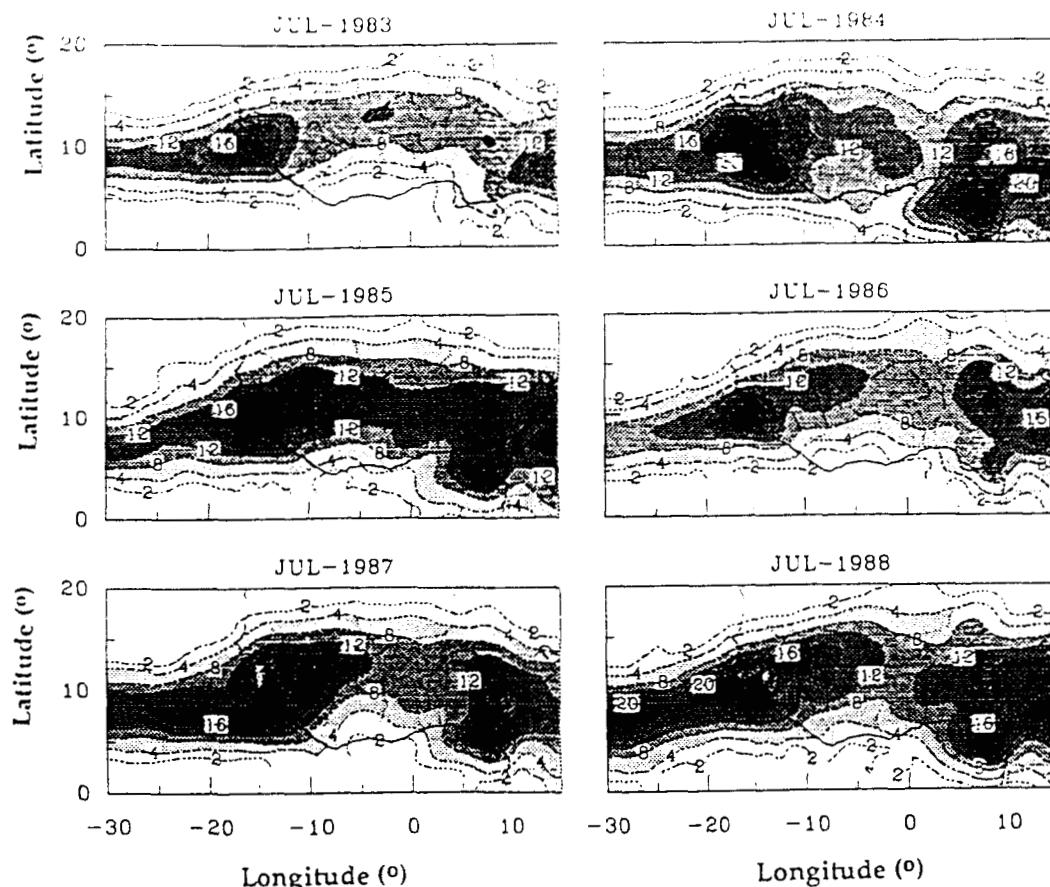


FIG. 15. Monthly maps of  $F$  over West Africa during the month of July for the years 1983–88.

rainfall results from vertically extended (cold) convective systems.

#### *b. Interannual variability of rainfall*

Studies of rainfall variability in the Sahelo-Soudanian region, where catastrophic droughts occur, require observations at a spatial resolution that the African rainfall networks do not readily provide. Significant errors may be introduced when rainfall fields are interpolated from the data available at the unevenly distributed surface observing stations or extrapolated from stations in data-sparse regions. In the analyses described in this section, both the impact of spatial sampling on the observed and derived estimates and the accuracy of satellite estimates of interannual variability of rainfall are examined. Initially, the mean fields for the 6-yr period of study are examined. Then, the spatial fields and areal averages for individual years are examined.

Equations (4)–(5), which result from a careful calibration against surface measurements, were used to derive the rainfall and, hence, anomaly fields with a spatial resolution of approximately  $1^\circ$  latitude  $\times$   $1^\circ$  longitude. In the computations, estimates over 32-km

areas (the original resolution of the Meteosat dataset at the equator) were simply averaged. No adjustment was made to account for latitude-varying pixel size, since the effect is not significant. Both techniques were used, but in cases where they performed about equally well the presentation of results is limited to the threshold method.

Figure 10 shows the spatial distribution of the 6-yr mean rainfall computed from surface observations (Fig. 10a) from Meteosat observations corresponding to surface stations (Fig. 10b) and from all Meteosat observations (Fig. 10c). The area of analysis is restricted to a zone between  $9^\circ$  and  $20^\circ$ N, and between  $18^\circ$ W and  $15^\circ$ E, where 78 stations were available during the period 1983–88. The agreement is good between the three seasonal rainfall fields. The north–south gradient of rainfall generally observed in the region is well retrieved by satellite-derived rain. However, the effect of sampling is obvious when comparing Figs. 10b and 10c. Since the two datasets are derived from the same source (Meteosat), the differences observed between the two fields (i.e., the isohyets of 100 and 200 mm shifted to the north) are due to sampling errors of the surface network. In Fig. 11, which depicts the absolute

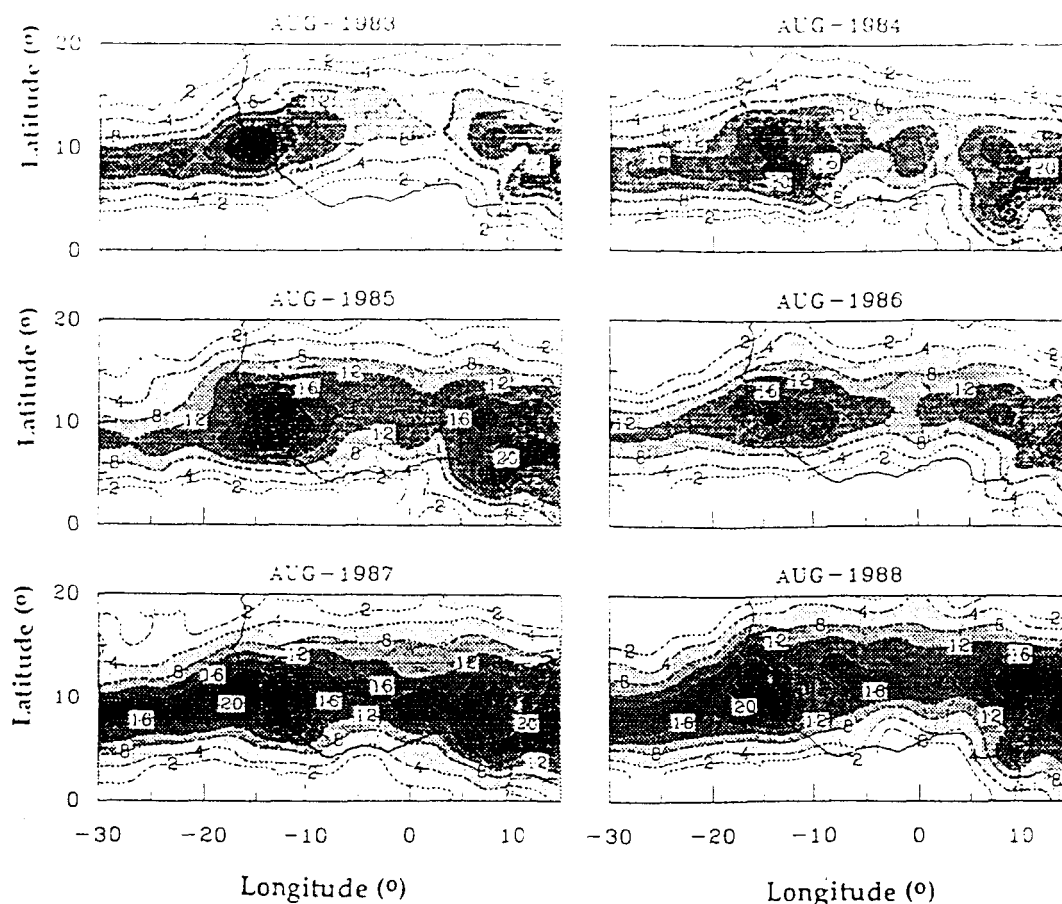


FIG. 16. Monthly maps of  $F$  over West Africa during the month of August for the years 1983–88.

differences between observed and estimated rainfall, one can notice that the amplitude of these differences are less than 50 mm (less than 10% of seasonal rainfall) over most of the region. The satellite tends to underestimate rainfall by about 100 mm (15% of seasonal rainfall) in the southwest part of the region and overestimate rainfall by 50 mm (15% of seasonal rainfall) in eastern Mauritania and by 100 mm (15%) to the south of Lake Chad.

Figures 12 and 13 show the patterns of seasonal rainfall anomalies with respect to the 6-yr mean, 1983–88, as computed from surface data (Fig. 12) and computed from all Meteosat data (Fig. 13). The observed and satellite-derived anomalies are consistent, but significant differences exist. The differences tend to occur in zones where surface data are few or nonexistent and, therefore, must be interpreted as an artifact due to interpolation techniques used for the surface network. The 1983 and 1984 seasons are generally drier than those of the other years, and the 1988 season is the wettest. Unlike the rainfall patterns (not shown here), the anomaly patterns do not exhibit a strong zonal character. Both satellite and surface observations show that the drought during 1983 affected almost the whole

region except the north of Burkina and the south of Niger. In contrast to 1983, 1984 was wetter by more than 100 mm in the southernmost part of the region of study (Guinea, Senegal) and by more than 50 mm north of Ghana and Benin, where the rainfall deficit was as large as 100 mm in 1983. The seasons of 1985 and 1986 were, in comparison, wetter almost everywhere, particularly between  $10^{\circ}\text{W}$  and  $10^{\circ}\text{E}$  along  $10^{\circ}\text{N}$  in 1985 and south of  $15^{\circ}\text{N}$  in 1986. The 1987 season is characterized by one zone with negative anomalies centered at  $12^{\circ}\text{N}$ ,  $10^{\circ}\text{E}$  (Nigeria), where the deficit reaches 100 mm. Positive values dominate the anomaly field in 1988, especially in the southeast (Niger, Nigeria, Chad), where rainfall is in excess of 200 mm.

The above results, in particular the nonzonal aspect of the anomaly fields, strongly suggest that care should be exercised when analyzing rainfall data averaged over latitudinal bands (e.g., Nicholson 1993; Lamb and Pepler 1992). Longitudinal variability in the anomalies is substantial, indicating that some sub-Saharan regions may receive above-average rainfall during a year cataloged as dry based on zonal averages. It is important to point out that the 6-yr study period may

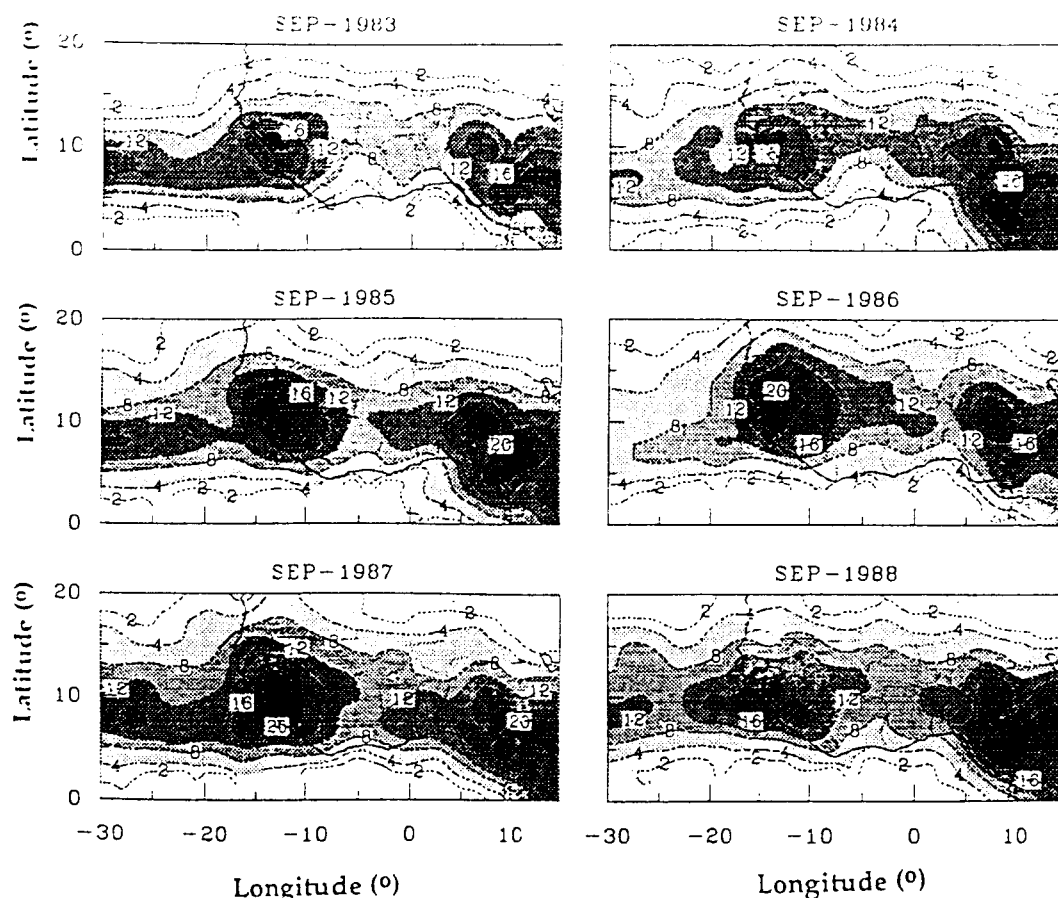


FIG. 17. Monthly maps of  $F$  over West Africa during the month of September for the years 1983–88.

not represent the long term. However, the satellite estimates are not affected by changes in the surface station network.

The results in Figs. 12 and 13 suggest that the satellites adequately capture the interannual variability of rainfall in the region. This is further tested using spatial averages within strips located between  $13^{\circ}$ – $16^{\circ}$ N and  $18^{\circ}$ – $5^{\circ}$ W (left) and  $13^{\circ}$ – $16^{\circ}$ N and  $5^{\circ}$ W– $15^{\circ}$ E (right) (Fig. 14). This tests the robustness of the algorithms geographically and temporally. There is good agreement between observations and satellite estimates, and the satellite estimates clearly capture the differences between the eastern and western sectors in the amount of rainfall. The agreement is somewhat better for the mean radiance method, but the threshold method does indicate somewhat greater interannual variability.

### c. The convergence zone over West Africa

Some of the earliest papers on the Sahel drought suggested that the primary cause of the drought was a simple equatorward displacement of the ITCZ over West Africa (e.g., Bryson 1973). Since that time a number of papers have examined the role of this factor,

with various authors reaching substantially different conclusions. Lamb (e.g., 1978a,b) and Hastenrath (1984), for example, have detected a correspondence between latitudinal position of the ITCZ and Sahel rainfall. Others, such as Tanaka et al. (1975), Nicholson (1981), and Newell and Kidson (1984), have demonstrated that anomalous ITCZ positions bear a relationship to rainfall in only some cases, notably years when rainfall is above normal in the Sahel but below normal in equatorial latitudes. Part of the reason for the difference of opinion is that the ITCZ is defined based on surface pressure and winds in some studies but on maximum rainfall or convection in others (Nicholson and Palao 1993). Also, some have examined the ITCZ over land, others over the adjacent ocean regions.

In general, the studies indicating a relationship between the ITCZ and Sahel rainfall are based on wind pressure and convergence patterns over the Atlantic Ocean, where there is minimal rainfall data, while those disputing it are based on rainfall over the continent, where wind and pressure data are poor. Since the ITCZ is considered to be a locus of maximum convection rather than maximum rainfall, the satellite data provide

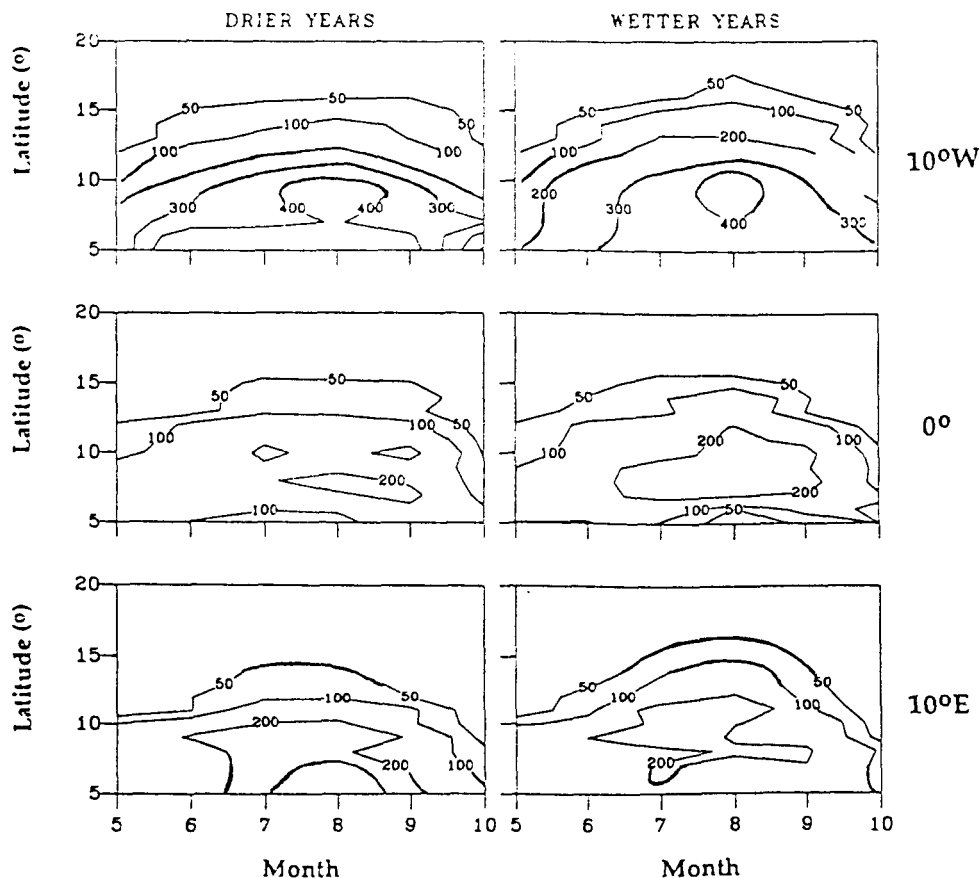


FIG. 18. Latitudinal cross sections of monthly rainfall for north-south transects in West Africa. (top)  $10^{\circ}\text{W}$ ; (middle)  $0^{\circ}$ ; (bottom)  $10^{\circ}\text{E}$ . On the left-hand side is a 3-yr-average "dry" composite for the years 1983, 1984, and 1987; on the right-hand side is a 3-yr-average "wet" composite for the years 1985, 1986, and 1988.

a third useful methodology for determining its position over land. Moreover, satellite analysis provides a way to directly compare the ITCZ position over land and water. Since the prevailing east-west line of maximum cloudiness indicates that the ITCZ is easy to identify in satellite images,  $F$  gives a way to describe its monthly mean location and intensity over both land and ocean.

Here, the monthly mean frequency of cold cloud index images ( $F$ ) is used to evaluate the north-south excursion of the ITCZ and also its convective intensity during the wettest summer months (July–September) of these six years. Both maps and latitudinal transects of convective activity and rainfall are used to evaluate the location and intensity of the ITCZ and the latitudinal extent of the associated cloud band.

Figures 15–17, containing monthly maps of  $F$  over West Africa, illustrate some interesting features of the convergence zone. The prevailing east-west line of maximum convection is broader farther north and more dynamic over land than over the adjacent ocean. The main features of the ITCZ remain fairly constant during the north-south excursion from July to Sep-

tember. One example is the persistence of maximum  $F$  cells over the highlands of Guinea and Nigeria. Between these cells lies a zone with relatively low values of  $F$  centered north of the Ivory Coast. This zone is generally observed in rainfall patterns as well, with its southern extremity corresponding to the anomalous "dry zone" along the Guinea coast.

These figures reveal changes from year to year in the intensity and latitudinal extent of the rain belt. The core region of maximum convection is generally located farther north during 1988, the wettest year. No differences are apparent between 1983 and the wet years of 1985 and 1986. The line of maximum convection was located somewhat farther south during 1984 and 1987, years corresponding to dry conditions in the eastern Sahel but wet conditions in the southwest (Guinea). The contrast between 1988, the wettest year, and 1983, the driest year, is readily apparent for July and August, with the rain belt being broader and convection more intense during the wetter year. The convection is, in general, more intense in the three wettest years (1985, 1986, and 1988) than during the three



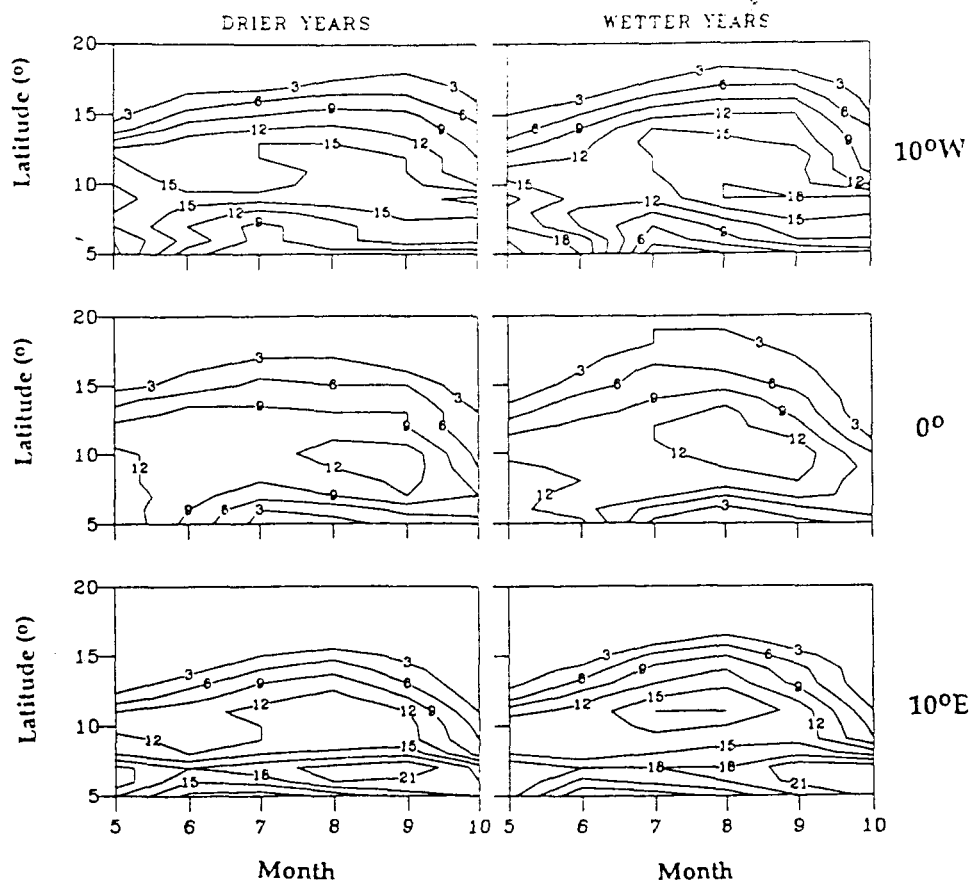


FIG. 19. Latitudinal cross sections of monthly convective intensity for north-south transects in West Africa: (top)  $10^{\circ}\text{W}$ ; (middle)  $0^{\circ}$ ; (bottom)  $10^{\circ}\text{E}$ . On the left-hand side is a 3-yr-average "dry" composite for the years 1983, 1984, and 1987; on the right-hand side is a 3-yr-average "wet" composite for the years 1985, 1986, and 1988.

driest (1983, 1984, and 1987). The contrast is particularly strong between 1988, clearly the wettest year, and 1983. During July and August 1983, the index values of the core region of maximum convection do not exceed 8. Only over the highlands of Guinea and Nigeria have index values exceeded these values. During August 1988, in contrast, the core region of maximum convection has index values exceeding 12.

The latitude and intensity of maximum convection is further illustrated in Figs. 18 and 19, latitudinal cross sections of monthly rainfall and convective intensity for three north-south transects in West Africa. One set is derived from observed rainfall, the other from cold cloud frequency  $F$ . In the latter case,  $F$  was not converted to rainfall because the rainfall-cold cloud frequency relationship used in producing Figs. 10b and 10c was derived from seasonal data and is not applicable on monthly scales. Nevertheless, there is qualitative agreement and both sets of transects can be used to roughly approximate the "center of gravity" (i.e., the ITCZ position over West Africa), and the intensity and latitudinal extent of the rain belt.

On the left-hand side of each figure is a 3-yr "dry" composite for the years 1983, 1984, and 1987; on the right-hand side is a "wet" composite for 1985, 1986, and 1988. Both Figs. 18 and 19 show a tendency for the maximum of convection and rainfall to be somewhat farther north during the wet composite than for the dry composite. The differences are most apparent in the eastern Sahel near  $10^{\circ}\text{E}$  and are least apparent in the western sector near  $10^{\circ}\text{W}$ . Stronger contrasts between wet and dry composites are apparent in the latitudinal extent and intensity of the rain belt.

Transects were also examined for each individual year and further suggested that the primary contrast between wet and dry years is the extent and intensity of convective activity rather than the location of the convective maximum, or ITCZ. The transects for the driest and wettest years, 1983 and 1988 (Fig. 20), clearly illustrate this contrast.

In 1983, the latitudinal location of maximum convective in July-September is approximately  $9^{\circ}$ - $10^{\circ}\text{N}$  at  $10^{\circ}\text{W}$ ,  $11^{\circ}$ - $12^{\circ}\text{N}$  at  $0^{\circ}$  longitude, and about  $6^{\circ}$ - $7^{\circ}\text{N}$  at  $10^{\circ}\text{E}$ . No systematic differences are apparent

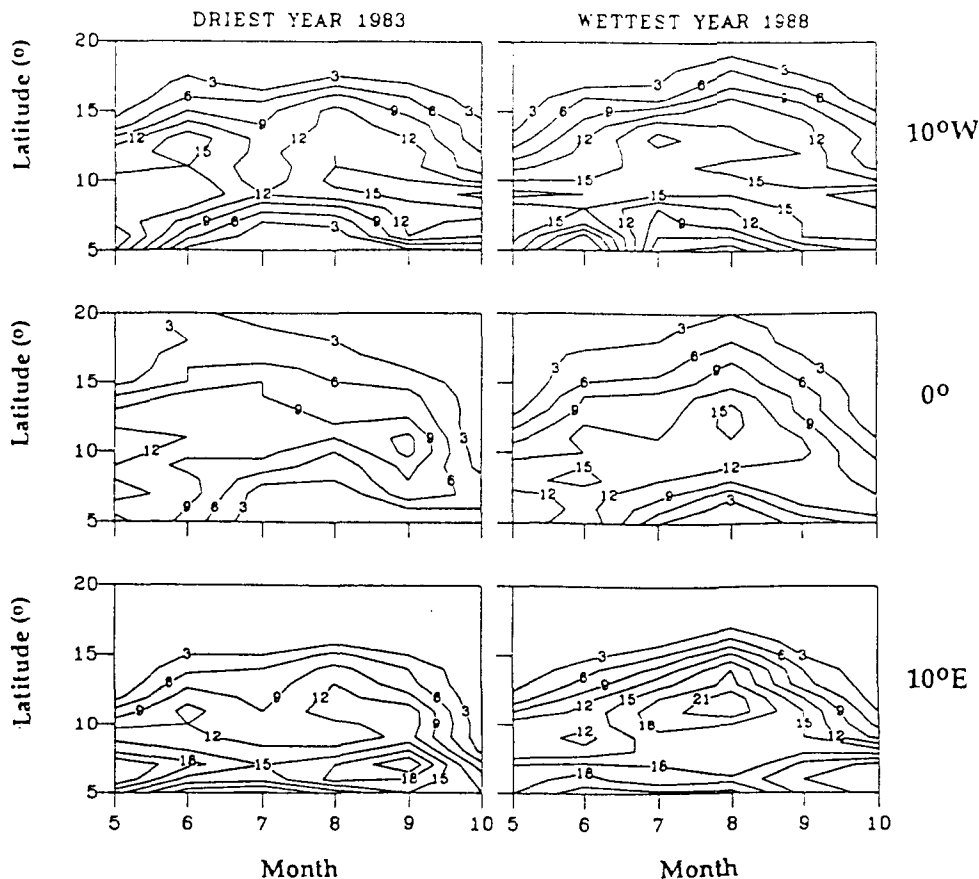


FIG. 20. Latitudinal cross sections of monthly convective intensity for north-south transects in West Africa: (top)  $10^{\circ}\text{W}$ ; (middle)  $0^{\circ}$ ; (bottom)  $10^{\circ}\text{E}$ . On the left-hand side is the driest year, 1983, composite; on the right-hand side is the wettest year, 1988, composite.

between 1983 and the wet years 1985 and 1986 (not shown here); however, the contrast with 1988 is striking. The convective maximum is clearly displaced northward in 1988 at  $10^{\circ}\text{W}$  and  $10^{\circ}\text{E}$  but not in the central Sahel at  $0^{\circ}$  longitude. Nevertheless, in all three cases, the contrast between 1983 and 1988 is more readily apparent in the intensity of convection. At  $10^{\circ}\text{W}$ , the core region of convection has index values exceeding 15 in 1988, but in 1983 values exceed 15 in a very limited area. At  $0^{\circ}$  longitude, a clearly defined core shows values in excess of 12 in 1988 but in excess of 9 in 1983. At  $10^{\circ}\text{E}$  index values exceeded 15 in a very limited area during July through September 1983, but the index exceeded 15 in most of the region in 1988. The size of the areas bounded by index values of 3 and 6 also clearly shows a broader zone of maximum convection during 1988 than during 1983.

Although the composite maps suggest that the ITCZ is farther north during wet years than during dry years, that difference is largely due to the significant northward displacement in 1988 alone (the wettest year). No systematic difference in the ITCZ location is apparent between the dry years and the remaining wet

years. On the other hand, differences are readily apparent in the intensity and spatial extent of the convective maximum, with the contrast between the wettest year and the driest year being particularly strong. This supports the conclusion of Nicholson (1981) that the ITCZ appears to be displaced northward in some, but not all, wet years in the Sahel, but that no anomalous southward displacement is evident in dry years. Drought in the Sahel is then apparently more clearly linked to reduced convective activity. These conclusions are also consistent with recent findings of Waliser and Gautier (1993), who demonstrate that there is no systematic relationship between the latitude of the ITCZ over West Africa and rainfall in the Sahel.

## 6. Conclusions

When appropriate calibrations are applied, Meteosat thermal infrared radiances combined into appropriate predictor variables can provide a good description of rainfall variability in the Sahelo-Soudanian region. Estimates for the analysis period of 1983–88, using  $F$  and  $\bar{R}$ , show good agreement with conventional data.

More than 80% of the spatial variance in the surface rainfall data is explained by either predictor variable in regions 1 and 2 (between 9° and 30°N). However, south of 9°N (region 3), where the monsoonal flow produces stratiform rain, poor correlations are obtained between estimated and observed rainfall. Thus, the satellite algorithms may not be applicable everywhere in tropical Africa and care must be exercised when attempting to generalize these techniques.

The satellite-derived spatial distribution of seasonal rainfall compares well with that obtained from the surface observations, except in regions where the station network is sparse. This is the case, for example, in the northern Sahel and Sahara, where the 100- and 200-mm isohyets are shifted substantially northward when the satellite estimates are computed at points corresponding to the station network. In this region, a sparse station network can produce errors of up to 50% in the rainfall estimates.

The satellite estimates of the interannual variability of rainfall are quite accurate using either predictor variable. In the western Sahelo-Soudanian region, satellite estimates showed 1983 and 1984 to be the driest years and 1988 to be the wettest, in agreement with observed rainfall. In the eastern Sahelo-Soudan, satellite estimates and the surface network data showed that 1984 and 1987 were the driest years and 1988 was the wettest.

This study further demonstrates significant interannual variability in the intensity of the convection associated with the ITCZ and in the latitudinal extent of the rain belt. The primary contrast between wet and dry years appears to be the intensity and extent of the convective activity rather than the location of the convective maximum. No systematic difference in ITCZ location is apparent between dry and wet years, except in 1988 (the wettest year) when the ITCZ was significantly displaced northward. This suggests that rainfall variability in the Sahel may be mostly controlled by factors governing the vigor of the convection, such as those determining the number and intensity of squall lines or the efficiency of the water vapor convergence within the region.

**Acknowledgments.** Funding for this work has been provided by the National Aeronautics and Space Administration through Grants NAGS-900, NAGW-1968, NAG-2727 (University of California, San Diego), and NAG5-1587 (The Florida State University) and by the California Space Institute. We wish to thank Dr. G. Dedieu of the Laboratoire d'Etudes et de Recherches en Télédétection Spatiale, Centre National d'Etudes Spatiales, France and Dr. P. Y. Deschamps of the Laboratoire d'Optique Atmosphérique, Université des Sciences et Techniques de Lille, France, for providing Meteosat data. Mr. J. Kim of The Florida State University for programming support, and Mrs. T. Weintraub of the University of California, San

Diego, for editing assistance. The authors are indebted to the reviewers for comments and suggestions that improved the manuscript.

## REFERENCES

- Albignat, J. P., and R. J. Reed, 1980: The origin of African wave disturbances during Phase III of GATE. *Mon. Wea. Rev.*, **108**, 1827-1839.
- Arkin, P. A., 1979: The relationship between fractional coverage of high cloud and rainfall accumulations during GATE over the B scale array. *Mon. Wea. Rev.*, **107**, 1382-1387.
- , and B. N. Meisner, 1987: The relationship between large scale convective rainfall and cold cloud over the western hemisphere during 1982-1984. *Mon. Wea. Rev.*, **115**, 51-74.
- , and P. E. Ardanuy, 1989: Estimating climatic-scale precipitation from space: A review. *J. Climate*, **2**, 1229-1238.
- Aspliden, C. L., Y. Tourre, and J. B. Sabine, 1976: Some climatological aspects of west African disturbance lines during GATE. *Mon. Wea. Rev.*, **104**, 1029-1035.
- Assad, E. D., B. Seguin, Y. Kerr, J. P. Frélaud, and J. P. Lagouarde, 1987: The possible applications of METEOSAT for monitoring the rain season in the Sahel zone: The case of Senegal. *Adv. Space Res.*, **7**, 67-71.
- Augustine, J. A., C. G. Griffith, and W. L. Woodley, 1981: Insights into errors of SMS-inferred GATE convective rainfall. *J. Appl. Meteor.*, **20**, 509-520.
- Ba, M. B., 1990: Estimation des précipitations au Sahel par imagerie satellitaire (in French). Ph.D. thesis, No. 571, Université Paul Sabatier, Toulouse, France, 185 pp.
- , and P. Y. Deschamps, 1990: Détermination des précipitations en régions soudano-sahélienne à l'aide de l'imagerie satellitaire: Tests de divers algorithmes (in French). *Annal. Geophys.*, **8**, 609-626.
- Barrett, E. C., 1970: The estimation of monthly rainfall from satellite data. *Mon. Wea. Rev.*, **98**, 322-327.
- , and D. W. Marin, 1981: *The Use of Satellite Data in Rainfall Monitoring*. Academic Press, 340 pp.
- , G. D'Souza, and C. H. Power, 1986: Bristol techniques for the use of satellite data in raincloud and rainfall monitoring. *J. Br. Interplanet. Soc.*, **39**, 517-526.
- Bhatt, U. S., 1989: Circulation regimes of rainfall anomalies in the African-South Asian monsoon belt. *J. Climate*, **2**, 1133-1144.
- Bryson, R. A., 1973: Drought in Sahelia: Who or what is to blame? *Ecologist*, **3**, 366-371.
- Bunting, A. H., M. D. Dennett, J. Elston, and J. R. Milford, 1976: Rainfall trends in the West African Sahel. *Quart. J. Roy. Meteor. Soc.*, **102**, 59-64.
- Burpee, R. W., 1972: The origin and structure of easterly waves in the lower troposphere of North Africa. *J. Atmos. Sci.*, **29**, 77-90.
- Cadet, D. L., and N. O. Nnoli, 1987: Water vapor transport over Africa and the Atlantic Ocean during summer 1979. *Quart. J. Roy. Meteor. Soc.*, **113**, 581-602.
- , and B. Guillot, 1991: Estimation des précipitations par satellite (in French). ORSTOM, French Ministry of Cooperation, 64 pp. [Available from Centre de Météorologie Spatiale, B.P. 147, 22302 Lannion, France.]
- Carn, M., J. P. Lahuec, D. Dagorne, and B. Guillot, 1989: Rainfall estimation using TIR METEOSAT imagery over the western Sahel (1986-1987). *Fourth Conf. on Satellite Meteorology and Oceanography*, San Diego, CA, Amer. Meteor. Soc., 126-129.
- Charney, J. G., 1975: Dynamics of deserts and droughts in the Sahel. *Quart. J. Roy. Meteor. Soc.*, **101**, 193-202.
- , W. J. Quirk, S. H. Chow, and J. Kornfield, 1977: A comparative study of the effects of albedo change on drought in semiarid regions. *J. Atmos. Sci.*, **34**, 1366-1385.
- de Felice, P., A. Viltard, and M. Camara, 1982: Vapeur d'eau dans la troposphère en Afrique de l'Ouest (in French). *La météorologie*, **6**, 129-134.

- Dugdale, G. V. D., McDougall, and J. R. Milford, 1990: Potential and limitation of rainfall estimates for Africa derived from cloud statistics. *Length Meteosat Scientific Users Meeting*, Norrköping, Sweden, Eumestat, EUM POB, 211-220.
- ESOC, 1986: METEOSAT contribution to ISCCP. ESA-ESOC Publ. 12, 93 pp. [Available from METEOSAT Exploitation Project Office, European Space Operations Centre, Robert-Bosch-Strasse 5, 6100 Darmstadt, Germany.]
- Flohn, H., 1964: Investigations on the tropical easterly jet. *Bonn Meteor. Abhandl.*, 26, 83 pp.
- Folland, C. K., T. N. Palmer, and D. E. Parker, 1986: Sahel rainfall and worldwide sea temperatures, 1901-1985. *Nature*, 320, 602-607.
- Fontaine, B., and S. Janicot, 1992: Wind-field coherence and its variations over West Africa. *J. Climate*, 5, 512-524.
- Germain, H., 1968: Météorologie dynamique et climatologie: application au régime des pluies au Sénégal (in French). ASECNA, Dakar, Senegal, 15 pp.
- Griffith, C. G., W. L. Woodley, P. G. Gruber, D. W. Martin, J. Stout, and D. N. Sikdar, 1978: Rain estimation from geosynchronous satellite imagery—Visible and infrared studies. *Mon. Wea. Rev.*, 106, 1153-1171.
- , J. A. Augustine, and W. L. Woodley, 1981: Satellite rain estimation in the U.S. High Plains. *J. Appl. Meteor.*, 20, 53-66.
- Hastenrath, S., 1984: Interannual variability and cycle: Mechanisms of circulation and climate in the tropical Atlantic sector. *Mon. Wea. Rev.*, 112, 1097-1107.
- Houze, R. A., Jr., and A. K. Betts, 1981: Convection in GATE. *Rev. Geophys. Space Phys.*, 19, 541-576.
- Janicot, S., 1992a: Spatiotemporal variability of West Africa rainfall. Part I: Regionalizations and typings. *J. Climate*, 5, 489-497.
- , 1992b: Spatiotemporal variability of West Africa rainfall. Part II: Associated surface and air mass characteristics. *J. Climate*, 5, 498-511.
- Janowiak, J. E., and P. A. Arkin, 1990: Rainfall variations in the tropics during 1986-1989 as estimated from observations of cloud top temperatures. *J. Geophys. Res.*, 96, 3359-3373.
- Joussauze, S., R. Sadourny, and C. Vignal, 1986: Origin of precipitating water in a numerical simulation of the July climate. *Ocean-Air Interactions*, 1, 43-56.
- Kanamitsu, M., and T. N. Krishnamurti, 1978: Northern summer tropical circulations during drought and normal rainfall months. *Mon. Wea. Rev.*, 106, 331-347.
- Kidson, J. W., 1977: African rainfall and its relation to the upper air circulation. *Quart. J. Roy. Meteor. Soc.*, 103, 441-456.
- Kilonsky, B. J., and C. S. Ramage, 1976: A technique for estimating tropical open-ocean rainfall from satellite observations. *J. Appl. Meteor.*, 15, 972-975.
- Kraus, E. B., 1977: Subtropical drought and cross equatorial energy transports. The seasonal excursion of the ITCZ. *Mon. Wea. Rev.*, 105, 1009-1018.
- Lamb, P. J., 1978a: Large-scale tropical Atlantic surface circulation patterns associated with sub-Saharan weather anomalies. *Tellus*, 30, 240-251.
- , 1978b: Case studies of tropical Atlantic surface circulation patterns during recent sub-Saharan weather anomalies: 1967 and 1968. *Mon. Wea. Rev.*, 106, 482-491.
- , 1982: Persistence of sub-Saharan drought. *Nature*, 299, 46-47.
- , 1983: West African water vapor variations between recent contrasting sub-Saharan rainy seasons. *Tellus*, 35A, 198-212.
- , and R. A. Peppier, 1992: Further cases studies of tropical Atlantic surface atmospheric and oceanic patterns associated with sub-Saharan drought. *J. Climate*, 5, 476-488.
- Lare, A. R., and S. E. Nicholson, 1994: Contrasting conditions of surface water balance in wet years and dry years as a possible land surface-atmosphere feedback mechanism in the West African Sahel. *J. Climate*, 7, 653-668.
- Lough, J. M., 1986: Tropical Atlantic sea-surface temperatures and rainfall variation in sub-Saharan Africa. *Mon. Wea. Rev.*, 114, 561-570.
- Martin, D. W., and A. J. Schreiner, 1981: Characteristics of West African and east Atlantic cloud clusters: A survey from GATE. *Mon. Wea. Rev.*, 109, 1671-1688.
- Mottell, C. E., and B. C. Weare, 1987: Estimating tropical rainfall using digital satellite data. *J. Climate Appl. Meteor.*, 26, 1436-1446.
- Newell, R. E., and J. E. Kidson, 1979: The tropospheric circulation over Africa and its relation to the global tropospheric circulation. *Saharan Dust, ISCU SCOPE 14*, C. Morales, Ed., Wiley and Sons, 133-169.
- , and —, 1984: African mean wind changes between Sahelian wet and dry periods. *Int. J. Climatol.*, 4, 27-33.
- Nicholson, S. E., 1980: The nature of rainfall fluctuations in sub-tropical West Africa. *Mon. Wea. Rev.*, 108, 473-487.
- , 1981: Rainfall and atmospheric circulation during drought periods and wetter years in West Africa. *Mon. Wea. Rev.*, 109, 2191-2208.
- , 1983: Sub-Saharan rainfall in the years 1976-80: Evidence of continued drought. *Mon. Wea. Rev.*, 111, 1646-1654.
- , 1988: Land surface-atmosphere interaction: Physical processes and surface changes and their impact. *Prog. Phys. Geogr.*, 12, 36-65.
- , 1989: African drought: Characteristics, causal theories and global teleconnections. *Understanding Climate Change*, A. Berger, R. E. Dickinson, and J. W. Kidson, Eds., Amer. Geophys. Union, 79-100.
- , 1993: An overview of African rainfall fluctuations of the last decade. *J. Climate*, 6, 1463-1466.
- , and I. M. Palao, 1993: A re-evaluation of rainfall variability in the Sahel. Part I. Characteristics of rainfall fluctuations. *Int. J. Climatol.*, 13, 371-389.
- Norquist, D. C., E. E. Recker, and R. J. Reed, 1977: The energetics of African wave disturbances as observed during Phase III of GATE. *Mon. Wea. Rev.*, 105, 334-342.
- Otomosh, J. B., 1985: The separate contributions of line squalls, thunderstorms, and the monsoon to the total rainfall in Nigeria. *Int. J. Climatol.*, 5, 543-552.
- Palmer, T. N., 1986: The influence of the Atlantic, Pacific, and Indian Oceans on Sahel rainfall. *Nature*, 322, 251-253.
- Pierce, R. P., and V. C. Mohanty, 1984: Onsets of the Asian summer monsoon 1979-82. *J. Atmos. Sci.*, 41, 1620-1639.
- Richards, F., and P. Arkin, 1981: On the relationship between satellite-observed cloud cover and precipitation. *Mon. Wea. Rev.*, 109, 1081-1093.
- Ropelewski, C. F., and M. S. Halpern, 1987: Global and regional scale precipitation and temperature patterns associated with El Niño/Southern Oscillation. *Mon. Wea. Rev.*, 115, 1606-1626.
- Rossow, W. B., E. Kinsella, A. Wolf, and L. Garder, 1985: International Satellite Cloud Climatology Project (ISCCP): Description of reduced resolution radiance data. World Climate Research Programme.
- Schiffer, R. A., and W. B. Rossow, 1983: The International Satellite Cloud Climatology Project (ISCCP): The first project of the World Climate Research Programme. *Bull. Amer. Meteor. Soc.*, 64, 779-784.
- Semazzi, F. H. M., V. Mehta, V. C. Sud, 1988: An investigation of the relationship between sub-Saharan rainfall and global sea surface temperature. *Atmos.-Ocean*, 26, 118-138.
- Shinoda, M., 1990a: Long-term variability of the tropical African rainbelt and its relation to rainfall in the Sahel and northern Kalahari. *J. Meteor. Soc. Japan*, 68, 19-35.
- , 1990b: Long-term Sahelian drought from the late 1960s to the mid-1980s and its relation to the atmospheric circulation. *J. Meteor. Soc. Japan*, 68, 613-624.
- Shukla, J., and Y. Mintz, 1982: Influence of land-surface evapotranspiration on the earth's climate. *Science*, 215, 1498-1501.
- Stout, J. E., D. W. Martin, and D. N. Sikdar, 1979: Estimating GATE rainfall with geosynchronous satellite images. *Mon. Wea. Rev.*, 107, 585-598.
- Tanaka, M., B. C. Weare, A. R. Navato, and R. E. Newell, 1975: Recent African rainfall patterns. *Nature*, 255, 201-203.

- Thieulin, V., and T. Lebel, 1991: EPSAT-NIGER: Study of rainfall over the Sahel at small time steps using a dense network of recording raingauges. *Hydrol. Process.*, **5**, 251-260.
- Thiao, W., D. L. Cadet, and M. Desbois, 1990: A note on estimation of rainfall due to squall lines over West Africa using METEOSAT imagery. *Meteor. Atmos. Phys.*, **42**, 69-76.
- Thompson, R. M., Jr., S. W. Payne, E. E. Recker, and R. J. Reed, 1979: Structure and properties of synoptic-scale wave disturbances in the intertropical convergence zone of the eastern Atlantic. *J. Atmos. Sci.*, **36**, 53-72.
- Toledo Machado, L. A., M. Desbois, and J. P. Duvel, 1992: Structural characteristics of deep convective systems over tropical Africa and the Atlantic Ocean. *Mon. Wea. Rev.*, **120**, 392-406.
- Waliser, D. E., and C. Gautier, 1993: A satellite-derived climatology of the ITCZ. *J. Climate*, **6**, 2162-2174.
- Ward, M. N., 1992: Provisionally corrected surface wind data, worldwide ocean-atmosphere surface fields, and Sahelian rainfall variability. *J. Climate*, **5**, 454-475.
- Wolter, K., 1989: Modes of tropical circulation, Southern Oscillation, and Sahel rainfall anomalies. *J. Climate*, **2**, 149-172.
- Woodley, W. L., C. G. Griffith, J. S. Griffin, S. C. Stromatt, 1980: The influence of GATE convective rainfall from SMS-1 imagery. *J. Appl. Meteor.*, **19**, 388-408.

## **Appendix E**

### **Reduction of bidirectional effects in NOAA/AVHRR data acquired during the HAPEX-SAHEL Experiment**

# Reduction of bidirectional effects in NOAA/AVHRR data acquired during the HAPEX-SAHEL Experiment

M.B. Ba<sup>1</sup>, G. Dedieu<sup>2</sup>, Y.H. Kerr<sup>2</sup>, S.E. Nicholson<sup>1</sup> and J. Lecocq<sup>3</sup>

<sup>1</sup>Department of Meteorology, The Florida State University, Tallahassee, FL 32306-3034 USA

<sup>2</sup> LERTS, Unité mixte CNES-CNRS, 18, avenue Edouard Belin, 31055 Toulouse Cedex, France

<sup>3</sup> Antenne ORSTOM au LTHE, BP 53, 38041 Grenoble Cedex 9

## Abstract

The study presents a model of Top Of the Atmosphere (TOA) and surface reflectances in the visible and near-infrared. The reflectance is parameterized as the product of an isotropic component (constant) of the reflection by normalized temporal and bidirectional functions. The bidirectional function uses a simple physical representation of viewing geometry. The temporal function is represented as a development in modified Fourier series. An iterative scheme is used to adjust the constants of the model. The analysis is applied to three individual locations consisting of 15 x 15 NOAA/AVHRR pixels acquired in 1992 during the HAPEX-SAHEL experiment (Niger). Clouds were screened using a threshold standard deviation of reflectance (visible) and mean brightness temperature (thermal channel 4). The study allowed the highest frequency fluctuations in the dataset to be reduced substantially (about 85% of the variance is explained) and enabled the temporal variation of the land surface cover to be detected. Comparisons between results obtained with TOA and atmospherically corrected surface reflectances show that there is a need to improve the monitoring of aerosols, however, the angular

effects were the largest contributors to high frequency fluctuations in the NOAA/AVHRR data.



## 1. Introduction

The increasing concern about climate change on a regional and global scale requires land surface characteristics, such as surface albedo and vegetation cover variables, be measured on a regular basis since these play a key role in the energy and water balances of the surface. At present, the Advanced Very High Resolution Radiometer (AVHRR) onboard the NOAA meteorological satellites acquire data in visible and near-infrared wavelengths on a daily basis, allowing one to monitor vegetation cover over the entire globe (e.g. Tarpley et al., 1984; Justice et al., 1985).

Long-term monitoring of land surface characteristics requires temporal stability of the satellite sensors and correction of angular and atmospheric effects. Angular effects have been studied for selected vegetation canopies (e.g. Kriebel, 1978; Kimes, 1983; Gutman, 1987; Roujean and Leroy, 1991). The magnitude of these effects may lead to large errors, especially when observing the vegetation phenological evolution on a regional scale (Gutman, 1987; Roujean and Leroy, 1991). To reduce the short-term fluctuations in the time series of visible and near-infrared reflectances, and thus, to calculate the Normalized Difference Vegetation Index (NDVI), measurements should be corrected from atmospheric and angular effects. One problem with the type of algorithms used to make these corrections is the uncertainty in the atmospheric data, which may be large (Roujean et al. 1992a; Soufflet et al., 1991). Another problem is the number and type of observations required to determine the surface Bidirectional Reflectance Distribution Function (BRDF). The number of observations must at least equal the number of parameters (generally 3 or more), and observations should not be too distant in time for the surface to be considered invariant (Roujean et al., 1992b). Since the surface BRDF is not known, one cannot readily account for surface anisotropy in the atmospheric correction scheme.

A common technique to minimize cloud contamination, angular and atmospheric effects calculates the maximum value of a vegetation index for a given target over a period of one week to 10-days. The maximum value is assumed to correspond to a minimum in aerosol and water vapor contents and cloud cover (Holben, 1986). However, this Maximum Value Composite (MVC) technique selects preferentially observations in the forward scattering direction (Gutman, 1991, Leroy, 1994). Because of random cloud contamination, this forward scattering direction is not always selected in data time series, leading to high directional noise in NDVI time profiles and moreover in corresponding reflectances (Qi and Kerr, 1994). Other proposed techniques for compositing AVHRR NDVI data have similar drawbacks (Qi and Kerr, 1994).

Most of studies on the BRDF have been carried out over uniform cover types at the plot scale (Deering et al., 1992; Holben, 1986; Kimes, 1983). There has been little attempt to translate the results from ground measurements to satellite measurements. Owing to the lack of a calibrated and physically based-model, this study used a simple empirical model as the product of an isotropic component (constant) of reflectance and normalized temporal and bidirectional functions. The BRDF used cannot fully represent any bidirectional effect for all geometries, it is simple and well-adapted to the range of solar and viewing angles corresponding to the NOAA/AVHRR data acquisition. The modeling assumed that angular and temporal effects on reflectances can be separated. If most of the variance can be explained by the model, then the temporal function will be indicative of phenological changes in surface vegetation. This model has already been tested using NOAA/AVHRR data acquired during the FIFE experiment (1987) over the Konza prairie (United States) (Ba et al., 1994). Here, the model is applied to three different locations selected inside the HAPEX-SAHEL site where AVHRR data were acquired from May to October 1992. Since the BRDF model used here is the same as

that applied to the FIFE site, a comparison will be made between the model parameters obtained at these two locations. These comparisons will help us to discuss the robustness of the model under varying conditions and to anticipate its validity. In this study, we used both TOA and atmospherically corrected reflectances. Model performance with each of these two data sets is discussed.

## 2. AVHRR data

From May to October 1992, the HAPEX-SAHEL Information System (HSIS) processed and archived 5 bands of AVHRR HRPT (NOAA 11 and 12) image data (Kerr et al., 1993) obtained through the AGRO-HYdro-METéorologique (AGRHYMET) center receiving station in Niger. The HAPEX images consist of 512 rows of 512 samples covering the area between 0° and 5°E and 11° and 16°N, which includes the HAPEX-SAHEL site (2-3°E, 13- 14°N).

HSIS calculated several variables from the satellite radiances: brightness temperature for channels 4 and 5, TOA-reflectance for channels 1 and 2, TOA-Normalized Difference of Vegetation Index (NDVI) and TOA- Modified Soil Adjusted Vegetation Index (MSAVI) obtained from channels 1 and 2, (Qi et al., 1994, Chehbouni et al., 1994), atmospherically corrected reflectances for channels 1 and 2 (surface reflectances), surface NDVI and MSAVI, surface temperature based on the improved Split Window algorithm (Kerr et al. 1992), and the zenith and azimuth angles for both the sun and the sensor.

To obtain the ground level reflectances, HSIS performed atmospheric corrections (Kerr et al., 1993) on channels 1 and 2 using the Simplified Method for the Atmospheric Corrections (SMAC) (Rahman and Dedieu, 1994), which is based on the 5S radiative transfer code (Tanré et al., 1990). These corrections take into account Rayleigh (molecules) and Mie (aerosols) scattering effects, as well as water vapor, ozone, oxygen and carbon dioxide absorption. Water vapor content was derived from a European Centre for Medium-range Weather Forecasts (ECMWF) model analysis and the ozone content is set to a constant of 0.25 atm.cm. Aerosol optical depths were not available over the whole area and were set to a constant value of 0.2 at 550 nm, which corresponds roughly to the less turbid days in the Sahelian regions (10% of the days) (Faizoun et al., 1994). A typical aerosol model, namely the continental model of the World Meteorological Organization (WMO), is

selected to generate the aerosol phase." Raleigh scattering and oxygen and carbon dioxide absorption are applied assuming a standard pressure at the ground level (1013 hpa).

Intensive measurements of hydro-meteorological parameters variables were made during the HAPEX-SAHEL field measurement campaign in three super-sites (Southern, Central East and Central West sites). For each of the three super-sites, we selected AVHRR sub-images consisting of 15 by 15 pixels centered at 13.2°N, 2.24°E; 13.54°N, 2.69°E; and 13.55°N, 2.57°E, respectively.

### 3. Processing of AVHRR data

#### *3.1 Times series of raw data*

We computed spatial averages and the standard deviation of reflectances (channels 1 and 2) and brightness temperature (channel 4) from all pixels inside the windows of the 15x15 pixels taken from each of the three super-sites. The time series of average reflectance (Figs 1a and 1b) show some high values, but these are not systematically associated with high standard deviations, which may indicate the presence of increasing cloud cover over the sites in some cases. This is confirmed by the brightness temperatures (Fig. 1c), which shows lower values at the same time as high reflectances. Clear sky conditions are characterized by high values of brightness temperatures, about 310 K in early and later summer and about 295 K in the middle of the rainy season (Fig. 1c), owing to the cooling effect of evapotranspiration associated with growing vegetation and rainfall. No seasonal signal can be detected in either channels 1 or 2 (Figs 1a and 1b).

#### *3.2 Cloud screening*

A common technique used to cloud-screen AVHRR data over land consists of an analysis of the local variance in the data (Coakley and Bretherton, 1982; Gutman et al., 1987, 1994; Ba et al., 1994). Over a relatively homogeneous surface, such as the HAPEX-SAHEL site, we expect higher spatial standard deviations of reflectance and brightness temperature in the presence of broken clouds. When clouds cover the entire site, the standard deviations may be as small as those in cloud-free conditions, preventing cloud detection using the standard deviation, but the average brightness temperature may be significantly lower in many cases, as shown in Figure 1c.

Based on these considerations, we examine the relationship between the spatial standard deviation of reflectances and the average brightness temperature in channels 1 and 4, respectively (Fig. 2). Clear sky conditions are characterized by low standard deviations in the visible (less than 0.025) with a brightness temperature larger than 285 K. A low standard deviation of reflectance and low brightness temperature indicates a uniform cover of cold clouds over the sites. Warm temperatures with a large standard deviation indicate broken cloud cover. We assumed thresholds of 0.025 and 295 K for the standard deviation and brightness temperature, respectively, provided the best cloud screening. From the original set of 534 data points (178 images  $\times$  3 sites), 371 were classified as cloud-contaminated for the three sites taken together. However, we did not expect that the cloud screening procedure would eliminate aerosol contaminated images, since aerosols induce a decrease in the scene contrast and a low variance with only a slight decrease of brightness temperature on the order of 1K for an increase of 0.2 (at 550 nm) of the optical depth (Tanré and Legrand, 1991).

After cloud screening, TOA reflectances still exhibited high frequency fluctuations (Fig. 3), but were substantially reduced when the reflectances in channels 1 and 2 ( $R_1$  and  $R_2$ ), were combined into the NDVI (Fig. 4a-c). The NDVI

time series suggests the seasonal cycle of the vegetation . Around Julian days 210 to 225, there was no data left after cloud screening. Figures 4d-f indicate that most of rain occurred during this period of time (see Lebel et al., 1992, for detailed description of the measurement network, and Lebel et al., this issue, for rainfall data analysis).

#### 4. Fitting reflectance profiles with temporal and bidirectional functions

Figures 5 displays the cloud screened data , as a function of the viewing angle,  $q_v$  . The values of  $q_v$  change rapidly from one day to the next because of the wide field-of-view of the sensor and the 9-day repeat cycle of the satellite; these range between  $-66^\circ$  and  $66^\circ$ . The negative and positive values correspond to antispecular (backward) and specular (forward) reflection/scattering conditions, respectively. For both TOA and surface reflectances, the plots show a strong dependence of the observed reflectances on the viewing angle. For channels 1 and 2, 60% and 66%, respectively, of the variance of TOA reflectance is explained by a second order polynomial in  $q_v$ , indicating that directional effects linked to the anisotropy of the earth-atmosphere system are a major contributor to the variability of the TOA reflectances. This simple model, however, explained only 30% of the variance of surface visible reflectance. For the surface near-infrared reflectance, on the other hand, 71% of the variance was explained, instead of 66% for TOA reflectances. Also the angular dependency of surface near-infrared reflectances was higher than for TOA data.

These results might be explained by a larger impact of aerosol optical depth on the visible rather than on the near-infrared measurements (Tanré et al., 1992) and the use of a constant optical depth for atmospheric correction. Near-infrared measurements, however, are less sensitive to aerosols, particularly when data with

large optical depths have been removed, but are still sensitive to atmospheric water vapor which has only been accounted for by ECMWF weather forecast model analysis predictions. The plots presented in figure 5 suggest that atmospheric effects tend to smooth the angular dependency of TOA reflectances, at least in the NIR channel.

Leaving aside the problems of sensor degradation, which are assumed to be taken care of in the pre-processing stage (Kaufman and Holben 1993, Kerr et al. 1993), we modeled the observed reflectance,  $R_i(t)$ , in channel  $i$  ( $i=1$  for VIS and  $i=2$  for NIR) over a given period as:

$$R_i(t) = R_{0i}F(t)G_i(q_s, q_v, f) \quad (1)$$

where  $R_0$  is the isotropic component of the reflection,  $F(t)$  describes the temporal evolution of  $R_0$ , and  $G$  is a function of the viewing geometry, namely the solar zenith angle,  $q_s$ , the viewing angle,  $q_v$ , and the relative azimuth,  $f = f_s - f_v$ , all of these angles varying with the time of the observation.

In the above equation, the  $F(t)$  function accounts for the evolution of  $R_{0i}$  driven by changes in surface properties such as vegetation growth and senescence. Fluctuations of bidirectional reflectances,  $R_i(t)$ , resulting in varying illumination and viewing conditions are accounted for by the bidirectional function  $G$  which is assumed to be constant throughout the study period. The underlying assumptions are that the bidirectional reflectance model changes at a slower rate than the amplitude of the reflectance.  $R_0F(t)$  should allow us to accurately monitor the temporal evolution of surface reflectance and infer information about surface



properties, e. g. vegetation phenology and soil albedo changes with water content. More details on the model can be found in Ba et al., 1994.

We assumed that the temporal variation of reflectances  $F(t)$  (i.e., phenological changes in the surface vegetation) over a season can be described as a Fourier series (e.g., see Sellers et al., 1994). The underlying assumption is that the vegetation response to environmental conditions (e. g., rainfall, drought, etc.) ranges every few days. The function  $F(t)$  reads:

$$F(t) = 1 + \sum_{n=1}^N \{a_n[\cos nwt - a_n'] + b_n[\sin nwt - b_n']\} \quad (2)$$

where  $w = 2\pi/184$  when  $t$  is the day (day 1 = May 1 and day 184 = October 31), and  $N$  the number of harmonics. As in Ba et al. (1994), we limit the number of harmonics to  $N = 5$  to include a sufficient number of harmonics to describe seasonal reflectance changes associated with vegetation changes. The constant  $a_n'$  and  $b_n'$  are introduced to normalize to the unity of the average  $F(t)$  over the study period. If  $P$  denotes the number of observations, and subscript  $j$  the observation at time  $t_j$ , we have:

$$a_n' = \frac{1}{P} \sum_{j=1}^P \cos nwt_j ; b_n' = \frac{1}{P} \sum_{j=1}^P \sin nwt_j \quad (3)$$

The bidirectional model is a combination of two angular functions  $f_1(q_s, q_v, f)$  and  $f_2(q_s, q_v, f)$ , and is given by:

$$G(q_s, q_v, f) = 1 + g_1[f_1(q_s, q_v) - f_1'] + g_2[f_2(q_s, q_v, f) - f_2'] \quad (4)$$

where  $f_1'$  and  $f_2'$ , like  $a_n'$  and  $b_n'$  of the temporal model, are constants which have to be empirically determined from the data. The right-hand side of Equation 4 is the sum of three terms that account for specific directional behaviors, namely isotropic, azimuthally-independent, and azimuthally-dependent, yet symmetric. A number of functions may be candidates to represent the functions  $f_1'$  and  $f_2'$ . As in the study conducted by Ba et al. (1994), using AVHRR data acquired in 1987 over the Konza Prairie during FIFE, the best results here were also obtained by the combination of functions given by:

$$f_1 = \frac{1}{\cos q_s + \cos q_v} \quad (5)$$

$$f_2 = \sin q_s \sin q_v \cos f \quad (6)$$

The function  $f_1$  in Equation 5 represents the angular effects associated with any isotropic volume scattering by a thin layer, such as a layer of vegetation or the atmosphere. It also represents the angular effects of attenuation/transmission through an absorbing medium. The function in Equation 6 accounts for asymmetric effects (the term  $f$ ) which increase with solar and viewing angles (the term  $\sin q_s \sin q_v$ ). This describes most of the anisotropic effects resulting from the roughness of bare soil and from the structure and inclination of leaves within the vegetation canopy.

The constants  $f_1'$  and  $f_2'$  are introduced, like  $a_n'$  and  $b_n'$  of the temporal model, to normalize the average  $G$  to unity. These are given by:

$$f_1' = \frac{1}{P} \sum_{j=1}^P f_1(q_s, q_v); f_2' = \frac{1}{P} \sum_{j=1}^P f_2(q_s, q_v, f); \quad (7)$$

where the subscript  $j$  denotes observation  $j$  of the dataset. With the average  $F$  and  $G$  normalized to unity,  $R_0$  in equation 1 represents the average reflectance over the study period.

An iterative scheme is used to determine the twelve parameters of the non-linear reflectance model defined by Equation 1. Since the bidirectional and temporal components of the model,  $F$  and  $G$ , are linear in cosine and sine functions, our approach was to retrieve  $F$  and  $G$  successively using a multivariate linear regression and to iterate until convergence occurs. Figure 6 shows this analysis graphically. The least square multiple linear regression to estimate the bidirectional model was between the observed reflectances,  $R(t)$ , normalized by the previously estimated (last iteration)  $F(t)$ , with  $F(t)$  equal to 1 as a first guess, and the two functions  $f_1$  and  $f_2$ . The results were the coefficients,  $R_0$ ,  $g_1$  and  $g_2$ . Similarly, the least square multiple linear regression to estimate the time model was between the observed reflectances,  $R(t)$ , normalized by the previously estimated  $G$ , and the series  $\cos nwt - a_n$  and  $\sin nwt - b_n$ . These results were the coefficients  $R_0$ ,  $a_n$  and  $b_n$ , for each of the channels. Thus, at each iteration,  $R_0$  is determined twice, but the difference between the two estimates was always negligible owing to the normalization of  $F$  and  $G$  (constants  $f_1$  and  $f_2$ ,  $a_n$  and  $b_n$ ). Convergence was obtained rather rapidly after a few iterations, but ten iterations were used to secure stable results.

## 6. Results

The iterative scheme was applied to each of the datasets for both TOA and surface reflectances. We first present separately the results obtained for TOA and

surface reflectances, then, we discuss the relative performance of the model with these two different data sets.

### 6.1. Results at TOA

For all sites and both channels, the model explained 85-88% of the variance (Table 1, Figs. 7a-7c and 8a-8c). Bidirectional model parameters derived for the three sites (Table 2) were rather stable, with a lower  $g_1$  parameter in the near-infrared band than in the visible. The residual errors after regression were quite small compared to average reflectances, and were only 5 and 4% of  $R_{01}$  and  $R_{02}$  for each of the sites, respectively.

The modeled NDVI, computed from the modeled reflectances, agreed well with the observed NDVI (Figs 9a-9c). An interesting feature was that the correlation was higher between the predicted and observed NDVI than between modelled and predicted reflectances : 90-94% of the NDVI's variance was explained by the model. A possible explanation is that the combination of visible and near-infrared reflectances in NDVI tends to limit the impact of bidirectional behavior which was not accounted for by the bidirectional function  $G$ .

Figures 10a-10c and 11a-11c show  $R_0F(t)$ , i.e. the temporal profiles of the isotropic component of the reflection, for the visible and near-infrared channels, respectively, and figures 12a-12c show the resulting NDVI.

### 6.2. Results with atmospherically corrected reflectances

For all sites, the model explained 79-81% of the variance in the visible, but 86-89% of the near-infrared variance (Table 1, Figures 7d-7f and 8d-8f). Bidirectional model parameters derived for the three sites (Table 2) were rather stable, with

higher values for the  $g_1$  and  $g_2$  parameters in the near-infrared than in the visible band. The residual errors after regression were 6% of  $R_{01}$  for visible reflectances and 4-5% of  $R_{02}$  for near-infrared reflectances.

The modeled NDVI, computed from the modeled reflectances, agreed well with the observed NDVI (Figs. 9d-9f). About 92% of the variance of NDVI was explained by the model. Figures 10d-10f and 11d-11f show  $R_0F(t)$  for the visible and near-infrared channels, respectively, and figures 12d-12f show the resulting NDVI.

### *6.3. Relative performance of the model with TOA and atmospherically corrected reflectances*

Atmospheric corrections only slightly increased (4-7%) visible reflectances (Table 2) since for reflectances of the order of 0.25-0.30 the effect of atmospheric scattering is nearly neutral. In other words, atmospheric reflectance correction (subtraction from TOA reflectance) is compensated by correction of total diffuse transmission. On the contrary, atmospheric corrections led to a large increase (35%) of near-infrared reflectances which can mainly be attributed to the correction of water vapor absorption.

In terms of explained variance and rms errors, the relative performances of the model with TOA and atmospherically corrected near-infrared were very similar. In contrast, in the visible channel, the results were slightly better with TOA than with atmospherically corrected reflectances. As previously mentioned, the main atmospheric effect in the near-infrared channel is water vapor absorption, while aerosols play a major role in the visible (Tanré et al. 1992). The better results obtained with near-infrared than with visible reflectances may have resulted from

more accurate data for water vapor content than aerosol optical depth (see Ouaidrari et al., 1994 for a comparison of ECMWF water vapor data with radiosondings). In addition, the water vapor amount was rather high during the rainy season and absorption quickly saturates. Errors in the water vapor amount have less impact on the surface reflectance estimates than inaccuracies in the assessment of aerosol optical properties (optical depth, phase function and single scattering albedo).

Atmospheric correction also modified the value of the bidirectional function parameters,  $g_1$  and  $g_2$  (table 2). The  $g_1$  parameters became rather similar in the visible and near-infrared channels (approximately 0.7) instead of approximately 0.8 and 0.5 in the TOA visible and near-infrared data, respectively. It is assumed that  $g_1$  accounts for isotropic volume scattering and absorption processes. It probably accounts for the water vapor absorption when fitting near-infrared TOA reflectances and, therefore, increases when this absorption is explicitly corrected. In other words, at large viewing angles, water vapor absorption lowers the TOA reflectances, while directional effects increase them. This compensating and smoothing effect of both processes on TOA reflectances is removed by an atmospheric correction, leading to an increase of the reflectance directionality and of the  $g_1$  parameter at near-infrared wavelengths. The  $g_2$  parameter was rather stable for channel 2, probably because water vapor absorption depends on the optical path but not on the relative azimuth.

In the visible channel, the values of the  $g_1$  and  $g_2$  parameters decreased when fitted with atmospherically corrected data, compared to the TOA measurements. The explanation is complex, since several processes interact and a more comprehensive analysis based on radiative transfer modelling would be needed : i) most of the AVHRR observations fell in the principal plane and in this configuration there is a strong difference of aerosol effects between backward and forward scattering, and, therefore, a strong directionality of TOA reflectances that is partly removed by the approximate correction of aerosol scattering we applied ; ii)

the surface reflectance was roughly 0.3, a value that leads to a slight decrease of TOA reflectance by scattering compared to the surface, this decrease being larger for high viewing angles and therefore partly compensating the increase of surface directional effects. Even though aerosol optical depths are not accurately accounted for, we expect that the applied correction partly removed the directionality due to aerosol scattering and led to a decrease of  $g_1$  and  $g_2$ .

#### *6.4. Comparison of model performances during dry and wet season*

As land surface characteristics change depending on the state of vegetation, particularly during the transition (growth/decay) phases, the bare soil and a fully developed canopy may have a different BRDF. We therefore apply the bidirectional function separately on TOA data collected in May-June (the end of dry season) and during the rainy season (August-September) when the vegetation is expected to be fully developed. For all three sites, 87-90% and 77-88% of the variance was explained by the bidirectional function in the visible and near-infrared, respectively, during the May-June period. During the August-September period, the bidirectional function explained 71-81% and 79-88% of the variance in the visible and near-infrared, respectively. Thus, the BRDF alone explained most of the variance of calculated reflectances under different phenological states of vegetation cover, and it also indicated that angular effects are major contributors to data fluctuations in agreement with a previous study (Ba et al., 1994). The constant,  $g_1$ , was two times greater for August-September than for May-June, but the constant,  $g_2$ , was in the same magnitude for the two periods with a slightly lower value during the rainy season. Although the value of these constants were different for the dry and rainy seasons, the results showed that the bidirectional model may be generally suited under different surface conditions. Determining the temporal function for the dry

and wet seasons would have required dividing the dataset and, thus, separately considering subsets containing too few observations for statistical significance. Still, the performance of the bidirectional model, applied with single constants  $g_1$  and  $g_2$  for the dry and wet season, was good. The values of constant  $g_1$  were more than seven times greater than those of constant  $g_2$ , indicating the predominance of non-azimuthally dependent effects over azimuthally-dependent ones. This is also in agreement with a previous study using the dataset acquired in 1987 over tall grass in the Konza Prairie (United States) during FIFE (Ba et al. 1994).

## 7. Summary and conclusions

Vegetation phenology can be monitored by the NDVI calculated from NOAA/AVHRR data over the entire globe. The composite of maximum NDVI over one week of a given period does not eliminate all cloud contamination, particularly for regions in which clouds are present for several consecutive days. However, in the present study, the normalization incorporated in the NDVI substantially minimized the angular effects in the HAPEX-Sahel data. A simple model was used to separate the temporal and bidirectional effects on NDVI. The temporal function represented the surface cover change over a long period of time. The study showed that most of the variance (79-88% ) was explained by the coupled time and bidirectional models.

The values of constant  $g_1$  found for the Konza Prairie were approximately two times greater than those for the HAPEX-SAHEL and the values of constant  $g_2$  were three times greater. It is to be expected that, the more vegetation there is present, the more these terms will be important and the less the short vegetation (as in the Sahel ), the less important they are. Thus, our results suggest that the two



bidirectional functions are well suited to represent the physical process of scattering and anisotropy of land surface vegetation generally.

The comparison of the results obtained with TOA and atmospherically corrected reflectances suggested that a more comprehensive study is needed to account for the various interacting processes. However, it does confirm that the impact of aerosols is a major issue in the Sahelian region and we have mentioned that our cloud filtering procedure does not eliminate every large aerosol event. A compositing procedure based on the maximum NDVI would probably work better, but the drawback would be to limit the angular sampling needed to fit the directional model. The development of a sunphotometer network (e.g. Lavenu 1993) and the availability of POLDER measurements and products by the end of 1996 (Deschamps et al., 1994) should allow for better correction for aerosols effects.

### **Acknowledgements**

Funding for this work has been provided by the National Aeronautics and Space Administration (NASA) through grants NAG5-1587 and NAGW-3101 to the Florida State University, the "Programme National de Télédétection Spatiale" and the Centre National d'Etudes Spatiales. We wish to thank Mr. J. Kim of the Florida State University for his programming assistance, and Dr. B. Berthelot, Mrs. T. Valéro and S. Wagner of the HAPEX-SAHÉL Information System, at LERTS for their technical support. We are grateful to the anonymous reviewers for comments and suggestions that improve the manuscript.

## REFERENCES

- Ba, M.B., P.Y. Deschamps, and R. Frouin, 1994: Error reduction in NOAA satellite monitoring of the land surface vegetations during FIFE. *J. Geophys. Res.*, in revision.
- Chehbouni, A., Y.H. Kerr, J. Qi, A.R. Huete, and S. Sorooshian, 1994: Towards the development of a multidirectional vegetation index. *Water Resour. Res.*, 30, 1281-1286.
- Coakley, J.A., and F.P. Bretherton, 1982: Cloud cover from high-resolution scanner data: Detecting and allowing for partially filled fields of view. *J. Geophys. Res.*, 87, 4917-4932.
- Deschamps, P.Y., F.M. Bréon, M. Leroy, A. Podaire, A. Bricaud, J.C. Buriez, and G. Sèze, 1994 : The POLDER mission: Instrument characteristics and scientific objectives. *IEEE Trans. Geos. Rem. Sens.*, 32, 598-614.
- Derring, D.W., T.F. Eck, and T. Grier, 1992: Shinnery oak bi-directional reflectance properties and canopy model inversion. *I.E.E.E. Trans. Geosc. Rem. Sens.*, 30, 339-348.
- Faizoun, C.A., A. Podaire, and G. Dedieu, 1994: Monitoring of Sahelian aerosol and atmospheric water vapor content characteristics from sunphotometer measurements. *J. Appl. Met.*, 33, 1291-1303.
- Gutman, G., 1987: The derivation of vegetation indices from AVHRR data. *Int. J. Rem. Sens.*, 8, 1235-1243.
- Gutman, G., D. Tarpley, and G. Ohring, 1987: Cloud-screening for determination of land surface characteristics in a reduced resolution satellite data set. *Int. J. Rem. Sens.*, 8, 859-870.
- Gutman, G., 1991: Vegetation indices from AVHRR: an update and future prospects. *Remote Sens. Environ.*, 35, 121-136.

- Gutman, G.G., A.M. Ignatov, and S. Olson, 1994: Reduction of cloud contamination in AVHRR composite images over land. *Proc. of the Seventh Conference on Satellite Meteorology and Oceanography* (Monterey, CA), Published by the Amer. Met. Soc., 315-318.
- Holben, B.N., 1986: Characteristics of maximum-value composite images from temporal AVHRR data. *Int. J. Rem. Sens.*, 7, 1417-1434.
- Justice, C.O., J.R.G. Townshend, B.N. Holben, and C.J. Tucker, 1985: Analysis of the phenology of global vegetation using meteorological satellite data. *Int. J. Rem. Sens.*, 6, 1271-1318.
- Kaufman, Y.J. and B.N. Holben, 1993: Calibration of the AVHRR visible and near\_IR bands by atmospheric scattering, ocean glint and desert reflection. *Int. J. Remote Sensing*, 14 21-52.
- Kerr, Y. H, J.P. Lagouarde, and J. Imbernon, 1992: Accurate land surface temperature retrieval from AVHRR data with use of an improved Split Window algorithm. *Rem. Sens. Envir.*, 41, 197-209.
- Kerr, Y.H., G. Dedieu, T. Valero, S. Wagner, P. Chibaudel, S. Thawley, L. Cunin, J.C. Berges, A. Chehbouni, F. Cabot, B. Berthelot, R. Dioffo, J.P. Lagouarde, and J. Imbernon, 1993: Level-1 AVHRR data, HAPEX SAHEL Information System. Available at LERTS, Toulouse, France.
- Kimes, D.S., 1983: Dynamics of directional reflectance factor distribution for vegetation canopies. *Applied Optics*, 22, 1364-1372, 1983.
- Kriebel, K.T., 1978: Measured spectral bidirectional reflection properties of four vegetated surfaces. *Applied Optics*, 17, 253-259.
- Lavenu, F., 1993 : PHOTONS programme document (Photométrie pour le Traitement Opérationnel de Normalisation Satellitaire). Technical document, Laboratoire d'Etudes et de Recherches en Télédétection Spatiale, Toulouse, France, 34pp (in french).

- Lebel, T., H. Sauvageot, M. Hoepffner, M. Desbois, B. Guillot, and P. Hubert, 1992: Rainfall estimation in the Sahel: the EPSAT-NIGER experiment. *Hydrol. Sci. J.*, 37, 201-215.
- Lebel, T., J.D. Taupin, and L. Le Barbé, 1996: Space-time fluctuations of rainfall during HAPEX-Sahel. *J. Hydrol.*, this issue.
- Leroy, M., 1994: Compositing reflectances measured from space for vegetation monitoring. *Proc. of the Sixth International Colloquium on Physical Measurements and Signatures in Remote Sensing*, Val d'Isère, France, 21-32. Available from CNES publication Division, Toulouse, France.
- Ouaidrari, H., J., Imbernon, and G. Dedieu, 1994 : Use of a meteorology model to correct atmospheric effects in NOAA-AVHRR data. *Int. J. remote Sensing*, 15, 2257-2271.
- Qi, J., and Y. Kerr, 1994 : On current compositing algorithms. *Proc. of the Sixth International Colloquium on Physical Measurements and Signatures in Remote Sensing*, Val d'Isère, France, 135-142. Available from CNES publication division, Toulouse, France.
- Qi, J., A. Chehbouni, A.R. Huete, Y.H. Kerr, and S. Sorooshian, 1994: A modified soil adjusted vegetation index. *Rem. Sens. Envir.*, 48, 119-126.
- Rahman, H. and G. Dedieu, 1994: A Simplified Method for the Atmospheric Corrections (SMAC) of satellite measurements in the solar spectrum. *Int. J. Rem. Sens.*, 15, 123-143.
- Roujean, J.L. and M. Leroy, 1991: Normalisation des effets bidirectionnels de la reflectance de surface sur une serie de donnees multitemporelle NOAA/AVHRR. *Proc. of the Fifth International Colloquium on Physical Measurements and Signatures in Remote Sensing*, Courchevel, France. Available from ESA publications division, ESTEC, Noorwijk, The Netherlands.

- Roujean, J.L., M. Leroy, A. Podaire, and P.Y. Deschamps, 1992a: Evidence of surface reflectance bidirectional effects from a NOAA/AVHRR multitemporal data set, *Int. J. Rem. Sens.*, 13, 685-698.
- Roujean, J.L., M. Leroy, and P.Y. Deschamps, 1992b: A bidirectional reflectance model of the Earth's surface for the correction of remote sensing data. *J. Geophys. Res.*, 97 (D18), 20455-20468.
- Sellers, P.J., C.J. Tucker, G.J. Collatz, S.O. Los, C.O. Justice, D.A. Dazlich, and D.A. Randall, 1994: A global 1° by 1° NDVI data set for climate studies. Part 2: The generation of global fields of terrestrial biophysical parameters from the NDVI. *Int. J. Rem. Sens.*, 15, 3519-3545.
- Soufflet, V., D. Tanré, A. Begué, A. Podaire, and P.Y. Deschamps, 1991: Atmospheric effects on NOAA/AVHRR data over Sahelian regions, *Int. J. Rem. Sens.*, 12, 1189-1203.
- Tanré, D., C. Deroo, P. Duhaut, M. Herman, J.J. Morcrette, J. Perbos, and P.Y. Deschamps, 1990: Description of computer code to simulate the satellite signal in the solar spectrum: the 5S code. *Int. J. Rem. Sens.*, 11, 659-668.
- Tanré, D., and M. Legrand, 1991 : On the retrieval of Saharan dust optical thickness over land: Two different approaches. *J. Geophys. Res.*, 96, 5221-5227.
- Tanré, D., Holben, B.N., and Y.J. Kaufman, 1992 : Atmospheric correction algorithm for NOAA-AVHRR products: Theory and applications. *IEEE Trans. Geosci. Rem. Sens.*, 30, 2, 231-248.
- Tarpley, J.D., S.R. Schneider, and R.L. Money, 1984: Global vegetation indices from NOAA-7 meteorological satellite. *J. Clim. Appl. Meteor.*, 23, 491-494.

Table 1. Comparison statistics between observed and modeled reflectances.

SOUTHERN SITE				
	VISIBLE (CH1)		NEAR-INFRARED (CH2)	
No. of points	58		58	
	TOA	GROUND	TOA	GROUND
Standard deviations before modelization	0.039	0.041	0.039	0.059
Explained variance (%)	87	79	85	86
RMS ERRORS	0.014	0.019	0.015	0.022
CENTRAL EAST SITE				
	VISIBLE (CH1)		NEAR-INFRARED (CH2)	
No. of points	49		49	
	TOA	GROUND	TOA	GROUND
Standard deviations before modelization	0.040	0.040	0.038	0.059
Explained variance (%)	88	81	88	88
RMS ERRORS	0.014	0.017	0.013	0.020
CENTRAL WEST SITE				
	VISIBLE (CH1)		NEAR-INFRARED (CH2)	
No. of points	55		55	
	TOA	GROUND	TOA	GROUND
Standard deviations before modelization	0.039	0.040	0.038	0.057
Explained variance (%)	87	81	88	89
RMS ERRORS	0.014	0.018	0.013	0.018

Table 2. Bidirectional model parameters

		SOUTHERN		CENTRAL EAST		CENTRAL WEST	
		TOA	GROUND	TOA	GROUND	TOA	GROUND
$R_0$	CH1	0.289	0.311	0.257	0.268	0.267	0.283
	CH2	0.334	0.450	0.312	0.421	0.317	0.427
$g_1$	CH1	0.741	0.667	0.852	0.686	0.847	0.658
	CH2	0.547	0.761	0.506	0.716	0.534	0.740
$g_2$	CH1	0.133	0.075	0.128	0.068	0.109	0.047
	CH2	0.104	0.089	0.124	0.119	0.097	0.088

Table 3: Summary of statistics: Averages (MEAN) and standard deviations (STDV) of reflectances in visible (R1 ) and near-infrared (R2 ) and NDVI computed at three individual sites.

Values before modelization							
		SOUTHERN		CENTRAL EAST		CENTRAL WEST	
		TOA	GROUND	TOA	GROUND	TOA	GROUND
MEAN	R1	0.288	0.310	0.256	0.267	0.266	0.281
	R2	0.334	0.450	0.312	0.421	0.317	0.427
	NDVI	0.075	0.184	0.101	0.223	0.089	0.205
STDV	R1	0.039	0.041	0.040	0.040	0.039	0.040
	R2	0.039	0.059	0.038	0.059	0.038	0.057
	NDVI	0.048	0.057	0.050	0.064	0.053	0.065
Values normalized by bidirectional function							
		SOUTHERN		CENTRAL EAST		CENTRAL WEST	
		TOA	GROUND	TOA	GROUND	TOA	GROUND
MEAN	R1	0.289	0.311	0.257	0.268	0.267	0.283
	R2	0.334	0.450	0.312	0.421	0.317	0.427
	NDVI	0.074	0.185	0.098	0.225	0.087	0.206
STDV	R1	0.028	0.037	0.027	0.038	0.029	0.039
	R2	0.021	0.031	0.017	0.028	0.020	0.029
	NDVI	0.049	0.055	0.053	0.062	0.057	0.062



## Figure Captions

Fig. 1. Time series of NOAA-AVHRR data averaged over windows of  $15 \times 15$  pixels selected from the HAPEX Sahel area (a) TOA-reflectance in visible, (b) TOA-reflectance in near-infrared, and (c) brightness temperature (channel 4). The spatial standard deviation associated with each average value is represented by a vertical bar. Data for all three sites (Southern, Central East and Central West) were considered together.

Fig. 2. Relationship between standard deviation (visible) and average brightness temperatures (channel 4). All three sites (Southern, Central East and Central West) are considered together.

Fig. 3. Time series of NOAA-AVHRR cloud-filtered data averaged over windows of  $15 \times 15$  pixels selected from the HAPEX Sahel area. TOA-reflectance in visible (left side hand) and TOA-reflectance in near-infrared (right side hand). For each average value selected as cloud-free, the standard deviation in visible is small and brightness temperature is high. The top, middle and bottom plots represent Southern, Central East and Central West sites, respectively.

Fig. 4. Time series of NDVI from NOAA-AVHRR (top) and rainfall (bottom). The left, middle, and right plots represent Southern, Central East and Central West sites, respectively. Within each site, we averaged rainfall measurements of about 5 stations.

Fig. 5. Reflectances in the visible (top) and near-infrared (bottom) as a function of viewing angle, all three sites considered together. TOA-reflectances (left) and ground-reflectances as computed from SMAC (right).

Fig. 6. Scheme to iteratively determine the parameters of the reflectance model.

Fig. 7. Observed versus modeled reflectances in the visible. TOA-analysis (left) and ground-analysis (right). The top, middle and bottom plots represent Southern, Central East and Central West sites, respectively.

Fig. 8. Observed versus modeled reflectances in the near-infrared. TOA-analysis (left) and ground-analysis (right). The top, middle and bottom plots represent Southern, Central East and Central West sites, respectively.

Fig. 9. Observed versus modeled NDVI. TOA-analysis (left) and ground-analysis (right). The top, middle and bottom plots represent Southern, Central East and Central West sites, respectively.

Fig. 10. Time series of observed and modeled reflectances in the visible. TOA-analysis (left) and ground-analysis (right). Crosses represent the observations. Dots represent the observations normalized by the bidirectional function. The top, middle and bottom plots represent Southern, Central East and Central West sites, respectively.

Fig. 11. Time series of observed and modeled reflectances in the near-infrared. TOA-analysis (left) and ground-analysis (right). Crosses represent the observations. Dots represent the observations normalized by the bidirectional function. The top, middle and bottom plots represent Southern, Central East and Central West sites, respectively.

Fig. 12. Time series of observed and modeled NDVI. TOA-analysis (left) and ground-analysis (right). Crosses represent the observations. Dots represent the observations normalized by the bidirectional function. The top, middle and bottom plots represent Southern, Central East and Central West sites, respectively.

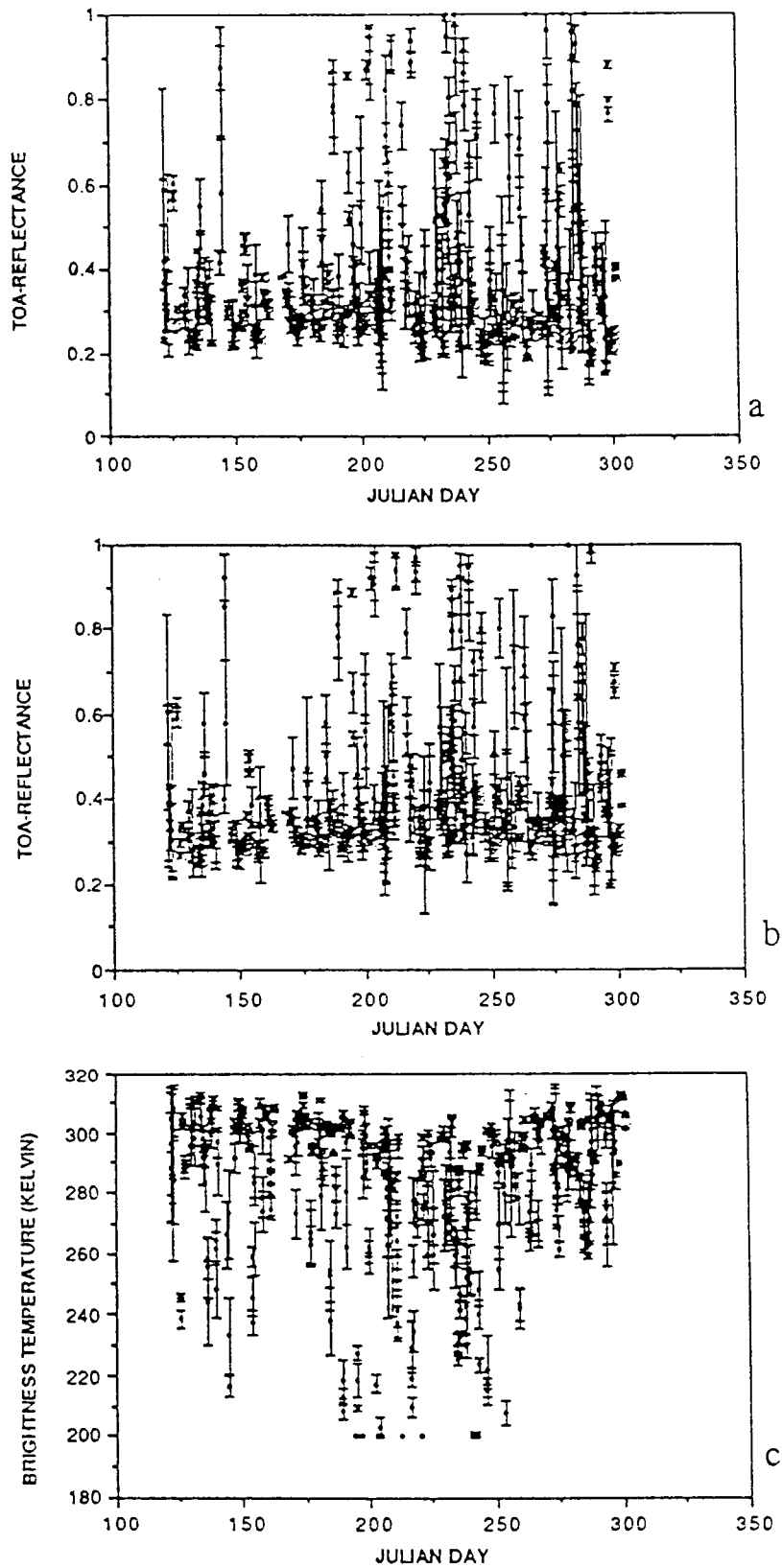


FIGURE 1

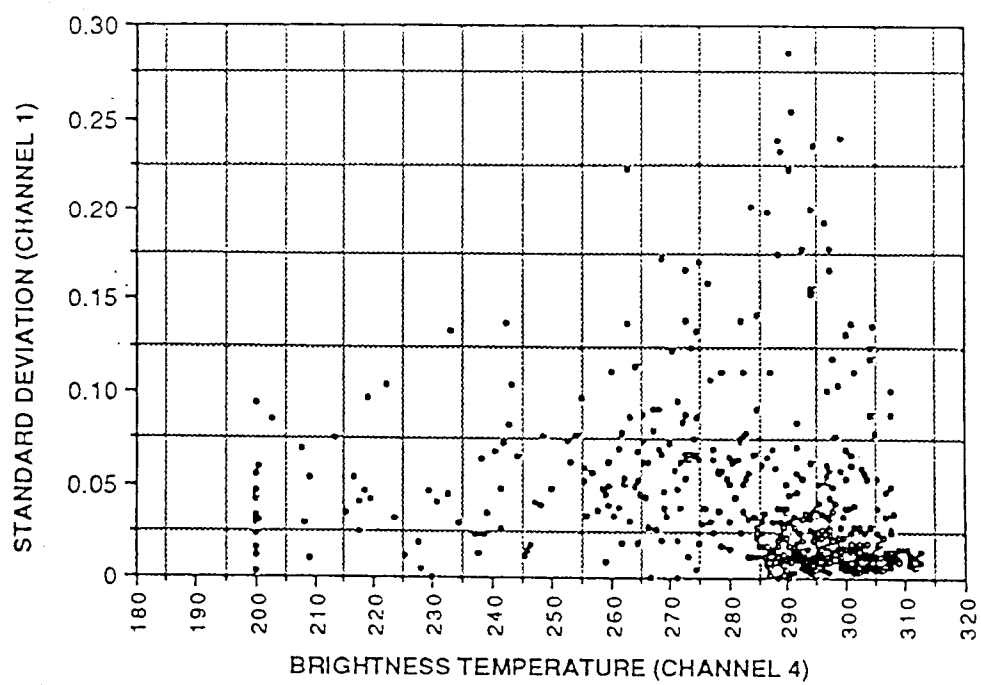


FIGURE 2

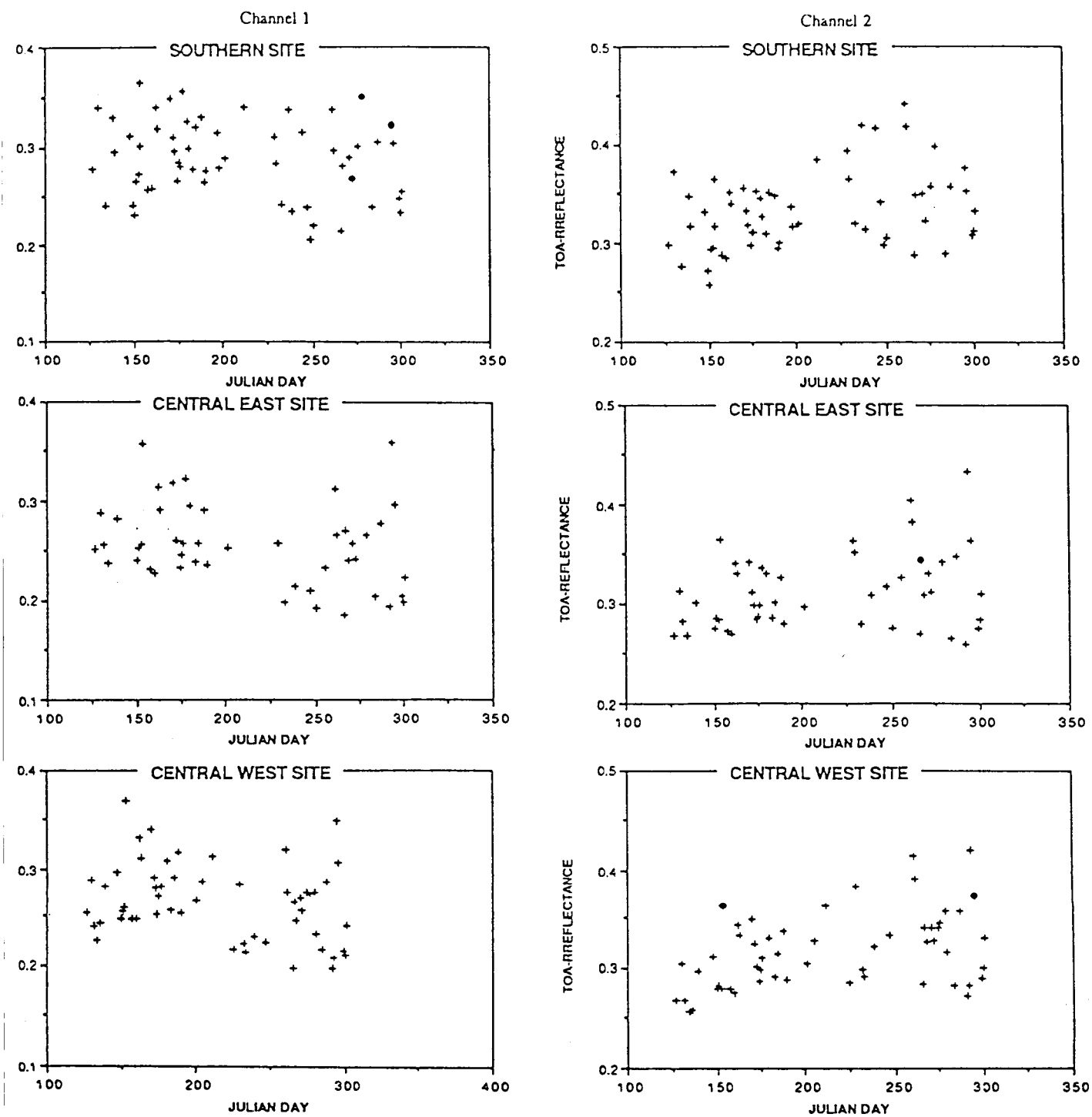


FIGURE 3

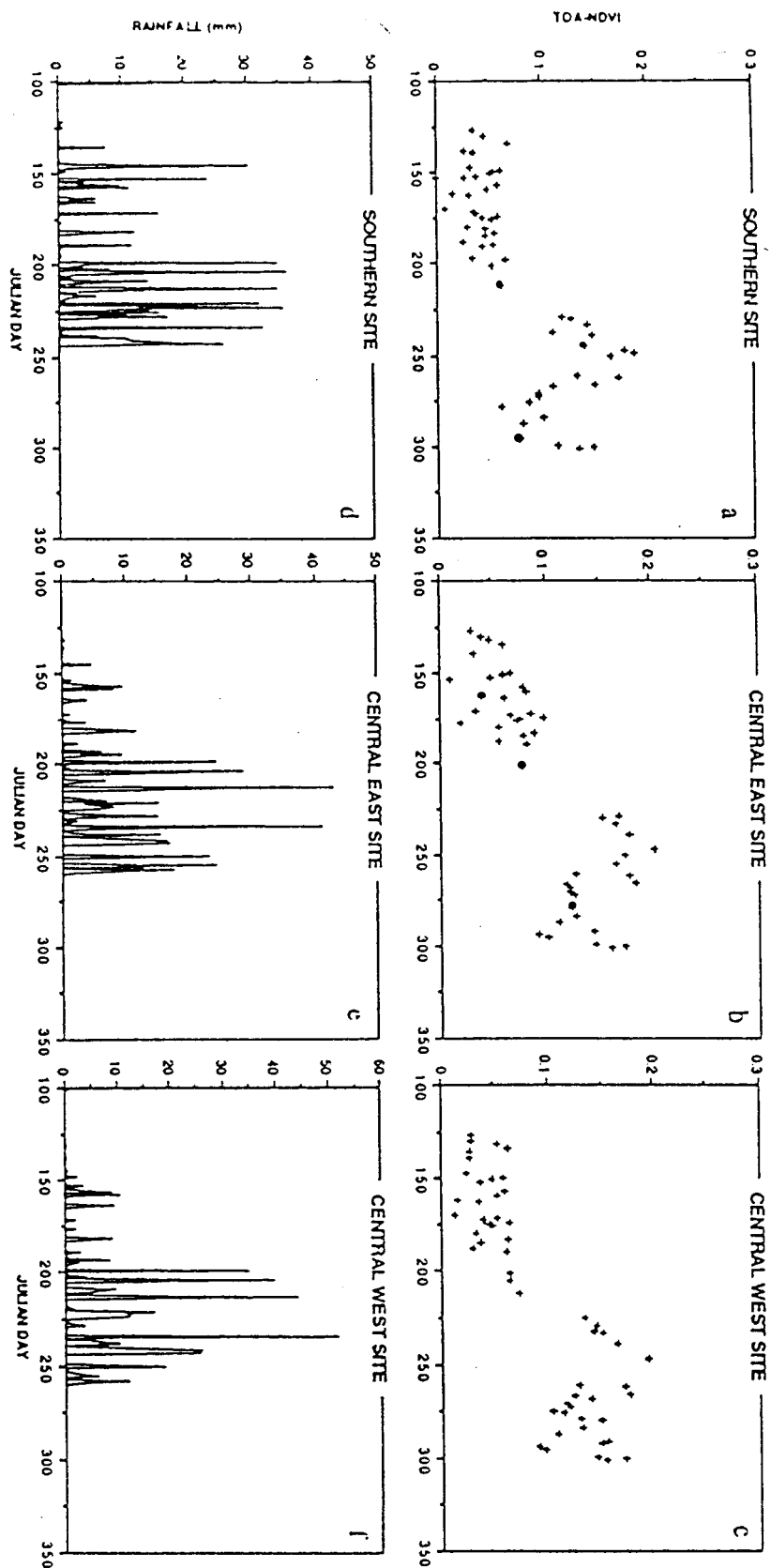


FIGURE 4

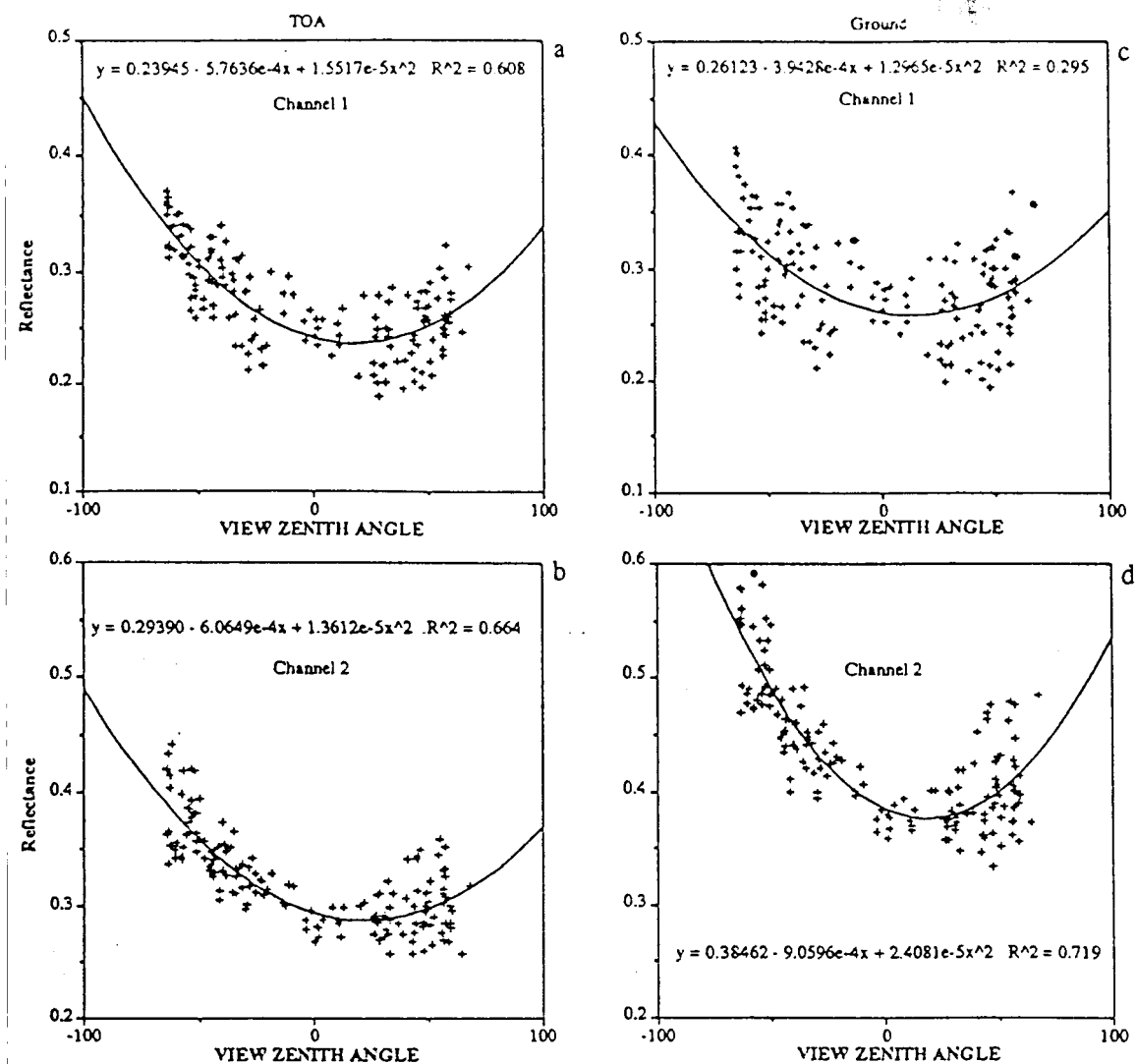


FIGURE 5

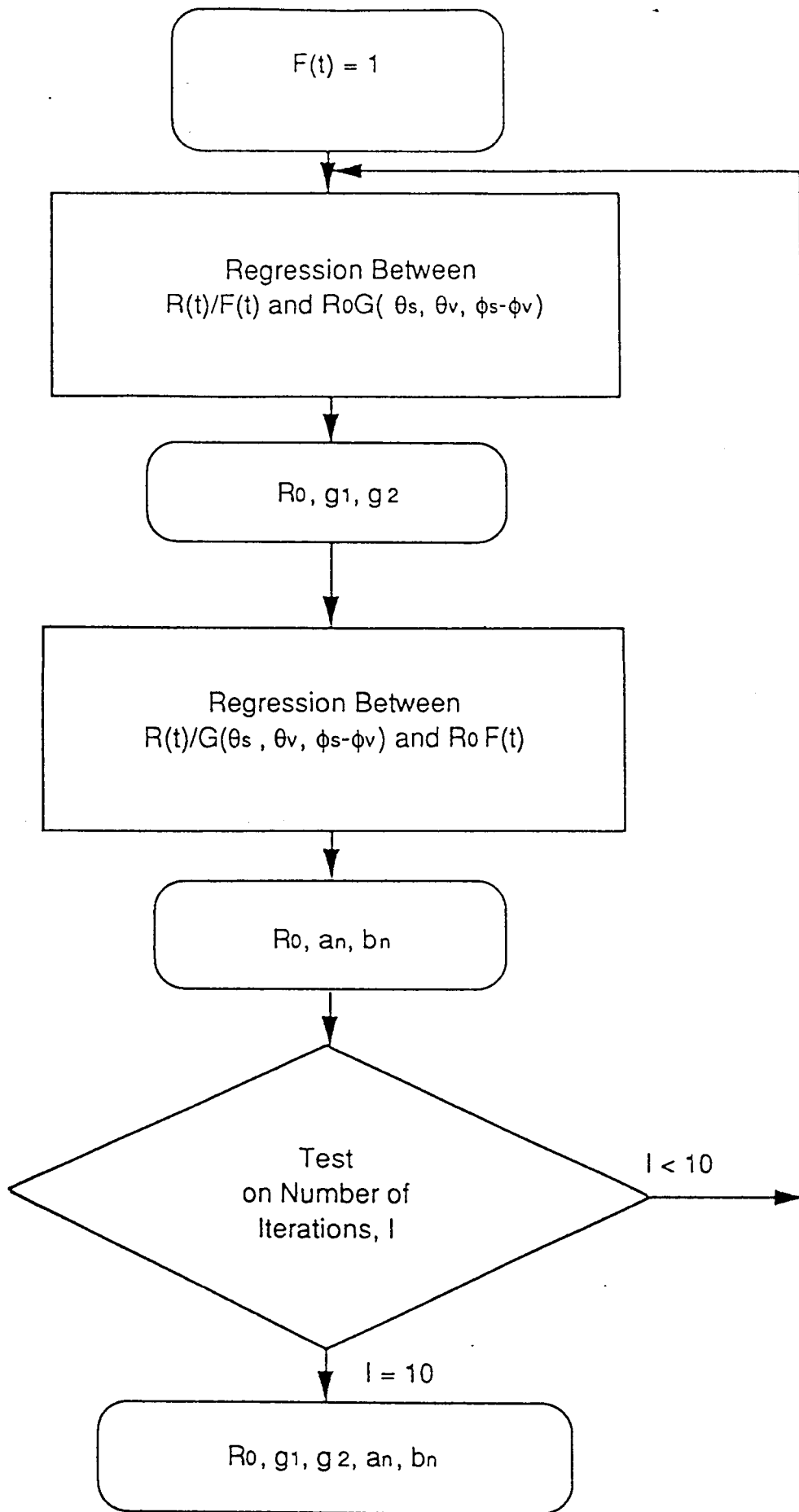


FIGURE 6



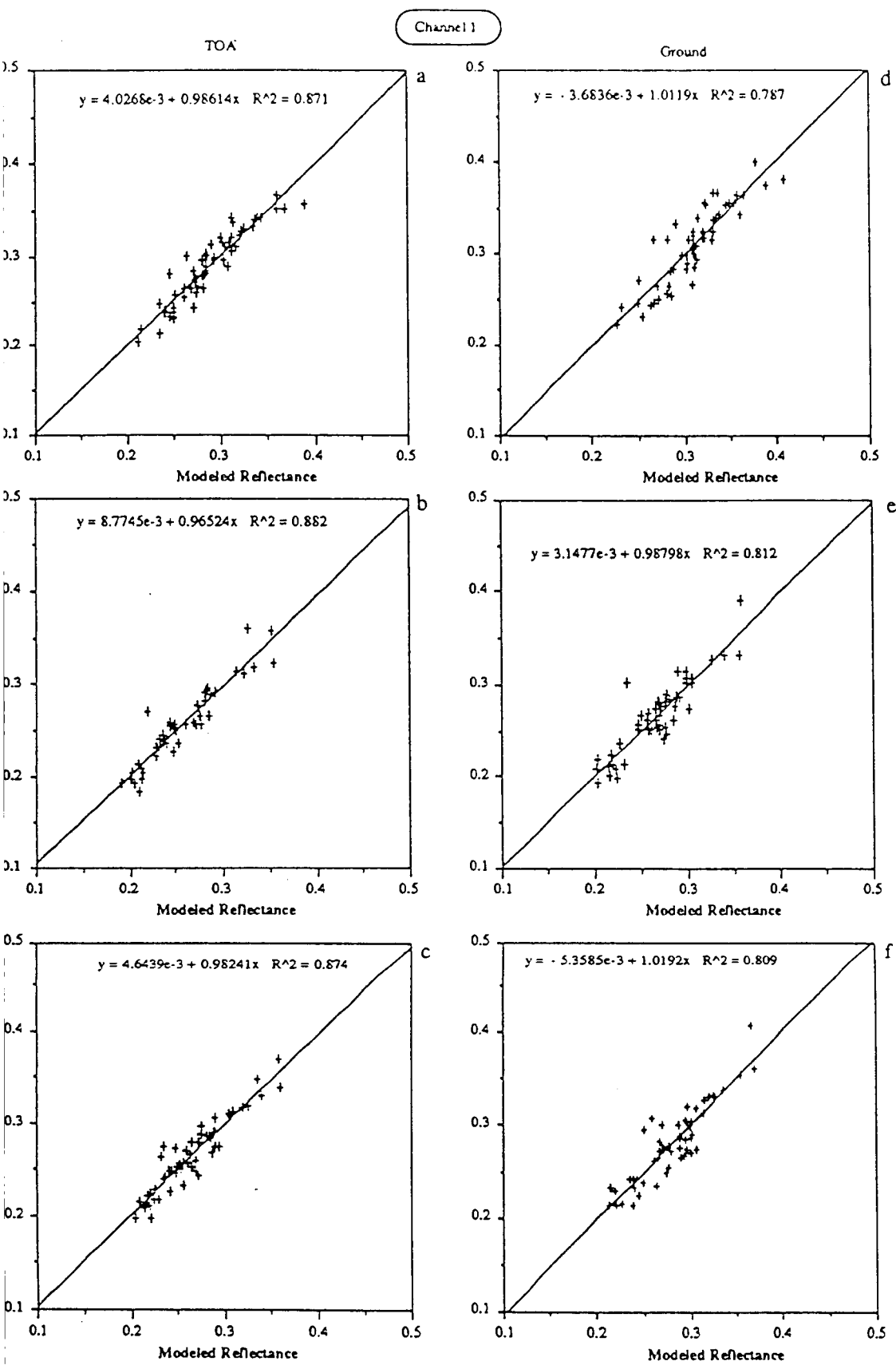


FIGURE 7

Channel 2

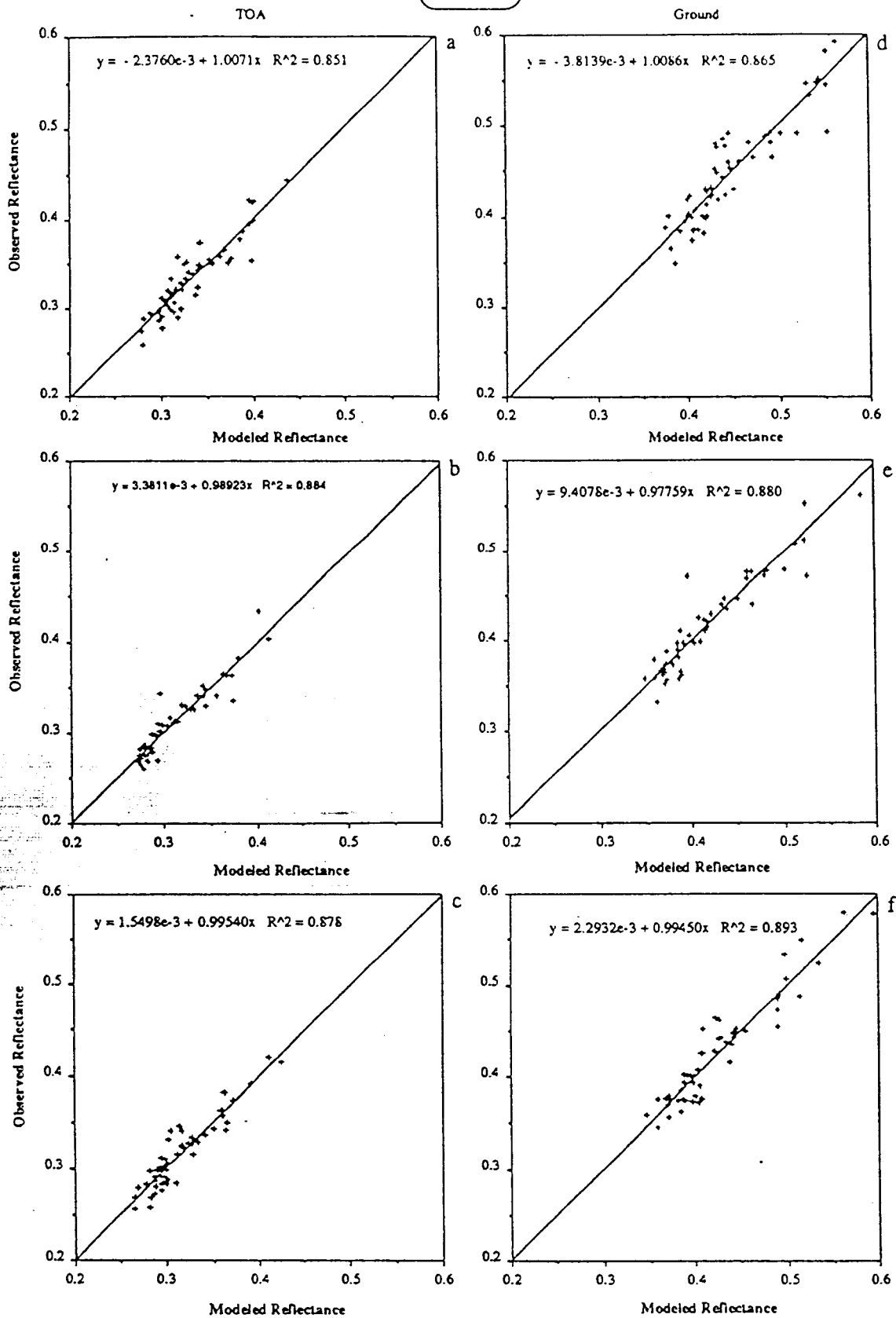


FIGURE 8

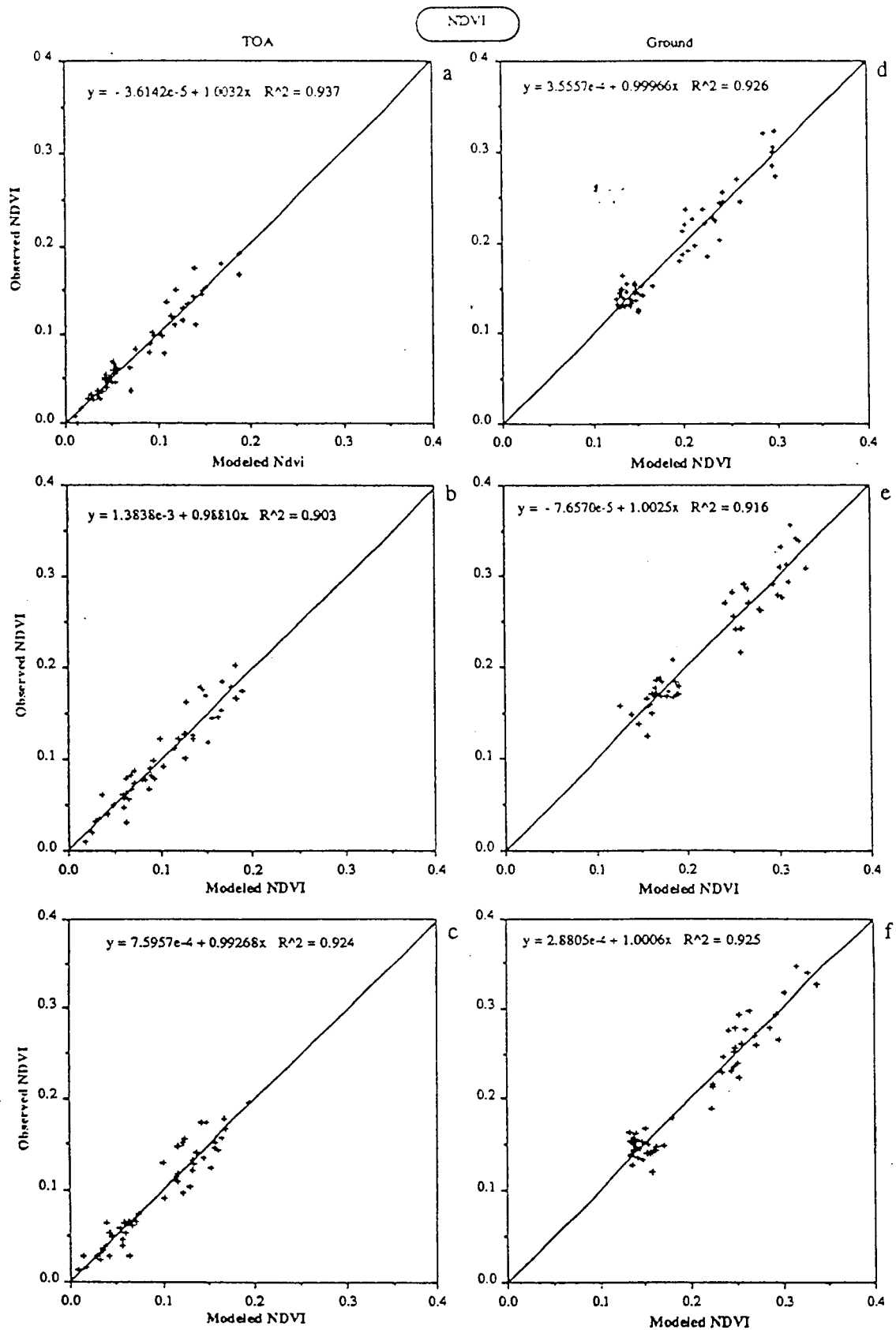


FIGURE 9

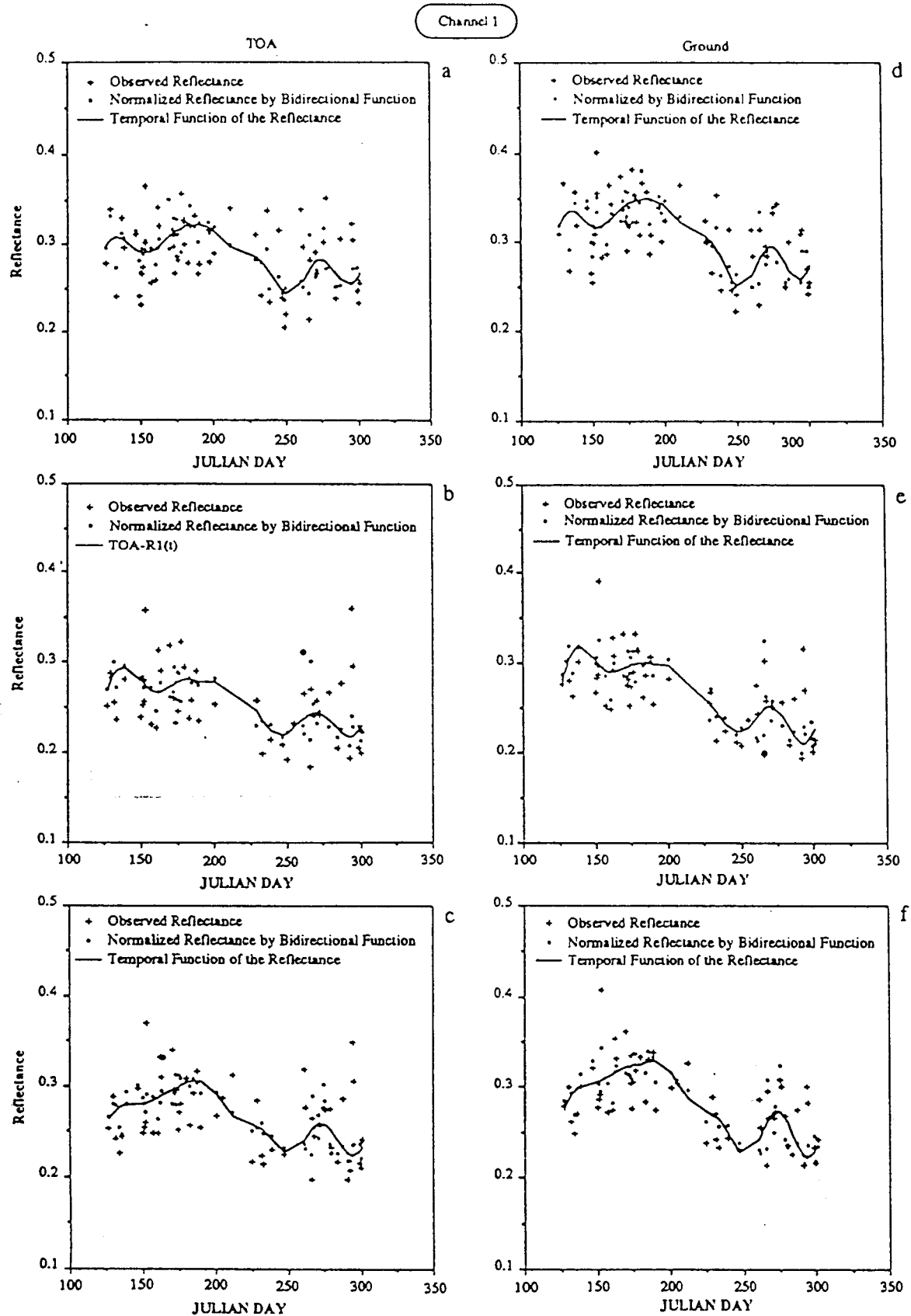


FIGURE 10

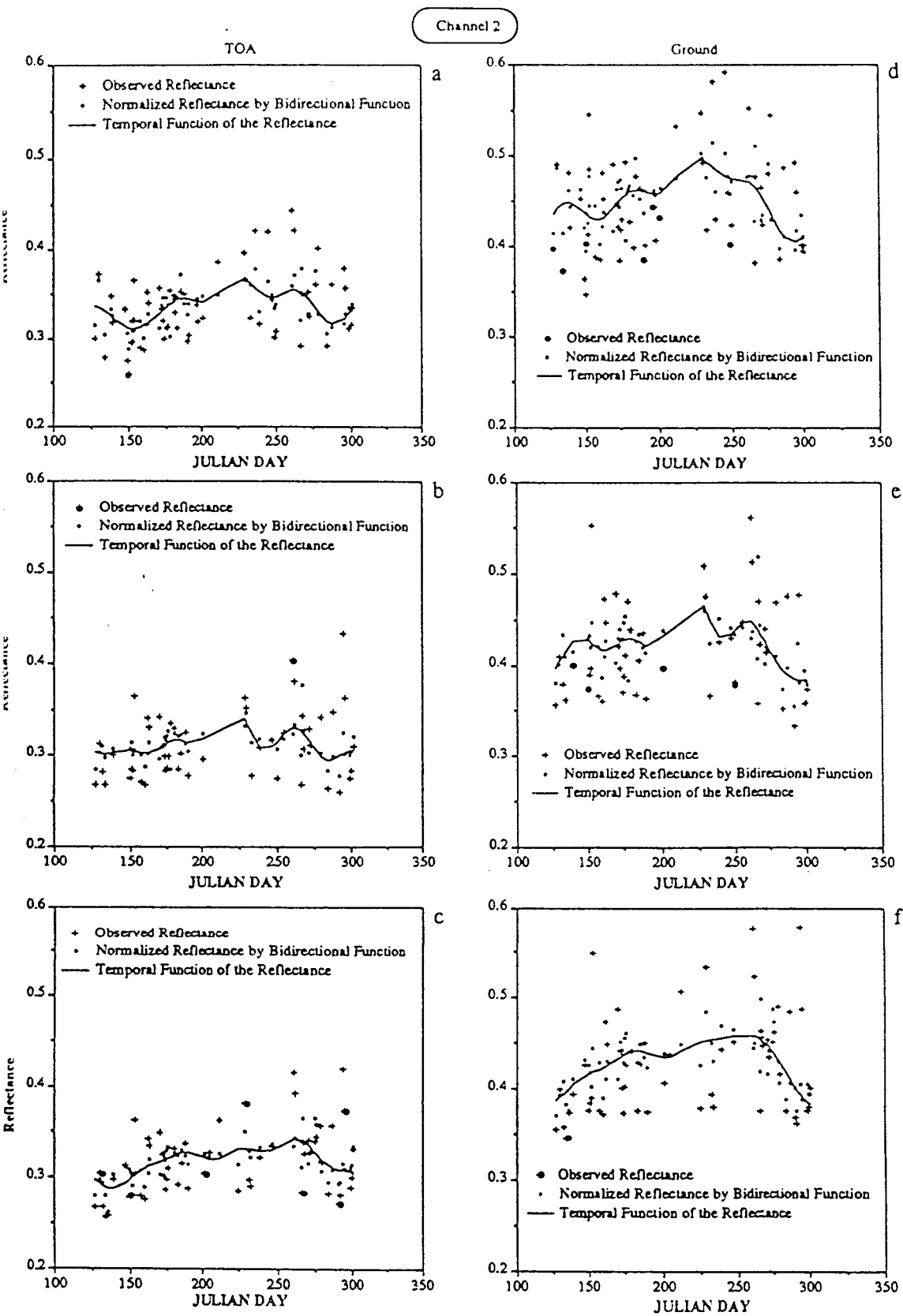


FIGURE 11

NDVI

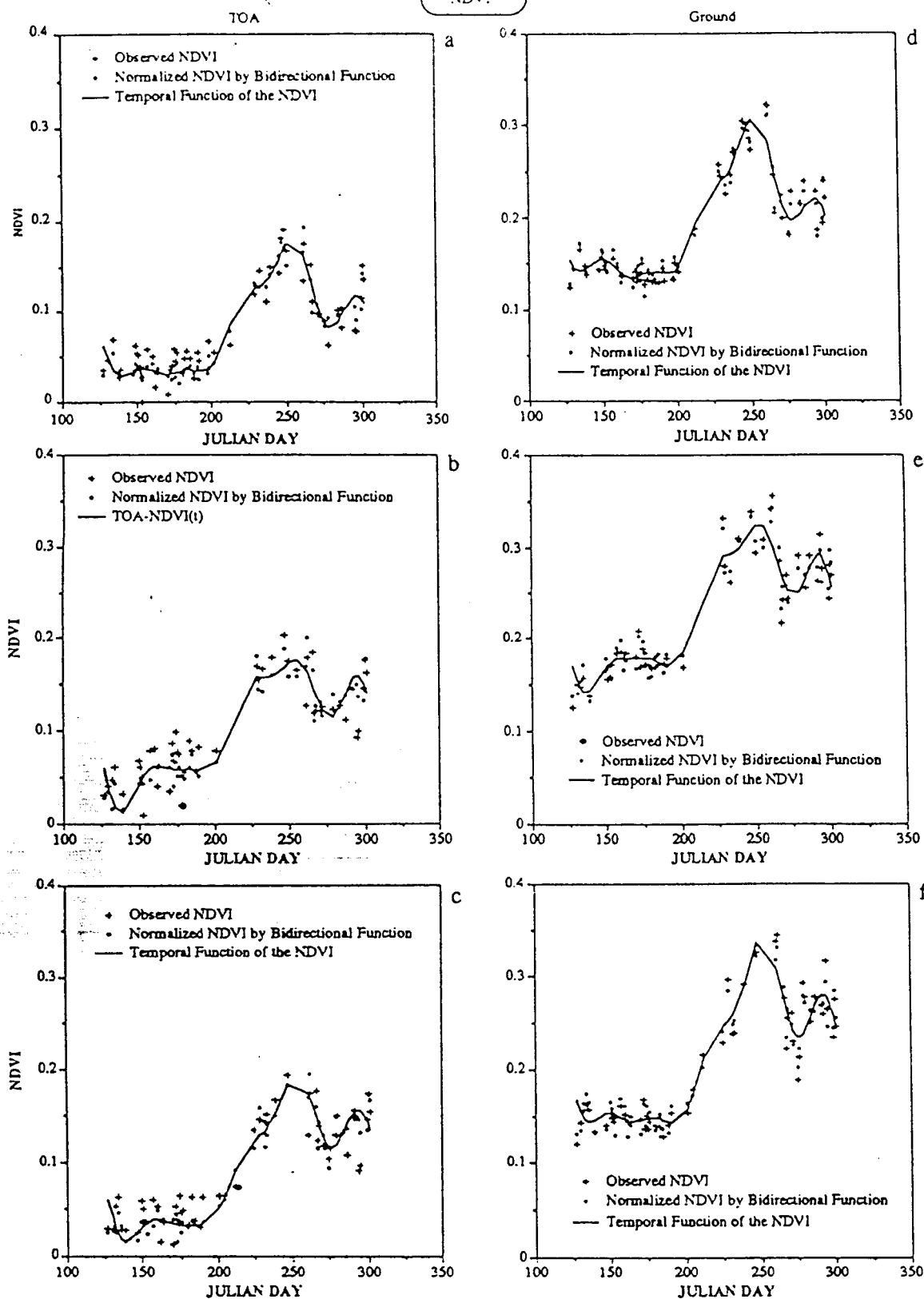


FIGURE 12

## **Appendix F**

### **Rainfall in the Sahel during 1994**

# Rainfall in the Sahel during 1994

S. E. Nicholson  
M. B. Ba  
J. Y. Kim

Department of Meteorology  
Florida State University  
Tallahassee, FL 32306

Submitted to Journal of Climate

June, 1995



## Abstract

This paper evaluates the rainfall conditions of 1994 in the West African Sahel. This analysis confirms that the year was relatively wet in the Sahel. The strongest positive anomalies occurred in the central Sahel and during the months of August, September and October. Conditions in the western Sahel were, as a whole, relatively dry. This year was the wettest for the region as a whole since 1969. Nevertheless, rainfall barely exceeded the long-term mean and was still slightly sub-normal in southern Sahel (i.e., the Soudan zone).

## 1.0 Introduction

A number of recent reports have suggested that 1994 was one of the wettest years of the last quarter century (e.g., LeCompte et al. 1994). Some contradictory information was recently offered by C. J. Tucker (personal communication), whose analysis of the Normalized Difference Vegetation Index in the "Sahel" (e.g., Tucker et al. 1991) suggested conditions similar to 1980, a relatively dry year. Some of the disagreement in the results can be attributed to the authors' definitions of the Sahel, i.e., differences in the analysis domain. Nevertheless, these discrepancies and a recent opportunity to obtain an expanded data set for the western "Sahel" prompted this note, which examines the 1994 season in detail.

The analysis is based on a regionalization (Fig. 1) used in previous studies (e.g., Nicholson and Palao 1993). This note focuses on the semi-arid zone west of Lake Chad, because rainfall data are unavailable for the eastern sector. A satellite analysis provides some information for the eastern sector. The analysis domain of LeCompte et al., which they term the "Sahel", runs from 8°N to 18°N. It coincides roughly with regions 13, 14, 15, 18, 19, 20 of Fig. 1. In our terminology, the Sahel is the northern half of this sector (regions 13, 14, 15), and the Soudan is the southern half of the sector (regions 18, 19, 20). Our regions 23 and 24, for which we have little data, are at the southern extreme of the domain and are termed the Soudano-Guinean zone (see Nicholson 1985). The station network for 1994 is illustrated in Fig. 1.

## 2.0 Spatial Distribution of Rainfall Anomalies

The first analysis is the rainfall departures for the whole region for the year 1994 and for the individual months of May through October (Fig. 2). Following

previous studies (e.g., Nicholson 1985, 1993), departures are standardized at each individual station by dividing the departure from the long-term annual mean by the standard departure of annual totals at the station.

For the year as a whole, the rainfall anomalies are not coherent throughout the Sahel/Soudan. This is in contrast to the most common mode of variability; zonally coherent anomalies, with anomalies often of the opposite phase to the north and south of 10 N (Nicholson 1980). No such zonal orientation is apparent. Strong positive anomalies, commonly one to two standard deviations, generally prevail in the sectors from c. 12 W to 5 W and c. 0 W to 15 E. Elsewhere negative anomalies prevail; these are quite variable in magnitude and exceed one standard deviation in several areas. In areas with above normally rainfall, percent departures from the long-term mean (not shown) are generally on the order of 20 to 60%, with equally large negative departures in the western Sahel.

The monthly anomaly patterns (Fig. 2) confirm the lack of coherence throughout the region; spatial variability is extremely high in most months. Overall the extent and magnitude of the positive anomalies increase throughout the rainy season. Rainfall is below average nearly everywhere during May; conditions in June and July are only marginally better. By August, positive anomalies on the order of .5 to 1 standard deviations are dominant in much of the Sahel/Soudan zone, but in the west there are negative anomalies of similar magnitude. September anomalies are strongly positive throughout most of the zone (generally 1 to 2 standard deviations), but equally strongly negative in the west. By October, positive anomalies are nearly ubiquitous and as much as several standard deviations in magnitude, while negative anomalies are limited to areas near the west coast.

The very strong anomalies in October are quite unusual in the region. This is near the end of the rainy season in most of the analysis sector. This may be a

manifestation of the ITCZ maintaining a northward position for an anomalously long time.

Fig. 2 clearly demonstrates the contrast between June-July and August-September. This confirms the findings of Nicholson and Palao (1993) that conditions in June and July are quite independent of conditions in August-September. It further underscores the point that reliable seasonal prognoses cannot be based on rainfall early in the season.

### 3.0 Comparison with Earlier Years

Fig. 3 compares 1994 with earlier years via times series (Fig. 3) for the period 1950 to 1994 for each region depicted in Fig. 1. The number of stations available during 1994 is indicated for each region is indicated in Tab. 1. Because in some regions fewer stations are available than during previous years, the time series were initially calculated in two ways. One used all available stations, the other, only stations available during 1994. The resultant time series were nearly identical, indicating the high degree of coherent variability within each of these regions.

These time series confirm that 1994 was still a dry year in the west (regions 13, 18), but that rainfall exceeded the long-term mean in the eastern sectors. In the central-Sahel/Soudan, 1994 was the wettest year since the 1960s (regions 14, 15, 19, 20), but barely reached the mean in the southern extremes of the Sahel (regions 23, 24).

The long-term variability for the Sahel, Soudan, and Soudano-Guinean zones as a whole is shown in Fig. 4. These suggest that 1994 barely exceeds the long-term mean in the Sahel and Soudan zones, and just reaches the mean in the Soudano-Guinean zone. Nevertheless, in the Sahel and Soudan, 1994 is the wettest

year since the late 1960s, but it is still very dry compared to the 1950s and many earlier years.

These time series are somewhat biased by the spatial distribution of stations, which is denser in the west. To overcome this problem, and to examine variability in the eastern Sahel, we have evaluated rainfall from Meteosat data. The cold-cloud frequency method described in Ba et al. (1995), which reproduces over 80% of the variance of rainfall, was applied to produce an areal average for the sector 9 N to 18 N (further south the method does not produce good estimates of rainfall) (Fig. 5). In this analysis, values are expressed as departures from the mean for the 1983 to 1994 period, since a longer term mean cannot be calculated from satellite data.

The satellite estimate shows excellent agreement with areally-averaged station data for this sector from the west coast to 15 E. It also indicates that the areally-averaged rainfall anomaly for the eastern Sahel (the sector 15 E to 30 E) is almost exactly the same as for the more western sector. The analysis confirms that 1994 was relatively wet, compared to recent years, but only marginally wetter than 1988, yet the wettest since 1969.

#### 4.0 Summary and Conclusions

Rainfall conditions during 1994 were extremely good in much of the Sahel, particularly the central Sahel, but well below normal rainfall prevailed in western sectors. For the zone as a whole, rainfall barely exceeded the long-term mean. Nevertheless, in the Sahel and Soudan, 1994 is the wettest year since the late 1960s, but still relatively dry compared to the 1950s and many earlier years.

The wet conditions are generally limited to the months of August, September and October; any seasonal estimates based on early season rainfall would have been highly inaccurate. The extent and magnitude of positive anomalies continually

increased during the course of the season. The strong anomalies in October and the prevailing zonal inhomogeneities are highly unusual.

#### Acknowledgements

We would like to acknowledge the assistance of several Meteorological Services and individuals in the collection of data: Mauritania, Guinea, Mali (I. Kone), Senegal, Niger, Ivory Coast, Burkina Faso. This work was supported by a grant from the Climate Dynamics Section of the National Science Foundation, ATM-9024340 and NASA Grant No. NGT 70273.

## REFERENCES

- Ba, M. B., R. Frouin, S. E. Nicholson, 1995: Satellite-derived interannual variability of West African rainfall 1983-88. *J. Appl. Meteor.*, 34, 411-431.
- LeComte, D., R. Tinker, J. Dionne, M. Halpert, and W. Thiao, 1994: *Wettest Rainy Season in 30 Years Across African Sahel*. Special Climate Summary 94/2, NOAA, Washington, D. C., 5 pp.
- Nicholson, S. E., 1980: The nature of rainfall fluctuations in subtropical West Africa. *Mon. Wea. Rev.*, 108, 473-487.
- Nicholson, S. E., 1985: Sub-Saharan rainfall 1981-84. *J. Clim. Appl. Meteor.*, 24, 1388-1391.
- Nicholson, S. E., 1993: An overview of African rainfall fluctuations of the last decade. *J. Clim.*, 6, 1463-1466.
- Nicholson, S. E., and I. Palao, 1993: A re-evaluation of rainfall variability in the Sahel. Part I. Characteristics of rainfall fluctuations. *Int. J. Climatol.*, 13, 371-389.

Table 1. Number of Rainfall Stations available in 1994, by Region

Region Number	Number of stations
13	11
14	8
15	6
18	29
19	15
20	8
23	13
24	9



## LIST OF FIGURES

Fig. 1 Station network and climatological regions in the Sahel and Soudan zones of West Africa.

Fig. 2 Top: Map of annual rainfall departures (% standard departure) for 1994.  
Bottom: monthly rainfall departures (% standard departure) for May through October of 1994. Areas with no available data are indicated by dashed lines.  
Units are standard departures.

Fig. 3 Annual rainfall departures (% standard departure) for regions depicted in Fig. 1 for the period 1950-1994. a. Sahelian regions, b. Soudanian regions, c. Soudano-Guinean regions.

Fig. 4 Annual rainfall departures (% standard departure) for the entire Sahel-Soudan zone, based on an average of all stations in the eight regions shown in Fig. 1.

Fig. 5 Spatially-averaged annual rainfall departures (% standard departure) for the area between  $9^{\circ}$  and  $18^{\circ}$  N. The solid line represents an average of station rainfall in this sector to  $15^{\circ}$  E, the dashed line represents satellite estimates based on a one-half degree grid; the dotted line represents satellite estimates for the area between  $15^{\circ}$  E and  $30^{\circ}$  E.

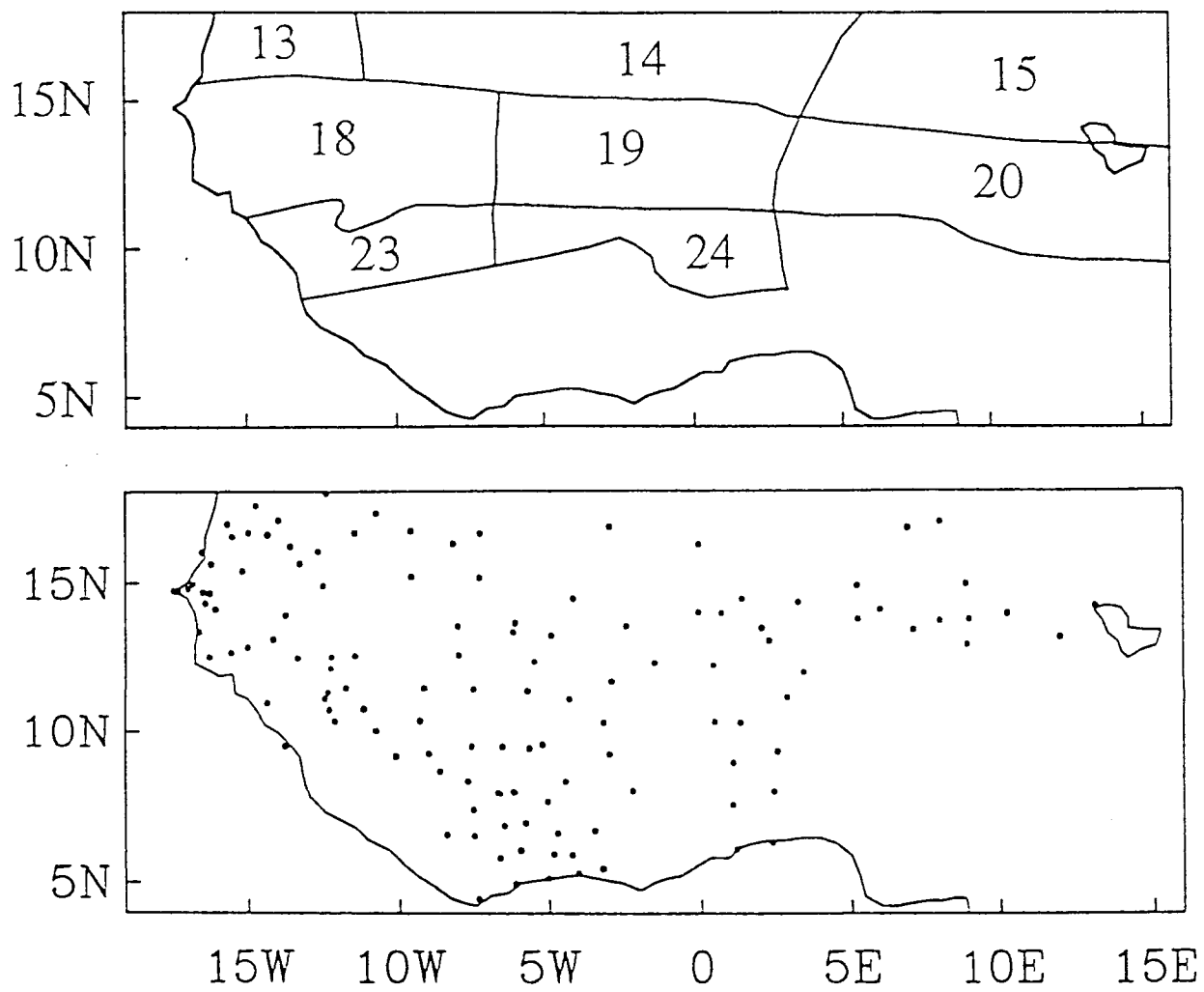


Fig.1

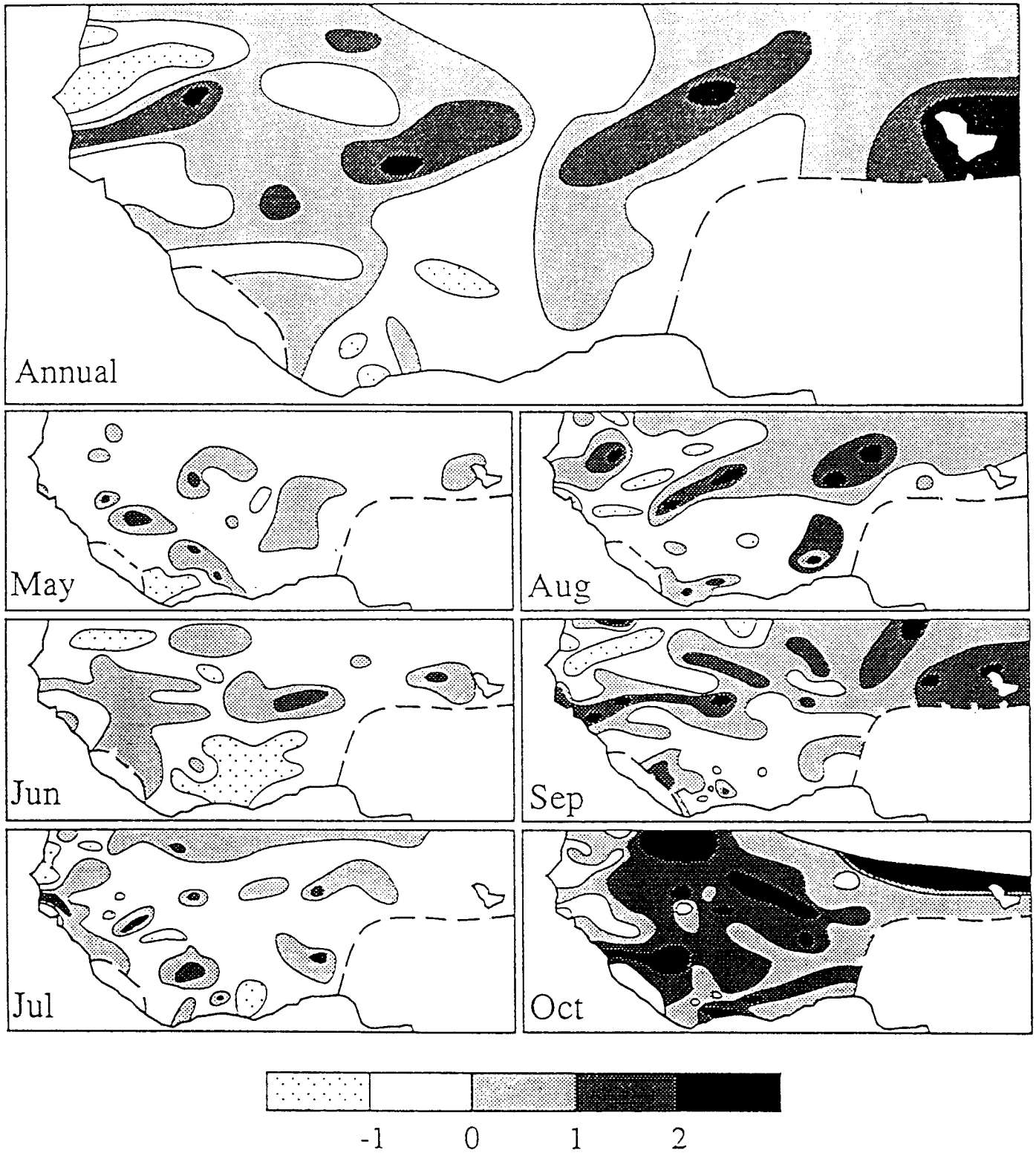
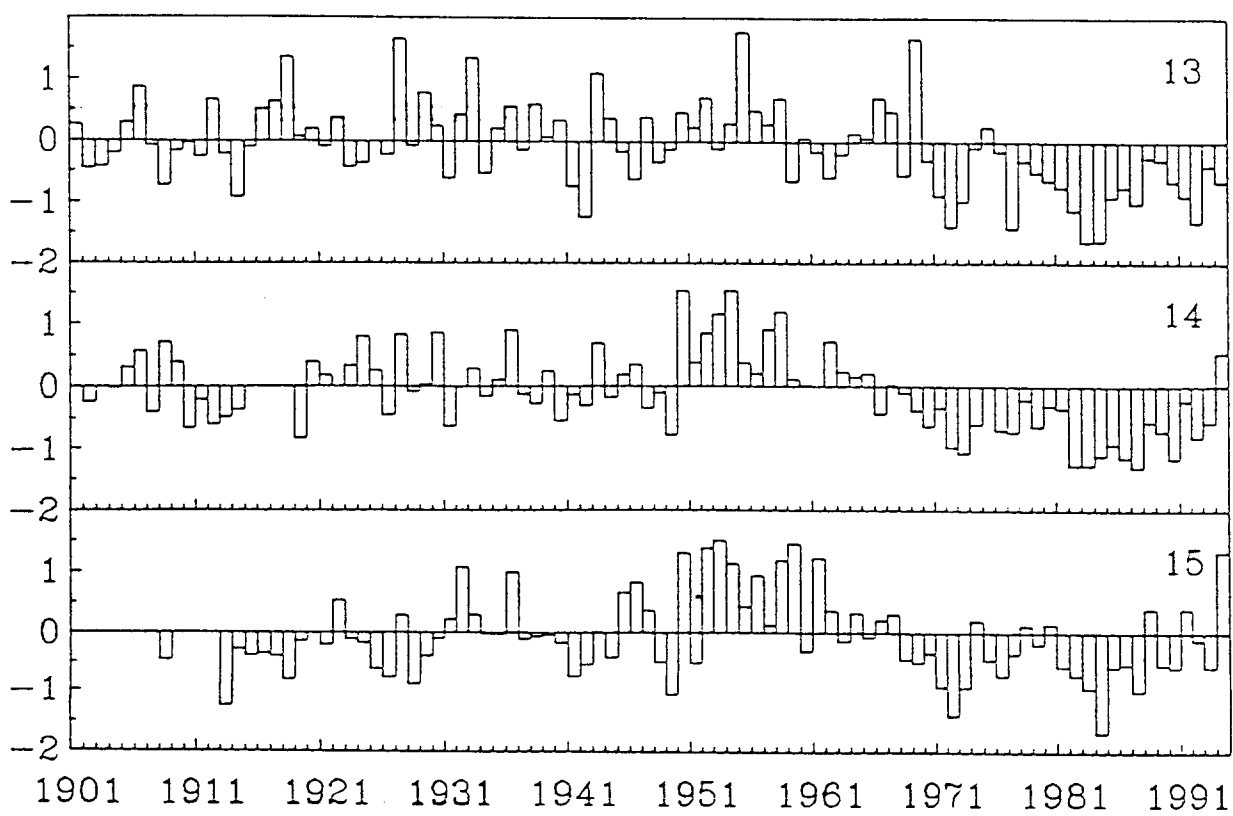


Fig.2



Sahel-04/fig x1

Fig. 3a

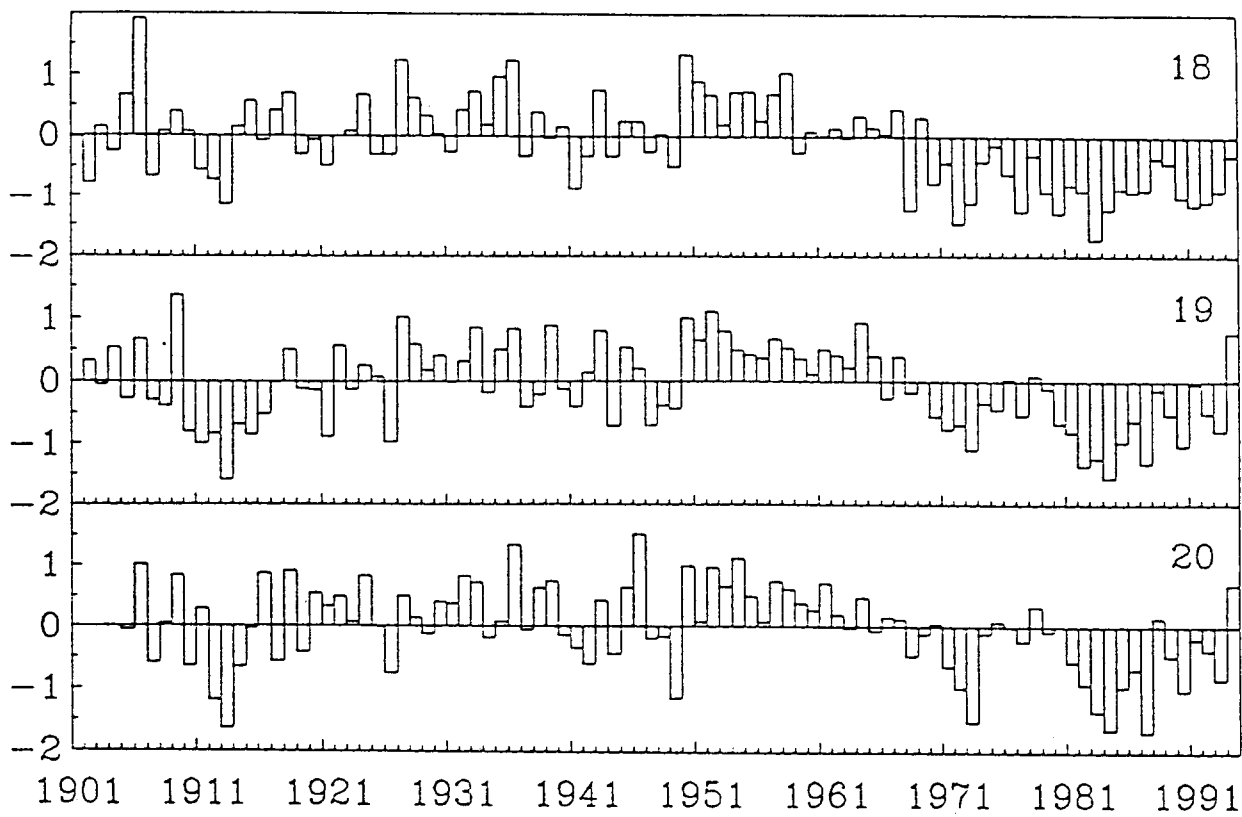
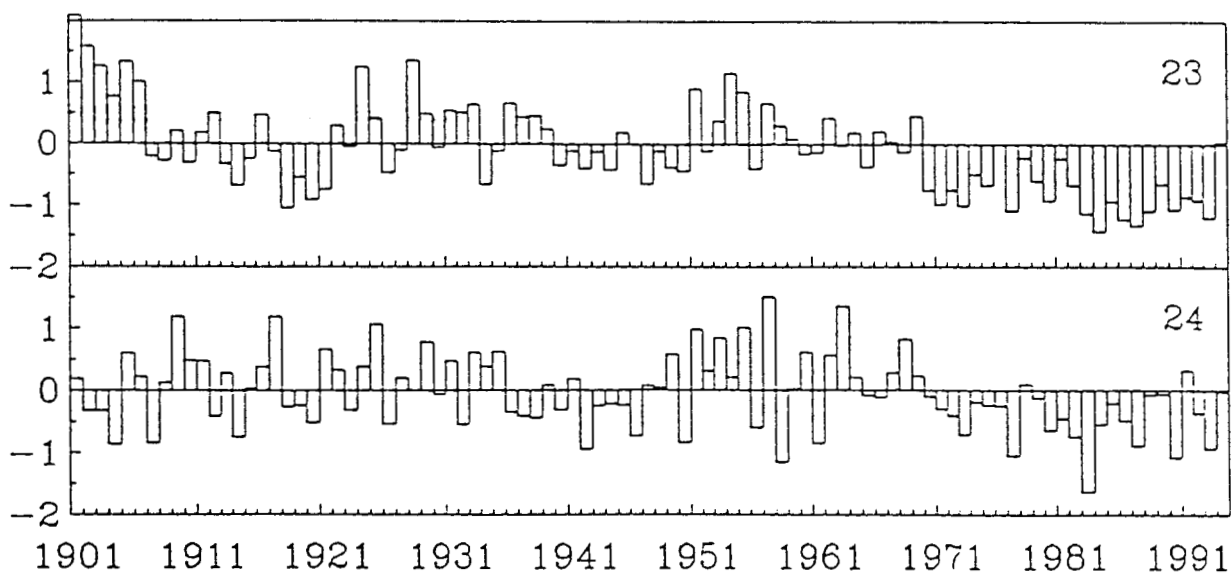


Fig. 3b



Sahel-94/fig x1

Fig. 3c

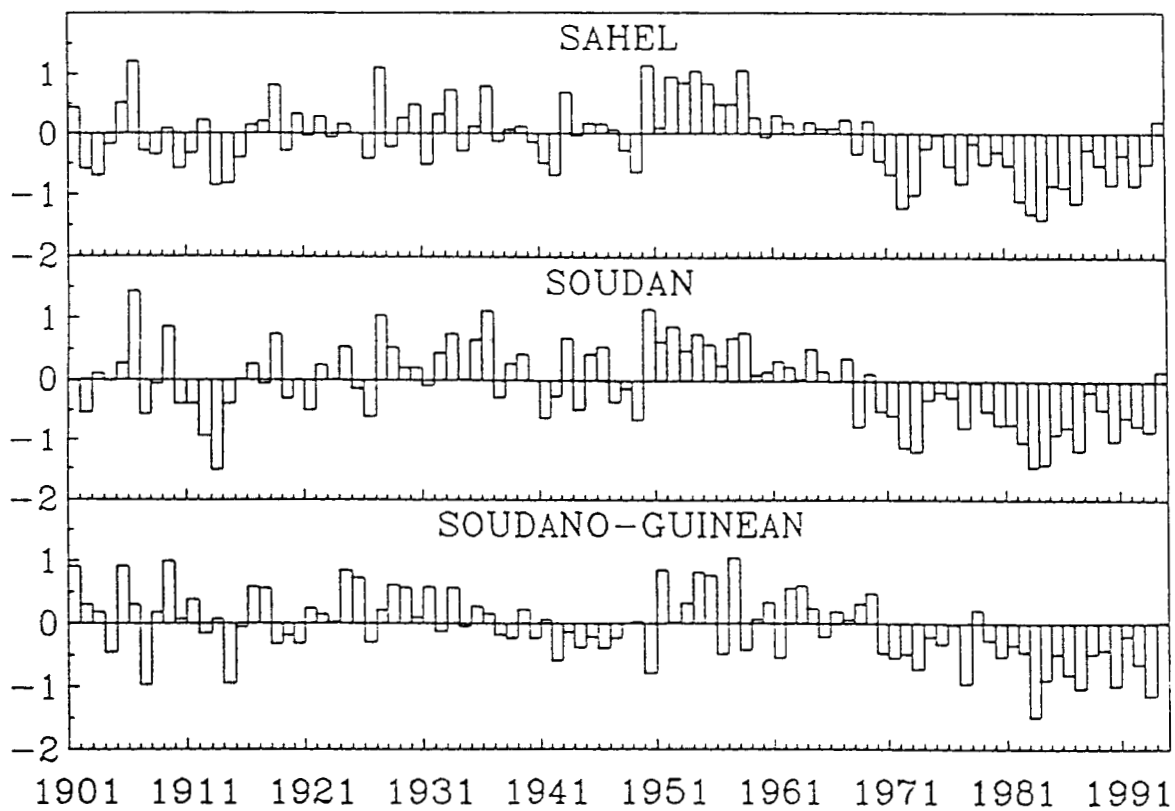


Fig. 4

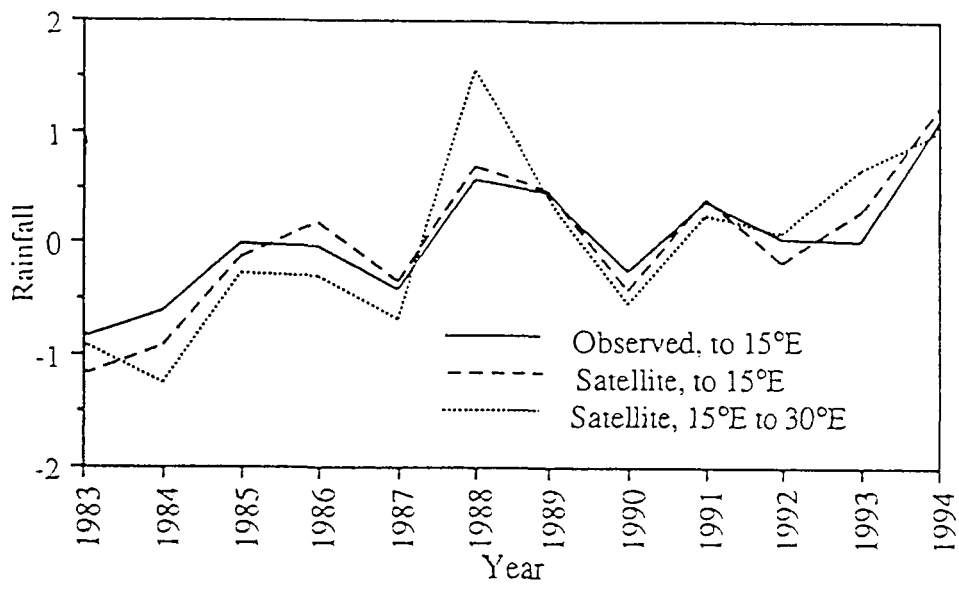


Fig. 5



## **Appendix G**

### **On the Use of NDVI for Estimating Rainfall Fields in the Kalahari of Botswana**

# On the Use of NDVI for Estimating Rainfall Fields in the Kalahari of Botswana

*Jeremy Grist*  
*Sharon E. Nicholson*

Florida State University  
Department of Meteorology  
Tallahassee, FL 32306

*Adzene Mpolokang*

Botswana Meteorological Services  
Gaborone, BOTSWANA

Submitted to Journal of Arid Environments

September 1995

## Abstract

This article presents the results of an experiment in estimating rainfall from the Normalized Difference Vegetation Index (NDVI). The study is carried out in the semi-arid region of south and southern Botswana, principally the Kalahari desert where few rainfall reporting stations exist. A statistical regression between NDVI and rainfall is developed for four areas with diverse soil conditions. These are used to estimate rainfall at an independent station or group of stations. The estimates reliably capture both the seasonal cycle and interannual variability. These regressions are used to produce a map of mean annual rainfall for the period 1982 to 1993, based on NDVI data, for the region 22 to 27 ° S and 20 to 26 ° E. The estimates are verified using all data available in the Meteorological Services' archive for these years.

## Introduction

In arid and semi-arid environments rainfall is a critically important, but in most such regions there are relatively few locations where rainfall is monitored. The rainfall records which exist are often cover only 20 or 30 years or less; in some remote desert locations they are insufficient to even reliably assess the seasonality of rainfall. For these reasons, the spatial and temporal variability of rainfall - fundamental determinants of environmental conditions - are not well documented in many dryland regions.

The Kalahari of Botswana illustrates this point well. Over an area of 60,000 km<sup>2</sup> there are 6 stations with rainfall records exceeding 35 years in length. A few scattered stations exist in the Kalahari's most arid core, but the data are discontinuous and, in some cases, of questionable quality. The available records suggest that mean annual rainfall throughout the region ranges from 250 to 450 mm (Fig. 1), but an aerial survey of vegetation density suggests that a more arid core may exist. Satellite methods developed for other areas of Africa have been applied by the Meteorological Services to assess rainfall, but do not appear to be appropriate for Botswana, where the rainfall regime is a hybrid between convective and frontal systems.

In this paper, we present the results of an experiment in estimating rainfall from vegetation, using vegetation-rainfall relationships demonstrated in previous studies of our lab (Nicholson and Farrar, 1994; Farrar et al., 1994). The basis of the methodology is a statistical regression between rainfall and the remotely sensed "Normalized Difference Vegetation Index", or NDVI. The Kalahari lends itself to such an experiment because of its relatively uniform soil and vegetation cover, its lack of significant topographic features, and the absence of surface water sources.

However, the method can be applied to many other arid and semi-arid environments which are also water-limited and relatively homogeneous.

### The Geographical Framework

Botswana encompasses nearly  $10^6$  km<sup>2</sup> in the latitudes 18 to 27° S. It sits on a plateau with average elevation of 1000 m and is surrounded by areas of higher relief. Most of the country is a semi-arid plain of unconsolidated sands, referred to as the "sandveld". This is the Kalahari, a region notable for its lack of permanent or even seasonal water courses (Thomas and Shaw, 1991). The "sandveld" is bounded in the east by a north-south ridge which separates it from the "hardveld", an area of well developed soils, small hills and undulating plains, and active erosion (De Wit and Bekker, 1990). To the north lie lacustrine and alluvial systems: the Okavango delta; the Linyanti, Chobe and other rivers; Lake Ngami, and the Mababe and the Makgadikgadi depressions.

Rainfall in the Kalahari is mostly convective and varies greatly from year to year. It is strongly seasonal; it occurs mostly from October to April, coincident with the period of highest potential evapotranspiration (Bekker and De Wit, 1991; Bhalotra, 1987). Rain occurs occasionally in May and September, but it is rare in June through August.

Vegetation is relatively uniform in the sandveld; there are relatively few species but markedly different plant communities with varying proportions of woody, herbaceous plants and grasses (Prince and Choudhury, 1989; Bekker and De Wit, 1991; Thomas and Shaw, 1991). The most widespread woody species is *Terminalia sericea*, but *Acacia* sp. are also common. The main grasses are *Aristida*, *Eragrostis* and *Stipagrostis*. The drier part of the sandveld is a shrub savanna also called the thornveld; the wetter northern part is predominantly a tree savanna.

The presence of the Kalahari sands, arenosols with a sand content of over 90%, distinguishes the Kalahari from the hardveld and other regions of Botswana. These soils are poorly developed. Although relatively uniform, three subtypes are recognized in the region: ferralic, luvic and haplic arenosols. The differentiation is based on iron content (ferralic), illuvial clay (luvic) and absence of any special profile features (haplic). Some areas are covered by rocky regosols. In the southeastern hardveld, which is included in our study area, lixosols and luvisols are the dominant soil types. These have a high sand content and an illuvial clay horizon, but little silt; the lixosol are also iron-rich (formerly called ferric luvisols).

### Background Studies on the NDVI-Rainfall Relationship

The differential reflection of vegetation in the red and infrared portions of the solar spectrum provide a widely used indicator of vegetation, termed the Normalized Difference Vegetation Index. Numerous studies (e.g., Sellers, 1985; Prince, 1991a; Prince et al., 1994) have shown that this index essentially represents photosynthetic activity. However, in arid and semi-arid locations it has also been shown to correlate with other vegetation parameters, including biomass, LAI, percent cover and net primary productivity. Because of the close links between these parameters and rainfall, NDVI-rainfall relationships have been studied in numerous locations (Justice and Hiernaux, 1986; Henricksen and Durkin, 1986). NDVI has been used to assess primary production and biomass (e.g., Prince and Tucker, 1986; Diallo, 1986; Prince, 1991b). It has been used operationally as an indicator of the interannual variability of rainfall and greenness, particularly over Africa.

Nicholson and Farrar (1994) studied the NDVI-rainfall relationship over Botswana in detail for the period 1982 to 1987, but did not attempt to use NDVI to

estimate rainfall. The analyses showed universally strong correlations between NDVI and rainfall and demonstrated that the interannual variability of rainfall at all locations is well depicted by the time series of NDVI. Correlation coefficients based on monthly data are generally on the order of .7 to .9, with the best correlations obtained being NDVI and a three-month average of rainfall in the concurrent plus two antecedent months. On an annual basis, the twelve-month integral of NDVI is even more strongly correlated with rainfall and the scatter lower.

There are, however, considerable differences in the quantitative relationship between the NDVI and rainfall at various locations in Botswana. These differences are strongly dependent on soil type (Fig. 2). The slope of the NDVI-rainfall regression ranges from 1.5 for the sandy arenosol soils to 2.0 for the clay-rich vertisols in the north (Nicholson and Farrar, 1994).

This paper builds upon these conclusions to design an experiment to actually estimate rainfall from NDVI in data sparse regions of the Kalahari. This previous work underscored the need to separately evaluate various soil types and demonstrated that NDVI represents a multi-month integral of rainfall. It also demonstrated the spatial variability of both NDVI and rainfall. Unlike the previous study, which had available only data from major stations, the current study details with data sparse regions of the Kalahari in detail. It utilizes rainfall records for recently opened rainfall stations in that region.

## Data

This study utilizes monthly rainfall totals and monthly-composited NDVI for the period 1982 to 1993. NDVI data were provided and processed by the GIMMS group at the Goddard Space Flight Center. NDVI is calculated from NOAA-AVHRR global area coverage (GAC) data, with a resolution of 4 km. The data are mapped to an equal-area projection with a grid cell of approximately 7.6 km (Tucker et al., 1991). For each rainfall station, a three-by-three grid cell average is utilized, with the center grid corresponding to station coordinates. A cloud mask is applied and daily values are formed into monthly composite images by using for each pixel the maximum NDVI within the compositing period (Holben, 1986). This minimizes the effects of atmosphere, scan angle and cloud contamination. The definition of NDVI as a ratio minimizes the influence of varying solar zenith angles and surface topography on the derived data set.

In addition, a correction was applied for stratospheric aerosols resulting from the Mt. Pinatubo eruption (see Los *et al.*, 1994). Aerosol optical depth in the visible and IR channels of AVHRR was determined for an area in Pacific where tropospheric aerosol content is low. The measured radiances in these channels were inverted to obtain optical depth, using King *et al.*'s (1984) stratospheric aerosols model. The model was then applied, together with data from radiance tables of Deuzé *et al.* (1989), to correcting NDVI for the period July 1, 1991, to June 30, 1992.

Quality control of the rainfall data was performed manually, because the standard statistical tests applied to such problems are inapplicable in semi-arid regions, where the rainfall distribution is highly skewed. Data were checked and evaluated in a manner consistent with quality control used on our laboratory's larger data set for the whole continent (e.g., Nicholson, 1986). Time series of data for



each station were graphed and compared with nearby stations; serious discrepancies among nearby stations were evaluated; and questionable data were eliminated.

## Methodology

### *Overview*

A linear regression model was developed to quantify the relationship between NDVI and rainfall on monthly and annual time scales. This was used as a basis for predicting rainfall from NDVI. The regression was derived from station groups and evaluated for individual stations or a station group. It was then applied to estimating rainfall throughout the sector 22 to 27 ° S and 20 to 26 ° E, producing a map of estimated mean annual rainfall for the period 1982 to 1993 in this sector.

This sector was chosen because it is relatively homogeneous with respect to topography, soils, and vegetation. The exception is the southeast corner, where a stark change of soils occurs and where there is slight topographic relief.

The regression was performed on stations groups in four areas selected with respect to location, soil type and length of rainfall record. These areas and the stations within them are shown in Fig. 3; station names and mean annual rainfall at each station are indicated in Table 1. For each area the regression was used to predict rainfall at an independent station or station group, also indicated in Table 1.

The areas and stations within them were chosen in such a way as to be able to examine the effects of soil type, soil homogeneity, and areally-averaging on the regressions and on the reliability of rainfall estimates. The areas selected represent two distinctly different soil types and a mixture of types.

Unfortunately, the quantity and quality of rainfall station records imposed a limitation on the design of the regression experiments. Areas 1 and 2, with relatively similar soils, were chosen to examine the effect of spatial averaging of rainfall on the regression-based rainfall estimates. Unfortunately too few rainfall data were available to produce good spatial averages. Area 3 was chosen to represent a mixture of soil types. The first three areas are in the sandveld, with soils being predominantly arenosols. Area 4 was chosen to represent a strongly contrasting region; it is an area of hardveld with a mixture of soils but mainly luvisols.

Area 1 consists of luvic arenosols. A regression between NDVI and rainfall is derived from three stations relatively far apart and used to estimate an areal average of rainfall, i.e., the average of three additional stations.

Area 2 represents ferralic arenosols. The regression is based on three stations and is used to predict rainfall at one, the synoptic station Tshane.

Area 3 represents a mixture of soil types. The regression is based on three stations representing a combination of regosols, ferralic arenosols, and luvic arenosols. It is used to estimate rainfall at the synoptic station Ghanzi, a location where both types of arenosols are common.

In area 4, representing the hardveld luvisols, the regression is based on three stations and used to estimate rainfall at a fourth. As with area 1, the stations are relatively distant from one another.

Monthly composited NDVI and monthly rainfall for the "predicted" stations and station group is shown in Fig. 4. Rainfall is a three-month average of that in the month concurrent with NDVI and the two preceding months.

### *Regression Analysis*

Separate regressions were run for annual and monthly data. Because the calendar year bisects the rainy season, annual totals of NDVI and rainfall were computed from the twelve month period beginning in July, the middle of the dry season. This means that for the period 1982 to 1993, the number of complete years of data for each station is reduced from 12 to 11. As there are 3 stations in each area used for the regression, the maximum number of points for each regression is 33. However, the actual number available is always less because of missing data. The minimum number of data points available was 14 for area 1. This was sufficient to perform a least squares linear regression.

The time series of monthly NDVI and rainfall presented in Fig. 5 shows a close relationship between the two variables. However, it is clear that the response is not immediate and that NDVI tends to lag rainfall by one to two months. Nicholson and Farrar (1994) showed that at the monthly scale the highest correlation is obtained by relating monthly NDVI to the average rainfall from the concurrent month and the two preceding months. For this reason, the linear regressions of NDVI versus rainfall are based on monthly composited NDVI and the three-month running mean for the concurrent and preceding months. After accounting for missing data there were between 217 (area 2) and 387 (area 4) points available.

#### *Regressions for Predictive Equations*

A predictive equation for rainfall can be obtained by running a regression of rainfall versus NDVI (as opposed to NDVI against rainfall). However, it is noted that on both annual and monthly scales non-zero values of NDVI correspond to zero rainfall. These 'baseline' values of NDVI are the intersects of the regressions.

They are associated with the background effects of soil and perennial vegetation. Their exact value varies spatially due to differences in soil and vegetation.

Without accounting for this baseline, there is a tendency for the predictive equation to underestimate rainfall in dry years. By first subtracting this baseline from the NDVI and then running a least squares regression of rainfall against this reduced NDVI a more reliable predictive equation is obtained. Therefore to obtain predictive equations, regressions of rainfall were run against reduced NDVI at annual and monthly time scales.

The predictive equations are in the form  $\text{rainfall } R = d + b \times (\text{NDVI} - a)$ . Here  $d$  essentially represents a minimum value of rainfall and  $b$  represents the slope of the NDVI-rainfall relationship;  $a$  is a correction applied to NDVI to account for the fact that it does not reach zero with vegetation growth declines to zero. The values of the coefficients for these equations are given in Tables 2 and 3 for the monthly and annual time scales, respectively.

## Results

### *Regressions*

At the annual scale, NDVI is very well correlated with rainfall (Fig. 5). The coefficient of determination, or  $r^2$ , is on the order of .6 for all for areas. Values range from .62 for area 2 to .66 for area 4. The correlation between NDVI and rainfall is significantly lower on monthly time scales than on annual (Fig. 6). The value of  $r^2$  ranges from 0.36 (area 1) to 0.53 (area 4).

The fact that the monthly correlation is lowest for area 1 may be related to the small data sample; for the entire three-station group, only 14 station-years were available for the period of analysis. However, the sample size is similar for area 2,

where the regression explains considerably more of the variance. Other possible factors are examined later.

### *Rainfall Estimates*

#### *Annual*

The annual time series of rainfall for stations or station groups representing areas 1-4, as estimated by their predictive equations, are compared to the observed time series in Fig. 7. In general, the estimates effectively capture the trends in interannual variability and the magnitude of rainfall. The agreement between estimated and observed is, however, poorer for area 1 than for the other areas of arenosols. For all three remaining areas, agreement is exceptionally good prior to 1989, but after that time the NDVI-rainfall relationship shows a systematic change in area 4.

For area 1 the predictive equation is used to estimate rainfall for a three-station average (Kang + Kokang + Mabutsane). The most serious discrepancy between estimated and observed rainfall occurs in 1987/88, an exceedingly wet year throughout Botswana. This discrepancy, noted to a lesser extent with area 4, almost certainly reflects the exceedingly high rainfall in individual months. NDVI is insensitive to high intensity rainfall, which is relatively ineffective for plant growth. Overall, the agreement between observed and estimated rainfall for the three-station average representing area 1 is poorer than for the other areas.

The estimate for Tshane (area 2) differs from the observed by over 100 mm in both 1983 and 1992, but otherwise the estimates capture both the trends of interannual variability and the magnitude of rainfall extremely well. In all cases rainfall is overestimated in both 1991 and 1992 rainfall is underestimated. This may be a result of problems with the NDVI data. This is suggested by anomalously high

dry season values in those years, a problem evidenced to some extent at Ghanzi as well (see Fig. 4). This possibility is considered in the discussion section.

The estimates for Ghanzi (area 3) show generally good agreement with observed rainfall, with the exception of 1988/89. NDVI underestimates the magnitude of rainfall in this anomalously wet year, although not in the preceding wet year. The NDVI-rainfall relationships in these years are considered in the discussion of possible sources of errors later.

The agreement between estimated and observed is poorer for Serowe (area 4) than for the other cases. NDVI over-estimates rainfall at Serowe in 1988/89, which was not a particularly wet year there. One explanation may be a residual effect of the previous wet year, an effect noted in the Sahel by both S. Prince and C. J. Tucker (personal communication). We feel that more likely the NDVI estimate for that year is in error, as high "growth" is indicated as early as October, the first month of the rainy season (see Fig. 4). Neither at Serowe or other nearby stations is high rainfall noted in October.

There appears to be a systematic overestimation of rainfall at Serowe during 1989 to 1992. The reason for this is not clear. Since it extends over a multi-year period, one possibility might be the introduction of agriculture or irrigation in this area. Agriculture is intense in some areas, such as Molopolole, and irrigation is practiced in the relatively nearby area of Tuli Block (Prince and Choudhury, 1989; Arntzen and Veenendall, 1986). Inquiry into this question found that a rhino sanctuary was recently created in this region (Dube, personal communication). The result would be relatively protected grazing that would increase the NDVI/rainfall ratio. This could account for an overestimation of rainfall from NDVI when the original regressions are used.

### *Monthly*

The estimated and observed time series for stations in areas 1-4 are shown in Fig. 8. Again, poorest agreement is for the three-station average representing area 1, yet even here the season cycle and interannual variability are captured reasonably well. The greatest discrepancies are those noted earlier: the wet year 1988 and the years 1991 and 1992. The incomplete time series of observed rainfall for this area 1 highlights the data problems suggested earlier as a source of error in the regression for area 1.

For Tshane (area 2) the wet season and the onset and ending of the rains is represented well. In most years the estimate of peak monthly rainfall is within 10 to 20 mm of the observed rainfall peak (the exceptions are the dry years 84, 85 and 87). A possible reason for the reduced accuracy in the dry years is that the vegetation withered prematurely under drought conditions. Other features include a slight but persistent tendency for the slope of the estimated end of wet season to be less steep than observed and occasionally the peak rainfall estimates are out of phase by plus or minus one month.

Ghanzi (area 3) shows the best estimates of the seasonal cycles. The rising and falling limbs of the onset and end of the rains are in excellent agreement. So too is the timing of the peak rainfall. The magnitude of the peak rainfall is within 20 mm for over half the years. The peak is generally under estimated, particularly in the wettest year.

For Serowe (area 4) the magnitude of the peaks are well estimated in all but two years. It is underestimated in the wet year (1988) and overestimated in the dry year (1990). The onset and end of the rains are captured well, but with less precision than for Ghanzi (area 3).

*Correlations between observed and estimated rainfall*

The correlations between observed and estimated rainfall are given in Tables 4 and 5. These range from .39 to .67 for annual data and .35 to .65 for monthly data. The latter is considered particularly good because the correlations are based on between 124 and 144 points. In both cases, the lowest correlation is for area 2 and the highest is for area 3 in the monthly case, but for area 4 in the annual case.

For the monthly estimates (Table 4), the mean error is also lowest (13.4 mm) for area 3 and highest (19.2 mm) for area 4. This is equivalent to a 15-20 % error in the wet months but higher in the dry months.

Much of the high correlation in the annual data results from NDVI's ability to reproduce interannual variability of rainfall, and not necessarily magnitude. The mean error (Table 5) ranges from 55 mm for area 3 to 116 mm for area 4; it averages 83 mm for all areas collectively. Nevertheless, these results are encouraging, especially for areas 2 and 3, and suggests that the regressions could be used for estimating the 11-year mean annual rainfall in the region. Indeed, because the errors are random and not biased, the estimate for mean annual rainfall is less than for individual years (Table 6).

#### Mean annual rainfall over the Kalahari and adjacent areas.

Fig. 9 is a map of mean annual rainfall in the analysis sector, based on the regressions with NDVI. To simplify calculations, soil type information has been generalized and the appropriate regression applied to the full set of NDVI data points, which has a 7.6 km resolution. For most of the map, the group regression based on the arenosol-dominated groups 1, 3 and 3 (Tab. 3) is applied; for appropriate areas of the hardveld, the group 4 regression is applied.

The map suggests a general increase in annual rainfall from the southwest, where it is less than 200 mm/an, to the northeast, where it reaches 300 - 350 mm/an.



From 25 ° S to 27 ° S there is a strong westward gradient, with mean annual rainfall exceeding 500 mm in the far southeast, and locally reaching 600 mm.

These estimates are based on the period 1982 to 1993, a relatively dry period throughout most of the continent (Nicholson, 1994). An analysis of annual totals at the few long-term stations in the region (Table 7) suggests that the long-term means (i.e., since the beginning of instrumental records, or roughly 60 to 70 years at most of these stations) are probably significantly higher than those indicated in the map in Fig. 9. At most stations mean annual rainfall for the recent period is 10 to 36% lower than the long-term mean.

The map in Fig. 9 differs from the conventional rainfall map (Fig. 1) in several ways, even when the above differences between the two periods of record are considered. There is a large area in the southwest where mean annual rainfall is less than 250 mm; within this is a more arid core with rainfall below 200 mm/an. The map based on rainfall indicates only a small sector with annual means below 250 mm and suggests annual means on the order of 300 to over 350 mm in much of the area where the NDVI-based map suggests less than 250 mm. It also indicates large sectors in the northwestern Kalahari with mean annual rainfall exceeding 400 mm, compared to about 300 mm on the NDVI based map. The NDVI-based map clearly indicates two distinct arid cores within the Kalahari, a feature not evident on the rainfall map. It is impossible to determine which of the two maps is most accurate; however, the paucity of rainfall stations in the region and the necessarily large degree of spatial interpolation would give weight to the NDVI-based estimates.

#### Discussion: sources of error

##### *Sources of Error*

In relatively dry regions NDVI and rainfall are highly correlated on both intra-annual and interannual time scales. Because of the complexity of factors affecting vegetation growth, a perfect correlation is not to be anticipated. This, of course, accounts for some of the errors in the rainfall estimates. Other source of error in the estimates include the rainfall data used to derive and validate the regression, spatial inhomogeneities in biophysical conditions, problems in the satellite estimates of NDVI.

#### *The NDVI-rainfall relationship*

Vegetation growth in arid and semi-arid regions is generally water-limited, so that to a first approximately the rainfall-NDVI relationship is linear. The primary growth factor is not rainfall, however, but soil moisture availability. Although soil moisture and rainfall are well correlated in these regions, high intensity rains are manifested more as an increase in runoff, particularly if the soil is already moist. Thus, the increased rainfall is relatively ineffective for vegetation growth. This factor appears to account for some of the major disparities between estimated and observed rainfall.

A good example is the wet year 1987/88; NDVI systematically underestimated rainfall in all years, but particularly so at the station Serowe. Moderate errors were registered for the estimates for Tshane and for the three-station average in area 1. The estimate was near perfect for Ghanzi. A look at monthly totals at these stations (Table 8) shows two months with exceedingly high rainfall at Serowe (241 and 380 mm in December and February, respectively); one month with rainfall approaching 200 mm in the other cases of Tshane and the three-station average, and a comparatively even distribution of rainfall within the season at Ghanzi, with the highest monthly total being 147 mm. Thus, the error in the estimates are roughly

commensurate with the peak monthly rainfall intensities. The errors are largest in the estimates based on NDVI in month with intense rainfall.

It is interesting to note that, in contrast to 1987/88, rainfall is underestimated at Ghanzi during 1988/89. Annual totals are roughly the same in the two years but during 1988/89 rainfall exceeding 200 mm in one month.

An additional reason that the NDVI-rainfall relationship breaks down under relatively wet conditions is that above some threshold, rainfall ceases to be the limiting factor in photosynthesis as the photosynthetic capacity of the vegetation cover is approached (Prince et al., 1994). Since NDVI most directly represents photosynthesis (Sellers, 1985; Tucker and Sellers, 1986), the NDVI-rainfall relationship breaks down. Previous studies in the region suggest that this occurs above a threshold of about 500 to 700 mm/ann (Nicholson and Farrar, 1994; Nicholson et al., 1990, 1995).

#### *Rainfall data*

The analysis was severely limited by the availability of rainfall data in the analysis sector. For areas 1 and 2, only fourteen and fifteen station-years, respectively, were available for the development of the predictive equations. Because of the spatial scale of rainfall variability in arid regions can be smaller than that representative by NDVI, an attempt was made to base the regressions on multi-station averages. These would better represent areally-averaged rainfall. For area 1, however, several years are represented by only station. This means both that the random variability of rainfall significantly affects the regression and that the regression is biased towards the years for which more than one rainfall station reported. Also, the small sampling affects the stability of the estimates.

Another problem is errors in the rainfall data. This is particularly a problem at the higher order stations reporting rainfall only. Readings are taken less

frequently and quality control is poorer, particularly in remote areas like the Kalahari. No estimate of the extent of this problem can be made. However, the initial quality control of the data suggested a significant problem. Unfortunately, only extremely anomalous readings can be flagged. In cases like 1991/92 for the three-station average in area 1, the near-rainless year indicated by the few monthly totals available is probably an error. Missing observations are often erroneously reported as zero. This can account for some discrepancies between estimated and observed rainfall and probably accounts for the error in the estimate for area 1 for 1991/92.

#### *Spatial inhomogeneities*

This method assumes a certain homogeneity of vegetation at nearby stations. This may be true to a first approximation, however, local vegetation anomalies may alter the relationship between rainfall and NDVI. Local differences in species composition, often related to local soil conditions, can play a role, as can vegetation that has been modified by human activities or that has been heavily grazed. Local areas with poor soil conditions likewise introduce variations in the NDVI-rainfall relationship, as does the introduction of irrigation.

When the regressions are applied to producing maps of rainfall in the region, relatively homogeneous soils throughout large areas are necessarily assumed. However, the spatial distribution of soils in the region is quite complex, and this assumption will introduce some error in the analysis.

In general, these inhomogeneities will be small in spatial scale compared to the spatial gradients of rainfall. Therefore this should not cause a serious problem for rainfall assessment over large areas, but will affect local estimates based on general regressions.

### *Systematic errors in satellite estimates of NDVI.*

Systematic errors in NDVI estimates can result from a number of factors, such as satellite calibration or changes in orbital characteristics. This may have been a factor in the systematic over-estimation of rainfall at Tshane (area 2) and Ghanzi (area 3) in 1991 and 1992, as noted earlier. An examination of NDVI there and at other stations similarly indicated anomalously high dry season values in 1991 and 1992, suggesting a systematic source of error. A switch occurred in September 1991 to NOAA-12, with a morning overpass, compared to a near-noon overpass for NOAA-11. Such a change could inflate NDVI values.

Another possibility relates to the Mt. Pinatubo eruption. This data set was corrected for the aerosol effects for the period July 1, 1991, to June 30, 1992. The spatial distribution of the stratospheric aerosols is not strictly homogeneous, while the correction was applied uniformly at each longitude but with a latitudinal variation based on the distribution in the Pacific. Moreover, the error in the correction is a function of vegetation and soil cover. The fact that the over-estimation of rainfall is spatially limited might implicate this source of error, as does the limitation of the problem to the 1991/1992 period.

### *Influence of soil types on the regressions*

In many arid regions, little soil information is available. To test the sensitivity of the results to the inclusion of soil specific regressions, a regression was derived based collectively all "predictor" stations in the four areas. This "bulk" regression was then applied to the estimation of rainfall in each area. Results of the estimates are indicated in Table 6.

In three of the four cases, the error in the estimate is increased on the order of 50% by using the "bulk" regression. Nevertheless, this results in a change of only 6

to 22 mm in the estimates of annual rainfall. In the fourth case, the "bulk" regression slightly improves the estimate. This may be because of the highly inhomogeneous soils in the region, so that a general formula may be more accurate for some locations. This is particularly true for the test station is Serowe, which lies between a zone of luvisols and arenosols.

### Summary and Conclusions

In the area of study, the arid Kalahari of Botswana, NDVI was used effectively to produce estimates of rainfall on monthly and annual time scales. Estimated values of month and annual totals, as well as long-term annual means, compared well with observed values.

There are some physiological limits to the usefulness of the methodology. These relate to high proportion of runoff during extreme rainfall events and the breakdown of the NDVI-rainfall relationship under conditions where moisture is not the limiting factor in growth and NDVI ceases to be a growth indicator. In the case of extreme rainfall events, the most intense rainfall tends to occur over a limited area. Thus, spatial aggregation of both the NDVI data and the rainfall amount predicted therefrom can increase the reliability of the estimates.

In this case study, the reliability of the estimates appeared to be influenced more strongly by problems with both satellite estimates of NDVI and reported rainfall. With proper satellite calibration and correction for orbital considerations and atmospheric and soil properties, NDVI should provide reasonably reliable rainfall estimates in arid and semi-arid regions. The results can also be improved with local geographic knowledge on vegetation and range conditions.

Overall the method is reasonably robust. Vastly contrasting soils do have an impact on the regressions but these changes annual estimates by only tens of mm.

The regressions appear to generally valid for all months and for a variety of rainfall regimes. Thus, NDVI affords an opportunity to extend our climatic knowledge of the world's arid and semi-arid lands.

#### ACKNOWLEDGEMENTS

The authors would like to acknowledge the assistance of the Botswana Meteorological Services in this study, particularly D. Dambe and G. Ramotwa. Much of the research for this article was carried on during the second author's sabbatical at the University of Botswana. We would like to acknowledge the support of the Fulbright Foundation, the National Science Foundation Grant No. ATM-9024340, and the National Institute of Development Research and Documentation of the University of Botswana.

## References

- Arntzen, J.W. and Veenendaal, E.M. (1986). *A Profile of Environment and Development in Botswana*, University of Botswana, Gaborone, 171 pp.
- Bekker, R.P. and De Wit, P.V. (1991). *Contribution to the Vegetation Clasasification of Botswana*, FAO/UNDP/Government of Botswana Project BOT/85/011, Field Document 34, Gaborone, 66 pp.
- Bhalotra, Y.P.R. (1987). *Climate of Botswana, Part II. Elements of Climate 1. Rainfall* Department of Meteorological Services, Gaborone, 40 pp.
- Deuzé, J. L., Herman, M., and Santer, R. (1989). Fourier series expansion of the transfer equation in the atmosphere-ocean system. *JQSRT*. 41: 483-494.
- De Wit, P.V., and Nachtergaele, F.O. (1990). *Explanatory Note on the Soil Map of the Republic of Botswana*, FAO/UNDP/Government of Botswana Project BOT/85/011, Field Document 30, Gaborone, 48 pp.
- Diallo, O., Diouf, A., Hanan, N.P., Ndiaye, A. and Prevost, Y. (1986). AVHRR monitoring of savanna primary production in Senegal, West Africa. *International Journal of Remote Sensing*, 12: 1259-1279.
- Farrar, T.J., Nicholson, S.E., and Lare, A.R. (1994). The influence of soil type on the relationships between NDVI, rainfall and soil moisture in semi-arid



Botswana. Part II. Relationship to soil moisture, submitted to *Remote Sensing of Environment*.

Henricksen, B. L. and Durkin, J. W. (1986). Growing period and drought early warning in Africa using satellite data. *International Journal of Remote Sensing*, 7: 1583-1608.

Holben, B.N. (1986). Characteristics of maximum-value composite images from temporal AVHRR data. *International Journal of Remote Sensing*, 7: 1395-1416.

Justice, C. O., and Hiernaux, P. H. Y. (1986). Monitoring the grasslands of the Sahel using NOAA AVHRR data: Niger 1983. *International Journal of Remote Sensing*, 7: 1475-1498.

King, M., Harshvardhan, D., and Arking, A. (1984). A model of the radiative properties of the El Chichon Stratospheric Aerosol layer. *Journal of Climate and Applied Meteorology*. 23: 1121-1137.

Los, S. O., Justice, C. O., and Tucker, C. J. (1994). A global 1° × 1° NDVI data set for climate studies derived from the GIMMS continental NDVI data. *International Journal of Remote Sensing*. 15: 3493-3518.

Nicholson, S.E. (1986). The spatial coherence of African rainfall anomalies; interhemispheric teleconnections. *Journal of Climate and Applied Meteorology*, 25: 1365-1381.

Nicholson, S.E., and Farrar, T.J. (1994). The Influence of Soil Type on the relationship between NDVI, Rainfall, and Soil Moisture in Semiarid Botswana. I. NDVI Response to Rainfall. *Remote Sensing of Environment*, 50: 107-120.

Nicholson, S.E., Davenport, M.L., and Malo, A.R. (1990). A comparison of the vegetation response to rainfall in the Sahel and East Africa, using Normalized Difference Vegetation Index from NOAA AVHRR. *Climatic Change*, 17: 209-241.

Nicholson, S.E., Lare, A.R., Marengo, J.A. and Santos, P. (1995). A revised version of Lettau's Evapoclimatology model. *Journal of Applied Meteorology*, (in press), 47pp.

Prince, S. D. (1991a). Satellite remote sensing of primary production: comparison of results for Sahelian grasslands 1981-1988. *International. Journal of Remote Sensing*, 12: 1301-1312.

Prince, S.D. (1991b). A model of regional primary production for use with coarse resolution satellite data. *International. Journal of Remote Sensing*, 12: 1313-1330.

Prince, S.D. and Choudhury, B. (1989). Interpretation of Nimbus-7 37 GHz microwave brightness temperature data in semi-arid southern Africa. *International Journal of. Remote Sens.* 10: 1643-1661.

Prince, S.D. and Tucker, C.J. (1986). Satellite remote sensing of rangelands in Botswana II: NOAA AVHRR and herbaceous vegetation. *International Journal of Remote Sensing*, 7: 1555-1570.

Prince, S. D., Justice, C.O., and Moore, B., III. (1994). Monitoring and modelling of terrestrial net and gross primary production. Joint IGBP-DIS-GAIM working paper no. 1.

Sellers, P.J. (1985). Canopy reflectance, photosynthesis, and transpiration. *International Journal of Remote Sensing*, 6: 1335-1372.

Soufflet, V., Tanré, D., Begue, A., Podaire, A, and Deschamps, P.Y. (1991). Atmospheric effects on NOAA AVHRR data over Sahelian regions. *International Journal of Remote Sensing*, 12: 1189-1204.

Thomas, D.S.G., and Shaw, P.A. (1991). *The Kalahari Environment*, Cambridge University Press, Cambridge, 284 pp.

Tucker, C.J., and Sellers, P.J. (1986). Satellite remote sensing of primary production. *International Journal of Remote Sensing*, 7: 1395-1416.

Tucker, C.J., Dregne, H.E., and Newcomb, W.W. (1991). Expansion and contraction of the Sahara Desert from 1980 to 1990. *Science*, 253: 299-301.

## FIGURES

1. Map of rainfall over Botswana, showing the approximate area of the Kalahari.
2. NDVI/rainfall relationships stratified by soil type for stations in Botswana (from Nicholson and Farrar, 1994).
3. Map of study area, including an outline of Botswana. Inner box (thin line) denotes area for which a rainfall map is produced from NDVI (Fig. 9). Dots indicate location of the stations; station groups used in the regression analysis are boxed and labeled with number corresponding to Table 1. The abbreviations used for group 1 are Kang (Ka), Kokong (Ko), Mabutsane (Ma), Takatokwane, Sekoma (Se) and Jwaneng (Jw). Shading indicate the "hardveld"; remainder of study region within Botswana is part of the "sandveld".
4. Time series of NDVI and rainfall for the three stations and one station group for which NDVI is used to estimate rainfall. Dashed line: NDVI. Solid line: monthly rainfall is in mm. The rainfall is a three-month average of rainfall in month concurrent with NDVI and the two preceding months. KKM refers to the combination of Kang, Kokong and Mabutsane.
5. Regression of annual rainfall and annually integrated NDVI for areas 1 through 4. The number of points in the analysis,  $r^2$ , and the slope of the line of regression are given in the lower right of each diagram. Values of B are multiplied by a factor of 10.

6. Regression of monthly rainfall and monthly composited NDVI for areas 1 through 4. The number of points in the analysis,  $r^2$ , and the slope of the line of regression are given in the lower right of each diagram. Values of B are multiplied by a factor of 10.
7. Time series of estimated and observed annual rainfall for the predictand station in areas 2 through 4 and for the three-station predicand group of area 1.
8. Time series of estimated and observed monthly rainfall for the predictand station in areas 2 through 4 and for the three-station predicand group of area 1.
9. Map of mean annual rainfall over the Kalahari and adjacent regions, based on the NDVI-rainfall relationship. In the "sandveld" (see Fig. 3) predictor equations are based on general regression combining areas 1 to 3; in the "hardveld" they are based on the area 4 regression.

Station	Group	Regression/ prediction	Annual mean(mm)
1. Jwaneng	1	r	328*
2. Takatokwane	1	r	252*
3. Sekoma	1	r	245*
4. Kang	1	p	211*
5. Kokong	1	p	254*
6. Mabutsane	1	p	125*
7. Lehututu	2	r	356*
8. Hukuntsi	2	r	290*
9. Lokgwabe	2	r	279*
10. Tshane	2	p	294
11. Hartebeespan	3	r	321*
12. Seribe	3	r	332*
13. Oakdene	3	r	409*
14. Ghanzi	3	p	363
15. Shoshong	4	r	365*
16. Kalamare	4	r	458
17. Mahalapye	4	r	422
18. Serowe	4	p	405

Table 1. Rainfall stations used in the study. Also indicated are their groups, if they were used in the regression (r) or if they were predictand stations (p) and the mean annual rainfall at the site for the study period. An asterisk indicates that observations of annual rainfall were not available for every year, so that the mean applies to a period shorter than 11 years.

Group(s)	d	b	a	n	r <sup>2</sup>
1	14.5	252.1	0.167	238	0.36
2	13.4	355.4	0.164	217	0.47
3	13.8	291.8	0.164	295	0.52
4	15.5	340.0	0.182	387	0.53
all	14.2	312.2	0.170	1137	0.50

Table 2. Details of predictive equations at monthly scale.

Rainfall =  $d + b \times (\text{NDVI} - a)$ , where  $n$  = number of points in the regression and  $r$  is the correlation between NDVI and rainfall.

Group(s)	d	b	a	n	r <sup>2</sup>
1	103.1	169.0	1.37	14	0.63
2	117.5	311.0	1.72	15	0.62
3	113.6	219.6	1.54	20	0.63
4	140.8	355.5	2.04	29	0.66
all	129.3	269.1	1.74	78	0.64
1, 2 and 3	125.6	213.0	1.52	49	0.61

Table 3. Details of predictive equations at the annual scale.

Rainfall = d + b x (NDVI- a), where n= number of points in regression and r is the correlation between NDVI and rainfall.



Group	n	mean error (mm)	$r^2$
1	103	13.4	0.35
2	144	14.0	0.46
3	144	15.1	0.65
4	144	19.2	0.58
ALL	535	15.6	0.53

Table 4. The mean error and the square of the correlation coefficient  $r$  between observed and estimated monthly rainfall, using regressions specific to each soil type and a general regression for all groups;  $n$  is the number of correlations pairs.

Group	n	mean error (mm)	$r^2$
1	10	92.5	0.56
2	11	62.8	0.39
3	11	55.2	0.64
4	11	116.6	0.67
ALL	43	82.7	0.59
1, 2 and 3	32	71.2	0.49

Table 5. The mean error and the square of the correlation coefficient  $r$  between observed and estimated annual rainfall, using regressions specific to each soil type, a general regression for all groups and a regression for groups 1, 2 and 3;  $n$  is the number of correlation pairs.

		Individual regressions		General regression	
Group	observed (mm)	estimated (mm)	difference (mm)	estimated (mm)	difference (mm)
1	242	283	41	305	63
2	295	276	19	263	32
3	364	355	9	349	15
4	405	472	67	461	56

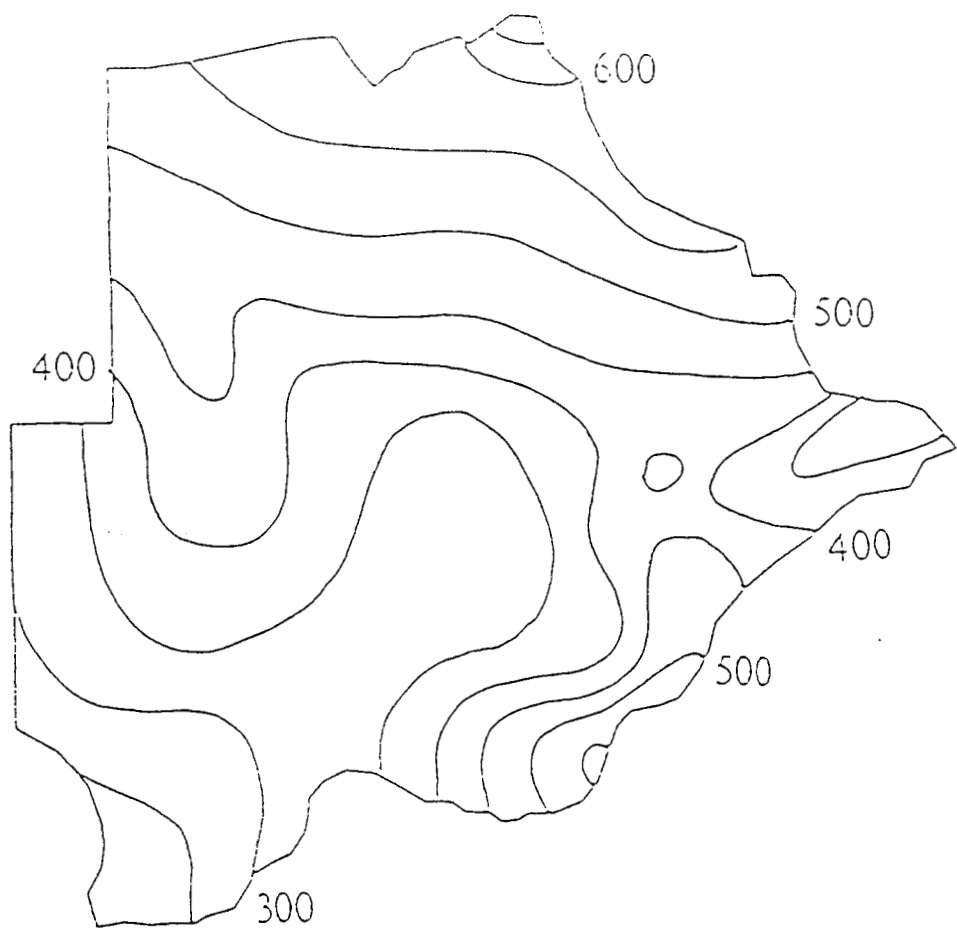
Table 6. Observed vs. estimated 11-year rainfall means for the test stations of groups 1 through 4, using firstly regressions specific to each soil type and then a general regression for all groups.

Station	long term mean	11 year mean	diff. (mm)	diff. %
Dibete	381	386	+5	+1
Gaborone	531	445	-86	-16
Ghanzi	430	363	-67	-16
Kalamare	448	458	+10	+2
Lobatse	565	447	-118	-21
Mahalapye	471	422	-49	-10
Mochudi	500	382	-118	-24
Molopolole	503	322	-181	-36
Phitshane	464	326	-138	-30
Ramatlabama	513	385	-128	-25
Serowe	459	405	-54	-12
Tshane	353	294	-59	-17

Table 7. Difference between long term mean annual rainfall and the mean annual rainfall from the study period. From this sample, the study period was on average 17% drier than the long term mean.

station and yr	Sept.	Oct.	Nov	Dec.	Jan.	Feb.	Mar.	Apr.
Tshane 87/88	1	5	36	126	2	186	60	34
Ghanzi 87/88	7	11	24	147	71	134	45	95
KKM 87/88	23	0	32	96	65	177	34	43
Serowe 87/88	21	5	111	241	89	380	161	95
Ghanzi 88/89	0	26	5	130	159	203	41	57

Table 8. Monthly rainfall at predictand stations for selected wet years. KKM is the average of the 3 Stations Kang, Kokong and Mabutsane (group 1).

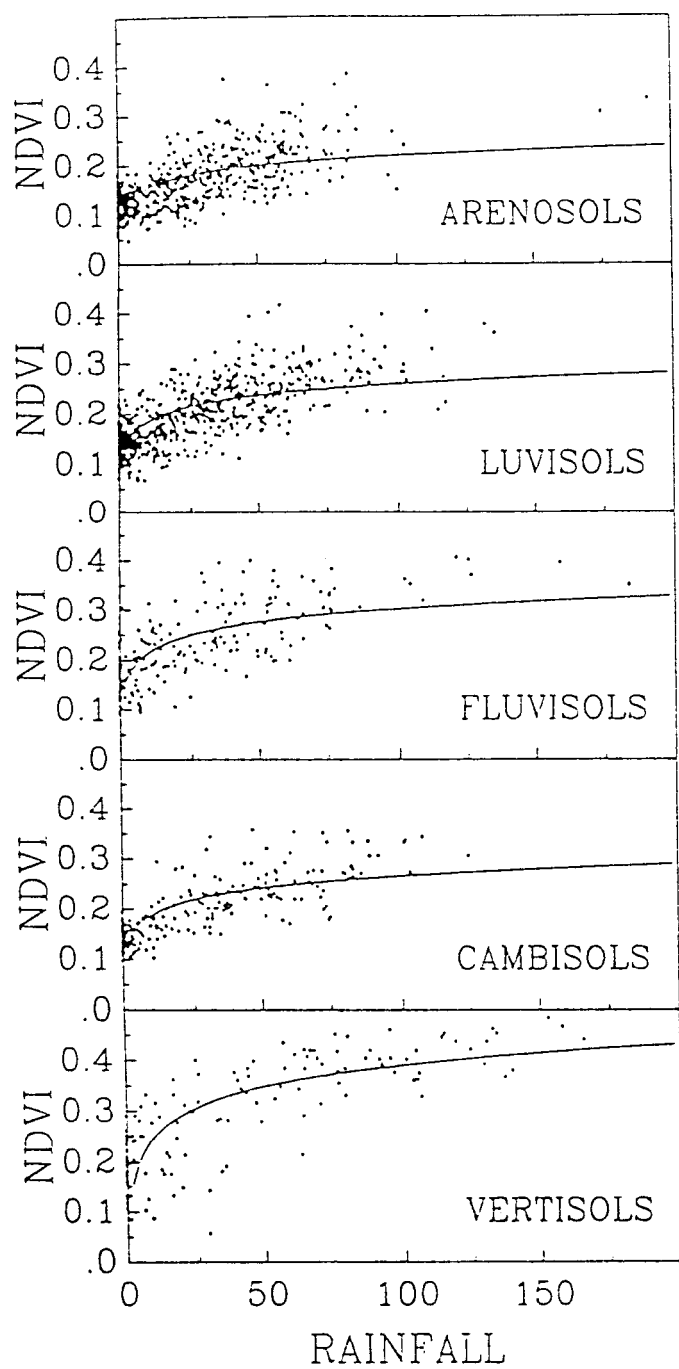


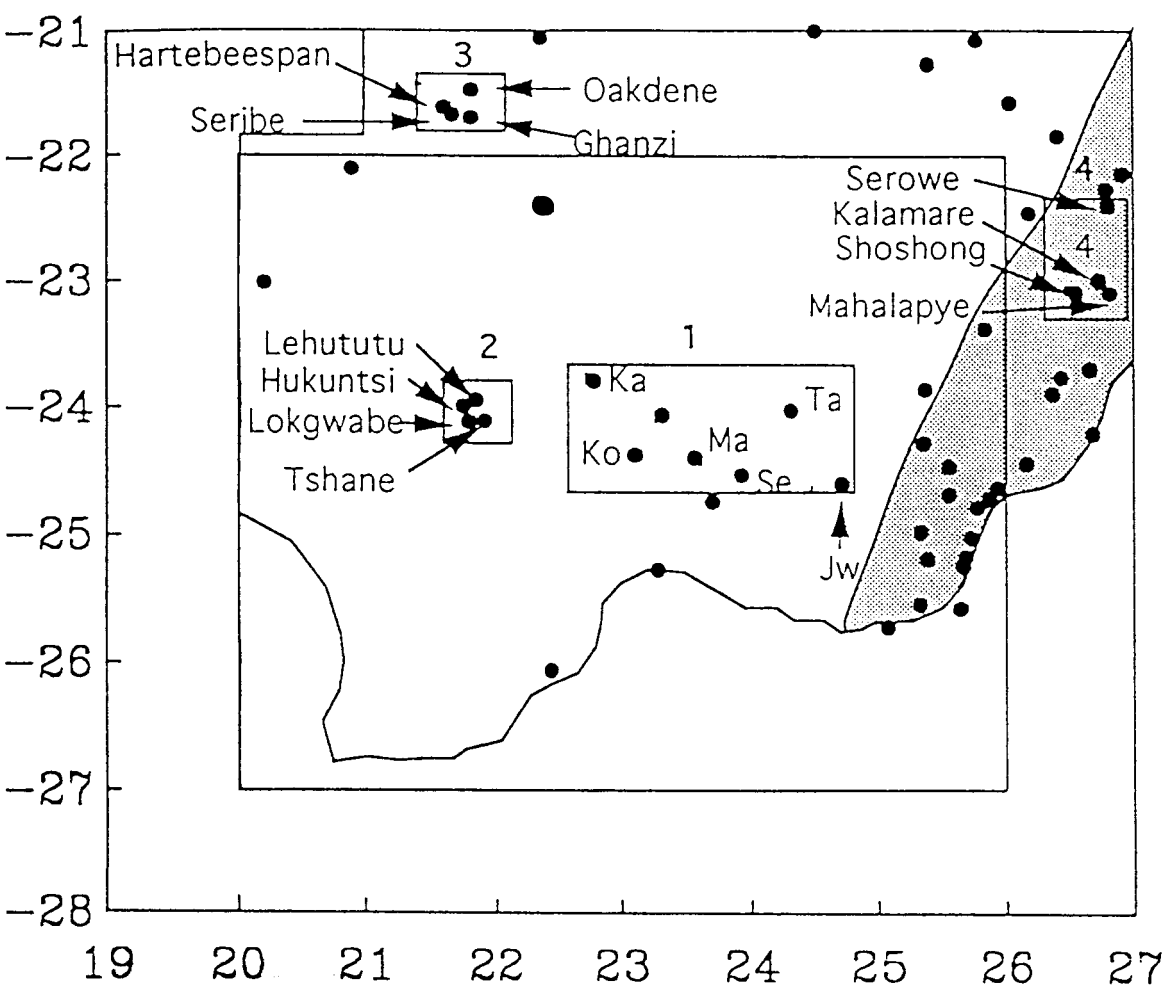
20

25

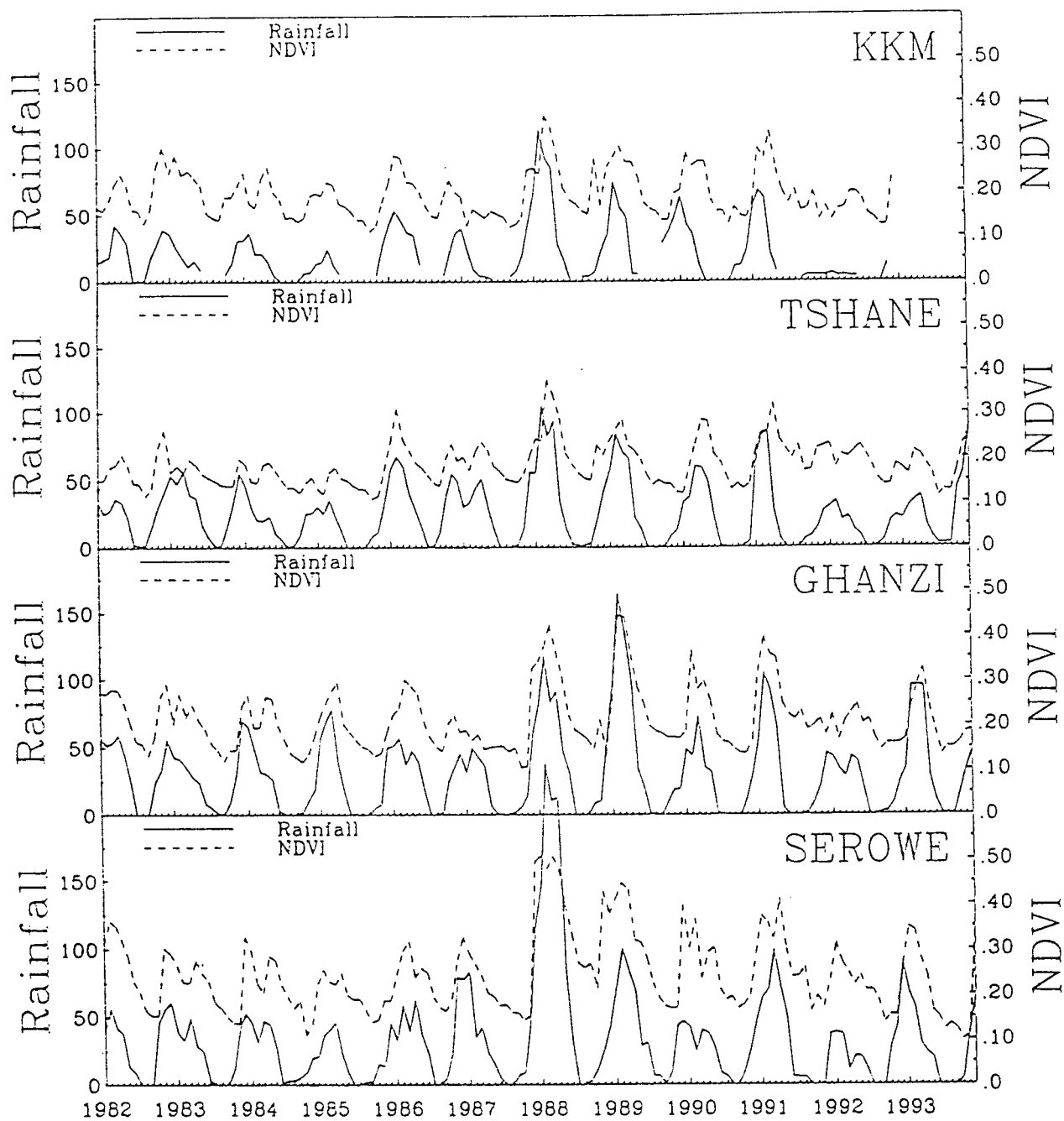
30

TM000

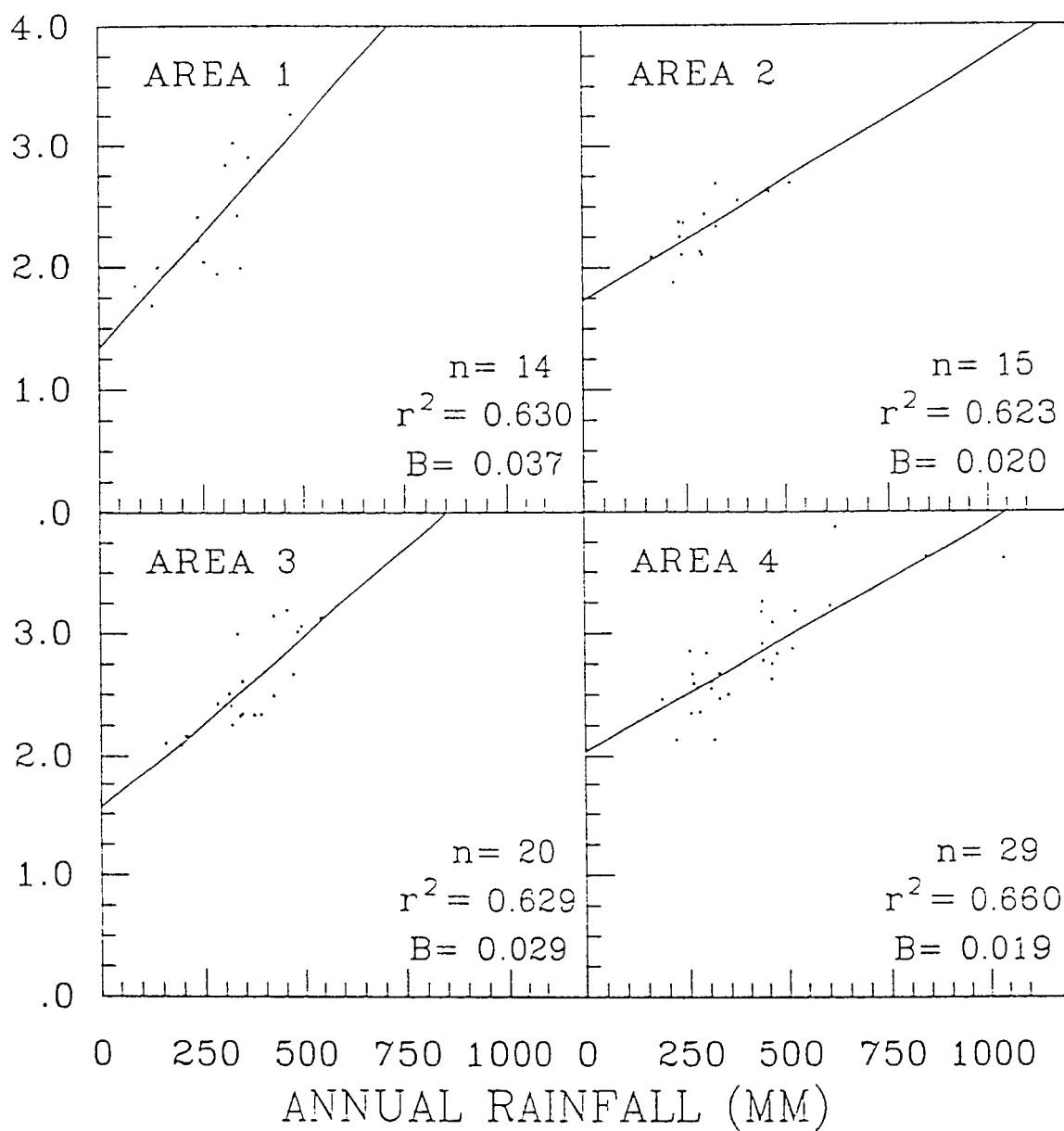


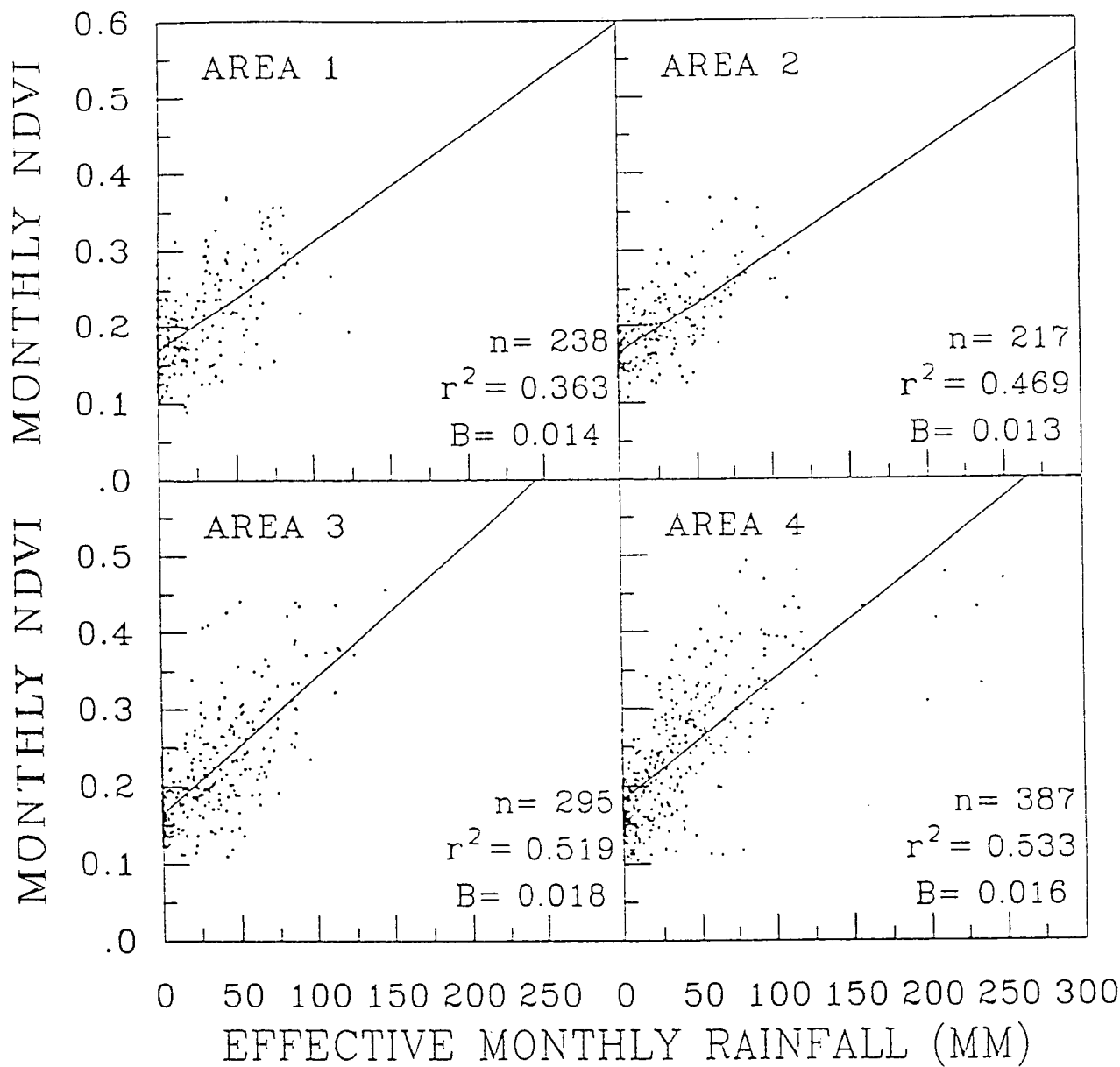


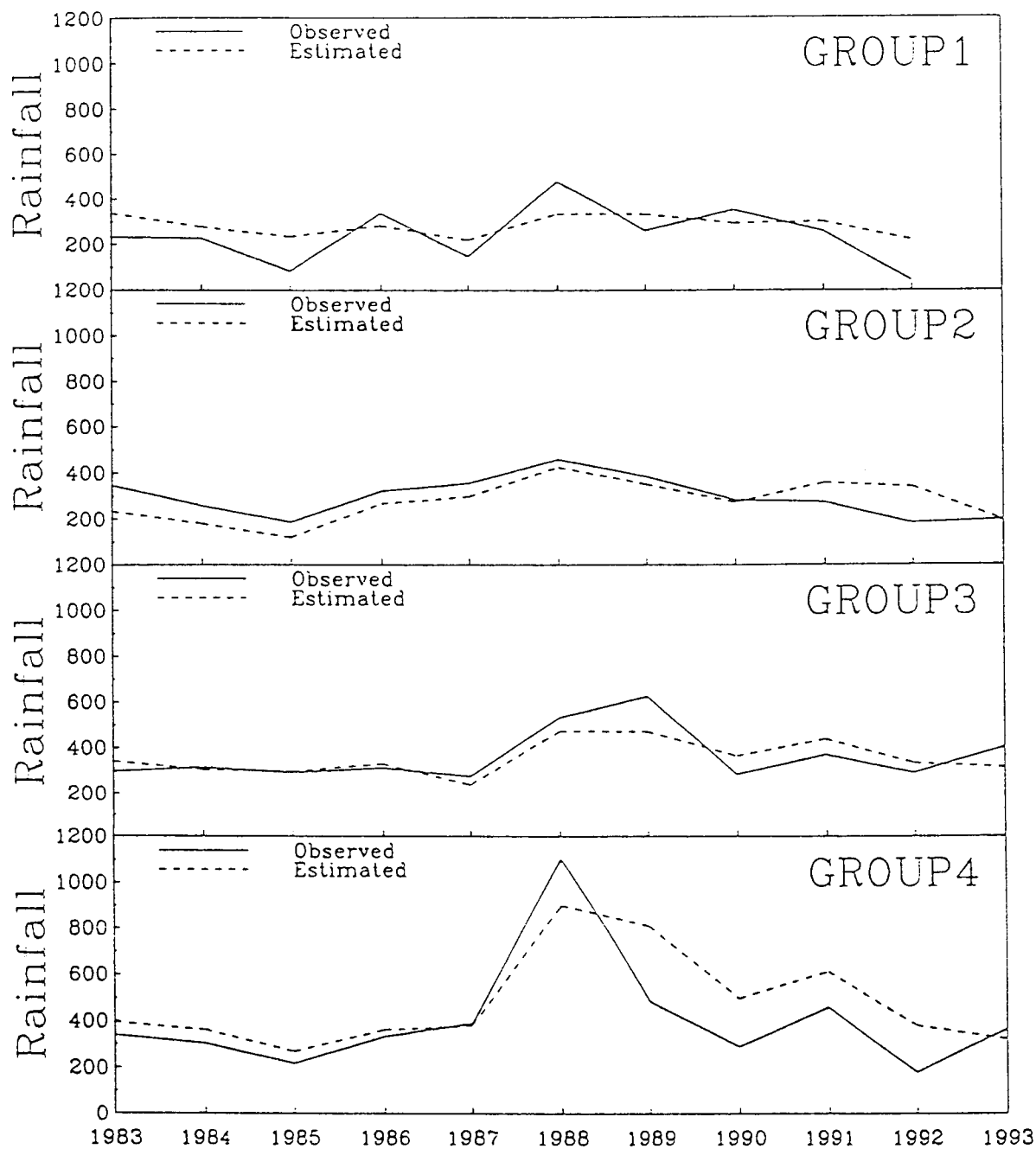


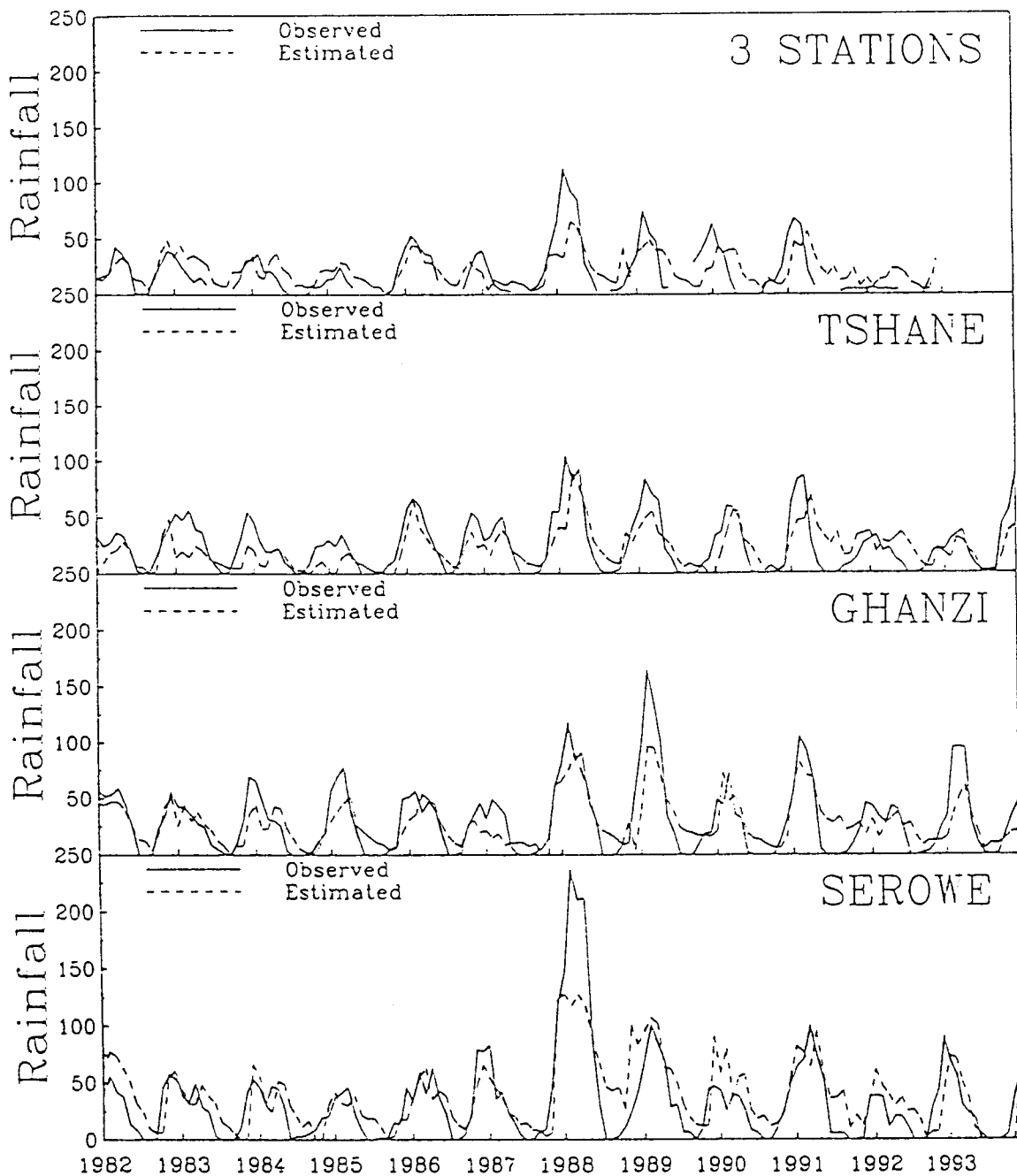


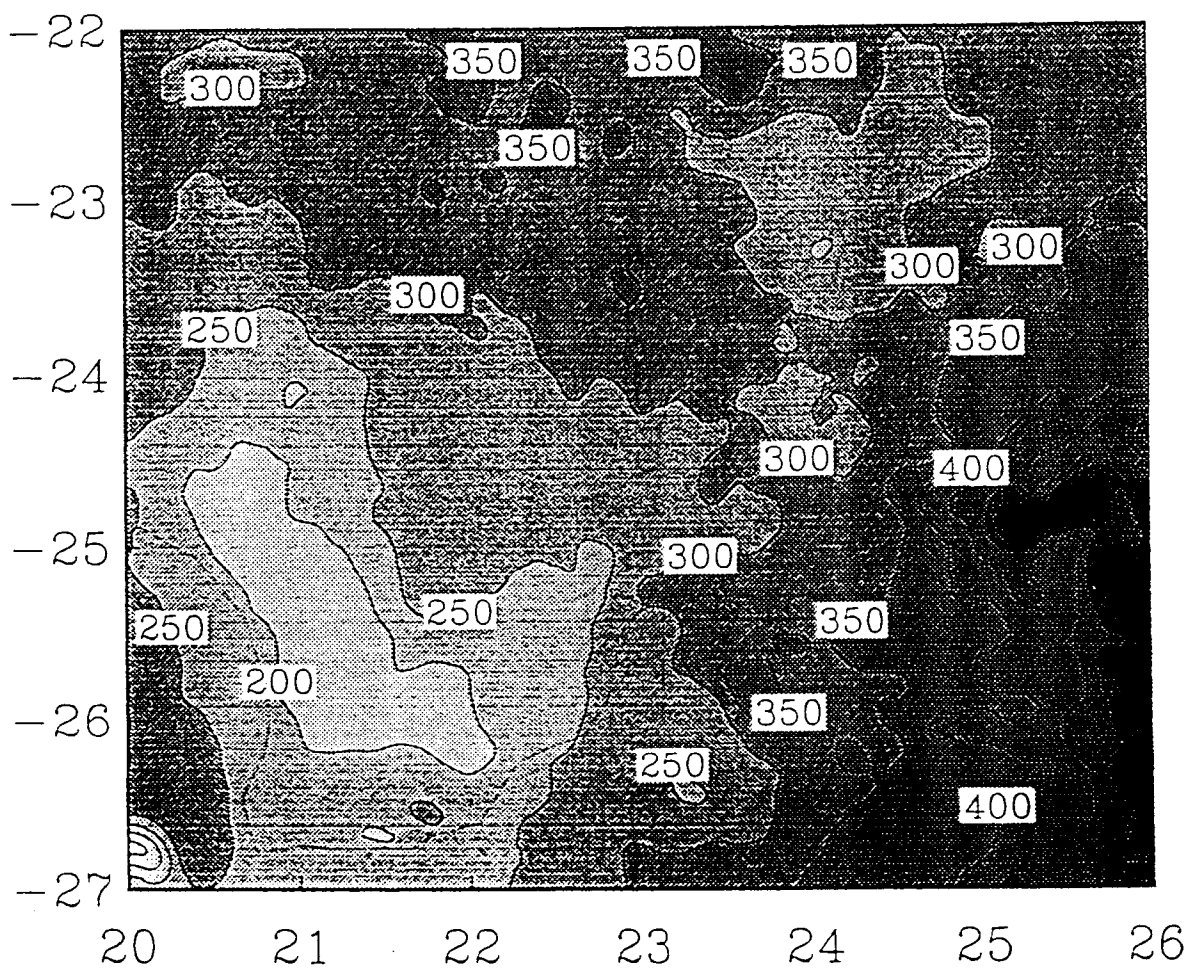
ANNUAL NDVI











## **Appendix H**

### **The mean surface water balance over Africa and its interannual variability**

# The mean surface water balance over Africa and its interannual variability

S. E. Nicholson, J. Kim, M. B. Ba

Department of Meteorology  
Florida State University  
Tallahassee, FL 32306

and

A. R. Lare

Applied Research Corporation  
NASA/GSFC- Code 913  
Greenbelt, MD 20771

Submitted to the *Journal of Climate*

February 1996



## Abstract

This article presents calculations of surface water balance for the African continent, using a new, physically based model. Calculations are based on approximately 1400 rainfall stations with records generally covering 60 years or longer. Continental maps of evapotranspiration, runoff and soil moisture are derived for January, July and the annual mean. The model is also used to provide a gross estimate of the interannual variability of these parameters over most of the continent and local water balance calculations for a variety of locations in Africa. The results are compared with four other comprehensive global water balance studies. The results of this study are being used to produce a  $1^{\circ} \times 1^{\circ}$  gridded data set for the continent, with potential applications for numerical modelling studies.

The important role of the hydrologic cycle in global weather and climate has become increasingly recognized, as the creation of the international GEWEX program attests (Chahine 1992a, b). Numerous studies have demonstrated that accurate representation of surface hydrology can improve weather forecasts (e.g., Walsh et al. 1985). Hydrological feedbacks modify the interannual variability over land (Entekhabi et al. 1992) and dramatically influence ocean-atmosphere interactions (Webster 1994). Recycled water can contribute as much as 50 % of the atmospheric water vapor over continents (Brubaker et al. 1993). Such feedbacks may have played a role in intensifying and prolonging the drought in the West African Sahel (Nicholson 1989).

During the past decade considerable effort has been put into the representation of hydrologic processes in numerical models. The recent project for Intercomparison of Land Surface Parameterization Schemes (PILPS) has uncovered significant shortcomings, particularly in runoff calculations (Pitman et al. 1993). In one comparison, model predictions of runoff for the "wet" month of August ranged from 30 to over 400 mm. Model improvements require accurate surface hydrologic data for initialization, boundary conditions, and validation.

Unfortunately, parameters such as evapotranspiration (ET) or runoff are rarely measured directly. The few measurements that exist are at local or basin scale. ET is generally calculated from empirical formulae or energy balance approaches. Runoff is generally calculated as a residual. Few data are available for continental or global-scale comparisons.

The best known comprehensive studies of global water balance are those of Baumgartner and Reichel (1975), Willmott et al. (1985), Henning (1989) and Mintz and Walker (1993). Henning's calculations are based on empirical formulae derived by Albrecht (1951, 1962) from data for one station in the Gobi desert; maps of ET, runoff and various radiative parameters are drawn manually from station records.

Baumgartner and Reichel (1975) produce maps of evapotranspiration and runoff from the station data produced by Thornthwaite and associates (e.g., 1962-65). Both studies use station data irregularly distributed and covering in many cases only a few years. Willmott et al. (1985) use basically the Thornthwaite method for calculations but improve on the data set; they present ET and soil moisture, but not runoff. Mintz and Walker (1993) use a simple water balance model with precipitation and potential evapotranspiration as input. Both of these last two studies extrapolate the areal integrals best suited for the gridded weather and climate models, but produce maps based on very coarse resolution ( $4^{\circ} \times 5^{\circ}$ ) data.

In this paper, we present calculations of surface water balance for the African continent, using a new, more physically based approach and a more comprehensive data set. Continental maps of evapotranspiration, runoff and soil moisture are derived using the "evapoclimatology" model of surface water balance (Nicholson et al. 1996). Calculations also provide a gross estimate of the interannual variability of these parameters over most of the continent and local water balance calculations for a variety of locations in Africa. Emphasis is placed on the drought-prone West African Sahel, a region where surface hydrology appears to play a major role in modulating the interannual variability of climate. The results of this work are being used to produce a  $1^{\circ} \times 1^{\circ}$  gridded data set that will be available through an anonymous FTP server through the Department of Meteorology at Florida State University ([ftp.met.fsu.edu](ftp://ftp.met.fsu.edu)).

## 2. Methodology

### 2.1 Data

The basic input data is precipitation for nearly 1400 stations reasonably well

distributed over the African continent (Fig. 1). This archive has been collected, processed and updated by the first author over many years and used in numerous research applications (e.g., Nicholson 1994). Quality control tests have been performed and resulted in discarding about 5% of the data. The water balance calculations utilize long-term means calculated as the arithmetic mean of data for all available years. The annual mean and means for January and July are shown in Fig. 2. Because of the strong interdecadal variability of rainfall over parts of Africa, most notably the Sahel, we have found the so-derived mean to be more stable than, for example, means for a standard 30-year period. Three-quarters of the stations records commence prior to 1925 and most records have been updated to 1990 or later. Thus, in most cases the long-term mean refers to a period of 60 years or longer. The subsequently calculated water balance parameters also represent means for these multi-decadal periods.

Other input data required for the climatology model are indicated in Fig. 3, showing an overview of the climatology model and the climate and radiative parameters and soil and vegetation information needed for its application. The resolution of the input data sets is quite varied, ranging from several kilometers to  $5^{\circ}$  of longitude and latitude. In all cases, data appropriate for the individual stations are extrapolated from the data sets.

Vegetation information is derived from two sources: (1) AVHRR data from the NOAA polar-orbiting satellites are used to calculate NDVI, with a resolution of approximately 7.6 km, and (2) the Dorman and Sellers (1989) vegetation data set, that includes 12 vegetation types and has a  $5^{\circ} \times 5^{\circ}$  resolution, provides gross estimates of type, coverage and emissivity. The coarser resolution of the latter is sufficient, since the model is considerably more sensitive to NDVI (Normalized Difference Vegetation Index). The NDVI data were provided by C. J. Tucker of the GIMMS group at NASA Goddard and are described in more detail in Nicholson and Farrar

(1994).

Soils information, including texture, organic matter and cation exchange capacity (CEC), is taken from Zobler (1986) and Webb et al (1991). Produced for climate models, the data have a  $1^{\circ} \times 1^{\circ}$  resolution.

The radiative parameters, global radiation at the surface and surface albedo, were derived from METEOSAT data for each station location. These represent means for the period 1983 to 1988. The estimation of these data is described in two companion articles by Ba et al. (1996) and Ba and Nicholson (1996).

## 2.2 The Evapoclimatology Model

Monthly and annual values of evapotranspiration, runoff and soil moisture are calculated by a surface water balance model termed "evapoclimatology". This is a revised version of the quasi-empirical model originally developed by Lettau (1969) and Lettau and Baradas (1973). Details of the model and model equations have recently been published in a number of sources (e.g., Lare and Nicholson 1994, Nicholson et al. 1996, Marengo et al. 1996), hence only a brief overview is presented here. The model was validated using data for the HAPEX-Sahel experiment, conducted over the central Sahel in 1992 (Nicholson et al. 1996, Marengo et al. 1996).

The evapoclimatology submodel is essentially a numerical solution to a simplified form of the hydrologic balance equation:

$$P = E + N + \frac{dm}{dt} \quad (1)$$

where  $P$  is precipitation,  $E$  is evapotranspiration,  $N$  is runoff, and  $dm/dt$  is the change in soil moisture storage. Three assumptions are made in order to maintain

simplicity (Lare and Nicholson 1990). The first is that for a continental region with a stable climate there is no net storage of moisture over sufficiently long time periods (i.e., for the multi-year period for which means of forcing functions are derived). Therefore:

$$\bar{P} = \bar{E} + \bar{N} \quad (2)$$

The second assumption is that the processes of runoff and evapotranspiration can be further subdivided into immediate (') and delayed (") parts. Thus:

$$E = E' + E'' \quad (3)$$

$$N = N' + N'' \quad (4)$$

Immediate processes are those that occur in the same month as the precipitation, while delayed implies processes that are associated with the rain which fell in previous months. For evapotranspiration,  $E'$  roughly corresponds to the contribution of soil evaporation and the evaporation of intercepted/detained surface moisture, while  $E''$  is roughly the transpirational component, which draws from the deeper soil moisture reservoirs. For runoff, the partitioning roughly corresponds to surface runoff vs. gravitational drainage.

The final assumption of the evapoclimatology submodel is that the delayed processes vary directly in proportion to soil moisture according to:

$$N''(t) = \frac{\bar{N}''m(t)}{\bar{m}} \quad (5)$$

$$E''(t) = \frac{\bar{E} m(t)}{\bar{m}} \quad (6)$$

where  $\bar{N}''$  and  $\bar{E}''$  are the mean quantities of delayed runoff and evapotranspiration. These quantities are combined in such a way as to yield a process parameter known as "residence time"  $t^*$ :

$$t^* = \frac{\bar{m}}{\bar{N}'' + \bar{E}''} \quad (7)$$

This represents the time required for a volume of water equal to the annual mean of exchangeable soil moisture to be depleted by the delayed processes of runoff and evapotranspiration.

With these considerations, the resultant hydrologic balance formula is:

$$P - E' - N' = \frac{m}{t^*} + \frac{dm}{dt} \quad (8)$$

By subtracting the annual means from each term in the above equation, an ordinary differential equation results:

$$P'(t) = \frac{m - \bar{m}}{t^*} + \frac{d(m - \bar{m})}{dt} \quad (9)$$

where

$$P'(t) = P - E' - N' - (\bar{P} - \bar{E}' - \bar{N}') \quad (10)$$

This is solved as:

$$m - \bar{m} = e^{-t/t^*} \left[ \text{constant} + \int e^{t/t^*} p' dt \right] \quad (11)$$

Because of the initial assumption of climatic stability, the bracketed term must approach 0, thus determining the integration constant.

This model requires the parameterization of immediate and delayed evapotranspiration and runoff and the estimation of two model parameters, the residence time  $t^*$  and a second process parameter termed evaporivity  $e^*$ , representing the efficiency at which solar radiation is used in the evaporation process. Immediate runoff  $N'$  is calculated following Warrilow (1986), using infiltration capacity and rainfall; delayed runoff  $N''$  is calculated as gravitational drainage, using the hydraulic conductivity and soil moisture content. Immediate evapotranspiration  $E'$  is calculated as the product of evaporivity and precipitation, prorated by the ratio of monthly to annual absorbed solar radiation for the month in question.  $E''$  is calculated as a residual.

The calculation of the process parameters  $e^*$  and  $t^*$  is more empirically-based. Residence time  $t^*$  is calculated after Serafini and Sud (1987) as a function of potential evapotranspiration, wilting point and field capacity, with an adjustment of values for various vegetation types. Wilting point and field capacity are determined according to Saxton et al. (1986) as a function of soil type (i.e., percent sand and clay content). The evaporivity  $e^*$  is defined as a nonlinear measure of the capacity of the land surface to use a portion of monthly solar radiation to evaporate precipitation received in the same month. It serves the same function as potential evaporation in traditional water balance models and is analytically derived by using the



Normalized Difference Vegetation Index, or NDVI (see Lare 1992).

In earlier versions of the model (Lare and Nicholson 1990, 1994; Nicholson and Lare 1990; Farrar et al., 1994), the soil moisture estimate only refers to exchangeable soil moisture (m), i.e., that available for the processes of runoff and evapotranspiration. The residual water content (rwc) must be added to the calculated exchangeable soil moisture to obtain the true soil moisture contents. Residual water content is determined after Rawls and Brakensiek (1989):

$$\text{rwc} = 10 \left[ 0.2 + 0.1 (\% \text{ om}) + 0.25 (\% \text{ clay}) (\text{cec})^{0.45} \right] d \quad (12)$$

where rwc is the residual water content in mm, (% om) is percent organic matter content, (% clay) is percent clay content, (cec) is cation exchange capacity, and d is the bulk density of the entire soil layer (0-100 cm).

### 3.0 Results

#### 3.1 Mean Maps

Annual average evapotranspiration and monthly averages for January and July are shown in Fig. 4. The 100 mm contour roughly bounds the Sahara on the north, its location varying from about 31 ° to 35 ° N, and on the south at 18 ° to 20 ° N. The 500 mm contour is situated near 15 ° N, running through Lake Chad. The position of both contours is essentially identical to that of the corresponding rainfall isohyets (Fig. 2), indicating low runoff throughout this region. Throughout most of the tropics, from about 12 ° N to 12 ° S, annual evapotranspiration exceeds 1000 mm; in three humid cores closer to the equator it exceeds 1500 mm, reaching 2000 mm in the wettest areas. Reduced values are evident on the eastern margins of these

latitudinal zones, reflecting the more arid climates of eastern Africa with evapotranspiration on the order of 500 to 750 mm. In the semi-arid subtropics of southern Africa it generally ranges between 200 and 750 mm, with small values reflecting the Namib desert and the karoo of South Africa.

Monthly values reflect the annual march of the ITCZ and rainy season over Africa. In July, evapotranspiration exceeds 100 mm in a core region extending roughly between the equator and  $15^{\circ}$  N. It exceeds 50 mm from there to about  $18^{\circ}$  N and  $5^{\circ}$  S. In the southern Sahel of West Africa ( $\sim 12$  to  $15^{\circ}$  N), it is on the order of 50 to 100 mm and 5 to 50 mm in the northern Sahel ( $\sim 15$  to  $18^{\circ}$  N). Elsewhere, it is generally in the range of 5 to 50 mm, except for the desert areas of the Sahara, the Namib and the central Kalahari. Within the central Sahara it exceeds 5 mm in two locations, a western sector where winter rainfall is not uncommon and the Tibesti highlands to the northeast of Lake Chad.

In January, the zone of maximum ET is shifted southward, values exceeding 100 mm roughly from the equator to  $20^{\circ}$  S. In the southern Sahel, ET has fallen to 5 to 50 mm during January. Values below 5 mm are evident in a much broader area surrounding the Sahara and including the northern Sahel, but are restricted to small coastal desert sectors in the Southern Hemisphere. In both months it is on the order of 5 to 50 mm in northern Africa.

Runoff is shown in Fig. 5. In the annual mean, the 1 mm contour extends to roughly  $15^{\circ}$  N, indicating no surface runoff in the northern Sahel. North of the desert it lies near  $35^{\circ}$  N, bounding small mountainous areas in the northwest where runoff can reach 50 mm. In tropical latitudes, excluding eastern equatorial Africa, runoff is on the order of 200 to 500 mm. In semi-arid southern Africa annual runoff ranges from about 10 to 200 mm, but there is a strong gradient between  $10$  and  $15^{\circ}$  S, so that it is below 50 mm throughout most of the region. It approaches zero in the Namib, southern Kalahari and karoo.

As with evapotranspiration, monthly values reflect the annual march of the ITCZ and rain belt. The core region with values exceeding 10 mm per month migrates from the northern tropics in July to the southern tropics in January. It exceeds 50 mm only during July in areas along the Guinea coast of West Africa.

Soil moisture is shown in Fig. 6. It generally ranges, in the annual mean, from about 10 mm in the Sahelo-Saharan region to over 200 mm in an equatorial core extending from roughly  $10^{\circ}$  N to  $5^{\circ}$  S. It ranges from about 10 to 50 mm in the semi-arid Kalahari and karoo of Southern Africa, but falls well below 10 mm in the Sahara and the coastal deserts of Southern Africa. These same ranges are evident in January and July, but the areas of maxima and minima are displaced, slightly northward in July and considerably southward in January.

### 3.2 Local water balance

The mean water balance for seven diverse locations in Africa is shown in Fig. 7. Algiers, along the Mediterranean coast, receives winter rainfall. The stations Tahoua, Sikasso, Gagnoa, and Bambesa represent a gradual transition from the "summer" rainfall region of the Sahel, through the savanna and woodlands to the equatorial forest with year-round rains. Harare and Gaborone represent the southern-hemisphere analogs to the Sahel, savanna regions with summer rainfall.

Runoff is almost negligible at Algiers, where the winter rains are frontal in nature and, therefore, low in intensity, promoting infiltration and subsequent evapotranspiration. Consequently, evapotranspiration continues throughout the dry season, drawing on the soil reservoir of moisture. Thus, the magnitude of the annual cycle of ET is considerably lower than that of rainfall. At Tahoua, in the northern Sahel, runoff is essentially zero; local runoff may occur and collect in internal drainage ponds, from which it later evaporates. Evaporation exceeds

rainfall during three months, but is negligible much of the year.

In the more tropical latitudes, runoff is considerably greater. At Sikasso, with a single, intense rainy season, it reaches about 30 mm/mo during August. There, ET exceeds rainfall during about half of the year and reaches a maximum of nearly 200 mm/mo in August and September. At Gagnoa, with roughly the same amount of rainfall, there are two, less intense rainy seasons and consequently lower peak runoff. Since both rainy seasons are preceded by dry seasons, the soil does not become strongly saturated, a contributing factor to the relatively low amounts of runoff. At Bambesa, with year-round rainfall, the soil moisture continues to increase throughout the season, hence both ET and runoff continue to increase throughout the rainy season. ET reaches about 130 mm/mo during the first peak in the rainy season, but about 170 mm/mo during the second, broader peak. Runoff reaches about 30 mm/mo during the first peak, compared with about 80 mm/mo during the second.

At the southern-hemisphere savanna stations, the picture is quite different. The rainy season is longer than in Sahelian locations with comparable annual amounts and therefore peak values of rainfall and ET are considerably lower. At Harare, rainfall reaches c. 170 to 190 mm in three months, while ET does not exceed 125 mm. Evapotranspiration continues throughout the long dry season. At Gaborone, rainfall barely reaches 100 mm/mo and ET does not exceed 70 mm/mo, but, as at Harare, continues throughout the dry season. This contrast with other tropical locations is due to the nature of the rain-bearing systems. In southern Africa, these are often frontal in nature, reflecting significant mid-latitude influences; convective systems prevail elsewhere. The water balance at Gaborone, with a "tropical" summer rainfall regime, is similar to that at Algiers, with an extra-tropical winter rainfall regime. The most apparent difference is higher dry-season evapotranspiration at Algiers, a consequence of its occurrence during the summer,

compared to the winter dry season at Gaborone.

### 3.3 Interannual variability

The African continent is well-known for the extreme interannual variability of rainfall, particularly in the semi-arid subtropics. This produces complex changes in the surface water balance. To provide a simple illustration of the magnitude of interannual variability of water balance parameters, the difference between values for one continentally wet year and one continentally dry year are shown in Figs. 8, 9 and 10. For select locations, calculations on a monthly scale are done for the wettest and driest ten years and compared to the long-term mean (Figs. 11 and 12).

Over most of the continent, rainfall in 1955 exceeds that in 1983, with the difference exceeding 250 mm in large areas. The exceptions are areas of the Sahara, where differences are negligible, and parts of equatorial Africa, where 1955 was actually the drier of the two years. Other than at these locations, these two years provide a reasonable estimate of the magnitude of interannual variability of evapotranspiration and runoff.

The excess rainfall during 1955 results in nearly the same excess in ET throughout most of the continent. Only in equatorial regions are differences distinguishable from the relatively coarse map in Fig. 9. Thus, ET varies by hundreds of mm from year to year over large sectors of Africa.

Large differences in runoff are apparent only in tropical latitudes and in areas of relatively high elevation: the Mediterranean coast, the Ethiopian highlands, coastal sectors of Angola, and the eastern half of the southern sub-continent. In these areas, the interannual variability of runoff is on the order of 25 to over 100 mm. North of c. 15° N, i.e., in the northern Sahel, the difference is negligible, with the increased rainfall in 1955 being totally manifested as increased

evapotranspiration. This characteristic was noted earlier by Lare and Nicholson (1994), who pointed out the resultant change in the latitudinal gradient of latent heating across West Africa, an effect potentially large enough to modulate the interannual variability of rainfall.

Fig. 11 underscores the interannual variability of runoff via calculations for the wettest and driest years at six of the locations shown in Fig. 7. An asymmetry is clearly apparent, with runoff not changing markedly during the dry years, but being dramatically enhanced during the wet years. At the low latitude stations of Gagnoa and Bambesa, this difference can be 150 to nearly 300 mm per month. At Harare in southern Africa similar differences are apparent in March. Differences are small in the more arid locations.

For evapotranspiration, the monthly differences at these stations (Fig. 12) are more symmetric between dry and wet years. During the wettest months the difference between dry and wet years is on the order 100 to 150 mm. An interesting trend is observed at Gagnoa, where ET has two peaks during the year in the mean and during the driest year, but essentially one peak from August to October during the wettest year. The latter probably reflects a diminished dry season intensity during the wet year and a continual increase in soil moisture throughout the season. A similar pattern is observed in the mean at Bambesa, the wettest station. However, during the wettest year at Bambesa, the two-peaked pattern in ET emerges, probably a manifestation of higher rainfall earlier in the year, when sun is nearly overhead and radiation (and hence potential ET) are high.

### 3.4 Long-term Trends

The long-term trends in rainfall and runoff are shown in Fig. 13 for each ten degrees of latitude from 40 ° S to 40 ° N for the period 1950-1989. These depict broad

continental scale trends, but may not capture some more local patterns in cases where climate anomalies are not zonally oriented, such as the subtropics of Southern Africa. Annual rainfall and runoff are calculated for the calendar year (January to December) by averaging the annual values at all stations in the zone.

The zone from  $10^{\circ}\text{N}$  to  $20^{\circ}\text{N}$  is the only one where a strong trend in either variable is evident over this 40-year period. Both rainfall and runoff show a steady downward trend over this period, with a marked decrease occurring around 1970. This zone encompasses the Sahel-Soudan region of West Africa, where the long downward trend is well known (e.g., Nicholson and Palao 1993). There is some semblance of this trend in the two equatorial zones ( $0^{\circ}$  to  $10^{\circ}\text{N}$  and  $0^{\circ}$  to  $10^{\circ}\text{S}$ ), but an increase is apparent in rainfall and runoff in both zones in the mid- to late-1980s. In the outer tropics of the southern hemisphere ( $10$  to  $20^{\circ}\text{S}$ ) there is a general downward trend over the 40-year period, as in the same latitudes of the northern hemisphere, but here rainfall and runoff begin to decrease earlier (in the mid-1960s), the trend is less steady, and relatively wet conditions interrupt the trend in the mid- and late-1970s. A similar course of rainfall and runoff is apparent further south in the zone from  $20^{\circ}$  to  $30^{\circ}\text{S}$ .

Thus, throughout the area from  $30^{\circ}\text{S}$  to  $30^{\circ}\text{N}$  there is a general trend towards drier conditions during the last few decades, a pattern also described in Nicholson (1994) using individual station data. However, in the extra-tropical latitudes a generally opposite trend is apparent. The period 1970-89 is somewhat wetter than the two previous decades, with the change in rainfall being more apparent than the change in runoff.

#### 4. Comparison with Results of Other Studies

The most comprehensive global water balance studies are those of

Baumgartner and Reichel (1975), Henning (1989), Willmott, Rowe, and Mintz (1985) and Mintz and Walker (1993). For several reasons, these are not strictly comparable to our study. For one, only Willmott et al. present the station distribution and indicate neither the years utilized to calculate water balance nor the mean rainfall in these years at the stations in their data set. (Baumgartner and Reichel do provide a map of rainfall.) Both this study and that of Mintz and Walker use very coarse grid averages. Nevertheless, a comparison with their results provides some interesting similarities and contrasts.

#### 4.1 Evapotranspiration Maps

The evapotranspiration maps of Willmott et al. (1985) (henceforth referred to as WRM) and Baumgartner and Reichel (1975) (henceforth referred to as BR), both calculated from Thornthwaite's data set, show excellent agreement with each other and good agreement with ours. Maximum values are found in the equatorial region and are in the range of 75 to 125 mm/mo on the WRM map (900 to 1400 mm/an), compared to 1000 to 1500 mm/an on ours. Their core region with ET in excess of 100 mm/mo lies close to our 1250 mm/an contour. Differences are more apparent in the higher latitudes. In the central Sahel, at about 15 ° N, our calculations give approximately 500 mm/an, compared to 50 mm/mo on the WRM map. Near the southern limit of the Sahara at c. 18 ° N lies our 200 mm/an contour, their 25 mm/mo contour. These same contours border the Namib desert in southern Africa. Differences of this magnitude can readily be accounted for by the coarse resolution of the WRM map (4 ° × 5 °) and the steep gradients in the semi-arid transition zones.

Our evapotranspiration calculations show the best agreement with those of Mintz and Walker (1993) (hence forth referred to as MW). Their annual map



indicates that ET reaches about 1100 mm/year in the equatorial regions, in reasonably good agreement with our values of about 1250 mm. On the July map, the 3 mm/day contour bounding the area of maximum ET coincides with our 100 mm/mo contour, encompassing the area between about 3 °N and 16 °N. MW show the 2 mm/day contour at about 18 °N, roughly the location of our 50 mm/mo contour. Both are located at about 5 °S in the southern hemisphere. In January, the area of maximum moves southward to encompass the area between 2 °N and 10 °S on the MW map, but extends to about 15 °S on our map. Similar agreement is apparent in areas of minimum ET as well, particularly in the southern hemisphere.

All four estimates are considerably higher than those of Henning (1989), especially in the equatorial belt. Near the southern limit of the equatorial maximum at 5 S, the estimates of WRM, BR and our own indicate about 1400 to 1500 mm/an, compared to about 1100 mm/an on the Henning map. Near 10 °N, where the semi-arid zone begins, Henning indicates 700 - 800 mm/an, compared to 900 to 1100 mm for the other estimates. One factor contributing to Henning's low estimates are the low values of net radiation he calculates for Africa from empirical formulae; they are considerably lower than satellite estimates (e.g., Ba and Nicholson 1996). The discrepancies are particularly large in arid and semi-arid regions, where his surface albedo values are smaller than generally accepted (e.g., 27% throughout the Sahara).

## 4.2 Runoff Maps

Runoff can be compared with both BR and Henning. On our map, runoff ranges from about 200 to 500 mm/an in equatorial latitudes bounded by roughly 8 °N and 10 °S. A second area with runoff exceeding 200 mm is found along the western Guinea coast, in the area of Sierra Leone and Guinea. This is quite similar

to the BR map, however they show a small core with values exceeding 600 mm/an, compared with 500 mm/an on our map. The location of the desert areas where runoff becomes negligible is also similar on both maps, but our map gives substantially higher runoff in some semi-arid regions. In the southern Sahel (c. 12 ° to 15 ° N), our map gives 10 to 50 mm/an, compared to less than 10 mm/an on the map of BR. The Henning calculations exceed these by nearly an order of magnitude in the outer tropics, but agree reasonably well with BR and with our estimates in the southern equatorial latitudes (c. 15 ° S to the equator), but give values 5 to 10 times larger in the northern equatorial latitudes to c. 12 ° N. Both BR and Henning show a very strong western equatorial maximum over Cameroon, a realistic feature captured in the manual map analysis, but missed in our computer contoured map.

Runoff calculations are extremely difficult to verify. Some confidence in our results can be gained with a rough comparison with river discharge in three diverse parts of Africa. The rivers with available data are the Niger in West Africa, the Zaire in western equatorial Africa, and the tributaries to Lake Victoria in eastern equatorial Africa. Data for these three are plotted in Fig. 14.

In each case, the catchment area was roughly approximated, as indicated in Fig. 14, and average rainfall and runoff for that area were calculated for each year for which discharge data were also available. Then the data were averaged for two sub-periods within the record, one constituting relatively dry conditions, another relatively wet. The resultant differences in rainfall, runoff and discharge are given in Tab. 1.

Overall, the trends of both rainfall and runoff are markedly similar qualitatively to that of discharge (Fig. 14). However, the reduction in discharge in the drier period is quantitatively closer to that in runoff than that in rainfall. For the Niger River area, rainfall was 62 % lower during 1970-88 than during 1950-69, while runoff was 26% lower. River discharge was reduced by 40 % during the second

period. For the Zaire River, rainfall, runoff and discharge were not significantly different in the earlier and later periods, so that shorter wet and dry period were chosen for comparison. Rainfall and runoff were 2 % and 10 % lower, respectively, during 1950-59 than during 1960-69, while discharge was 18% lower. For the Lake Victoria area, with a shorter discharge record, rainfall was 13% lower during 1956-69 than during 1970-78, while runoff was 5% lower. The discharge of tributaries into the lake was virtually the same during the two periods. Thus, our runoff estimates are reasonably consistent with discharge data. Better agreement might result if calculations were done for precise catchment areas.

#### 4.3 Zonal Averages

A more precise comparison with BR and Henning can be mapped using continental and zonal averages, which they present. Tab. 2 gives, for each 5 degrees of latitude, the average evapotranspiration and the evaporation and runoff ratios as calculated in this study (i.e., the ratios of these quantities to precipitation). For comparison, the zonal averages of ET from Henning and the evaporation ratio from BR are used.

There is reasonably close agreement with BR except in the equatorial latitudes and at 15 ° to 20 ° S, where our evaporation ratios exceed theirs by 10 % or more. The difference can be accounted for by the higher rainfall totals on our maps in this region. There is also a discrepancy in the region of the Sahara, but this is considered insignificant in view of the low mean annual rainfall there, on the order of a few tens of mm or less in most areas. The discrepancy results in part by BR's addition of evaporation from surface waters in the Saharan region, producing the evaporation ratios that exceed 1.

In contrast, our ET figures greatly exceed those of Henning, by hundreds of

mm in several cases; there is reasonably good agreement in the outer tropics and subtropics. The low ET of Henning is consistent with the excessively high runoff in their study. Our ET calculations show a weak, relative minimum in equatorial latitudes, a consequence of higher cloudiness in equatorial regions. That feature is not apparent in the ET calculations of Henning.

#### 4.4 Soil Moisture

Only WRM provide continental estimates of soil moisture. The soil moisture fields strongly resemble the ET fields in both shape and magnitude. Despite the close agreement between our ET calculations and theirs, there are large differences in soil moisture estimates. In the central Sahel near  $15^{\circ}\text{N}$ , there map indicates mean soil moisture below 25 mm, compared to 50 mm on our map. There is better agreement in the southern hemisphere, with 25 mm near  $20^{\circ}\text{S}$  and 50 mm near  $15^{\circ}\text{S}$  on both maps. The biggest discrepancy is in the equatorial latitudes. WRM indicate a core with soil moisture exceeding 75 mm; it exceeds 100 mm in only about half of this area. Our calculations generally give over 200 mm throughout this area, compared with a maximum of about 125 mm in a very small core on the WRM map.

Our values, which have been verified for the central Sahel (Marengo et al. 1996), seem more realistic. In the equatorial region the water holding capacity of the soils is 200 - 500 mm. Thus, soil moisture values as low as 75 to 100 mm imply a low degree of soil saturation, which is unlikely in the equatorial tropics with year-round rainfall. WRM's calculations suggest values of at most 100 to 150 mm in the wet season, well below that needed to sustain evapotranspiration at the potential rate.

Calculations of MW suggest a much higher degree of soil saturation, and are

thus consistent with our results. However, a direct comparison with their results is not possible because they present maps of soil "wetness", the ratio of soil moisture to water holding capacity. The annual average in the equatorial regions is over 70%. It reaches 90% in both July and October, but about 70% in January and April. The latitudes of maximum saturation (exceeding 90%) shift from a narrow zone just north of the equator in July to a wide latitudinal band south of the equator in January. These areas correspond closely with the area in our maps where mean monthly soil moisture exceeds 200 mm.

## 5. Summary and Conclusions

This study has produced high-resolution estimates of evapotranspiration, runoff and soil moisture over the African continent. ET generally exceeds 1500 mm/an in the equatorial regions, with a few areas where ET is in excess of 2000 mm/an. It ranges from about 500 to 750 mm/an in the semi-arid regions of eastern Africa and about 200 to 750 mm/mo in the semi-arid regions of the subtropics. On a monthly scale, maxima are on the order of 100 mm/mo or more. It is on the order of 5 to 50 mm/an in the semi-arid regions bordering the deserts. Runoff is about 200 to 500 mm/an in the equatorial latitudes, but generally less than 50 mm/an in semi-arid regions of Africa. It approaches zero for mean annual rainfall below 500 mm.

Interannual variability is particularly large for ET. In some areas, the difference between wet and dry years exceeds 500 mm/an. It can exceed 250 mm/an over much of the continent. Runoff can vary by over 100 mm/an from year to year in wetter regions of West Africa. In the equatorial latitudes, even zonal means can vary by over 200 mm/an, compared to a long-term mean on the order of 350 mm/an. In the semi-arid sub-equatorial latitudes, the zonal means can vary by 100 to 150 mm/an.

Overall, there is good agreement between our calculations of ET and those of several other studies. Nevertheless, a considerable range of values for the African continent appears in the literature. There is less agreement in the case of soil moisture, although our values are consistent with the recent estimates of Mintz and Walker (1993). Some earlier studies appear to have dramatically underestimated ET. This is partly a consequence of the relatively low values of net radiation obtained from traditional formula, as compared to modern satellite estimates. Differences in assumed surface albedo, particularly in desert areas such as the Sahara, are a contributing factor.

#### ACKNOWLEDGMENTS

This work was sponsored by the TRMM project via NASA Grant NAG5-1587.

Tab. 1 Differences in river discharge, rainfall and runoff between a relatively wet and a relatively dry period (See Fig. 14). Rainfall and runoff are for areas roughly approximating the catchment areas, as indicated in the caption of Fig. 14. The periods are given in the second column, with negative values for rainfall, runoff and discharge indicating higher values in the first period.

Basin	Years	Rainfall	Runoff	Discharge
Niger	(50~69) - (70~88)	-62%	-26%	-40%
Zaire	(50~59) - (60~69)	-2%	-10%	-18%
Victoria	(56~69) - (70~78)	-13%	-5%	0%

Tab. 2 Water Balance Parameters for Five-Degree Latitudinal Zones over Africa. First three columns are the annual runoff ratio, the annual evaporation ratio, and annual evapotranspiration, as calculated by this study. The four column is Henning's estimates of evapotranspiration and the fifth column is Baumgartner and Reichel's estimate of the evaporation ratio.

	N/P	E/P	E	$E_H$	$E/P_{BR}$
35~40°N	10	90	594	655	89
30~35°N	1	99	215	186	105
25~30°N	0.0	100	23	55	117
20~25°N	0.0	100	35	58	97
15~20°N	0.2	100	244	198	97
10~15°N	5	95	727	517	93
5~10°N	14	86	1193	773	81
EQ~5°N	13	87	1144	846	74
5°S~EQ	12	88	1178	958	77
10~5°S	9	91	1058	880	84
15~10°S	12	88	1023	772	86
20~15°S	5	95	730	715	85
25~20°S	2	98	446	559	91
30~25°S	3	97	450	428	93
35~30°S	3	97	441	423	92



## REFERENCES

Albarecht, F., 1951: Die Methoden zur Bestimmung der Verdunstung der natürlichen Erdoberfläche. *Arch. Meteor. Geoph. Biokl., Ser. B*, III, 1-38.

Albrecht, F., 1962: Die Berechnung der natürlichen Verdunstung (Evapotranspiration) der Erdoberfläche aus klimatologischen Daten. *Ber. Deutschen Wetterdienstes*, 14, Offenbach a. M., Germany, 54 pp.

Ba, M. B., G. Dedieu, S. E. Nicholson, 1996: Seasonal and Interannual variability of surface radiation budget over African continent as derived from Meteosat. Part I: Derivation of Insolation and Surface Albedo. To be submitted to *J. Climate*.

Ba, M. B., and S. E. Nicholson, 1996: Seasonal and Interannual variability of surface radiation budget over African continent as derived from Meteosat. Part II: Surface Insolation, Albedo and Net Radiation Climatology and Interannual variability. To be submitted to *J. Climate*.

Baumgartner, A., and E. Reichel, 1997: *The World Water Balance*. R. Oldenbourg, Munich/Vienna, 179 pp.

Brubaker, K., D. Entekhabi, and P. Eagleson, 1993: Estimation of continental precipitation recycling. *J. Climate*, 6, 1077-1089.

Chahine, M. T., 1992a: GEWEX: The global energy and water cycle experiment. *EOS*, 73, 9-14.

Chahine, M. T., 1992b: The hydrologic cycle and its influence on climate. *Nature*, 359, 9-14.

Dorman, J. L., and P. J. Sellers, 1989: A global climatology of albedo, roughness length, and stomatal resistance for atmospheric general circulation models as represented by the Simple Biosphere Model (SiB). *J. Appl. Meteor*, 28, 833-855.

Dümenil, L., K. Isele, H.-J. Liebscher, U. Schröder, M. Schumacher, and K. Wilke, 1993: Discharge data from 50 selected rivers for GCM validation. Report No. 100, Max-Planck-Institut für Meteorologie and Global Runoff Data Center (Issn 0937-1060), Hamburg, 61 pp.

Entekhabi, D., I. Rodriguez-Iturbe, and R. Bras, 1992: Variability in large-scale water balance with a land surface-atmosphere interaction. *J. Climate*, 5, 798-813.

Farrar, T. J., S. E. Nicholson, and A. R. Lare, 1994: The influence of soil type on the relationships between NDVI, rainfall and soil moisture in semi-arid Botswana. Part II. NDVI response to soil moisture. *Rem. Sens. Environ.*, 50, 121-133.

Henning, D., 1989: *Atlas of the Surface Heat Balance of the Continents*. Gebrüder Borntraeger, Berlin, 402 pp.

Howell, P., M. Lock and S. Cobb, 1988: *The Jonglei Canal: Impact and Opportunity*. Cambridge University Press, New York, 537 pp.

Lare, A. R., 1992: An investigation into land-surface feedback and the African drought using climatology modeling. Ph.D. dissertation, Department of

Meteorology. Florida State University, 333 pp [available from Department of Meteorology, Florida State University. Tallahassee, FL 32306].

Lare, A. R., and S. E. Nicholson, 1990: A climatonic description of the surface energy balance in the Central Sahel. Part I: Shortwave radiation. *J. Appl. Meteor*, 29, 123-137.

Lare, A. R., and S. E. Nicholson, 1994: Contrasting conditions of surface water balance in wet and dry years as a possible land surface-atmosphere feedback mechanism in the West African Sahel. *J. Climate*, 7, 653-668.

Lettau, H. H., 1969: Evapotranspiration climatology. I. A new approach to numerical prediction of monthly evapotranspiration, runoff and soil moisture storage. *Mon. Wea. Rev.*, 97, 691-699.

Lettau, H.H., and Baradas, M.W., 1973: Evapotranspiration climatology II: Refinement of parameterizations exemplified by application to the Mabacan River watershed, *Mon. Wea. Rev.* 101, 636-649.

Marengo, J. A, S. E. Nicholson, A. R. Lare. B. Monteny, and S. Galle, 1996: Application of evapoclimatology to monthly surface water balance calculations at the HAPEX-Sahel supersites. *J. Appl. Meteor.*, in press.

Mintz, Y., and G. K. Walker, 1993: Global fields of soil moisture and land surface evapotranspiration derived from observed precipitation and surface air temperature. *J. Appl. Meteor.*, 32, 1305-1334.

Nicholson, S. E., 1989: African drought: Characteristics, casual theories and global teleconnections. In Berger, A., and Dickinson, R.E., and Kidson, J.W., editors, *Understanding Climate Change* (A. Berger, R. E. Dickinson and J. W. Kidson, eds.), AGU, 79-100.

Nicholson, S. E., 1994: Recent rainfall fluctuations in Africa and their relationship to past conditions over the continent. *The Holocene*, 4, 121-131.

Nicholson, S. E., and A. R. Lare, 1990: A climatonic description of the surface energy balance in Central Sahel. Part II: The evapoclimatology submodel. *J. Appl. Meteor.* 29, 138-146.

Nicholson, S. E., and I. Palao, 1993: A re-evaluation of rainfall variability in the Sahel. Part I. Characteristics of rainfall fluctuations. *Int. J. Climatol.*, 13, 371-389.

Nicholson, S. E., and T. J. Farrar, 1994: The influence of soil type on the relationships between NDVI, rainfall and soil moisture in semi-arid Botswana. Part I. NDVI response to rainfall. *Rem. Sens. Environ.* 50, 107-120.

Nicholson, S.E., A. R. Lare, J. A. Marengo, and P. Santos, 1996. A revised version of Lettau's evapoclimatology model. *J. Appl. Meteor.*, in press.

Pitman, A. J., and co-authors, 1993: PILPS: Results from off-line control simulations (Phase 1a). WCRP/IGPO Publication Series, No. 7, World Meteorological Organization, Geneva, 47 pp.

Rawls W. J., and D. Brakenzieck, 1989: Estimation of soil water retention and hydraulic properties. *Unsaturated Flow in Hydrologic Modeling: Theory and Practice* (H. J. Morel-Seytoux, Ed.), Kluwer Academic Publishers, 275-300.

Saxton, K. E., W. J. Rawls, J. S. Romberger, and R. J. Papendick, 1986: Estimating generalized soil-water characteristics from texture. *Soil. Sci. Soc. Am. J.*, 50, 1031-1036.

Serafini, Y. V., and Y. C. Sud, 1987: The time-scale of the soil hydrology using a simple water budget model. *J. Climatol.*, 7, 585-591.

Walsh, J. E., W. H. Jasperson, and B. Ross, 1985: Influence of snow cover and soil moisture on monthly air temperature. *Mon. Wea. Rev.*, 113, 756-768.

Warrilow, D., 1986: The sensitivity of UK meteorological office atmospheric general circulation model to recent changes to the parameterization of hydrology. *Proc. ISLSCP Conference, Rome, Italy, 2-6 December 1985*, ESA SP-248, 143-149.

Webb, R. S., C. E. Rosenzweig, and E. R. Levine, 1991: A global data set of soil particle size properties. NASA Tech. Memo. 4286, 33 pp.

Webster, P. J., 1994: The role of hydrological processes in ocean-atmosphere interactions. *Rev. Geophys.*, 32, 427-476.

Willmott, C. J., C. N. Rowe and Y. Mintz, 1985: Climatology of the terrestrial seasonal water cycle. *J. Climatol.*, 5, 589-606.

Zobler, L., 1986: A world soil file for global climate modeling. NASA Tech. Memo.  
87802. 76 pp.

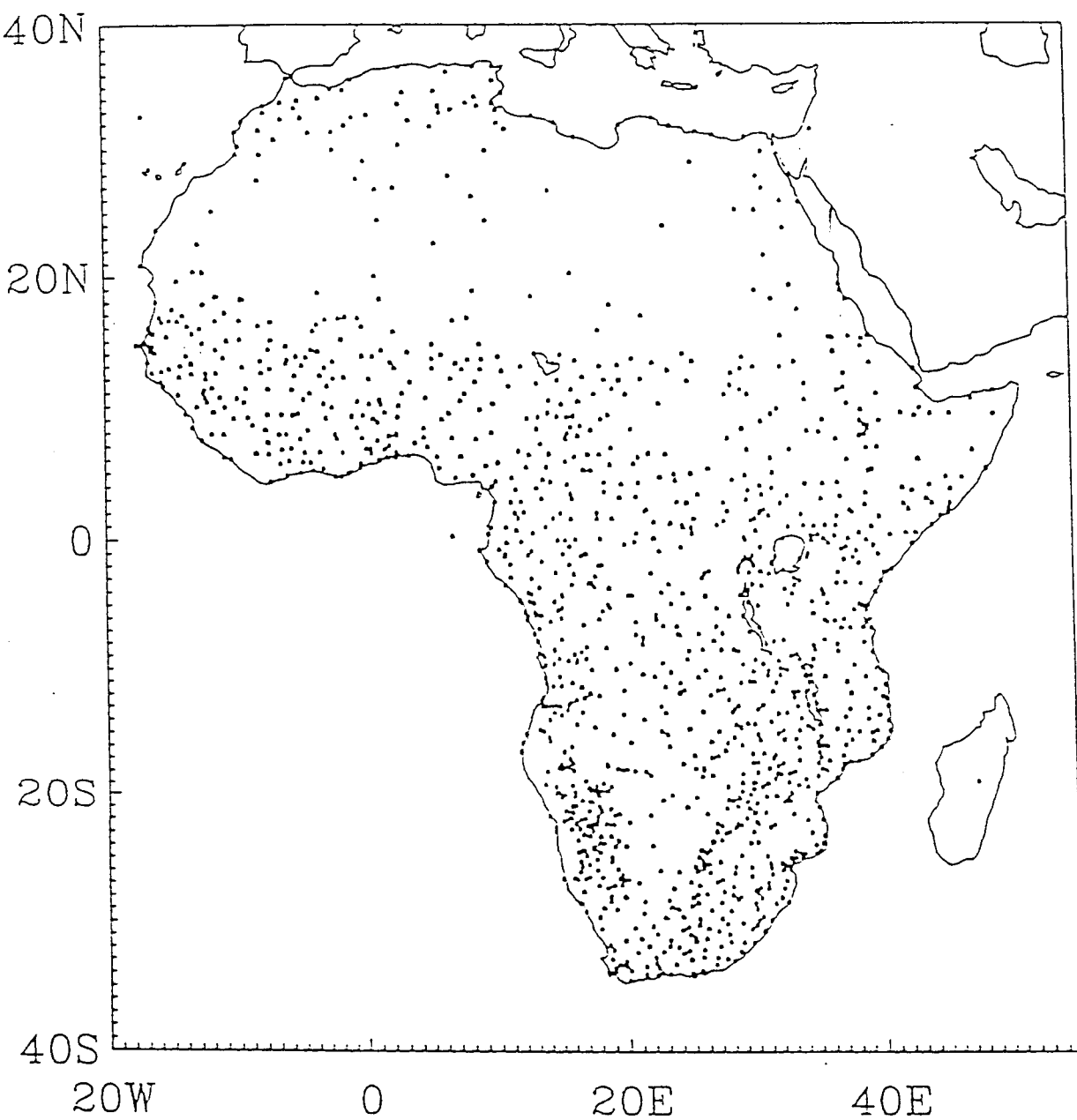
## FIGURES

1. Distribution of rainfall stations used to calculate water balance.
2. Mean rainfall (in mm) over Africa during 1950 to 1989. Top diagram: annual mean; bottom left: January mean; bottom right: July mean.
3. Overview of the evapoclimatology model used to calculate water balance parameters in this study.
4. Mean evapotranspiration over Africa, as calculated by the evapoclimatology model. Top diagram: annual mean (mm/an); bottom left: January mean (mm/mo); bottom right: July mean (mm/mo).
5. Mean runoff over Africa, as calculated by the evapoclimatology model. Top diagram: annual mean (mm/an); bottom left: January mean (mm/mo); bottom right: July mean (mm/mo).
6. Mean exchangeable soil moisture (in mm) over Africa, as calculated by the evapoclimatology model. Top diagram: annual mean; bottom left: January mean; bottom right: July mean.
7. Mean water balance at seven diverse African locations. Top diagram: solid line is rainfall, dashed line is evapotranspiration, and dotted line is runoff, all in mm/mo. Bottom diagram: mean monthly exchangeable soil moisture in mm. Mean annual rainfall (in mm) is given in the upper right.

8. Difference (in mm) between annual rainfall in 1955 and 1983, continentally an exceedingly wet and an exceedingly dry year, respectively.
9. Difference (in mm) between annual runoff in 1955 and 1983, continentally an exceedingly wet and an exceedingly dry year, respectively.
10. Difference (in mm) between annual evapotranspiration in 1955 and 1983, continentally an exceedingly wet and an exceedingly dry year, respectively.
11. Monthly runoff (in mm) at six locations in wet years and in dry years. The dashed line indicates the mean for the ten wettest years during the 1930-1990 period; the dotted line indicates the mean for the ten driest years during this period; and the solid line indicates the mean for the entire period.
12. Monthly evapotranspiration (in mm) at six locations in wet years and in dry years. The dashed line indicates the mean for the ten wettest years during the 1930-1990 period; the dotted line indicates the mean for the ten driest years during this period; and the solid line indicates the mean for the entire period.
13. Zonal averages of rainfall and runoff (mm/an) over the African continent during the period 1950 to 1989 for each ten degrees of latitude from 40 °N to 40 °S. Vertical axis on the right refers to runoff, indicated in solid bars; vertical axis on the left refers to rainfall, indicated in open bars.
14. Time series of annual rainfall, runoff and river discharge for three basins over Africa (discharge data from Howell et al. 1988 and Dümenil et al. 1993). For each



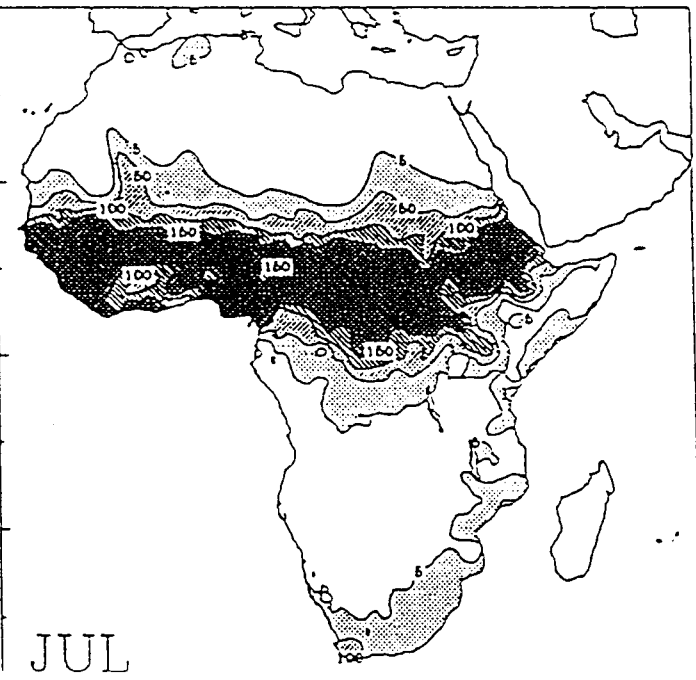
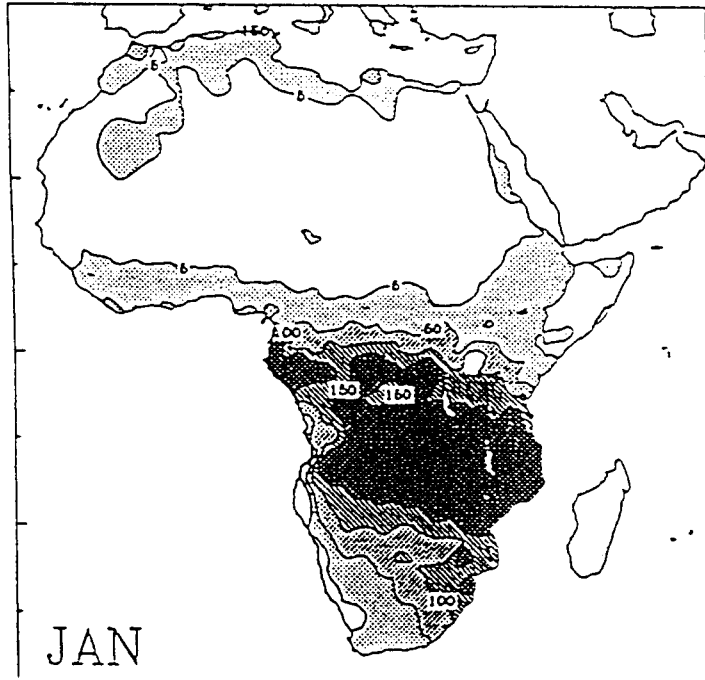
basin, the top diagram indicates rainfall (open bars) and runoff (shaded bars) in mm, with the left hand axis referring to rainfall, the right hand axis referring to runoff, and the bottom diagram indicates discharge (lightly shaded bars). For the Niger and Zaire rivers, discharge is in  $\text{m}^3/\text{s}$ ; for the Victoria tributaries, discharge is in mm and represents an annual average normalized by the area of the lake. The Niger River discharge is compared with rainfall and runoff in the area bounded by 10 and 20 °N and 15 and 0 °W. The Zaire River discharge is compared with rainfall and runoff in the area bounded by 5 °N and 15 °S and the Atlantic coast and 30 °E. The discharge of the Lake Victoria tributaries is compared with rainfall and runoff in the area bounded by 3 °N and 5 °S and 30 and 38 °E.



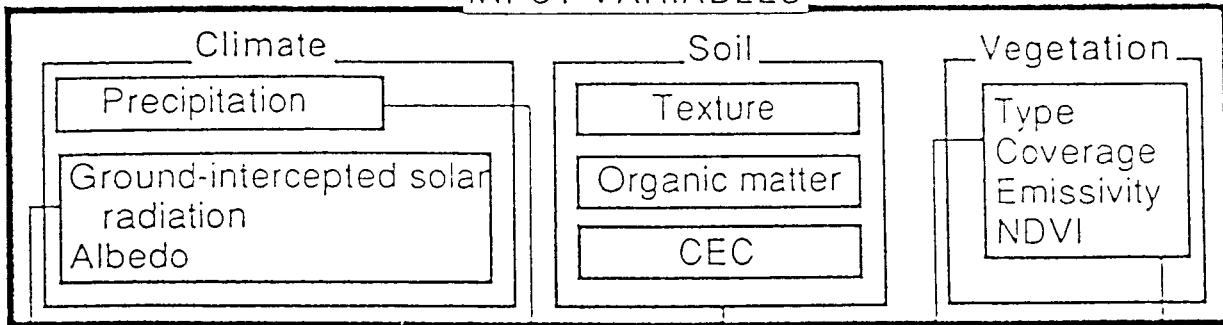
|



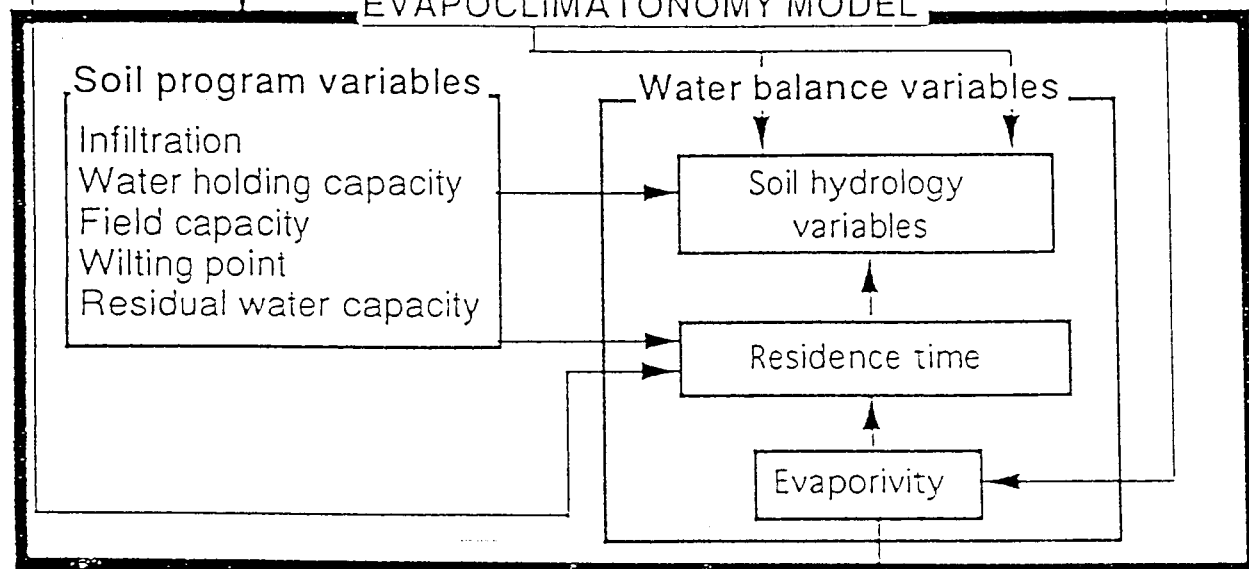
Annual Rainfall



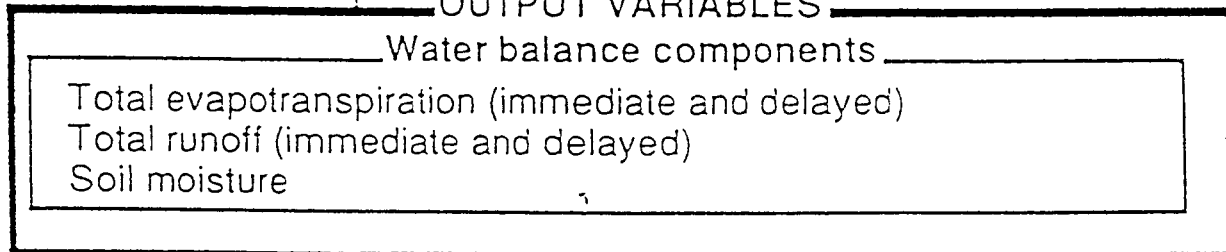
## INPUT VARIABLES



## EVAPOCLIMATONOMY MODEL

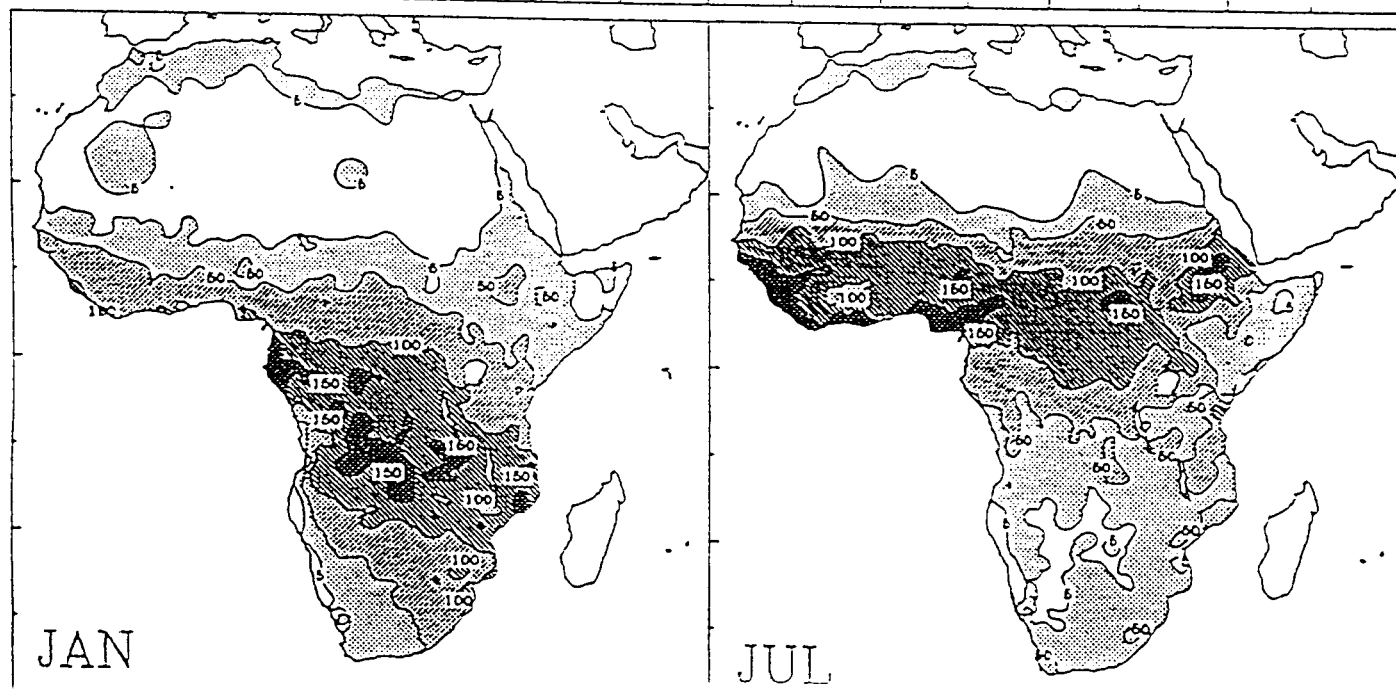


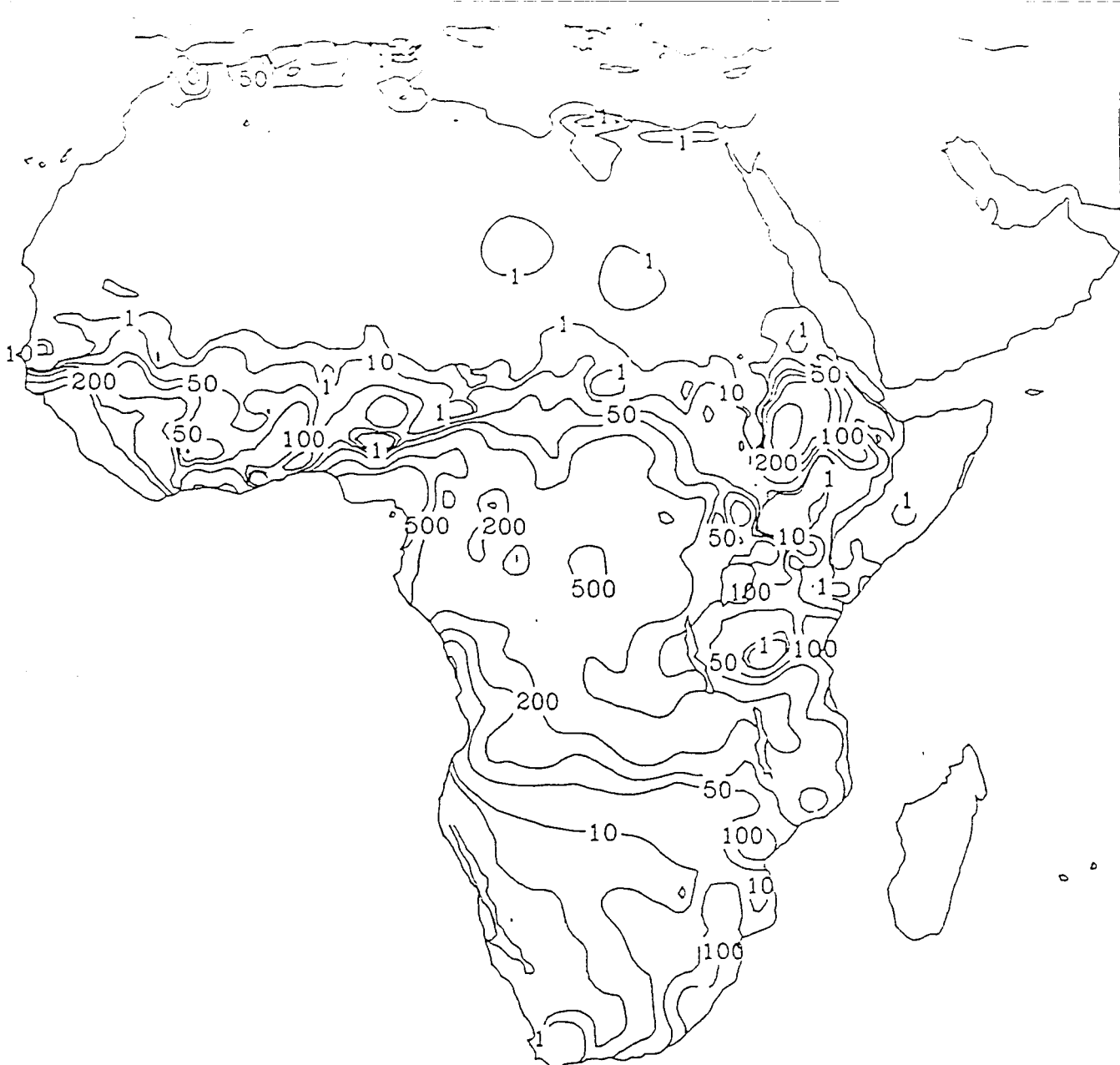
## OUTPUT VARIABLES



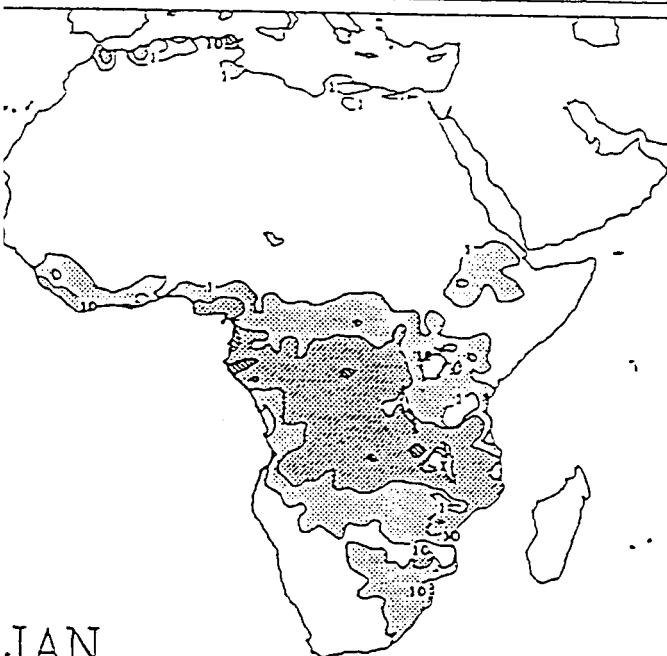


Annual Evapotranspiration

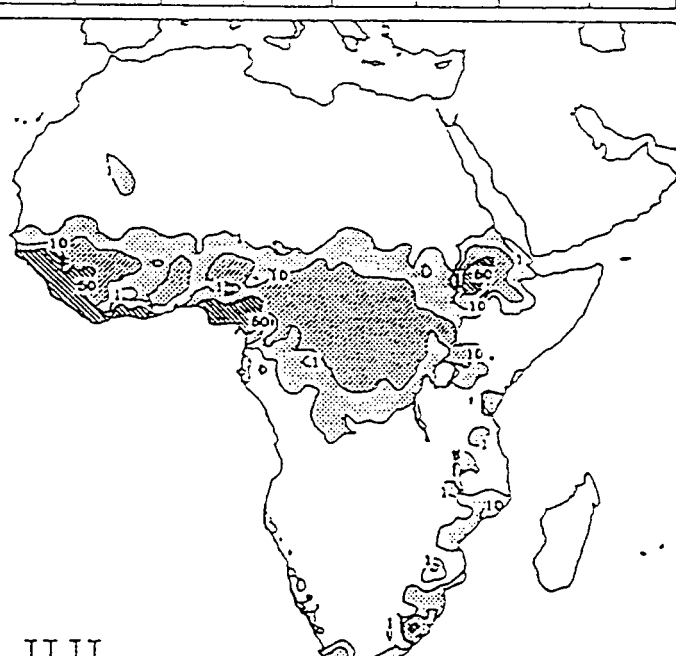




Annual Runoff



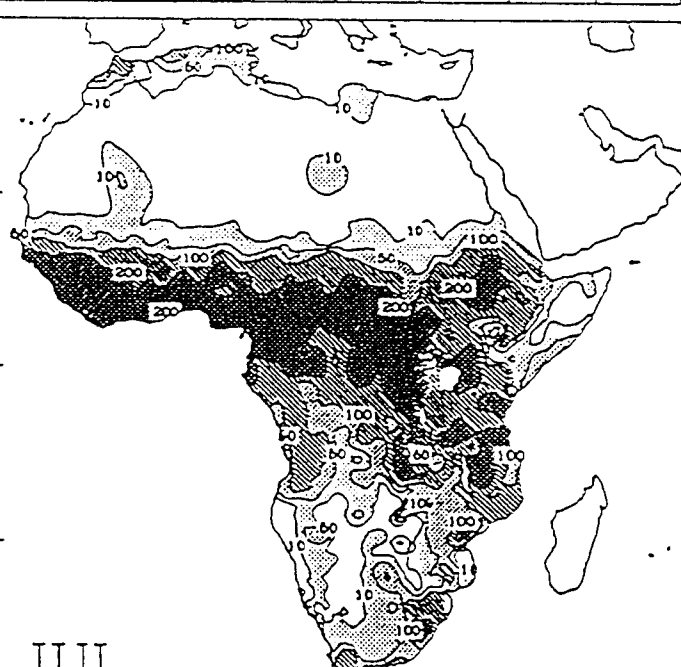
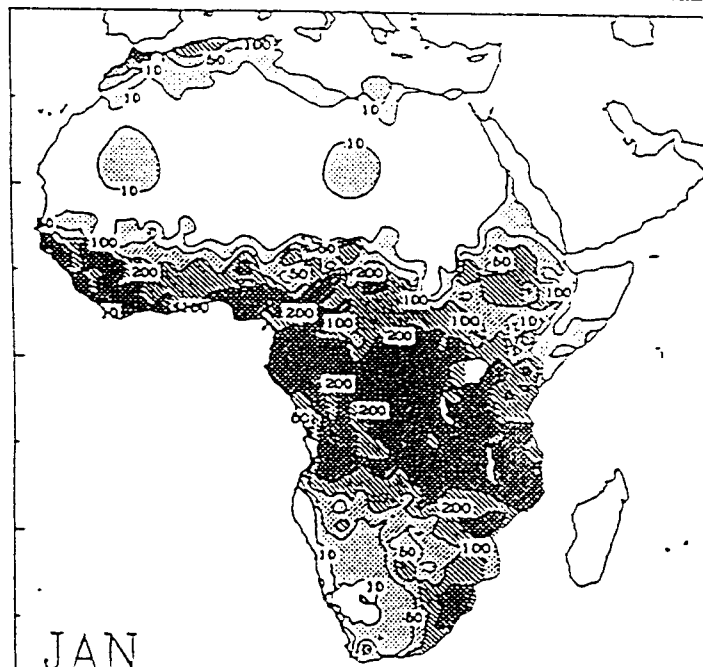
JAN

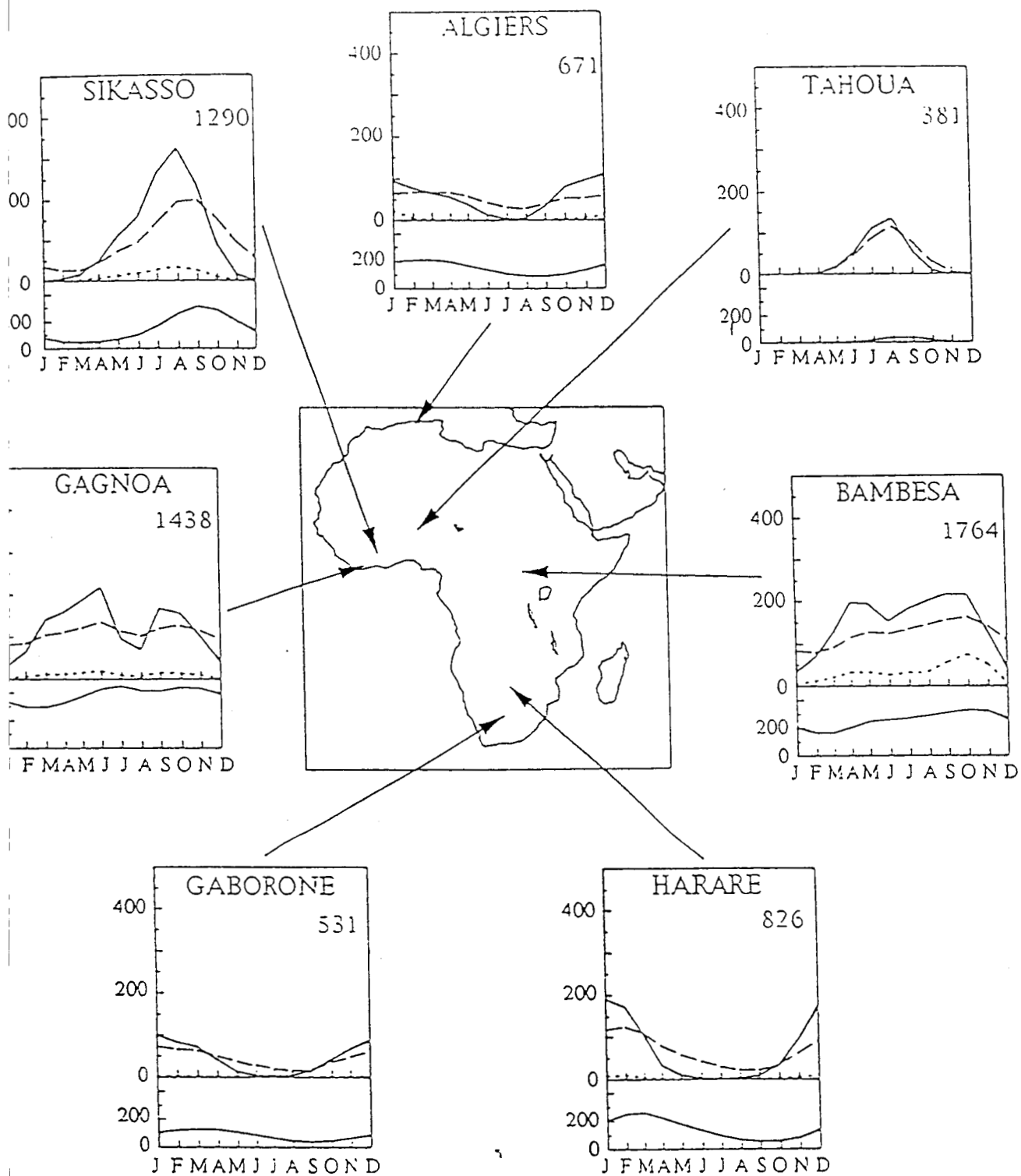


JUL

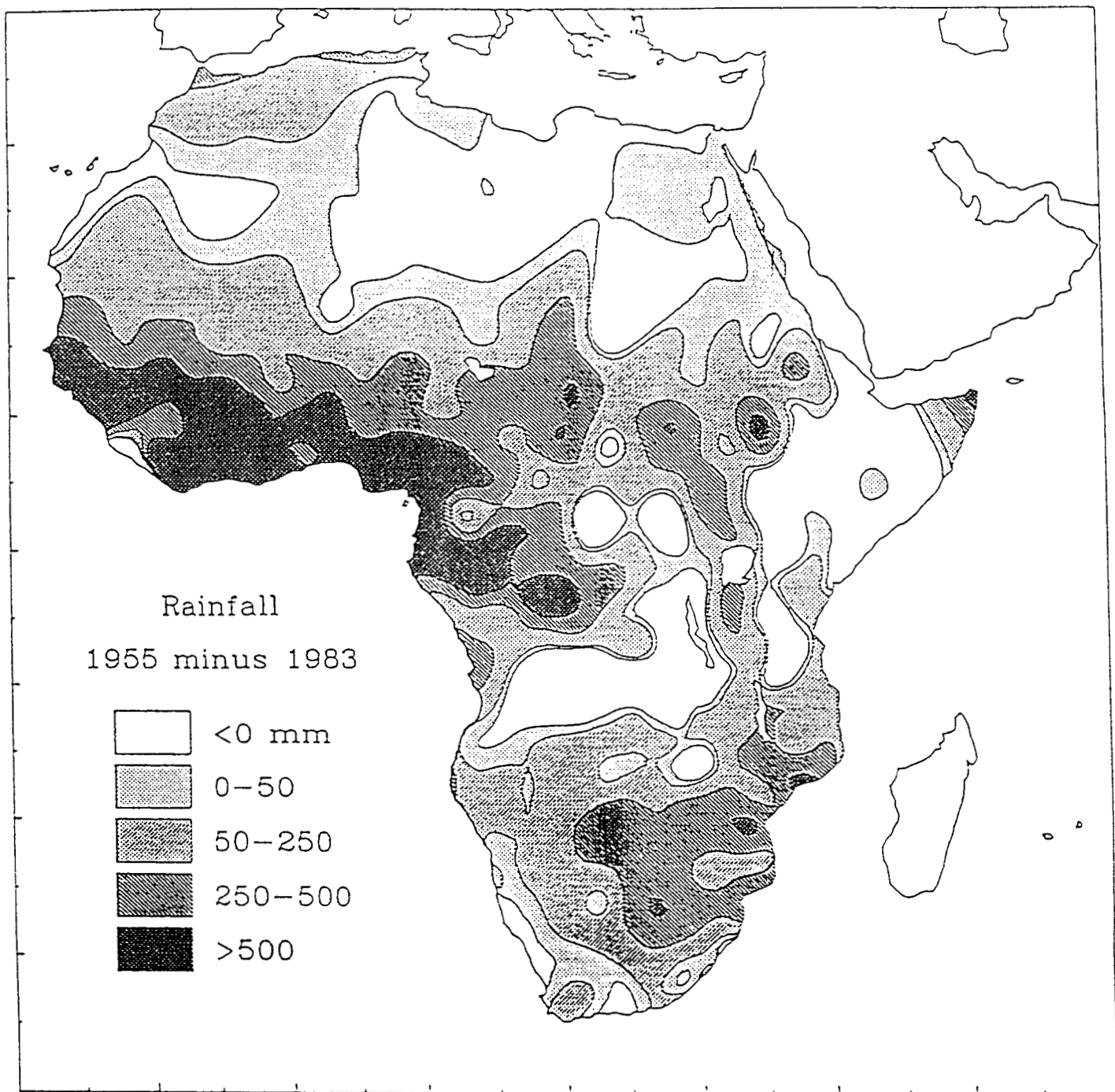


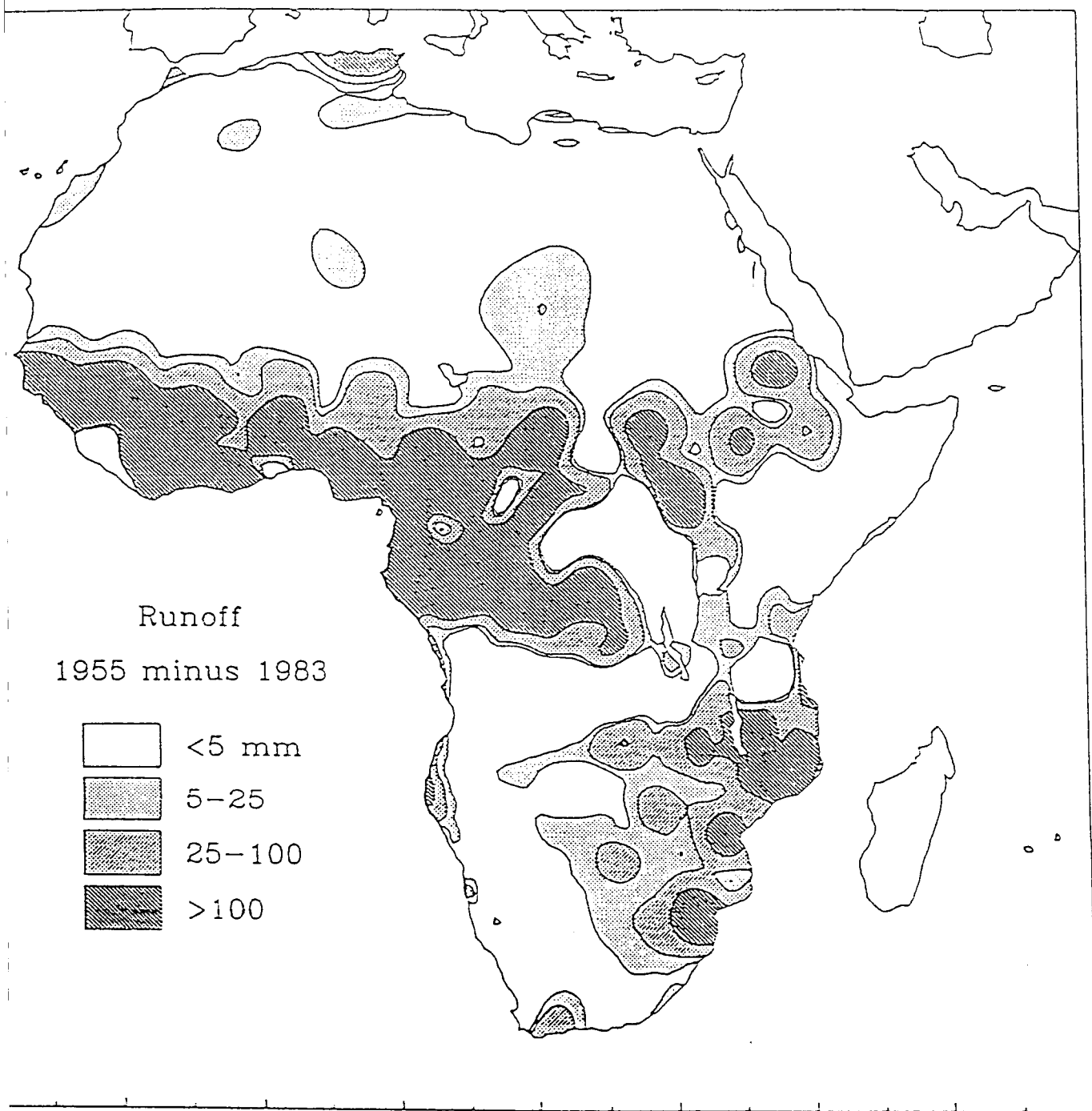
Annual Soil Moisture



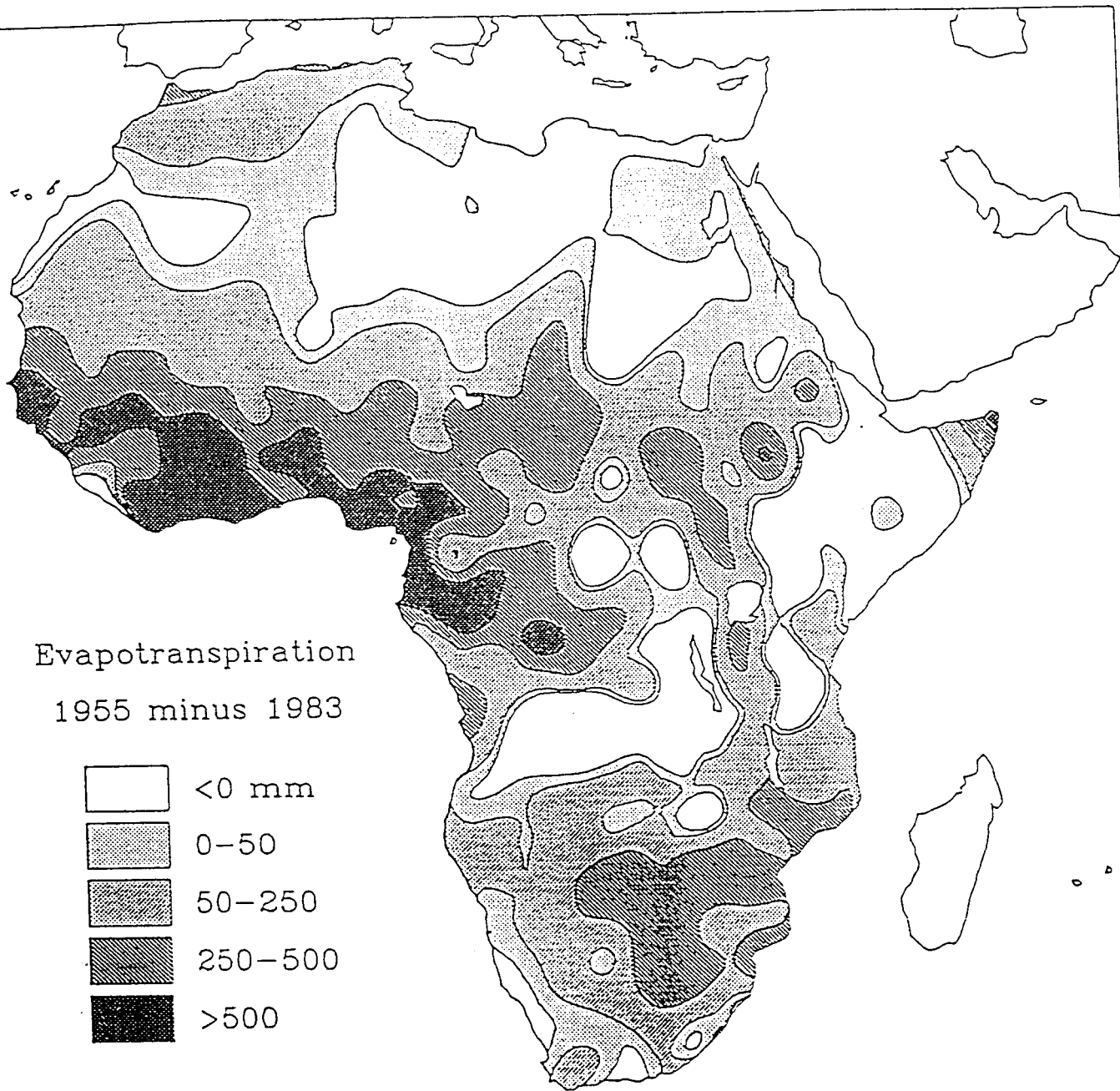
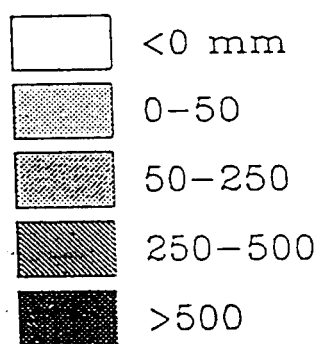


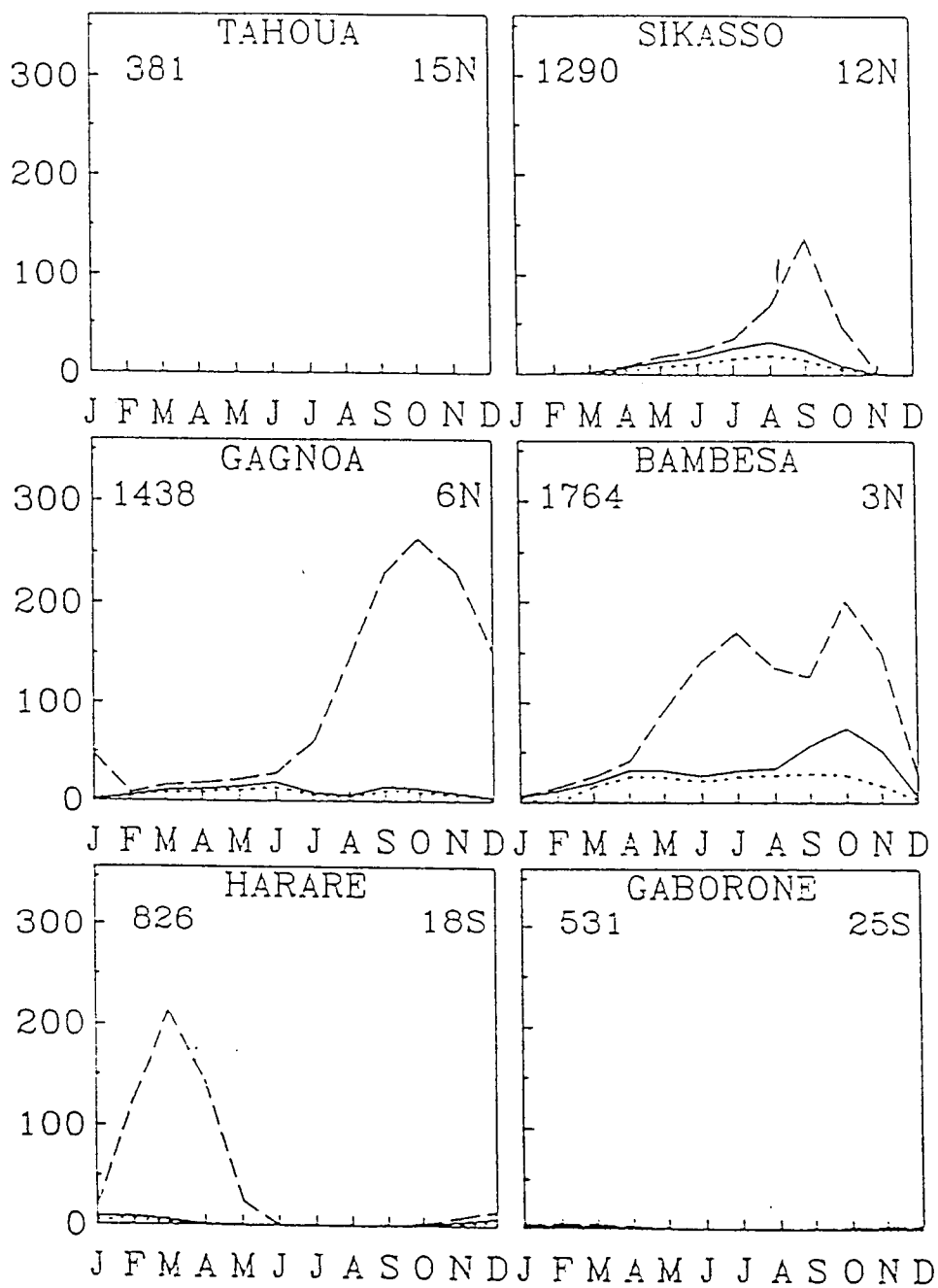




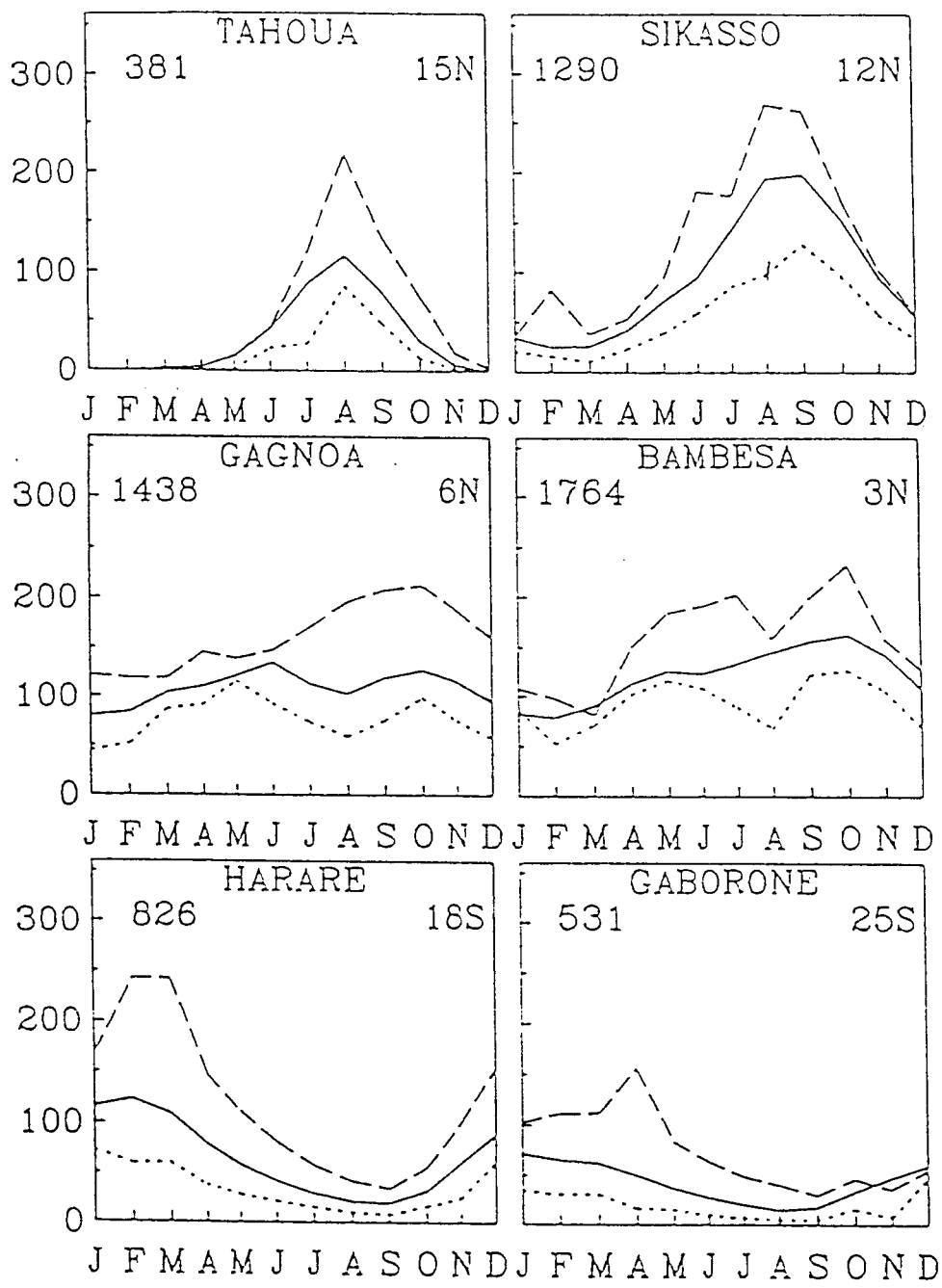


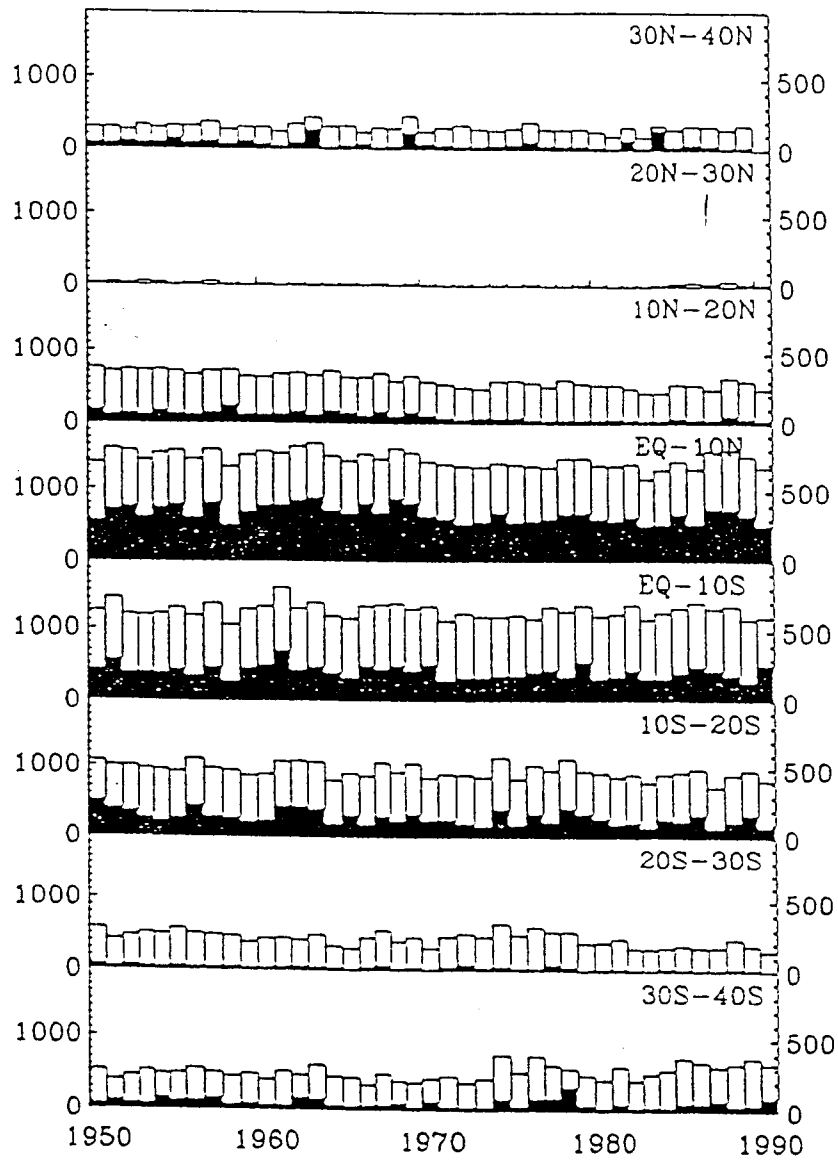
Evapotranspiration  
1955 minus 1983





TRMM-W/Bol Fig11 Runoff





TRMM-W/Bal Fig 13 Rainfall/Runoff

